A New Individual-Based Modelling Framework for Bacterial Biofilm Growth Applied to Cold Plasma Treatment

By Yi-Ping Lo

A Doctoral Thesis

Submitted in partial fulfilment of the requirements for the award of Doctor of Philosophy of Loughborough University

Date: 12/02/2013

I would like to dedicate this thesis to my loving parents ...

Acknowledgements

The writing of this thesis has been an emotional and intense journey. There are several people I would like to express my gratitude to, for their guidance, encouragement, advice and support throughout my whole PhD journey.

First and foremost I would like to thank my main supervisor, Dr. John Ward. Many thanks for his encouragement, support, and patient guidance. I am grateful to be finishing this research with him.

I would like to thank Prof. Michael Kong, Dr. Felipe Iza and Dr. Robert Seager for all of their valuable comments, providing data and sharing their knowledges.

I would also like to thank Dr. Keith Watling for the technique support and Department of Mathematical Sciences and School of Electronic, Electrical and Systems Engineering for the financial support.

I also want like to thank my parents, Li-Lin Lee and Sez-Tsen Lo, and my sister, Dr. Ko-Yun Lo, for being so supportive of my education and decisions I made throughout my life. Many thanks for their understanding and always being there for me.

I also want to thank Xin Wang for her support and company, especially during a very difficult time of my life.

Abstract

Biofilms are colonies of bacteria attached to the surface at a solid-fluid interface. Bacteria in biofilm produce exo-polysaccharides (EPS) that form a gel-like matrix in which the bacteria are embedded. Biofilms have numerous consequences in industrial and medical settings, both positive (bioreactors, digestion) and negative (blocking, as corrosive damage of materials/devices, food contamination, clinical infection). The use of antibiotics or mechanical clearing can be effective at removing biofilms, but such treatments are not always effective or appropriate in all situations. Recently, non-thermal atmospheric plasma treatments have been proposed as an alternative (or complementary) form of treatment, that can target sites of infection with minimal damage to the surroundings (e.g. host cells in a clinical setting). These plasmas generate a multitude of chemical species, most of which are very short lived, that can infiltrate and diffuse into the biofilm killing the bacteria within. The aim of this thesis is to develop a multi-dimensional mathematical model to investigate the effect of a non-thermal plasma on biofilms in time and space and to identify key factors that determine effectiveness of the treatment.

Most of the chemical products of cold plasmas are too short lived, or too reactive, to be effective in killing the biofilms, it is the longer live species, e.g. ozone, hydrogen peroxide, acid species, that penetrated the biofilm and do the most damage. However, the EPS in biofilms is an effective barrier against ozone and hydrogen peroxide. No published biofilm model combines multi-dimensional growth with a detailed description of EPS production, hence a new mathematical model is developed and applied to simulating plasma treatment.

The thesis is split broadly into two parts. The first part presents a new biofilm model framework that simulates growth in response to any number of substrates (e.g. nutrient, oxygen). The model combines an Individual based model (IbM) description of bacteria (individuals or clusters) and substrates are described as a continuum. Novel features of the framework are the assumption that EPS forms a continuum over the domain and the explicit consideration of cellular energy (ATP). Simulations of this model demonstrate the contrast between biofilm grown with topical nutrient sources (forming irregular, bumpy biofilm) and basal nutrient source with topical oxygen such as biofilm grown on agar (forming regular spatially uniform biofilms).

The former is in broad agreement with experiments whilst the latter, to our knowledge, has been the subject of very little experimental study.

The second part extends the modelling framework to consider the effect of the plasma species. The simulations demonstrate that penetration is a key factor in their effectiveness, for which EPS plays a key role in preventing spread within and beyond the plasma treated zone. The simulations provide estimates of the timescale of equilibration of the main plasma species, predict the effect of combining these species and demonstrate how the constituents of the biofilm can change following treatment. A number of recommended suggestions for future theoretical and experimental study are discussed in the conclusions.

Contents

Chapter 1

Introduction

Biofilms are slimy colonies of bacteria, which grow on solid surfaces in a fluid environment. Some kinds of biofilms are used in the production of industrial goods or for water treatment. However, some of them cause damage in an industrial setting and disease in humans. A characteristic feature of most bacterial biofilms is the presence of an exopolysacchurades matrix produced by the bacteria, which helps maintain the structure of the biofilm. These substrates offer the bacteria an ideal living environment and help protect the bacteria from antibiotic agents. Consequently, the removal of harmful biofilms is not always an easy task. Among the more recent methods of biofilm removal is the application of cold plasma [1, 2, 3, 4, 5, 6, 7, 8, 9, 10]. In this thesis we discuss a new mathematical modelling framework designed to describe biofilm growth and use this model to investigate the cold plasma treatment of biofilms. In this chapter, Section 1.2 will give a brief introduction of bacterial biology and biofilms, which will later form the basis of the modelling framework. The next section will discuss the basic biology of biofilms, including their living environments, metabolism, formation, structure, effects, uses, the extracellular polymeric substance (EPS), and its functionality.

1.1 Biology of Bacteria

In microbiology, cells are categorised into prokaryotic and eukaryotic. Eukaryotic cells are all cells of unicellular and multicellular microorganisms which contain a nucleus. This category contains all animal, plant, and fungal cells. Prokaryotes have, in the past, been viewed as a group that largely exists as single cells, with a few exceptions (e.g. myxobacteria [11, 12]); however, more recently, as our understanding of microbiology and biofilms has become greatly enhanced, it has been generally realised that biofilms share many of the features of multicellular organisms. It is estimated that there are about $4 - 6 \times 10^{30}$ prokaryote cells on earth [13]. They are divided into two groups, namely, bacteria and archaea [14]. Though they have similar morphological features, the metabolic processes of these two kingdoms are quite different: Archaea have metabolic pathways more in common with the Eukaryotes (e.g. gene translation and transcription). Bacteria are a larger group among the prokaryotes, and play an important role in all natural environments. They decompose organic material, such as dead animals, plants, and the waste from the metabolic pathways of living organisms, and in turn become food for other creatures. Bacteria also play a key role in maintaining the balance of the atmospheric gasses, such as by consuming carbon dioxide and generating oxygen.

In the following subsections, we will discuss in some detail the biology relevant to the modelling in the future chapters.

1.1.1 Bacteria Morphology

The size of bacterial cells may vary, depending on their environment [15], but they are typically 1–5 μm in length [16]. The smaller sized bacteria cells are able to take up nutrients and export waste from their metabolism faster than can larger cells, therefore, they gain more nutrients and grow faster than larger cells under low nutrient concentrations. The shape of a single cell is either spherical or rod-shaped (round-ended cylinders), the so-called cocci and bacillus, respectively. Sometimes cells aggregate together and form various shapes of clusters or chains as shown in Figures 1.1 and 1.2.

The internal structure of bacterial cells is shown in Figure 1.3. The bacte-

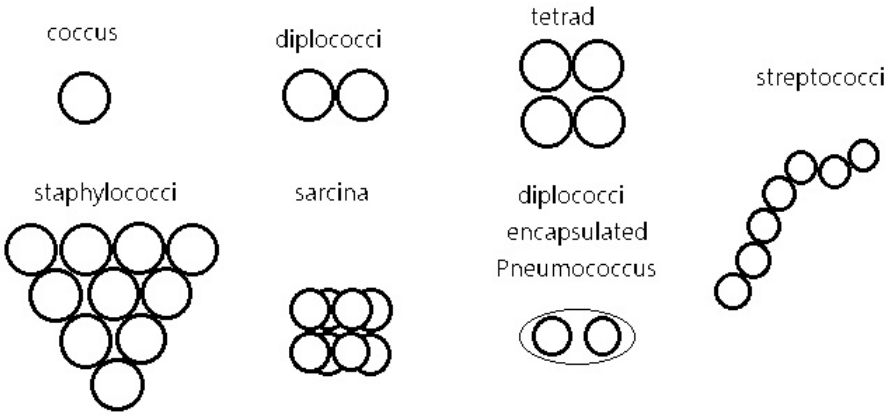

Figure 1.1: Example of the various aggregation arrangements in cocci cells.

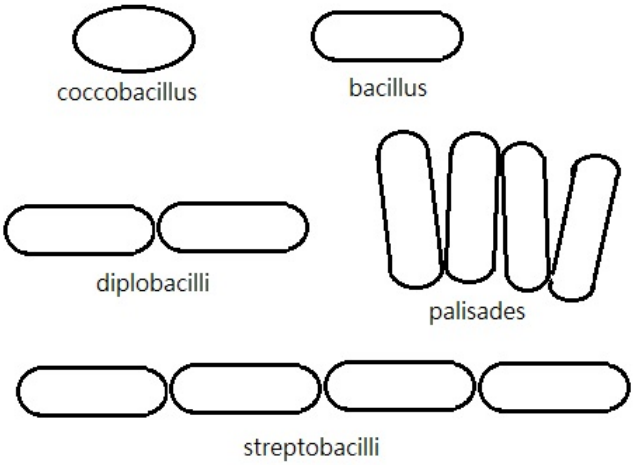

Figure 1.2: Example of the various aggregation arrangements in bacillus cells.

rial circular DNA (Deoxyribonucleic acid) are irregularly shaped and form the nucleoid. The nucleoid, unlike in eukaryote cells, has no bounding membrane, therefore some of the DNA molecules are replicated and isolated from chromosomal DNA, and form the plasmids [17]. The largest number of molecules in bacterial cells are called ribosomes. Their function is to read the inherited factor from RNA (Ribonucleic acid) to synthesise amino acids and form protein

molecules. There is a thick liquid called the cytoplasm, which fills the void space inside the cell membrane and contains all the organelle of the bacteria cells including the nucleoid, plasmids, and ribosomes. Some of the important metabolic pathways occur in the cytoplasm, such as glycolysis and the TCA cycle, which produce energy. Energy production will be discussed in detail in Section 1.1.3. There are two groups of bacterial cell walls: Gram-positive and Gram-negative cell walls (see Figure 1.4). In general, Gram-positive cell walls consist of plasmide membrane, periplasmic space, and petidoglycon. The Gram-negative cell walls contain a further two layers outside of these, with another layer of periplasmic space and an outer membrane. The outer membrane prevents the bacteria from being phagocytosed by macrophages when in an animal body, or digested by enzymes, and works as a barrier to protect the cell from antibiotic agents. Outside the cell wall, there are a number of short protein tubes all around the cell surface. The short protein tubes are called fimbrias, so-called pili. The function of the pili is cell adhesion to other biotic and abiotic surfaces. Other cell mobilities, such as swimming and cell rotation [18], depend on flagellas, which are long, whip-like, and consist of more than 20 proteins [19]. Flagellas also involve cell adhesion to solid surfaces [18]. Different species of bacteria may have different numbers of flagella, with various arrangements (see Figure 1.3b) [19].

1.1.2 Environment

Any environment that can sustain life will harbour at least one, but probably many, species of bacteria. The favoured environment, however, can vary considerably across species, depending on the temperature, pH, levels of oxygen, carbon dioxide, sulphur, etc. Most bacteria grow in temperatures between 25–30$°C$ and pH values of about neutrality (pH 7)[16] though they will tolerate to a certain extent conditions outside those which could be considered optimal.

All bacteria require some form of organic compound from which to generate new proteins and use for energy production. The necessary molecules contain carbon, hydrogen, nitrogen, sulphur, and some iron. For example, bacterial cells require carbon and nitrogen to generate energy ATP (Adenosine-5'-triphosphate, see Section 1.1.3) via respiration; for the production of new protein and amino

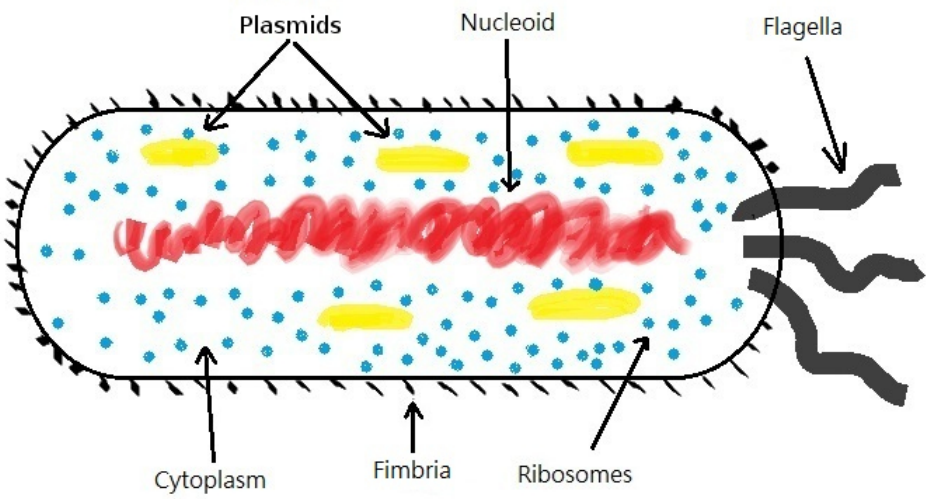

(a)

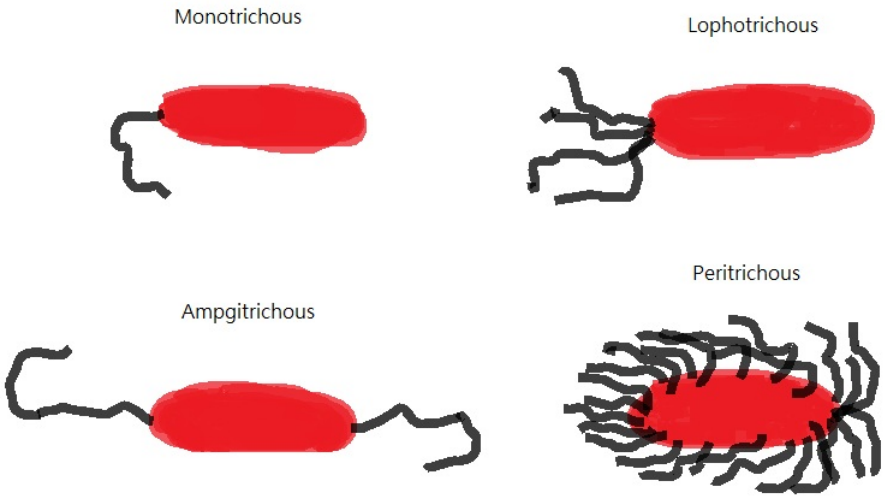

(b)

Figure 1.3: Schematic of (a) bacteria cell structure (b) flagella of Monotrichou, Lophotrichous, Amphitrichous and Peritrichous.

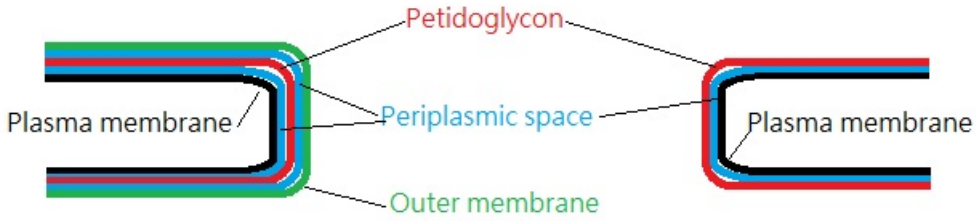

Figure 1.4: Schematic of Gram-negative (left) and Gram-positive (right) cell walls.

acids, nitrogen as well as sulphur are also required. These essential compounds are all absorbed from the environment and processed to form those molecules which are required for the cell to function, grow, and divide. The specific requirements for bacteria vary considerably from species to species, e.g. oxygen is highly toxic for some bacteria [20] but greatly enhances energy creation in others.

1.1.3 Cell Energy: Adenosine-5'-triphosphate (ATP)

In order for a bacterial cell to function, including cell growth, division, and movement, an intracellular energy source is requires. Adenosine-5'-triphosphates (ATPs) is a kind of coenzyme, used to release the intracellular energy in many cellular processes, such as digestion, compound synthesis, cell mobility, growth, and division [16, 21]. A single molecule of ATP consists of three phosphate groups, a ribose sugar, and an adenine ring (Figure 1.5a). These three phosphate groups are connected by two high energy phosphoanhydride bonds. The process of breaking down high-energy bonds between two phosphate groups is known as hydrolysis and releases energy by forming a lower-energy bond [22, 23, 24], reducing the ATP molecule to adenosine diphosphate (ADP) (Figure 1.5b). ADP can be recycled and converted back to ATP by adding a phosphate group. The concentration of ATP in a living cell is about 1-10 μM [25], which is typically a thousand times higher than the concentration of ADP. This means there is a

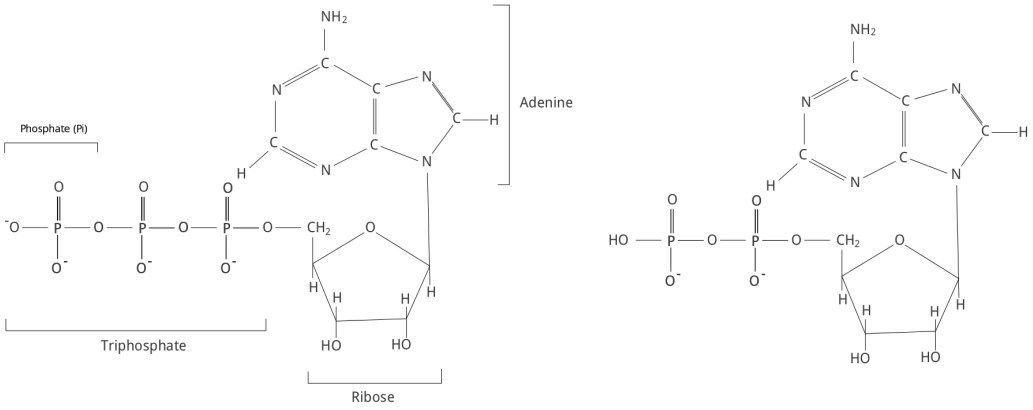

(a) (b)

Figure 1.5: The chemical composition of (a) ATP and (b) ADP.

large amount of free energy available to the cell [26].

The most well known energy producing metabolic process is that of glucose. ATP can be produced from glucose by several metabolic processes, including glycolysis, the tricarboxylic (TCA) cycle, and electron transport [27] (requiring oxygen) resulting in glucose being broken down into carbon dioxide and water. Glycolysis is a series of reactions that converts a molecule of glucose into two pyruvate molecules, and occurs in both aerobic and anaerobic conditions. In the first stage of glycolysis, two molecules of ATP are hydrolysed to ADP and release the energy stored in the high energy bond for catabolism of the glucose from the structure of a six-carbon ring to two three-carbon molecules. However, in the following reactions, four ATP molecules are synthesised with two molecules of NADH. The net products of the glycolysis metabolism are two molecules of ATP and two molecules of NADH.

NADH is a reduced form of the coenzyme NAD^+ (nicotinamide adenine dinucleotide phosphate). This process maintains the ratio of NAD^+ to NADH, like ATP and ADP, to be about constant. After the NAD^+ has been reduced to NADH, replenishment by oxidation is required. The reactions which convert between NAD^+ and NADH are examples of redox reactions. These reactions, which

operate in both aerobic and anaerobic respiration, are summarised as follows.

$$NAD^+ + H^+ + 2e^- \leftrightharpoons NADH$$
$$(\longleftarrow \quad oxidation; \quad \longrightarrow \quad reduction)$$

Two pyruvates, the end products of glycolysis, are converted to two *acetyl-Coenzyme A*, the so-called acetyl-CoA, molecules. While the reduction reactions are taking place, two NADH molecules are reduced from NAD^+ molecules. Acetyl-CoA enters an aerobic respiration metabolism called the tricarboxulic (TCA) cycle, also called the Krebs cycle or the citric acid cycle, and is oxidised to CO_2 and water completely, in some aerobic organisms. One molecule of ATP, three molecules of NADH, and one molecule of $FADH_2$, which is another co-enzyme involved in the citric acid cycle, are produced during one turn of the TCA cycle.

The electron transport chain is a series of reactions that transfers electrons from electron donors, NADH and $FADH_2$, to the electron acceptors, which are oxygen molecules in oxygen presented conditions, and interact with hydrogen ions to form water. This series of reactions induces ATP syntheses. The oxidation of one molecule of NADH to NAD^+ induces 2.3 molecules of ATP. Similarly, the oxidation of one molecule of $FADH_2$ induces 1.4 molecules of ATP [27]. Through the overall metabolisms of glycolysis, the TCA cycle, and the electron transport chain under aerobic conditions, a glucose molecule induces 29.85 ATP molecules (Figure 1.6) [27]. In anaerobic conditions, anaerobic respiration takes place. The electron transport chain uses inorganic molecules with less redox potential, such as nitrate or sulphate, instead of oxygen, as electron acceptors. Therefore, fewer ATP molecules are synthesised [16].

1.1.4 Energy Storage

Some living cells produce polysaccharides, lipids, and polyphosphate as energy storage substrates to store energy [28]. One such compound, produced only by some bacterial cells, is called poly-β-hydroxybutyrate (PHB). PHB is produced and stored by bacterial cells in well nourished conditions and is consumed in the

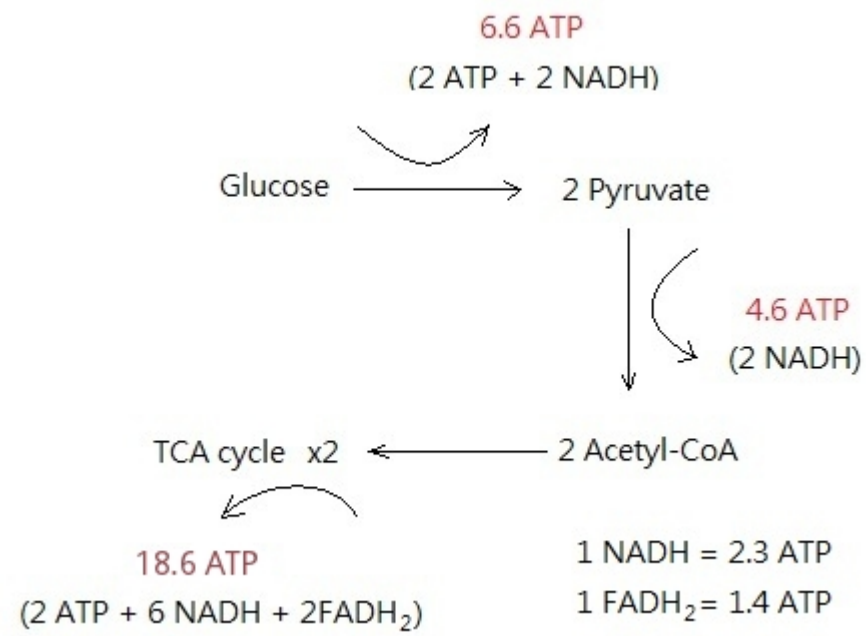

Figure 1.6: Schematic of ATP production during cellular respiration.

synthesis of ATP when carbon sources, such as glucose, are in short supply [29]. The amount of PHB contained in a bacterial cell is, at most, 50% of dry weight of the cell [29]. In some bacterial species, such as *Bacillus cereus*, PHB can only be produced during aerobic respiration [29], whilst others are able to produce PHB during both aerobic and anaerobic respiration [30, 31]. However, PHB synthesis is inhibited when the oxygen concentration exceeds 5% [29]. When cells metabolise PHB to generate energy, the reaction rate in anaerobic degradation is slower than in aerobic degradation[29]. The energy produced by PHB degradation seems to be utilised for cell survival with growth mostly suppressed. The biomass production by PHB is about 4%–10% of the production by nutrient [30]. However, cell division is completely suppressed, due to its much higher energy demands [29].

PHB production, like ATP synthesis, is a series of oxidation reactions using glucose as the source. The glucose is converted to pyruvate via glycolysis, then further transformed to acetyl-CoA, in the same processes as ATP synthesis. For PHB production, acetyl-CoA does not entirely enter the TCA cycle, but instead enters the cycle of the PHB production-degradation metabolic process and is

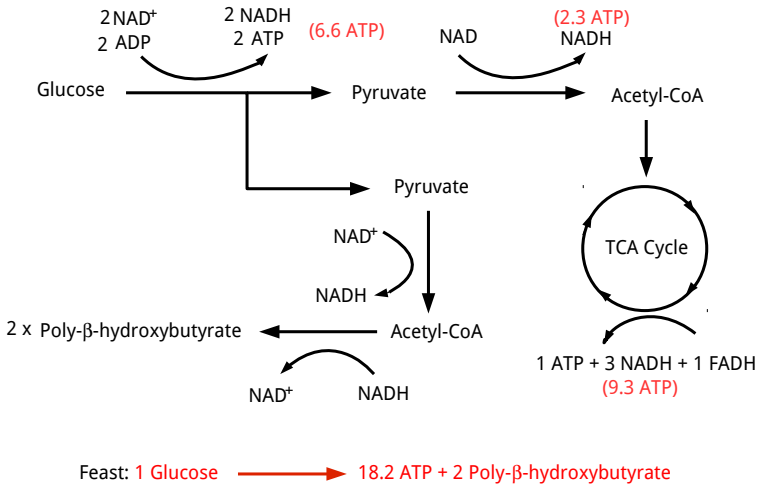

(a)

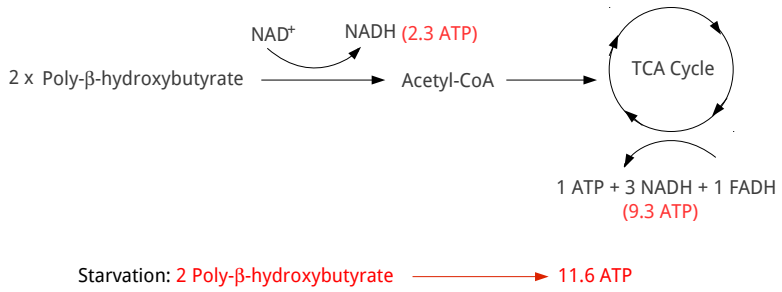

(b)

Figure 1.7: Schematic of PHB production and degradation metabolisms in (a) feast [31] and (b) starvation conditions [29].

converted to poly-β-hydroxybutyrate. While in starvation, PHB is converted back to acetyl-CoA and enters the TCA cycle to produce ATP (Figure 1.7). One molecule of PHB may produce up to 4.925 molecules of ATP [32] and 0.54 molecules of ATP under anaerobic conditions [33].

1.2 Introduction of Biofilms

The biofilm phenotype is one of the bacterial phenotypes. Others are the planktonic, the spore, and the ultramicrobacteria phenotypes [34]. These three living forms have their own benefits for bacterial growth and proliferation.

1. **Planktonic phenotype**. This phenotype is where bacterial cells move by swimming with their flagella freely in liquids. Therefore, they are able to find the environment most suitable for their growth and away from any toxic activity.

2. **Spore phenotype**. A spore is a bacteria cell that has a cell coat. Therefore, these bacteria are highly resistant to a poor living environment. Spores are able to survive in extreme conditions, in environments which may be acidic, hot, cold, or toxic. Some of the planktonic species can form themselves into spores under pool living conditions and then transform back to plankton when the environment improves [35].

3. **Ultramicrobacteria (UMB)**. Ultramicrobacteria are very small bacteria, with a size of from 0.2 to 0.3 μm [36]. These kinds of bacteria are the dormant forms of large cells, i.e., the UMB cells have reduced their metabolic rate and have stopped growing. This form allows bacteria to survive under extreme conditions [37].

4. **Biofilm phenotype**. The main differences between biofilm cells and planktonic cells are a community structure. Biofilm cells are connected by pili and interact with each other [34]. Some of the planktonic cells are able to lose their flagella and adopt this phenotype. Once planktonic cells lose their flagella, they may aggregate and produce a matrix of an extracellular polymeric substrate (EPS) to form biofilms. The growth rate and gene transcription of bacterial cells in biofilms are different from those of their planktonic forms [38]. The cells in mature biofilms may detach from the biofilms. The detached biofilm cells return back to the plankton phenotype and swim using their flagella to find new places and to form new biofilms.

Biofilms are hydrophilic structures developed by biofilm phenotype bacterial cells. The definition of a biofilm is that the bacterial cells are embedded in a matrix of extracellular polymeric substances (EPS), which are produced by the cells and irreversibly attached to various surfaces [38]. They are highly hydrated structures [39]. The constituents of a biofilm can vary considerably and dynamically, consisting mostly of water, bacteria, and the EPS [39, 40], as well as abiotic materials, such as ions, in dependence on the growth environment. Biofilms adhere to various surfaces such as solid–air, air–water, and mostly solid–liquid interfaces, including water pipes, blood vessels, teeth, medical devices, and river beds [38, 40, 41, 42, 43]. The extracellular polymeric substrates, which account for 50%–90% of the total organic carbon of the biofilm [44, 45, 46], is composed of polysaccharides and various ingredients. The details of the EPS and its function will be discussed in Section 1.2.2. The structure of biofilms can vary considerably, depending on the cell species, the nutrient loading, and the bulk flow. Liquid flow encourages bacterial adhesion and biofilm formation. The fluid transports substrates, including nutrients and oxygen, to the biofilm and through the water channels between the cells or between the cells and the EPS in the biofilm [47], thereby creating the ideal environment for bacterial growth [39, 41]. The nutrient and oxygen concentration gradients depend on the hydrodynamics, the mass transport, and biofilm activities [48] such as consumption. The hydrodynamics and the mass transfer (diffusion) boundary layers are formed above the biofilm surface in the bulk fluid. The boundary layer is thinner in a high turbulence condition than in a static or low-flow liquid, and, therefore, the cells are able to obtain more nutrients than in low-flow or static environments. However, too strong a turbulence may cause the biofilm cells' detachment [45]. The distribution of nutrient and oxygen concentrations in the biofilm environment affects the cells' growth and the biofilms' formation [40, 43]. The structure of biofilms has been investigated extensively using confocal laser scanning microscopy (CLSM) [40, 43, 49, 50]. Observations show that the shape of the biofilms is mushroom-like or finger-like and is formed smoothly at the surface under nutrient reach conditions. Conversely, at low-nutrient levels, the biofilm surface tends to be more uneven and the bacterial cells are aggregated [43, 51]. The internal distribution of the cells and the EPS in a biofilm has also been investigated by CLSM

[52, 53, 54]. Due to the difference in nutrient concentrations, the bacteria are not uniformly distributed in biofilms [52]. Bacteria cells are mostly close to the biofilm surfaces and the bacterial cells near the surface are more active than the embedded cells [51, 54, 55, 56, 57, 58, 59, 60, 61].

1.2.1 Biofilm Formation

Biofilm development can be described as a sequence of processes involving initial attachment, cell growth, EPS production, biofilm maturation, and bacteria detachment. Once the bacterial cells have adhered to a surface, they start growing and producing EPS to form a biofilm. The general steps of biofilm formation are as follows (see Figure 1.8):

1. **Adhesion.** Drifting or actively swimming bacterial cells can use their flagella to adhere irreversibly to a surface [40]. The flagella of the bacteria cells overcome the surface's electro-static repulsive forces between the cell surface and the substratum, reducing the attachment energy required [40, 62, 63]. After the cells adhere to the surface, they tend to aggregate and adhere to each other using external structures of fimbriae and pili [40].

2. **Colonisation and EPS production.** Once settling on a surface, bacterial cells start growing and produce EPS to form a biofilm; amongst the functions of EPS is to maintain the structure of the biofilm and enhance the attachment to the surface as it develops [40]. In some species, e.g. *Pseudomonas aeruginosa*, EPS production is regulated by a cell–cell signalling process called quorum sensing [64, 65, 66, 67], whereby extensive production of EPS is delayed until the initial colony has reached a sufficient population: presumably this means that lone, newly colonised individual cells are better able to survive by not needlessly wasting energy on EPS, which would have limited benefit for the early biofilm. Biofilm growth depends on a range of environmental factors, such as pH, temperature, and nutrient levels (e.g. oxygen, carbon source, and nitrogen) ([16, 38, 68, 69, 70, 71, 72, 73, 74, 75, 76, 77]). When a nutrient is at sufficient levels, a wide range of bacterial species produce EPS and an energy

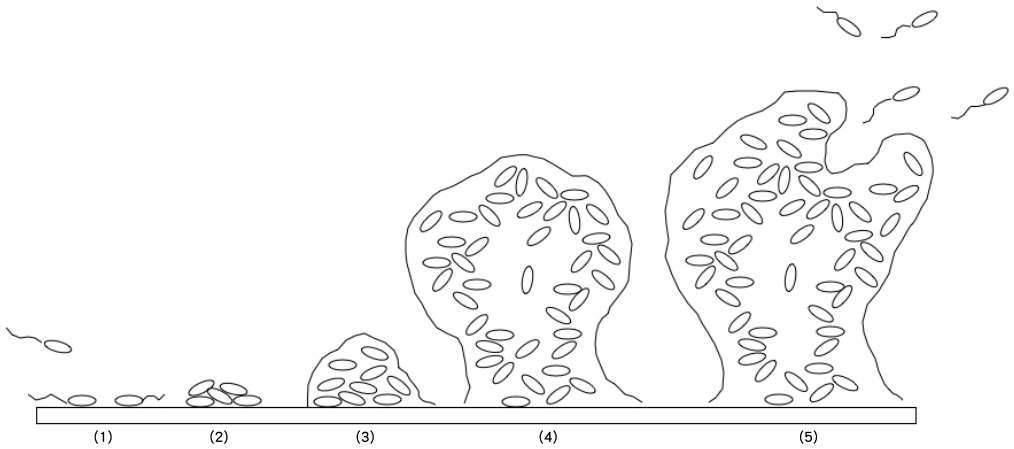

Figure 1.8: Schematic of the development of a biofilm from initial colonisation to maturation. (1) Individal bacterial cells adhere to a surface. (2) Cells aggregate and form an early micro-colony with low EPs, (3)–(4) Biofilm development and maturation to form complex structures (e.g., mushroom formations). (5) Detachment and spread to new locations.

storage substrate poly-β-hydroxybutyrate (PHB) [29], a metabolic product. When starved of carbon and other energy sources, cells take their energy from the PHB in order to survive [29].

3. **Detachment.** Biofilms studied in the laboratory are often grown on a surface over which flows a fluid containing nutrients. The shearing force of the bulk flow of this fluid can lead to the shedding of individual cells and to their detachment, or sloughing, from the biofilm material [40]. The environment can also influence bacterial detachment, for example, nutrient limitation enhances dispersal [40]: the detached cells may settle elsewhere to form a new colony [40].

In laboratory experiments, it has been observed that biofilms grow more readily in high-shear flow conditions than in laminar-flow conditions [38, 40]. One reason for this is that the cells are in contact with the surface more frequently in turbulent flow, enhancing the cells' adherence to surfaces [38]. In turbulent flow, biofilms tend to form streamline patches and filamentous streamers, (see Figure 1.8) due to the drag force of the bulk flow. Downstream from the flow, biofilms

tend to become tapered, due to the lift force and recirculation [40].

1.2.2 Extracellular Polymeric Substrate (EPS)

Extracellular polymeric substrate (EPS) is a highly hydrated gelatinous matrix which can be more than 90% of the total dry mass of the biofilm [78]. The chemical components of EPS vary, depending on the bacterial species and the growth environment [79]. They generally consist of glycolipids, lipids, proteins, peptides, nucleic acid, and mostly, but not necessarily, lipopolysaccharides [80, 81, 82]. In some cases, extracellular DNA (e-DNA) is found in EPS [83]. EPS not only encloses the bacteria, but also plays an important role in biofilm formation and growth. Flemming *et al.* [83] divided the function of EPS into seven categories: structural, sorptive, surface-active, enzymatic, redox-active, informative, and nutritive.

Structural EPSs fill and form the space between the cells. They are responsible for the biofilm's adhesion to biotic and abiotic surfaces [82, 83] and water retention, by which a large amount of water molecules are bonded by the hydrogen bonds in the EPS molecules [39, 47]. An example of structural EPS is neutral extracellular polysaccharides, or exopolysaccharides. Exopolysaccharides are long, linear and branched molecules which sustain the biofilms' structure and expand the biofilm volume [59, 84]; therefore, biofilms are able to form complex structures, such as mushroom-like or finger-like[50, 78] shapes, rather than flat, thin and well compacted structures. Additionally, during the expansion, the water channels and the void spaces formed in the biofilm enhance the transportation of solutes including oxygen [47, 85]. This leads to the biofilm cells's obtaining more easily the nutrients and oxygen than through these compounds' diffusing directly through the EPS matrix. However, antibiotics are also able to diffuse into the biofilms through these water channels and void spaces. It has been reported that compounds that do not react with the EPS and with a molecular mass of less than 10,000 Dalton, are able to diffuse into an EPS–water mixture without diffusion limitation, because of the high volume fraction of the water and the water channel in biofilms [46]. However, those compounds which react with EPS have such penetration hindered. Due to diffusion limitation, biofilm cells grow

more slowly but survive more easily than when in the planktonic form [39, 40].

Sorptive EPSs refer to charged polymers [82, 83]. These EPSs are able to accumulate nutrients and xenobiotics, such as ion charge and toxic metal ions [78]. Therefore, in some cases, biofilms are used for water purification [86, 87, 88, 89, 90, 91, 92, 93].

The functions of surface-active EPSs is to export those cell components which are waste substances from the cell metabolism [78, 82, 83]. The surface-active EPSs, for example amphiphilics, are also able to react and destroy any antibacterial and antifungal activity [82] to protect the bacteria in the biofilm. Some of the enzymes which surround the bacterial cells are able to digest and degrade the EPS to low molecular-mass organic molecules, which can be used by cells as nutrient sources [78, 94, 95]. All of the EPS components are able to be degraded and become a nutrient source. However, some components are more complex and therefore the degradation processes are slow [78, 96, 97].

Informative EPSs are involved in biofilm cohesion and cell aggregation. These EPSs develop networks between cells for cell–cell recognition and communication [78]. Due to lots of genes' being released from the cells, genetic material exchange occurs in the EPS [82]. Additionally, redox activity also occurs in the EPS, due to the EPS's being negatively or positively charged [98] and acting as an electron acceptor or donor [78].

One of the structural EPS molecules, polysaccharide, is the most recognised EPS conpound in biofilm studies. Polysaccharide is a large-sized compound composed of various types of monosaccharide units: the most basic unit is formed of carbohydrates and the chemical formula is $C_nH_{2n}O_n$, where $n \in [3, 10]$, connected by a glycosidic bond [99, 100]. The sizes of the EPS molecules are larger than 100 kDa[1] [101, 102] and are about 2.3×10^6 Da on average [103]: therefore, an EPS molecule consists of several hundred or thousand monosaccharide units.

1.2.3 Biofilm Effects and Uses

The bacterial cells living in a biofilm are generally more resistant to unfavourable environments than when in a planktonic state. The fact that a biofilm provides

[1]Da is an atomic mass unit equal to the molar mass, g/mol.

a stable and robust environment in which bacteria can grow and divide is exploited in many industrial applications. For example, in water purification and soil cleaning [86, 87, 88, 89, 90, 91, 92, 93], biofilms absorb the metal ions in the water, use their structure to block contamination, and consume these pollutants as nutrients. The gelling structure of the biofilms are being used to increase the viscosity of food and industrial products, such as frozen food and toothpaste [46]. Recently, scientists have been investigating the use of biofilms as biofuels [104] and sources of plastics [105].

Biofilms can have a severe negative impact in health care, through bacterial infection, and in industry. They cause some health problems in the human body, for example, bacteraemia and endocarditis may occur due to biofilm's developing in the blood vessels and medical devices [42]; bacterial cells of *Vibrio cholerae* from a biofilm can survive acid environments such as the human stomach [106, 107] and then transform back to the planktonic form once in the small intestine and cause cholera; cystic fibrosis results from *Pseudomonas aeruginosa* formed biofilms in the lungs [108, 109]; and can cause other diseases and infections such as leprosy, syphilis, dental caries [108, 110], urinary catheters [109], infactious kidney stones [111], and chronic wound [112]. In industrial settings, for example, microbial contamination can induce corrosion of metals [113], damage the water cooling system due to adhesion and blocking of the water flow as well as decreasing the heat transfer [86]; water retention due to the biofilm can lead to battery self-depletion while biofilms develop on the cells of the batteries [86]. Current techniques to remove or reduce biofilms include the application of mechanical force and of toxic chemicals, such as shearing forces and antibiotics [114, 115, 116, 117]. However, these methods are not suitable for the biofilms which grow on living tissue, and they do not kill the bacteria effectively. An additional issue that has arisen in the last 50 years is the increasing emergence of multiple drug-resistant strains such as MRSA (Multiple-resistant *Staphylococcus aureus*), due to the extensively use of antibiotics [118]. The development of antimicrobial strategies is very important, whether to replace antibiotic treatments or to at least reduce the dependence on them. A novel strategy that is being investigated by many research groups is the application of cold plasma therapy to destroy biofilms [2, 5, 119, 120, 121]. The aim is to treat exposed biofilm with plasma

and leave the underlying host tissue undamaged. This will be discussed further in Chapter 5.

1.3 Thesis Synopsis

The aim of this thesis is to propose a new modelling framework for biofilm growth, which will qualitatively match the experimental observations, and to use this framework to investigate the effects of plasma treatment on biofilms. The thesis is divided into two parts. The first part aims to develop a modelling framework of biofilm growth. In Chapter 2, the previous methods used in biofilm growth models are reviewed and evaluated. In Chapter 3, a new model framework of biofilm growth with a compressible diffusible continuous EPS matrix is developed. The model assumes that the bacterial cell behaviour depends on the intracellular energy (e.g. ATP) produced by themselves. In Chapter 4, the model framework is examined, using various simulations, to investigate the effect of EPS on the biofilm formation and multi-species biofilm growth. Furthermore, the model is applied to simulate the biofilm growth on agar plates. The second part of the thesis, a brief introduction to non-thermal atmospheric plasma and its biological effects, is given in Chapter 5. In Chapter 6, the various models of plasma treatment on biofilms are presented. Some conclusions and perspectives for future research are located in Chapter 7.

Chapter 2

Review of Mathematical Models of Biofilm Growth

Mathematical modelling of biofilm growth can help understand key aspects of biofilm growth and provide a relatively inexpensive framework to investigate new ways to control biofilm growth. Mathematical modelling of biofilms is a developing field in biological mathematics. Over the past 30 years, biofilm models have tried to simulate the range from single species models growing in a one-dimensional setting [122, 123] to multi-dimensional, multi-species models [124, 125]. A wide range of modelling approaches has been employed in biofilm modelling: they can be divided broadly into continuum, discrete [126], or hybrid models, combining continuum modelling with either cellular automata, Clazier–Graner–Hogeweg [151], or individual-based models. In this chapter, a brief review of these models with their advantages and disadvantages for biofilm simulations will be discussed.

2.1 Continuum Models

Continuum models treat the cell components of the biofilm, the EPS, and all the substances considered as continuous materials and use differential equations [123, 127, 128, 129, 130, 131, 132, 133]. Such approaches have been used to investigate not only higher dimensions and to attempt to describe the various shapes observed

using recent microscopy techniques [52, 134, 135], but have also examined the various biofilm mechanisms, for example, the role of EPS in biofilm formation [52], cell mobility due to biofilm growth [122, 128], and biofilm disinfection [133]. The benefit of the continuum models is that the systems of differential equations in the continuum approaches can be solved relatively quickly by standard numerical methods, or even analytically for the simpler models, and the results successfully provide the fractions of both live and dead cells in the population and the EPS in the biofilm. The approaches, however, present the biofilm globally rather than the micro-structure.

2.2 Cellular Automaton Models (CA Models)

A cellular automaton (CA) model divides the computational system domain into a fixed regular grid to form a lattice. Each grid-cell in the lattice will be in one of a limited number of statuses, e.g., not occupied by any cell, occupied by the species "A," occupied by the species "B," ...etc. The first CA approach to describe biological behaviour was a discrete model referred to as "John Conway's game of life" [136]. In this model, the grid-cell can have one of two statuses: alive or dead, where the process of switching the status of a cell from one to the other depends on simple rules based on the status of the neighbouring cells. The model describes the simplest system of change in a cell population in discrete time. Since then, the CA approach has been widely used for biological population simulation. One of the most famous examples is the simulation of growth patterns in bacterial colonies presented by Ben-Jocob *et al.* [137]. The bacterial simulation considers nutrient diffusion and consumption, bacterial movement, proliferation, sporulation, and communication. The individual cells are treated as "walkers" and walk in the system randomly, depending on the intracellular energy. The intracellular energy is produced by consuming nutrients. When the energy reaches a critical level, cell division occurs.

The first application of the CA approach to biofilm growth simulation was presented by Wimpenny and Colasanti [138]. They took the nutrient concentration to be discrete and to be stored in the grid-cells of the lattice. Thus, the status of a grid-cell consisted of the nutrient concentration and whether the cell was

alive or dead. Cell growth was governed by the level of nutrient in the grid-cell which the cell occupied. When the cell density reached a fixed critical level, the cell divides. During reproduction, the new cell is inserted into that neighbouring empty grid-cell with the highest nutrient concentration. They used this framework to investigate the role of nutrients in the growth of a multi-species biofilm. Around the same time, Picioreanu *et al.* [139] also presented a biofilm model which applied the CA approach and modelled a limiting substrate, e.g. a nutrient, as a continuum described by reaction–diffusion equations. This hybrid model has been widely used in various studies of biofilms, not only multi-dimensional biofilm growth [140] and multi-species [141], but also the effects of liquid flow on biofilm detachment [142, 143], substrate transportation in biofilms [144, 145, 146], and the effects of nutrient availability on biofilm formation [144, 145, 147]. Simulations using the CA approach produce results that mimic well the growth and formation of irregular structures. However, an important factor of biofilm formation, extracellular polymeric substrate (EPS) production, has been neglected in those simulations. Laspidou and Rittmann [148] proposed a theory of EPS and investigated EPS production. In their further study [92], they presented a unified multi-component cellular automaton (UMCCA) model, combining the CA approach and the theory they proposed about the EPS and the other two microbial productions [148, 149]. The EPS was taken as the third possible status of the grid-cell, in addition to active and inert biomass. They used this model to investigate the biomass and the EPS distribution in the biofilm and the effects of the nutrient and the microbial products on the biomass distribution [150].

2.3 Cellular Potts Model (CPM)

The Potts model was proposed by Potts in 1951. It is widely used in the research of lattice statistics. The model approach assumes that for each node of the lattice has a state from among a limited number of spin states. The spin of the nodes may be changed by interacting with neighbouring nodes, and this interaction is described by a Hamiltonian formulation. The Potts model was first applied to the simulation of biological behaviour by Glazier and Graner in 1992 [151]. They extended the Potts model to simulate biological cell sorting. The extended

model is called the cellular Potts Model (CPM) or the Glazier–Graner–Hogeweg (GGH) model. In this approach, the spin of the lattice site in the Potts model is referred to as the index of an individual cell, and a cell can occupy more than one grid-cell, therefore, the cells' shape was deformable, rather than fixed; furthermore, the model described the cell surface energy by a Hamiltonian. This very early CPM approach did not consider cell behaviour such as growth and division. Since then, the Cellular Potts Model has been further developed and widely used in the simulation of biology including avascular tumour development [152] and biofilm growth [153]. Cell growth is considered as increasing the volume of the cell by occupying the neighbouring lattice sites. The extracellular matrix (ECM), such as EPS, is assumed to be an infinitely compressible, non-diffusible and non-deformable special cell located in the lattice sites other than the sites which are occupied by bacterial cells [153, 154]. The Hamiltonian formulation is used to describe the cells' movement due to cell–cell and cell–ECM interactions by the change of their surface energy. The nutrients and oxygen are taken to be diffusible substrates and described by continuum diffusion–reaction equations due to the fact that the size of their molecules is relatively small compared to the size of the cell. Although Poplawski *et al.* [153] considered EPS in their paper, they focussed on the interaction of the cells and the EPS and neglected some important properties of EPS, for example, its production and movement. The small scale size of the cellular Potts model ensures the accurateness of the size and the shape of a single cell, however, it can be computationally expensive in a large domain simulation [155]. The most famous computation program for the cellular Potts model is called CompuCell3D (`http://www.compucell3d.org`).

2.4 Individual-based Models (IbMs)

Individual-based models (IbMs), sometimes referred to as agent-based models, are widely used for cellular simulation, such as tumour growth [156, 157, 158], tissue growth and folding [159], activated sludge flocs [160], myxobacteria [161] and biofilm formation [162, 163, 164, 165, 166], as well as biofilm control [167, 168]. The IbM approach is similar to the CA and CPM approaches: the bacterial biomass is taken to be discrete, and the diffusible substrates are modelled as con-

tinua. However, the IbM assumes the cells are circular (2D) or spherical (3D) particles, or, most commonly, a group of cells. Therefore, cell particles are not bounded by the lattice sites but are able to move freely in the system. Furthermore, Janulevicius *et al.* [161] simulated the bacterial cells with streptococci aggregation by a chain of circular particles.

Most of published works using IbM approaches to biofilm formation have investigated the growth, death, and detachment of the cell particles as dependent on diffusible substrates, such as the nutrients, nitrite, and oxygen. Such research has focussed on particle growth [125, 169], substance transport [170], multi-species [164], etc. However, EPS have been absent from these models until the relatively recent works of Kreft, Wimpenny [162] and Xavier *et al.* [166]. In these models, under certain conditions, the bacterial particles shell EPS as new, incompressible, circular/spherical, inert particles. This approaches has the advantage of being relatively simple, but can not predict EPS levels over the whole of the biofilm only concentrations of EPS at localised zones. EPS matrix of biofilms has been treated as the continuum matrix by Alpkvist *et al.* [171] and Mabrouk *et al.* [172]. They combined the continuum EPS matrix with the IbM approach to simulate biofilm growths. In their hybrid models, the bacterial biomass was assumed to form the discrete circular/spherical particles adapted from the IbM approach, and EPS was described as a incompressible viscous fluid modelled as a continuum. The movement of cell particles were described by pushing by EPS flux which caused by release the pressure generated during the biofilm growth in the model of Alpkvist *et al.* [171]. However, in the simulations of Mabrouk *et al.* [172], they were described by the Brownian motion with a movement constant depends on the local EPS concentration.

2.5 The modelling approach developed in this thesis

After reviewing these models, I concluded that each model has its own advantages and disadvantages. The continuum model treats the biomass, the extracellular polymeric substrate (EPS), the nutrients and oxygen as continuous structures,

and therefore the system of equations is continuous. The equations can be solved quickly by a series of numerical methods. However, stochastic or random events are not so easy to incorporate and the results are only able to describe the general structure of biofilms, rather than their details. Furthermore, the application of continuum models in 2D and 3D requires that the force balances between the particles, the EPS, and the extracellular fluid to fully characterise the movement of the cells and other biofilm components. One such approach would be the application of mixture theory which has been investigated in a recent thesis of Newstead [173], using and extending the ideas of a tumour growth model [174]. The main issue within this approach is the suitable choice of assumptions for the force balancing, as there is a paucity of data for the parameters. For example, in the viscous elastic model of Newstead's thesis, the model is based on a viscous flow, which is only relevant to biofilms grown in static environments or very low shear flow. The issues of flow regimes and force balance in biofilm is an interesting one, but will not be pursued in this thesis. The hybrid approaches of CPM and CA models are able to illustrate the biofilm structure in detail by describing the biomass and EPS concentrations in a discrete lattice; furthermore, CPM approaches are able to simulate the deformable cell structure. However, the position of the biomass and EPS of those approaches are limited by the mesh. The individual-based model (IbM) amends the disadvantages of the previous models of the discrete approaches; only the IbM approaches are not restricted by the geometry of the mesh used, so that the direction of the particle movement is governed by the growth and environment but not the geometry.

In this thesis we are concerned with designing a framework that will well describe, both qualitatively and quantitatively, the biofilm growth and the effect of a cold plasma treatment on the biofilm structure. For this we need our model to simulate the collation of live and dead cells and diffusible substrates. The IbM approach is well suited to these requirements and is the approach adopted in this thesis. The framework builds on the previous approaches proposed by [156, 160, 164, 166, 169, 171]. There are minor amendments in the handling of particle movement but the main difference is the treatment of the EPS, which is assumed to be a compressible, diffusible substrate that can force the movement of particles at high concentration. This is discussed in detail in the next chapter.

The framework is then used in a novel study of plasma treatment in Chapters 6; the relevant biology, chemistry, and physics of which will be discussed in Chapter 5.

Chapter 3

The New Framework Model of Biofilm Growth with Compressible EPS Matrix

In this chapter we propose a new hybrid individual-based modelling (IbM) framework for biofilm growth. As discussed in Chapter 2, IbMs of biofilm growth have been proposed by several research groups. In Kreft *et al.*, [169], EPS was generated as an incompressible outer surrounding shell of material around a circular/spherical cell particle, which was able to be a shell to form separate EPS particles. In Alpkvist *et al.* [171], EPS was treated as a incompressible viscous fluid phase in a multiphase model. In both their models, the EPS was either present at a fixed concentration or completely absent at a particle's point within a biofilms: a consequence of this is that the EPS will always propagate movement where the growth of one particle can force the movement of a distant particle even though there is only EPS between them. In the approach presented in this chapter, the EPS is compressible and will only exert a pressure and propagate movement at high concentrations, for example, an elastic-like expansion force or repulsion via electrostatic forces between closely packed EPS strands. A consequence of this new approach is that particles will not necessarily move due to the movement or growth of distant particles, as the EPS will not automatically transmit this movement, as it does in the aforementioned modelling approaches. This

modelling approach is relevant for simulations in 2D and 3D scenarios, though there will be a greater focus on the 2D case. As with all the existing IbM approaches to biofilms, the bacterial particles will treated as discrete objects, and all other agents, such as the nutrients, the oxygen, and the chemical species, will be treated as continua.

3.1 Simulation Domain and Meshing

The biofilm system discussed in this thesis will be simulated on two dimensional domains, defined by the region $x \in [0, L_x]$ and $z \in [0, L_z]$, where the substratum is set at $z = 0$. In presenting the framework, it is convenient to label the various domains in the system, which are illustrated in Figure 3.1. Let Ω be the compact, but not necessarily connected, domain occupied by the particles and/or the EPS, and let the line $\Phi(x, z, t) = 0$ be the line of the biofilm and water–air interface. The region within Ω occupied by particles is defined by

$$\begin{aligned} \Gamma &= \{\boldsymbol{x} \in \Omega \ : \ \boldsymbol{x} \text{ is inside a particle}\}, \\ \Gamma_\kappa &= \{\boldsymbol{x} \in \Omega \ : \ \boldsymbol{x} \text{ is inside the particle } \kappa, \text{for } \kappa = 1..N(t)\}, \end{aligned}$$

where $N(t)$ is the total number of particles present at time t, which may change in time. Since the particles are not allowed to overlap with each other, we have $\Gamma_i \cap \Gamma_j = \emptyset$ for indices $i \neq j$ $(i, j = 1..N(t))$ and that $\Gamma = \Gamma_1 \cup \Gamma_2 \cup ... \cup \Gamma_N$. For $\boldsymbol{x} \in \Omega$, we define a function $W_j(\boldsymbol{x}, t)$ by

$$W_\kappa(\boldsymbol{x}, t) = \begin{cases} 1 & \text{if } \boldsymbol{x} \in \Gamma_\kappa(t); \\ 0 & \text{if } \boldsymbol{x} \notin \Gamma_\kappa(t). \end{cases} \tag{3.1}$$

The function $\varepsilon_\Omega(t)$ is defined as the total void volume fraction in the domain Ω, namely

$$\varepsilon_\Omega = \frac{\int_\Omega \sum_{\kappa=1}^{N} (1 - W_\kappa(\boldsymbol{x}, t)) d\boldsymbol{x}}{\int_\Omega d\boldsymbol{x}}. \tag{3.2}$$

The particle volume fraction is thus $1 - \varepsilon_\Omega(t)$.

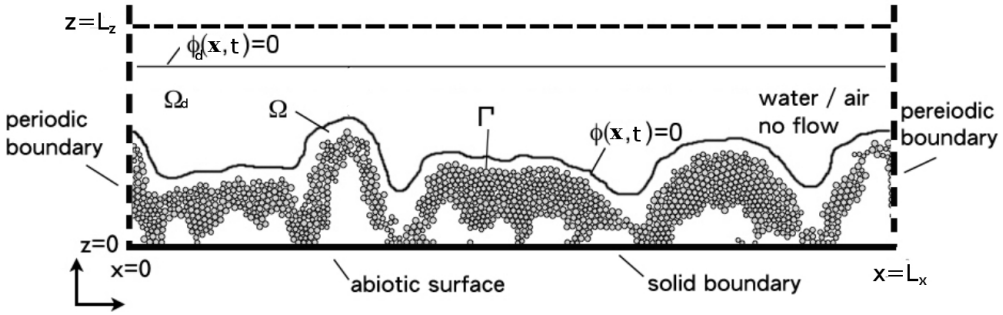

Figure 3.1: Schematic of a biofilm domain. The biofilm occupies the region Ω, the particles occupy the region Γ, and the biofilm and water/air interface is defined by $\Phi(\boldsymbol{x}, t) = 0$.

The system domain is divided into a grid of rectangular cells, which, in general, are of size $dx \times dz$. However, throughout this thesis, we set $dz = dx$, hence the simulation domain consists of a uniform square grid, as shown in Figure 3.2, to be used to determine the position of the particles. Particle growth and movement are affected by any number of substrates, such as EPS, nutrients, and oxygen, and the concentrations of these are calculated at the mid-point of each cell, bounded by the solid line in Figure 3.2a. We note that particles are not constrained by the grid and are free to move in any direction. The dashed grid connects the mid-points of the solid line grid, along which the finite volume approximation for the continuous variables is made. The grid size is chosen so that the grid squares cannot be entirely occupied by particles, otherwise the finite-volume method described in Section 3.5 will fail without extensive modification. However a grid that is too large makes particle overlap detection very computationally expensive. More details regarding the grid size are given in Section 3.6.

3.2 Particle Growth and Death

The framework in 2D assumes that the particles are rigid discs representing individual bacteria or single-species clusters of bacterial cells (this is discussed further in the next section). Particles that represent bacterium will be in one of two states: alive and dead. When they represent a cluster of cells, then they will

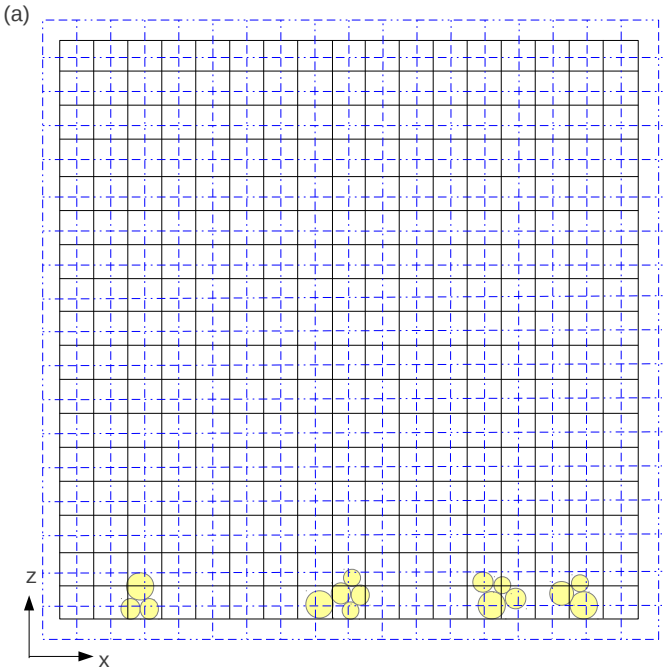

Figure 3.2: Diagram showing the domain meshes. The solid lines show the mesh used for the particles, whilst the continuum variables are calculated on the nodes of the dashed grid, located at the centre points in the solid mesh.

consist of a mixture of live and dead biomass denoted by C_L and C_D, respectively, such that $C_L + C_D$ equals the total biomass of a single paricle cylinder of thickness L_y. The choice of this thickness is completely arbitrary and it follows that the total biomass $C_L^\kappa + C_D^\kappa$ is proportional to L_y. The growth and death of particle j can be written using ordinary differential equations of the form

$$\frac{dC_L^\kappa}{dt} = \Psi_b^\kappa - \Psi_d^\kappa, \tag{3.3}$$

$$\frac{dC_D^\kappa}{dt} = (1-\phi)\Psi_d^\kappa - \Psi_s^\kappa, \tag{3.4}$$

where Ψ_b^κ is the rate of biomass production by bacterial growth, Ψ_d^κ is the biomass death rate, Ψ_s^κ is the dead biomass degradation rate, and $\phi \in [0,1]$ is the fraction of the live biomass that is released as a nutrient source when the live biomass dies [166]. In general, the biomass growth and death rates depend on many environmental factors, such as the nutrient level, the oxygen level, and the pH.

All forms of bacterial behaviour require a single factor, the intracellular energy source in the form of Adenosine-5'-triphosphate (ATP). This was discussed in some detail in Chapter 1, Section 1.1.3. We assume that the energy available to a cell is propotional to the concentration of APT. The reaction ATP $\rightarrow$ ADP releases energy for cellular processes whilst the reverse reaction ADP $\rightarrow$ ATP requires nutrients and possibly oxygen. The turnover of ATP is assumed to be rapid in comparison to particle growth, and we assume that the ATP level in particle κ, as a normalised variable $A_\kappa \in [0,1]$, is in a quasi steady-state:

$$A_\kappa = \sum_{m=1}^{M} F_m^\kappa(\boldsymbol{X}), \tag{3.5}$$

where M is the number of ATP generating pathways, $F_m^\kappa(\boldsymbol{X})$ is the ATP generation rate from pathway m, and $\boldsymbol{X}$ is the concentration of the ATP generating substances, such as glucose and poly-β-hydroxybutyrate (PHB).

3.3 Computational Particles: Cell or Clusters

The choice of whether a particle is a single cell or a cluster is an important one computationally. Later in the thesis we will be simulating a biofilm containing many millions of cells, which, if treated individually, would take many weeks to run on available machines. As a consequence, in all the simulations to follow, the particles are assumed to represent clusters of cells, so that such cell numbers can be represented by relatively few particles. Henceforth, "particle" will refer to a cluster of cells, though many aspects will be relevant also to single cell particles.

The radius of particle κ, $\kappa = 1..N(t)$ is determined from the formula

$$r_\kappa = \sqrt{\frac{C_L^\kappa + C_D^\kappa}{\rho_c \pi L_y}}, \tag{3.6}$$

where ρ_c is the density of the biomass and L_y is the particles thickness discussed in Section 3.1.

To avoid an infinite growth of the particles, the particles are limited to a maximum size with maximum radius R_{max}. When a particle grows, it may divide to produce two identical daughter cell particles (Figure: 3.3). The threshold radius for the division of a particle κ, R_D^κ, is determined on the formation of the particle, and is chosen randomly from a normal distribution with mean $= (R_{min} + R_{max})/2$ and variance 5 (the random number generator was created by Chandler and Northrop [175]) such that $R_D^\kappa \in [R_{min}, R_{max}]$; a random value lying outside this range will be set to R_{max} or R_{min} as appropriate. As a cell divides, we assume the mother cell divides equally into two daughter cells with no biomass loss. In contrast to previous studies, we have assumed that the arrangement of the daughter cells is such that the centre of mass is maintained on division, which has a greater physical foundation than does assuming that one of the daughters shares the same centre point as the mother cell, assumed in [164, 166, 169]. The orientation of the daughter cells following the division is chosen at random with a uniform distribution.

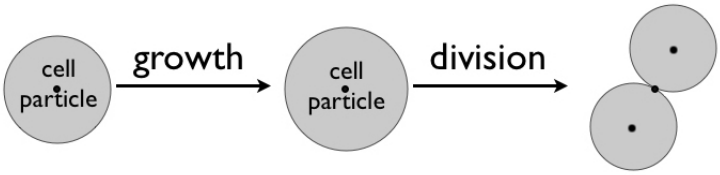

Figure 3.3: Schematic of cell particle growth and division. The centre of mass of the mother and daughter cells is maintained during growth and division.

3.4 Inter-Cellular Variables

The cell particles are assumed to contain intracellular agents either produced within the particles or absorbed from the environment. The agents could be inside live cells, dead cells, or both, for example, ATP and PHB are two agents that belong inside particles. Note that in both these examples, we are interested only in their levels in the live cells. To write down a general equation for the evolution of an agent, we let Z^κ be the mean amount of an agent per unit mass of the appropriate cells, i.e., live cells, dead cells or both. The unit of measurement for the agents can be the concentration, the mass, or any unit required. Therefore, the change of the amount of agent in the particles κ can be written as

1. **Agent in live cells:**

$$\frac{d(C_L^\kappa Z^\kappa)}{dt} = R_Z^\kappa C_L^\kappa + J_Z^\kappa - \Psi_d^\kappa Z^\kappa. \tag{3.7}$$

2. **Agent in dead cells:**

$$\frac{dC_L^\kappa Z_L^\kappa}{dt} = R_{Z_L}^\kappa C_L^\kappa + J_{Z_L}^\kappa - \Psi_d^\kappa Z_L^\kappa, \tag{3.8}$$

$$\frac{dC_D^\kappa Z_D^\kappa}{dt} = \Psi_d^\kappa Z_L^\kappa + R_{Z_D}^\kappa C_L^\kappa + J_{Z_D}^\kappa - \Psi_s^\kappa Z_D^\kappa. \tag{3.9}$$

3. **Agent in both live and dead cells:**

$$\frac{d((C_L^\kappa + C_D^\kappa)Z^\kappa)}{dt} = R_Z^\kappa (C_L^\kappa + C_D^\kappa) + J_Z^\kappa - \Psi_s^\kappa Z_D^\kappa. \tag{3.10}$$

The parameters Z_L^κ and Z_D^κ are the mean amount of an agent per unit mass of, respectively, live and dead biomass in the particle κ; the $R_{Z_i}^\kappa$ are the net production of the agent per target biomass; the $J_{Z_i}^\kappa$ are the net absorption rate of agent into/out of the particle from/to the environment; and the $\Psi_i^\kappa Z_i^\kappa$ are the amount of agent gain or loss when the live biomass dies and the dead biomass decomposes. The equations (3.7) to (3.10) can be rewritten by applying Equation (3.3) and (3.4), yielding

1. **Agent in live cells:**

$$\frac{dZ^\kappa}{dt} = R_Z^\kappa + \frac{J_Z^\kappa}{C_L^\kappa} - \frac{\Psi_b^\kappa}{C_L^\kappa} Z^\kappa. \tag{3.11}$$

2. **Agent in dead cells:**

$$\frac{dZ_L^\kappa}{dt} = R_{Z_L}^\kappa + \frac{J_{Z_L}^\kappa}{C_L^\kappa} - \frac{\Psi_b^\kappa}{C_L^\kappa} Z_L^\kappa, \tag{3.12}$$

$$\frac{dZ_D^\kappa}{dt} = R_{Z_D}^\kappa + \frac{J_{Z_D}^\kappa}{C_D^\kappa} + \frac{\Psi_d^\kappa}{C_D^\kappa} Z_L^\kappa - (1-\phi)\frac{\Psi_d^\kappa}{C_D^\kappa} Z_D^\kappa. \tag{3.13}$$

3. **Agent in both live and dead cells:**

$$\frac{dZ^\kappa}{dt} = R_Z^\kappa + \frac{J_Z^\kappa}{(C_L^\kappa + C_D^\kappa)} + \frac{(\phi\Psi_d^\kappa Z^\kappa + \Psi_s^\kappa Z^\kappa - \Psi_s^\kappa Z_D^\kappa - \Psi_b^\kappa Z^\kappa)}{(C_L^\kappa + C_D^\kappa)}. \tag{3.14}$$

3.5 Freely Diffusing Substances

A number of chemical species can freely diffuse throughout the biofilm domain and will even cross bacterial cell walls, e.g., oxygen, glucose, and other small-molecule agents. We will assume that such small molecules form a continuum in the domain. As extra cellular fluid flow is expected to be very slow, the evolution of these substances will be dominated by their reaction and motion via diffusion. Thus the general equation to describe the evolution of such an agent, say X, will be of the reaction–diffusion type, i.e.,

$$\frac{\partial X}{\partial t} = -\nabla \cdot \boldsymbol{J_X} + R_X, \tag{3.15}$$

where J_X is the flux of agent X and R_X is the net production rate. In cases where the flux and reactions occur much more rapidly than the other processes, then the quasi-steady form, namely

$$0 = -\nabla \cdot \boldsymbol{J_X} + R_X, \tag{3.16}$$

could be adopted. Specific forms for J_X and R_X will be discussed in later sections. Since the particles are discrete object in the domain, R_x is not going to be a smooth function for most agents. For ease of notation, we rewrite Equations (3.15) and (3.16) in finite volume form

$$\frac{\partial}{\partial t}\int_{\Omega_c} X d\Omega_c = -\int_{\partial\Omega_c} \boldsymbol{J_X}\cdot\boldsymbol{n} d\partial\Omega_c + \int_{\Omega_c} R_X d\Omega_c, \tag{3.17}$$

$$0 = -\int_{\partial\Omega_c} \boldsymbol{J_x}\cdot\boldsymbol{n} d\partial\Omega_c + \int_{\Omega_c} R_X d\Omega_c, \tag{3.18}$$

where $\Omega_c \subseteq \Omega$ is a compact region, $\partial\Omega_c$ is the boundary of the region, and $\boldsymbol{n}$ is the normal vector in the outward direction to the boundary, $\partial\Omega_c$.

3.6 EPS Production and Diffusion

The approach to modelling the EPS sets this current work apart from all previous IbM models. The EPS consists of long strands of polysaccharides, each one being a chain of up to 6000 saccharide links. Though these molecules are large they will be diffusible, though at considerably lower rates than the oxygen and glucose. At low concentrations, the EPS is not likely to spread quickly or impact much on particle movement. At sufficiently high concentration then, the EPS is assumed to expand in order to lower the local concentration, creating a pressure that can influence particle motion. This expansion force could be due to an elastic response, rather like sequencing and then letting go of a ball of hair, or by the presence of electrostatic forces between the EPS strands. Thus, in this modelling framework, the EPS is compressible until it reaches a high concentration due to, for example, compression by particles.

We assume that the EPS exists only in the spaces between the particles, and

denote by $E(\boldsymbol{x}, t)$ the extracellular concentration of the EPS. The pressure force generated by a high concentration of the EPS will force the EPS into regions of lower concentration, and we will assume that the EPS flux will be proportional to the negative of its gradient $(-\nabla E)$; the motion of EPS will be mathematically identical to diffusion. The flux of the EPS in the space between particles is given by

$$\boldsymbol{J_E}(E) = -D_E K(E) \nabla E, \tag{3.19}$$

where D_E is a "diffusion coefficient" and $K(E)$ is a switch function between negligible and non-negligible pressure force due to EPS concentration. Suitable functional forms of K_E are open to question. As EPS is a large molecule, the diffusion rate is likely to be very small when E is small, i.e., $K_E(E) \backsimeq 0$. As E increases, we expect $K_E(E)$ to increase, hence $K'_E(E) \geqslant 0$. As E gets large, then $K_E(E) \backsimeq$ constant or $K_E(E) \propto E$ may be reasonable assumption. In what follows we assume $K_E(E) \to 1$ as $E \to \infty$, so that E will diffuse linearly with diffusion coefficient D_E. We assume a Hill function form for $K_E(E)$, i.e.,

$$K(E) = \frac{E^\eta}{E^\eta + K_E^\eta}, \tag{3.20}$$

where K_E and η are the constants of the Hill function, such that $K(K_E) = 1/2$ means that at $E = K_E$, the EPS is diffusing at half of the maximum rate and η determines the steepness of the switch. Since EPS is produced by particles and exists only in the extra-particular space, the most compact form for expressing the evolution equation for E is to write the equation in finite volume form. Let $\Omega_c \subseteq \Omega$ be a region of the biofilm and let $\Gamma_c \subseteq \Gamma$ be the region in Ω_c occupied by particles, so that $\Omega_E = \Omega_c / \Gamma_c$ is the region of the extracellular space. Then the conservation of EPS concentration in Ω_c is given by

$$\frac{\partial}{\partial t} \int_{\Omega_c} \varepsilon_c E d\Omega_c = -\int_{\partial\Omega_c} \boldsymbol{J} \cdot \boldsymbol{n} d\partial\Omega_c + \int_{\Omega_c} Q^{\Lambda(\kappa)} d\Omega_c - \int_{\Omega_c} \varepsilon_c E d\Omega_c, \tag{3.21}$$

where ε_c is the volume fraction of extracellular space in Ω_c, given by

$$\varepsilon_c = \frac{\int_{\Omega_c} \sum_{\kappa=1}^{N} (1 - W_\kappa(\boldsymbol{x}, t)) d\Omega_c}{\int_{\Omega_c} d\Omega_c}, \tag{3.22}$$

where $W_\kappa(\boldsymbol{x}, t)$ is given by Equation (3.1). The function $\boldsymbol{J}$ represents the effective EPS flux across the boundaries of Ω_c with outward normal $\boldsymbol{n}$. Since EPS can only diffuse through extracellular space, the effective flux is given by

$$\boldsymbol{J} = \boldsymbol{J_E}(\boldsymbol{E}) \sum_{\kappa=1}^{N} (1 - W_\kappa(\boldsymbol{x}, t)). \tag{3.23}$$

The EPS production rate $Q^{\Lambda(\kappa)}$ in Ω_c is proportional to the live biomass and we write

$$Q^{\Lambda(\kappa)} = \sum_{\kappa=1}^{N} W_\kappa(\boldsymbol{x}, t) \mu_E^{\Lambda(\kappa)} U_E^{\Lambda(\kappa)} \Theta_\kappa, \tag{3.24}$$

for $\boldsymbol{x} \in \Omega_c$, where $\mu_E^{\Lambda(\kappa)}$ is the maximum EPS production rate, $U_E^{\Lambda(\kappa)}$ is a normalised production rate function dependent on substrates X, and Θ_κ is the live cell fraction, defined as

$$\Theta_\kappa = \frac{C_L^\kappa}{C_L^\kappa + C_D^\kappa}. \tag{3.25}$$

Suitable functional forms for $U_E^{\Lambda(\kappa)}$ will be discussed later.

The final term in Equation (3.21) represents the EPS decay and consumption rate, which will be discussed in detail in Sections 4.1.2 and 6.1.5.

The finite volume form of Equation (3.21) will be used in the numerical solution, where Ω_c will represent a $dx \times dz$ grid cells of the lattice described in Section 3.1. For numerical purposes, EPS is assumed to be released into the dashed lattice sites where the particle is located (see Figure 3.4). The ratio of the EPS production rate in these lattice sites is proportional to the volume fraction of particles in the sites. The numerical algorithm assumes that within each grid cell Ω_c there is extracellular space, into which EPS can be released from a particle.

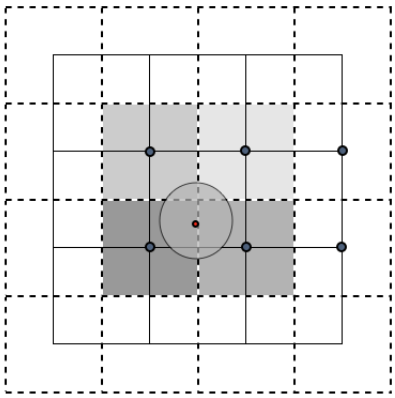

Figure 3.4: EPS concentration in four neighbouring grid cells containing a particle. The particle will release EPS into each of the four grid cells at a rate proportional to the fraction of particles in the cell. It is assumed that this EPS disperses evenly in each cell, leading to concentration differences between cells and hence EPS gradients.

If the size of the grid is smaller than the maximum particle size, then a particle may occupy a whole lattice site, in which case there will be no space available in this site into which to release EPS, consequently the numerical algorithm will fail in its present form. Hence, the size of the grid has to be set to be at least larger than the particle size, i.e., $dx \geq 2R_{max}$.

3.7 Movement of Cell Particles

In the absence of other particles, EPS, and solid boundaries, the particles will grow and divide and, at least for the first division, the centre of mass of the particles will be fixed. As particles grow it is inevitable that they will overlap with their neighbours, and thus the particle must move, and move its neighbours, if necessary, to arrange themselves so that the overlaps have been eliminated. Overlapping solid boundaries must also be avoided in the algorithm. Furthermore, at high EPS concentrations, the "EPS pressure" can generate movement. The modelling framework takes into account all these factors.

Let $\boldsymbol{B}_{\boldsymbol{p}}^{\boldsymbol{\kappa}}$ be the total displacement vector of the particle index κ over a time

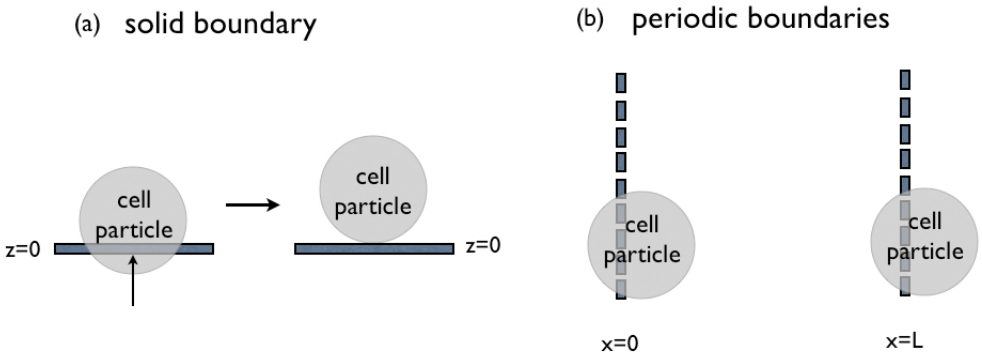

Figure 3.5: The boundary conditions: (a) Impenetrable boundary at $z = 0$. When a particle overlaps with the boundary $z = 0$, it moves upward to just attach to the boundary. (b) Periodic boundaries at $x = 0$ and $x = L$ where L is the length of the domain. If a particle penetrates the boundary $x = 0$ ($x = L$) then an identical particle appears with the relative position at the other boundary $x = L$ ($x = 0$).

increment, then the net movement is given by the sum of those factors described above, namely

$$\boldsymbol{B}_{\boldsymbol{P}}^{\boldsymbol{\kappa}} = \boldsymbol{B}_{\boldsymbol{C}}^{\boldsymbol{\kappa}} + \boldsymbol{B}_{\boldsymbol{E}}^{\boldsymbol{\kappa}} + \boldsymbol{B}_{\boldsymbol{B}}^{\boldsymbol{\kappa}}. \tag{3.26}$$

where $\boldsymbol{B}_{\boldsymbol{C}}^{\boldsymbol{\kappa}}$, $\boldsymbol{B}_{\boldsymbol{E}}^{\boldsymbol{\kappa}}$, and $\boldsymbol{B}_{\boldsymbol{B}}^{\boldsymbol{\kappa}}$ are the displacement vectors due to the pushing by neighbouring cell particles, the EPS pressure, and the solid boundaries, respectively. During the movements, the moving particles may cross the boundaries (see Figure 3.5). If the boundary is impermeable, the particles will "bounce" back in the direction normal to the surface so that it just touches it (Figure 3.5(a)), i.e., $\boldsymbol{B}_{\boldsymbol{B}}^{\boldsymbol{\kappa}} = p_\kappa \boldsymbol{n}$ where p_κ is distance through which the particle of index κ crossed the solid boundary and $\boldsymbol{n}$ is the normal vector to the surface (Figure 3.5(a)). If the boundary the particle crosses is periodic, then $\boldsymbol{B}_{\boldsymbol{B}}^{\boldsymbol{\kappa}} = 0$ and the overhanging part of the particle will appear at the other end of the domain (see Figure 3.5(b)). In the present framework, the only impermeable boundary is at $z = 0$ and the two side boundaries are assumed to be periodic. We note that $B_B^\kappa = 0$ for all interior particles.

Particles may push neighbouring particles to gain space for growth. To check

whether a "primary" particle overlaps its neighbours, it is convenient to set the size of computational grid to be $dx = 2R_{max}$ (see Sections 3.1 and 3.6). Due to the fact that the maximum radius of a particle does not exceed R_{max}, a particle occupies at most four lattice squares next to each other. Therefore, the algorithm for checking for overlapping particles examines the distance of the particles located in the 3×3 grid-cells around the centroid of the primary particle. If an overlap is detected, then the overlapped particles are forced to move apart (Figure 3.6(b)) by the displacement vector $\boldsymbol{B_C^\kappa}$ for $\kappa = 1..N(t)$, which is a modified from that of Kreft *et al.* [168], given by,

$$\boldsymbol{B_C^\kappa} = \sum_i \frac{\varpi r_\kappa + r_i - d_i}{1 + \left(\frac{r_\kappa}{r_i}\right)^2} \boldsymbol{f_i}, \tag{3.27}$$

where i is the index of the neighbouring particles which overlap the primary particle, r_κ and r_i are the radius of the primary particle and neighbouring particle i, respectively. The overlapping distance of primary and neighbour particle is represented by d_i. The constant ϖ is a factor to adjust the average minimum distance between particles to a realistic value (we used $\varpi = 1.3$, [169]). The direction of movement of the particles is parallel to the vector $\boldsymbol{f_i}$, which is the unit vector in the direction of the line connecting the centres of the primary and neighbouring particle i. There are two features of Equation (3.27) that improve on related forms in previous IbM biofim studies [162, 164, 165, 166, 168, 176]. Firstly, the equation ensures that the smaller particles move further than the larger ones when they are in contact. Secondly, it conserves the centre of mass of the particles.

As discussed in Section 3.6, a high EPS concentration can generate an EPS expansion force in the direction $-\nabla E$. This pressure has the ability to move the particles. The vector, $\boldsymbol{B_E^\kappa}$ for $\kappa = 1..N(t)$, is the movement of the particle of index κ by the EPS, and is assumed to be proportional to the flux of the EPS, $\boldsymbol{J_{i_\kappa}}$, hence

$$\boldsymbol{B_E^\kappa} = \sigma \Delta t \boldsymbol{J_{i_\kappa}}, \tag{3.28}$$

where σ is a drag coefficient, Δt is the numerical time increment, and i_κ is the

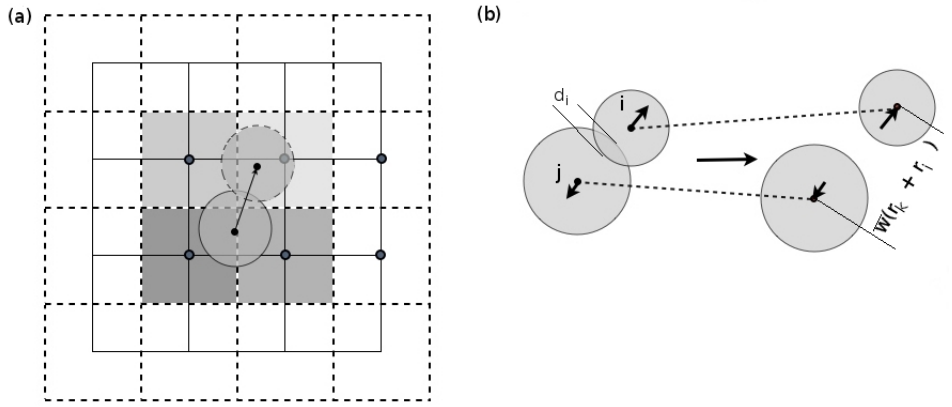

Figure 3.6: (a) Schematic of the effect of a very high EPS concentration (dark grey) on cell motion as EPS spreads to low concentration regions. (b) Diagram of particle spread to avoid overlap, with the centre of mass preserved.

index of the dashed grid-cell in which particle κ is located. This expression represents the cumulative effect of the EPS gradient in the neighbouring boxes around the particle.

3.8 Boundary Conditions

The boundary conditions of the computational domain are assumed to be periodic at the two side boundaries and impermeable at the bottom boundary (see Figure 3.1). The figure also illustrates the biofilm free surface, which changes in time through expansion of particles and EPS. In this thesis, two scenarios of biofilm growth are considered: biofilm growth in water and on a growth medium (see Figure 3.7). For the diffusion of substances, the upper boundary is either at the line $\Phi_d(\boldsymbol{x}, t) = 0$, which is defined by h_z above the highest point of the biofilm and perpendicular to the substratum (see Figure 3.7a), in the case of a biofilm growing in water; or at the biofilm surface, $\Phi(\boldsymbol{x}, t) = 0$, in the case of a biofilm growing in air. For the models of biofilm growth in water, the line of the upper boundary is the interface of the bulk fluid and the diffusion layer. The concentrations of the solutes are set to be constants in the bulk fluid and diffuse from the boundary. For the models of the biofilm growing in air, the nutrient source is placed at the

base of the system, and diffuses up to the biofilm–air interface, $\Phi(\boldsymbol{x}, t) = 0$; the other agents, such as oxygen and antibiotics, are set to diffuse downward from $\Phi(\boldsymbol{x}, t) = 0$. In the present framework, the bulk fluid is assumed to be static, therefore, there is no shear stress in the system. The boundary conditions are given by

1. **Periodic boundaries:**

$$\begin{aligned} X(0, z, t) &= X(L_x, z, t) \quad \text{for } z \in [0, L_z] \text{ and } t \geq t_0, \\ \frac{\partial X(0, z, t)}{\partial x} &= \frac{\partial X(L_x, z, t)}{\partial x} \quad \text{for } z \in [0, L_z] \text{ and } t \geq t_0. \end{aligned} \tag{3.29}$$

2. **Case of solutes diffused from bulk fluid:**

$$\begin{aligned} X(x, L_z, t) &= X_0 \quad \text{for } x \in [0, L_x] \text{ and } t \geq t_0, \\ \frac{\partial X}{\partial z} &= 0 \qquad \text{at } z = 0. \end{aligned} \tag{3.30}$$

3. **Case of solutes diffused from the substratum:**

$$\begin{aligned} X(x, 0, t) &= X_0 \quad \text{for } x = 0..L_x \text{ and } t \geq 0, \\ \nabla X \cdot \boldsymbol{n} &= 0 \qquad \text{at } \Phi(\boldsymbol{x}, t) = 0. \end{aligned} \tag{3.31}$$

   where $\boldsymbol{n} = (\pm)\nabla\Phi/|\nabla\Phi|$ is the outward normal.

3.9 Computational Algorithm and Methods

In the simulations to follow, the domain is seeded with a few cells, randomly positioned on the solid surface. Features such as the initial particle size and particle division size, R_D^κ, are set. The lattice spacing is set to form a grid of cells of size $dx \times dx$, where $dx = 2R_{max}$ is the optimum, not being too small (so there is always space for EPS to be introduced during production) or too large (minimising the number of neighbouring particles for overlap checking). The computational time-step for the particle growth is chosen by $\Delta t \leq \frac{R_{max}^2}{\mu R_{min}^2}$, where μ is the maximum growth rate of the particle, such that the particles cannot grow

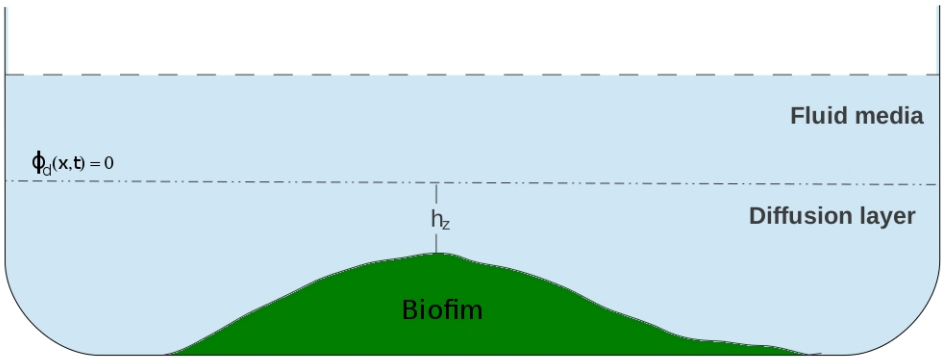

(a)

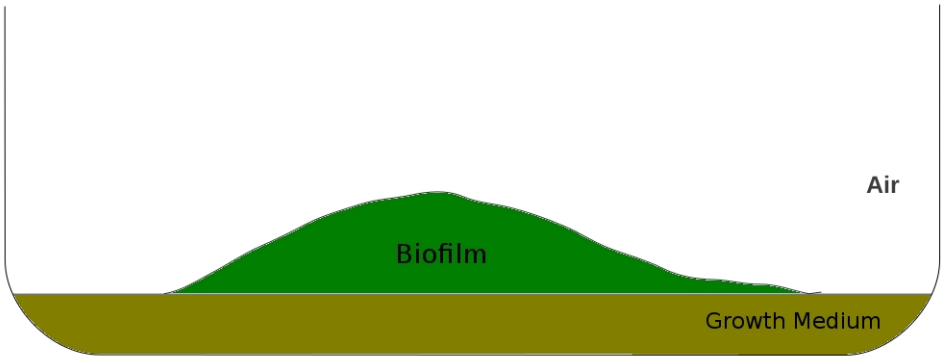

(b)

Figure 3.7: The model settings of biofilm growth. Biofilm growth in (a) water and (b) on a growth medium.

to exceed the maximum radius in one time-step. The global parameters including the size of the computational domain and the time and space steps are listed in Table 1 in Appendix A. The computational algorithm divides the framework into

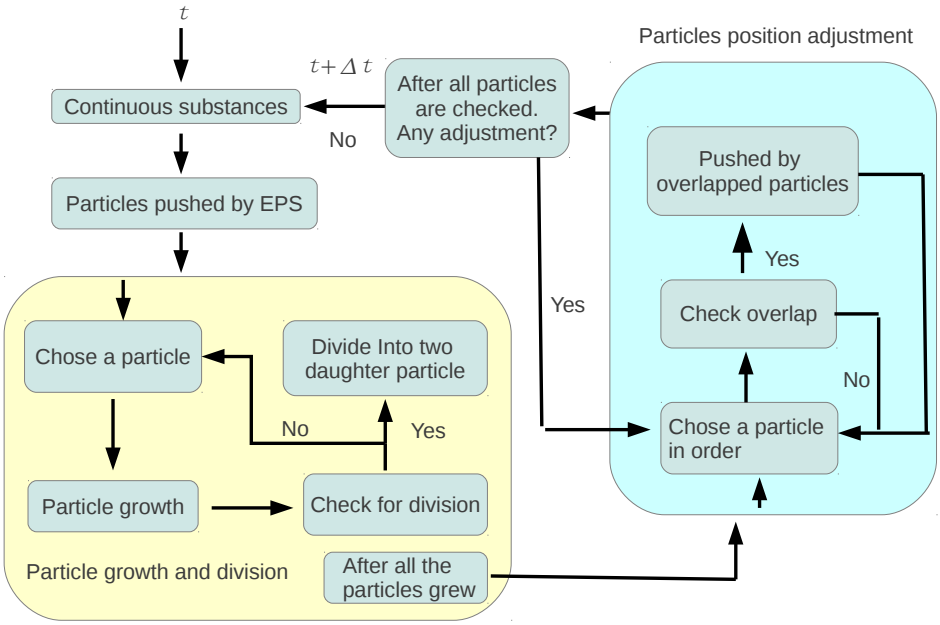

Figure 3.8: The computational procedure of biofilm model simulation.

four distinct units. For each time-step, these units are executed in sequence. These units are

1. **Continuous substance unit:** The aim of this unit is to solve for the continuous extracellular substances, for example, EPS, oxygen, and nutrient concentrations in the system, by applying the finite volume method discussed in Sections 3.5 and 3.6. The time dependent reaction–diffusion equations are solved by the alternating direction implicit (ADI) method and the quasi steady-state reaction–diffusion equations are solved by the inexact overlapped block Broyden's method [177]. Furthermore, Equation (3.21) being a nonlinear PDE, is discretised using standard central differences and an Euler time-step.

2. **Particles pushed by EPS unit:** In this unit, the new positions of the particles are determined following their displacement by EPS pressure. Firstly, a particle is chosen at random to be the target particle, then it is pushed

by the EPS, in the direction $\boldsymbol{B_E}$ determined in Section 3.7. Next a second particle is chosen at random and then displaced by the local pressure of the EPS. This process is repeated until all the particles have been chosen, at which point the algorithm moves to the next unit.

3. **Particle growth and division unit:** This unit is a sub-loop for particle growth and division. Firstly, a particle is randomly chosen from among the N particles, and then the Equations (3.3) and (3.4) are solved for the particle growth and death, respectively, using a simple Euler method. After that, the radius of the particle is determined by Equation (3.6) and then a check is made to see if the particle has exceeded its division size. If the radius of the particle is greater than the division radius then it divides into two identical daughters as discussed in Section (3.3). When this has been done, a second particle is chosen randomly from the remaining $N-1$ particles. This procedure is then repeated until all the particles have been treated, and checked for cell division.

4. **Particle position adjustment unit:** The aim is to eliminate particles that overlap. Those particles are moved to a non-overlapping arrangement. Firstly, a "reference state" of the particles is recorded. Secondly, a particle is chosen randomly as the primary particle, then a check is made as to whether it overlaps with any of its neighbours according to the reference position. If overlap(s) are found, then the primary particle is moved according to Equation (3.26) discussed in Section 3.7. A second particle is then selected at random, which becomes the new primary particle. Once more, a check is made for any overlaps in the reference state, and it is moved if required. The process is repeated for all particles. If no overlaps were detected then the algorithm is complete for this time-step. However, if there were overlaps, then a new "reference state" of the particles is recorded and then the process of random selection, overlap check, and particle movement is repeated. This will continue until a reference state has no overlaps, at which point the time-step is complete.

We note that in units 2, 3, and 4, particles are selected at random, rather than in a fixed sequence. This is to ensure there is no behavioural bias that may

result from particles in one region being dealt with before particles in another region.

3.10 Summary

In this chapter, a new IbM framework of biofilm growth was presented. Bacterial cells are assumed to form circular/spherical particles representing an individual or a cluster of live and dead cells. In Sections 3.7 and 3.9, we described how the framework eliminates particle overlap caused by particle growth. The activity of particles is governed primary by the energy (A_κ) which in turn is governed by the availability of environmental agents, e.g., oxygen and nutrients. In Section 3.2, 3.4-3.6 the evolution equations were presented in generic form for particle state and energy (Section 3.2), inter-cellular variables (Section 3.4), environmental agents (Section 3.5), and EPS (Section 3.6); they almost always involve differential equations. Though the ODEs that result can be solved using any standard numerical method, the discrete nature of the particles means that finite volume techniques are the the most efficient. The new features of the framework are

1. Compressible diffusible EPS. The diffusion depends on the pressure gradient caused by concentration differences.

2. Energy production. Particle behaviour, including growth, EPS production, and oxygen and nutrient consumption, are governed by the energy level of the particles.

3. Inter-cellular agent production. The agents are contained in either or both live and dead biomass.

4. Improvement in the particle displacement vector. The improved vector ensures that the smaller particles move further than larger ones when they are in contact, and conserves the centre of mass of the particles.

In Chapters 4 and 6 we will apply the framework to investigate growth and plasma treatment. There, specific reaction and flux terms will be presented.

Chapter 4

The Biofilm Growth Model

In this chapter, the modelling framework presented in the previous chapter is examined in a range of scenarios of biofilm growth. The various scenarios include single species, two species, topical nutrient sources (i.e., biofilm growth on a solid substratum), and basal nutrient source (e.g., biofilm growth on semi-permeable agar matrices). In our investigation we will pay particular attention to the role of the EPS in biofilm formation and structure.

4.1 Scenario 1: Single Species – EPS Producing Strain

4.1.1 Cell Mechanism

In this section, we will describe the application of the model framework to simulate the growth of a single species biofilm, in which the bacteria have the following relevant properties,

1. Produces EPS.
2. Is a facultative anaerobe, i.e., an aerobic bacterium that has some capacity to survive in low oxygen environments.

Many bacteria have such properties, including *Pseudomonas aeruginosa*, *Staphylococcus*, and *E. coli*. Figure 4.1 summarises the key metabolic pathways assumed

in the simulation. Bacteria take up nutrients (i.e., carbon sources) and oxygen to reproduce biomass, manufacture EPS, and generate energy (in the form of ATP). The intracellular energy enhances cell growth and division and inhibits cell death. When cells die, they may shrink by losing water and/or biotic compounds, whereby the biotic compound are then made available as nutrients. The rates of cell growth and the death of cells in the particles are described by Equations (3.3) and (3.4), where for the functions Ψ_b^κ, Ψ_d^κ, and Ψ_s^κ, we use

$$\Psi_b^\kappa = (\mu + \beta g(1))A_\kappa H(X_s, K_{X_s b}, m_{X_s b})C_L^\kappa, \tag{4.1}$$

$$\Psi_d^\kappa = \beta g(A_\kappa)C_L^\kappa, \tag{4.2}$$

$$\Psi_s^\kappa = \phi\beta g(A_\kappa)C_L^\kappa, \tag{4.3}$$

so that

$$\begin{aligned}\frac{dC_L^\kappa}{dt} &= ((\mu + \beta g(1))A_\kappa H(X_s, K_{X_s b}, m_{X_s b})) \\ &\quad -\beta g(A_\kappa))C_L^\kappa,\end{aligned} \tag{4.4}$$

$$\frac{dC_D^\kappa}{dt} = (1-\phi)\beta g(A_\kappa))C_L^\kappa. \tag{4.5}$$

The constant μ is the maximum growth rate of the particle (i.e., the growth rate at $A_\kappa = 1$), and β is the maximum death rate; ϕ is the ratio of dead biomass decomposed and converted to nutrients when live cell biomasses die; and X_s is the available nutrient concentration. Nutrient availability is described by the Hill function $H(X_s, K_{X_s b}, m_{X_s b}) \in [0, 1]$; namely

$$H(X, K_X, m_X) = \frac{X^{m_X}}{X^{m_X} + K_X^{m_X}}, \tag{4.6}$$

where the constant K_X is the Hill coefficient, such that $H(K_X, K_X, m_X) = 1/2$, and m_X governs how fast the function "jumps" from 0 to 1 in the vicinity of $X = K_X$. The Hill function becomes a simple switch function when $m_{X_s b}$. The function g is a death switching function, which is assumed to be monotonically

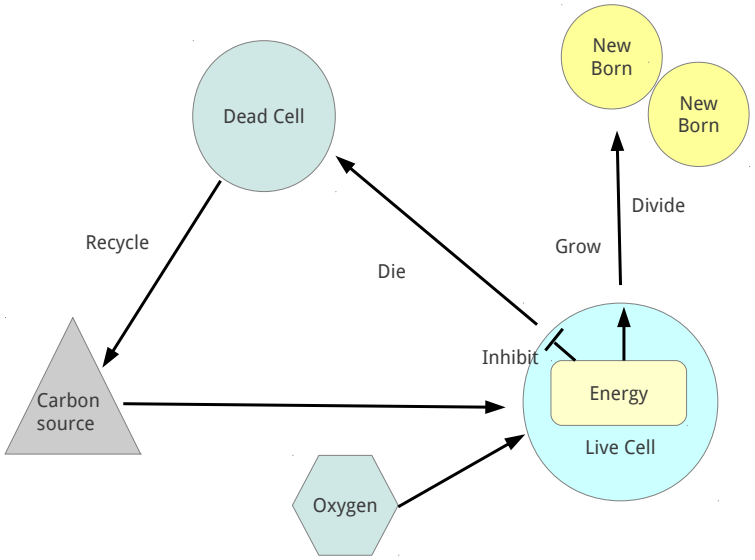

(a)

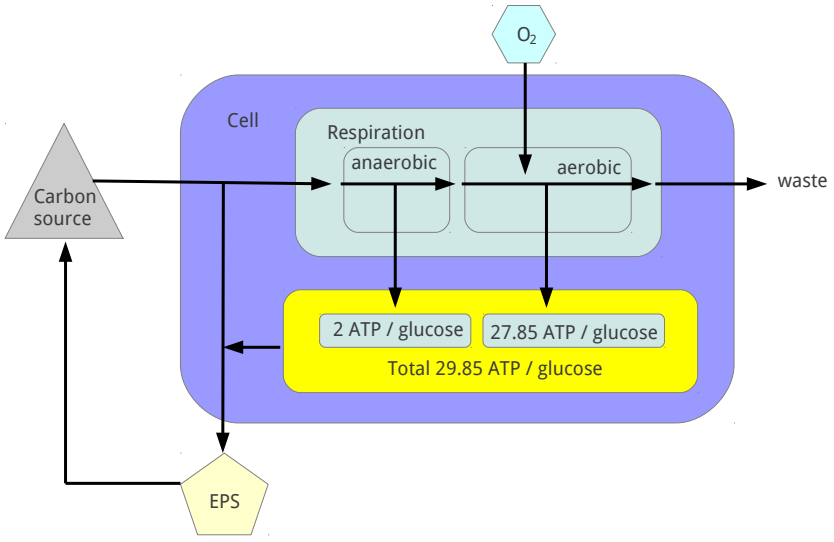

(b)

Figure 4.1: Plot of (a) general bacterial cell mechanism and (b) metabolism of EPS and ATP syntheses.

decreasing in $A_\kappa \in [0,1]$. The form for $g(A_\kappa)$ we adopt is

$$g(A_\kappa) = \frac{1}{1 + A_\kappa/k_a}, \tag{4.7}$$

where k_a is an energy "threshold" level. The assumption that the cells are facultative anaerobes means that if there are plenty of nutrients, then the cells will grow, or at least survive, in the absence of oxygen (see Figure 4.2). As discussed in Section 1.1.3, the metabolism of glucose has anaerobic and aerobic parts in which we assume a fraction of ω and $(1-\omega)$, respectively, of the total amount of ATP produced. As shown in Figure 4.1, for glucose $\omega \backsimeq 2/29.85$. We further assume that the bacteria does not compensate for any lack of oxygen by metabolising more glucose along the anaerobic pathway. Applying these assumption, the equation for A_κ is as follows

$$A_\kappa = H(X_s, K_{X_sA}, m_{_{X_sA}})(\omega + (1-\omega)H(X_{Ox}, K_{X_{Ox}A}, m_{_{X_{Ox}A}})), \tag{4.8}$$

where X_{Ox} is the available oxygen concentration. The level of aerobic respiration is governed by a Hill function switch in oxygen concentration, so that in low oxygen conditions, the level of ATP will be a fraction ω of its maximal level given a nutrient concentration. Figure 4.3 shows the energy level (non-dimensionlised, $A_\kappa \in [0,1]$) as a function of the nutrient and oxygen concentrations. The energy level drops to zero as the nutrient concentration decreases, but does not necessarily drop to zero with low oxygen, as the cells are able to generate energy anaerobically with sufficient nutrient.

4.1.2 EPS Production

The pathway of the processes including EPS production is summarised in Figure 4.1b. EPS production by live cells requires both nutrients and energy. In the extracellular environment, EPS can break up into smaller molecules due to digestion enzymes which are then available again as a nutrient. We assume the EPS production rate depends on the nutrient and energy levels as follows

$$U_E(A_\kappa, X_s) = A_\kappa H(X_s, K_{X_sE}, m_{_{X_sE}}), \tag{4.9}$$

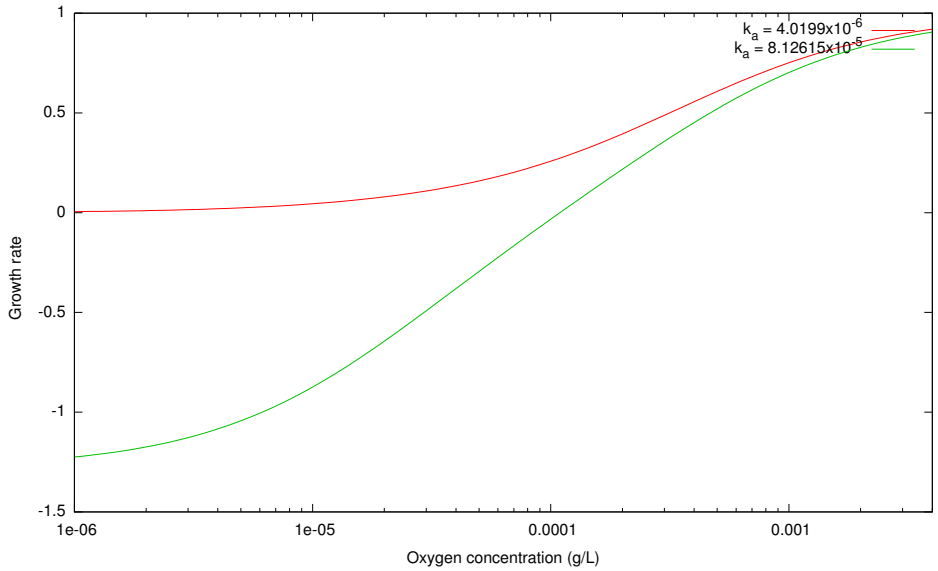

Figure 4.2: The growth rate against the logarithm of oxygen concentration in a nutrient-rich environment for the indicated value of k_a (dimensionless). The upper curve (red) is a profile aspected from a facultative anaerobe and the lower curve (green) is the profile of the bacteria which need oxygen to survive. The negative growth indicates death of the biomass.

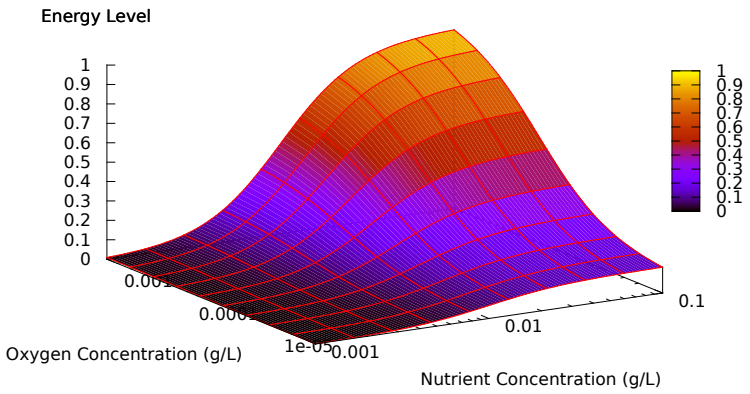

Figure 4.3: Plot of energy level against oxygen and nutrient concentrations. The values of the parameters are listed in Table 2 in Appendix A.

and that the decay rate is linear,

$$R_E = \beta_E E, \tag{4.10}$$

where β_E is the EPS decay constant; noting that as we are only considering one species in this section, the A_κ term has been dropped. We have assumed that substantial EPS will only occur in the presence of sufficient nutrients, described once again by a Hill function $H(X_s, K_{X_sE}, m_{X_sE})$. The equation for EPS, expressed in finite volume notation, is thus

$$\frac{\partial}{\partial t}\int_{\Omega_c} \varepsilon_c E d\Omega_c = -\int_{\partial\Omega_c} \boldsymbol{J}\cdot\boldsymbol{n} d\partial\Omega_c + \int_{\Omega_c} Q d\Omega_c - \beta_E \int_{\Omega_c} \varepsilon_c R_E d\Omega_c, \tag{4.11}$$

where

$$Q = \sum_{\kappa=1}^{N} W_\kappa(\boldsymbol{x}, t)\mu_{_E} A_\kappa H(X_s, K_{X_sE}, m_{X_sE})\Theta_\kappa. \tag{4.12}$$

and the ε_c is the extracellular void fraction in a computational grid box Ω_c. We recall that $\mu_{_E}$ is the maximum EPS production rate and Θ_κ is the fraction of live biomass at the point $\boldsymbol{x}$, where $\boldsymbol{x} \in \Gamma_\kappa$ and $W_\kappa(\boldsymbol{x}, t)$ is given by Equation (3.1).

Figure 4.4 shows the EPS production rate as a function of the nutrient and oxygen concentrations. Due to the fact that EPS production is dependent on nutrients and energy but not explicitly on oxygen, the shape of the plot of EPS production is similar to that in Figure 4.3.

4.1.3 Freely Diffusing Substrates

Oxygen and the nutrient are assumed to freely diffuse around the whole domain, through particles, cell membranes, as well as the extracellular space. They are consumed within the live portion of the particles. The time scales for the reaction and diffusion of the nutrient and oxygen are rapid, over $O(100\mu\text{m})$ in comparison to growth, the quasi steady form of the reaction–diffusion equations are applied for these agents. For simplicity, we will bundle all carbon source compounds into one generic nutrient variable. Thus, the mass balance equation of the nutrient

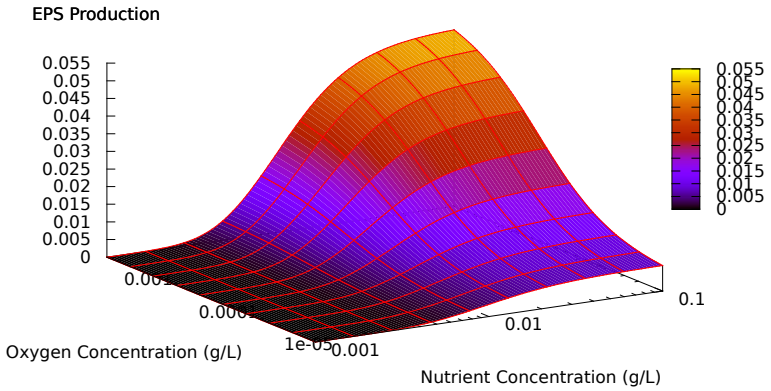

Figure 4.4: EPS production plotted against oxygen and nutrient concentrations. The values of the parameters are listed in Table 2 in Appendix A.

and oxygen concentrations are, in finite volume form,

$$0 = -\int_{\partial\Omega_c} \boldsymbol{J}_{\boldsymbol{X_s}} \cdot \boldsymbol{n} d\partial\Omega_c + \int_{\Omega_c} R_{X_s} d\Omega_c, \tag{4.13}$$

$$0 = -\int_{\partial\Omega_c} \boldsymbol{J}_{\boldsymbol{X_{Ox}}} \cdot \boldsymbol{n} d\partial\Omega_c + \int_{\Omega_c} R_{X_{Ox}} d\Omega_c, \tag{4.14}$$

where $\boldsymbol{J}_{\boldsymbol{X_s}}$ and $\boldsymbol{J}_{\boldsymbol{X_{Ox}}}$ are the fluxes and R_{X_s} and $R_{X_{Ox}}$ are the net consumption rates for the nutrient and oxygen, respectively. We assume Flick's law for the fluxes, hence

$$\boldsymbol{J}_{\boldsymbol{X_s}} = -D_{X_s} \nabla X_s. \tag{4.15}$$

$$\boldsymbol{J}_{\boldsymbol{X_{Ox}}} = -D_{X_{Ox}} \nabla X_{Ox}, \tag{4.16}$$

where D_{X_s} and $D_{X_{Ox}}$ are the diffusion coefficients of the nutrient and oxygen; because we have assumed there are no barriers to diffusion, then their value will be approximately that of water. The nutrient is only consumed at a point within a particle, i.e., $\boldsymbol{x} \in \Gamma$, during the processes of biomass reproduction, energy synthesis, and EPS production; and obtained within particles while cells die and extracellularly while the EPS decays. Furthermore, nutrient consumption only

occurs in live cells, thus the general reaction rate of the nutrient is given by

$$R_{X_s} = R_{X_sEX_s} + \sum_{\kappa=1}^{N} W_\kappa(\boldsymbol{x}, t)\Theta_\kappa(R^\kappa_{X_sd} - R^\kappa_{X_sA} - R^\kappa_{X_sE} - R^\kappa_{X_sb}), \tag{4.17}$$

where $R_{X_sEX_s}$ and R_{X_sd} are the rates of nutrient generation from decomposed EPS and dead biomass, respectively; and R_{X_sA}, R_{X_sE}, and R_{X_sb} are the rates of nutrient consumption from energy production, EPS production, and cell growth, respectively. In each case the nutrients are produced or consumed at a rate proportional to the rates of each process, hence

$$\begin{aligned}
R_{X_sEX_s} &= \mu_{_{X_sE}}\lambda E, && (4.18)\\
R^\kappa_{X_sd} &= \mu_{_{X_sb}}\phi\beta g(A_\kappa), && (4.19)\\
R^\kappa_{X_sA} &= \delta_{X_sA}H(X_s, K_{X_sA}, m_{_{X_sA}}), && (4.20)\\
R^\kappa_{X_sE} &= \mu_{_E}\rho_{_{EX_s}}A_\kappa H(X_s, K_{X_sE}, m_{_{X_sE}}), && (4.21)\\
R^\kappa_{X_sb} &= \delta_{X_sb}(\mu + \beta g(1))A_\kappa H(X_s, K_{X_sb}, m_{_{X_sb}}), && (4.22)
\end{aligned}$$

where $\mu_{_{X_sE}}$ and $\mu_{_{X_sb}}$ are the amount of nutrient produced per concentration of EPS decomposed and per volume of decomposed biomass, respectively; δ_{X_sA} is the consumption rate constant for energy synthesis (noting that nutrients are consumed here at the same rate regardless of the presence of oxygen); $\rho_{_{EX_s}}$ is the amount of nutrient mass per unit EPS mass; μ_E is the EPS production rate constant (see Equation (4.12)); and δ_{X_sb} is the mass of nutrient per unit volume of cells during growth.

Since oxygen is only consumed during aerobic respiration in ATP synthesis in live cells, the reaction of oxygen, R_X, is given by

$$\begin{aligned}
R_{X_{Ox}} = R^\kappa_{X_{Ox}A} &= \sum_{\kappa=1}^{N} W_\kappa(\boldsymbol{x}, t)\Theta_\kappa\delta_{_{X_{Ox}AX_s}}((1-\omega)\\
&\times \quad H(X_s, K_{X_sA}, m_{_{X_sA}})H(X_{Ox}, K_{X_{Ox}A}, m_{_{X_{Ox}A}})), \qquad (4.23)
\end{aligned}$$

where $\delta_{X_{Ox}AX_s}$ is the oxygen consumption rate constant for energy synthesis. The term $((1-\omega)H(X_{Ox}, K_{X_sA}, m_{_{X_sA}})H(X_{Ox}, K_{X_{Ox}A}, m_{_{X_{Ox}A}}))$, which is adapted from

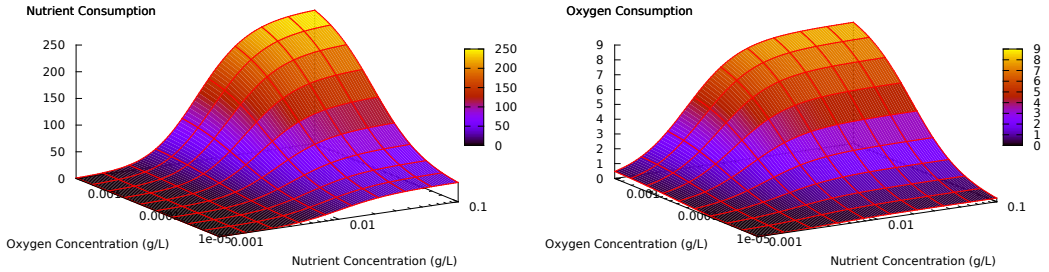

(a) (b)

Figure 4.5: Plot of (a) nutrient and (b) oxygen net consumption against nutrient and oxygen concentrations. The values of the parameters are listed in Table 2 in Appendix A.

Equation (4.8), indicates the level of oxygen consumption in energy generation via aerobic respiration. As an example, the net consumption rates of nutrients and oxygen are plotted in Figure 4.5a and 4.5b.

4.1.4 Simulations and Results

In this section, we present the results from some simulations of the model under various settings. The aim is to verify whether the system can generate results consistent with observation, and to check whether changing the parameters leads to results that would be expected when using different bacterial strains (mutants) or under altered environmental conditions. First, the simulations will be presented using parameters that will be referred to as the standard parameter set. Secondly, we will investigate how varying the parameters affects the long term biofilm development. Following this, the results from simulations with a nutrient source placed at the bottom of the system will be presented. As far as I know, this case has not been investigated before using mathematical models. Last, the simulation of bacterial cells which are able to survive in anaerobic conditions will be presented.

In order to visualise the results, the health and activity of a particle is defined by the fraction of the live cell biomass in the particle and will be presented

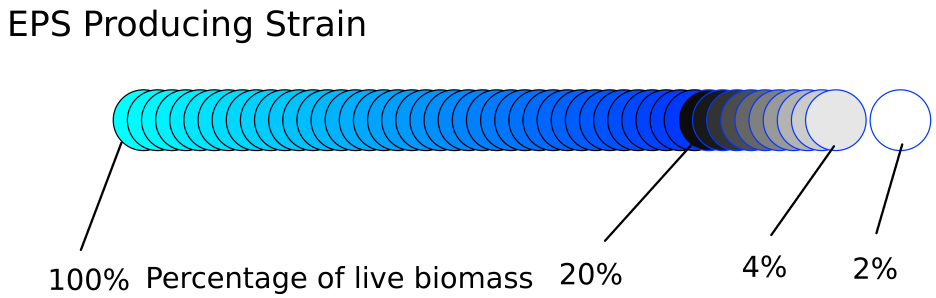

Figure 4.6: The colour of particles illustrates the percentage of live cell biomass in the particles.

using the colour scheme shown in Figure 4.6. In general, particles will be shown with a darker shade of blue as the dead biomass increases, becoming black when 80% of the cells are dead. As biomass dies, the "sickly" particle will be grey and alternately white when there is $< 2\%$ live biomass. It is assumed that all biological behaviour, including growth and EPS production, stop when the live cell biomass $< 2\%$, and will therefore be treated as completely dead. The parameters and their values are listed in Table 2 in Appendix A.

4.1.4.1 Simulation 1: Standard Single Species of Biofilm Growth Models

In this section, two "standard" simulations of single-species biofilm growth are presented. In the first case, a single particle is seeded at the centre of the base and the radius of the particle is chosen randomly within the range $r_1 \in [R_{min}, R_{max}]$. In the second simulation, twenty particles are randomly seeded at the bottom of the domain and the size of those particles are also randomly chosen, i.e., $r_\kappa \in [R_{min}, R_{max}]$, for $\kappa \in [1, 20]$. Figure 4.7 shows the domain of this standard biofilm growth. The "standard simulation" refers to the case in which the following statements are satisfied:

- Biofilms grow in a bulk fluid and attach at the bottom of the domain. Biofims are attached to the bottom and grow in a nutrient/oxygen diffusion layer. The depth of this layer is a fixed distance to the top of the biofilm.

Table 4.1: Crucial parameters and their values used in the simulation

[a] dimensionless
[b] the ratio of EPS prduction per biomass formed, $f_{Eb} = \rho_E/\rho_b = 0.2$

parameter	description	value	reference
k_a	energy threshold	8.126×10^{-5} [a]	Assumed
μ_E	maximum EPS production rate	0.0544 1/h	[178]
D_E	EPS diffusion coefficient	150 μ m^2/h	Assumed
σ	drag coefficient of particle movement pushed by EPS	2 [a]	Assumed
$\delta_{X_s b}$	nutrient consumption for biomass reproduction	138.598 g/L	Calculation [b]

- Above the diffusion layer is the "bulk fluid" which contains nutrient and oxygen at fixed concentrations.
- The bulk fluid is assumed stationary.
- EPS are produced by all live cells and released to the space between particles.

According to the assumptions, the boundary conditions (3.29) and (3.30) are applied. Table 4.1 shows some of the crucial parameters used in this section. The parameters may change between the simulations depending on the model settings.

Results

Two simulations of single-species biofilm growth were followed for up to 10 days from seeding. Simulation 1-1 is the biofilm formation starting with one particle placed at the centre of the base of the domain; Simulation 1-2 is the biofilm growth starting with 20 particles seeded randomly at the bottom boundary. In both simulations, the initial size of the particles is set randomly. Figure 4.8a and

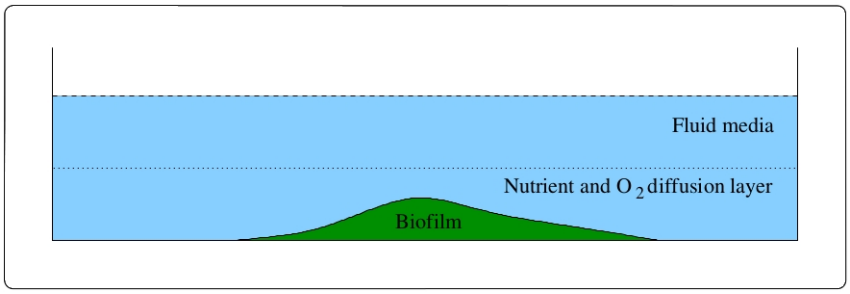

Figure 4.7: Plot of the "standard" biofilm growth scenario.

Figure 4.8b show the initial seeding of the particles in Simulations 1-1 and 1-2, respectively.

In the early stage, the nutrients and oxygen are able to penetrate through the biofilm so that all particles are adequately nourished (Figure 4.9) and EPS is produced at a high production rate and expands the particles to form a loose structure (see Figures 4.8c and 4.8d). The biofilms form a semi-circular bulge (Figure 4.8c) and several irregular bulge shapes (Figure 4.8d). Inside the biofilm, a high EPS concentration pushes the particles, resulting in the sparse distribution of the particles, leading to their occupying more space. However, the particle distribution is denser at the biofilm surface due to the fact that the higher nutrient and oxygen concentration there leads to more growth and division: EPS production, however, is not rapid enough to build up such high concentrations that will force cells to expand there. We note, in Figure 4.8d, the emergence of three bulges correspond to the initial particle clusters shown in Figure 4.8b. Figure 4.9 shows the nutrient and oxygen concentrations in the biofilms after two days growth. At this stage, nutrient and oxygen are able to penetrate through both biofilms, resulting high energy level in both biofilms. Consequently, biofilms produce high concentration of EPS (See Figure 4.10).

Figures 4.11a and 4.11b show the simulated old biofilm after four days for Simulations 1-1 and 1-2, respectively. In both cases, a region of dead/inert particles is located at the centre of the base of the biofilm due to the inability of nutrients and oxygen to penetrate the outer layer of live cells (Figure 4.12). Since the particles near the surface of the biofilm are have access to higher levels of nutrients and oxygen, they have more energy available and produce EPS at a greater

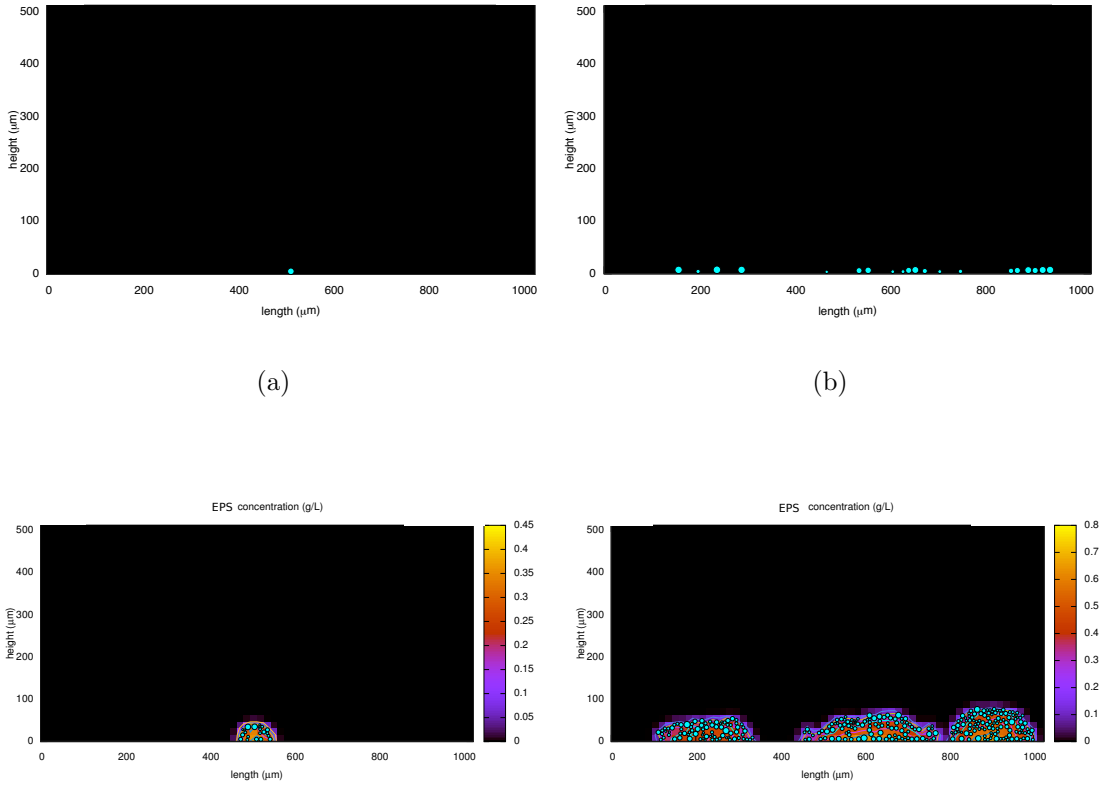

(a) (b)

(c) (d)

Figure 4.8: Particle distributions of initial seeding and after one day of biofilm growth. (a) Initial seeding of Simulation 1-1; (b) initial seeding of Simulation 1-2; (c) after one day of growth in Simulation 1-1; and (d) after one day of growth in Simulation 1-2.

rate(Figure 4.13). The region of highest EPS concentration inside the biofilm is moved from the bottom to near the surface of the biofilm. Here EPS is at a sufficient concentration to force particles apart and be fairly uniformly spread. In this stage, the biofilm in Simulation 1-1 becomes a larger semi-circular bulge, and, in Simulation 1-2, the irregular bulges have merged to form a thick bed of biofilm across the surface.

After 10 days, the biofilms have grown very large, 600μm thick or more, which

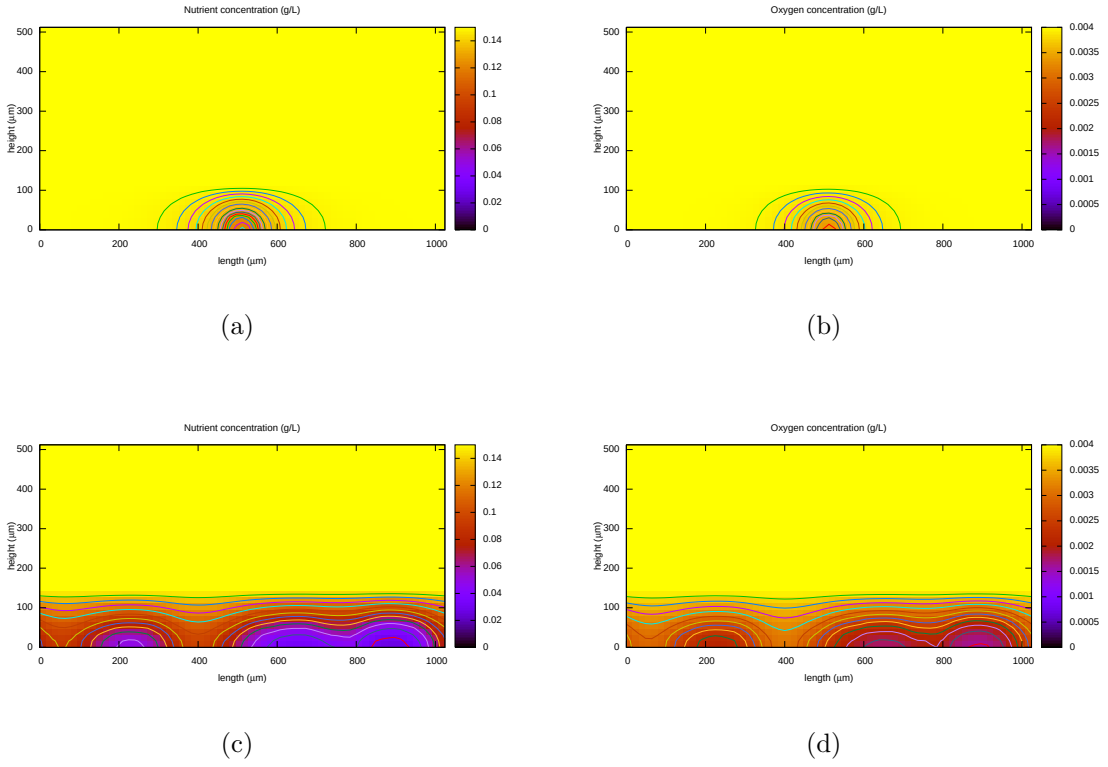

Figure 4.9: Plot of nutrient and oxygen concentration in both cases of biofilms at 1 day old. (a) and (c) show nutrient concentration distribution for Simulations 1-1 and 1-2, respectively. (b) and (d) show oxygen concentration for Simulations 1-1 and 1-2, respectively.

would be at the upper end of that observed in experiments [85]. In Simulation 1-1, the biofilm has grown into a tower-like structure (Figure 4.14): such structures are often described as "mushroom", though in most experiments, the biofilms are grown in flow chambers in which the shear force from the flowing bulk fluid flattens the top of the towers, and hence are more mushroom-like in shape. As cells near the top of the tower have access to more nutrients and oxygen (Figure 4.16a and b), they will grow faster and produce more EPS then those at the side: hence the growth in the vertical direction exceeds that in the horizontal direction, leading to the formation of a tower-like structure. For Simulation 1-2, in Figure 4.15, the results are more interesting. Here the three towers, noting that

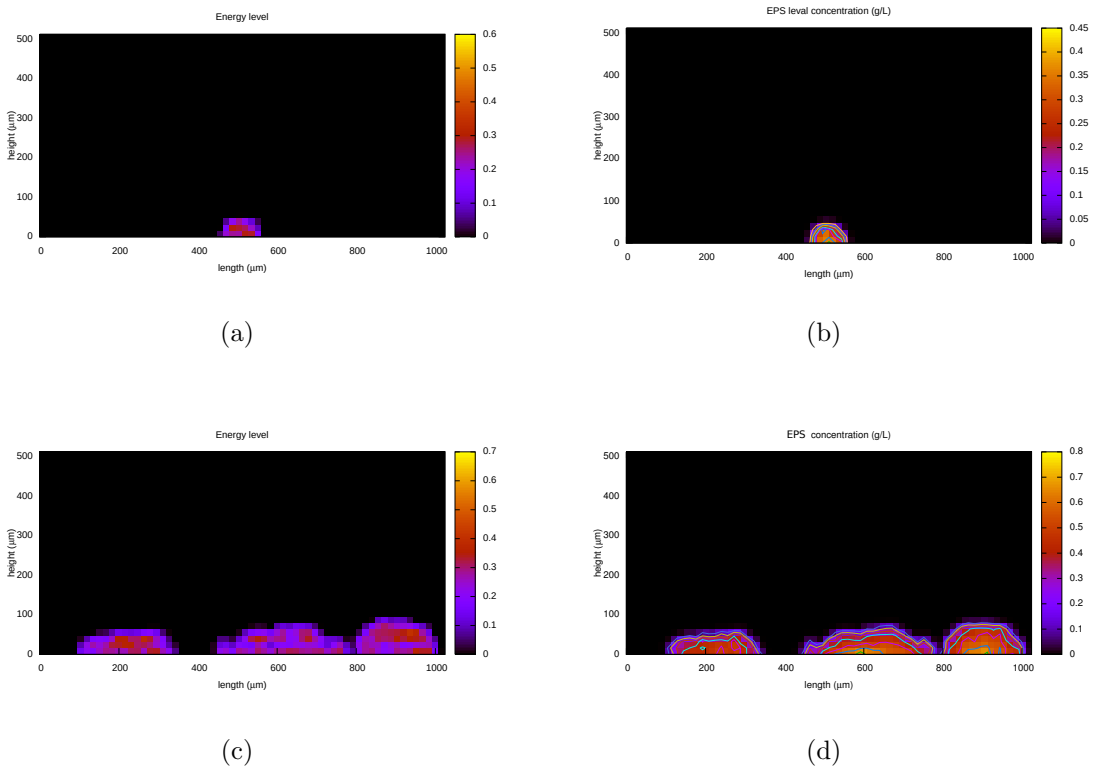

Figure 4.10: Plot of energy level and EPS concentration distribution in both cases of biofilms after one day. (a) and (c) show the energy distributions for Simulations 1-1 and 1-2, respectively. (b) and (d) show the distributions of EPS concentration for Simulations 1-1 and 1-2, respectively.

the left and right towers are the same from the periodic boundary condition, are developing at different rates, where the larger one, being closer to the nutrients, appears to be out competing the two smaller towers. Close examination of the live particles near the surface (or Figure 4.17(d) for energy level) show that the thickness of the live layer (the blue particles) is almost double that of shortest one. We note the tallest tower originated from the densest initial cluster towards the right of the domain in Figure 4.11b. This simulation seems to highlight the advantage of cells clustering early on, so as to form a biofilm, or tower, that will out compete its neighbours. The results are perhaps not unexpected, in the taller tower, being closer to the nutrient/oxygen source will grow faster and will in time

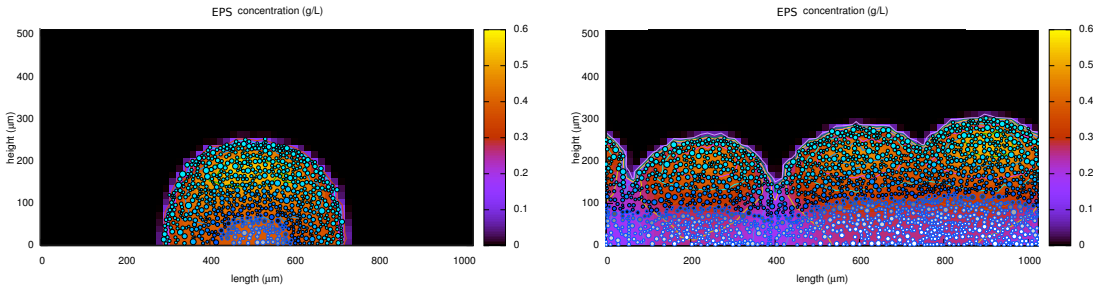

(a) (b)

Figure 4.11: Plot of four-day old biofilm structure with particle distribution and EPS concentration for (a) Simulation 1-1 and (b) Simulation 1-2.

kill off the smaller towers.

Figure 4.18 illustrates the profile of the biofilm thickness and the contribution of the live and dead biomass in the biofilm through 10 days of growth. The thickness is defined as the height of the highest tower in the biofilm, volume fraction of live/dead particles along the biofilm depth is calculated by the total volume of live/dead contribution of particles in the calculation depth divided by the volume of biofilm at the same depth. The biofilm increases its thickness linearly; however, the total live biomass becomes nearly stationary (in fact it is slowly decreasing, probably due to the smaller towers struggling because of the larger tower). The peak of the mean volume fraction of the live biomass travels at a nearly constant speed (Figure 4.18) with the increasing biofilm thickness, whilst the highest point of the average volume fraction of dead particles steadies at the bottom (Figures 4.18c and 4.18d). The nutrients and oxygen are able to penetrate the biofilm during the first two days, but are exhausted before reaching the bottom as the biofilm grows large (Figures 4.19a and 4.19b). Figures 4.19c and 4.19d show the average EPS concentration with the height of the biofilm throughout 10 days and the total concentration growth with time.

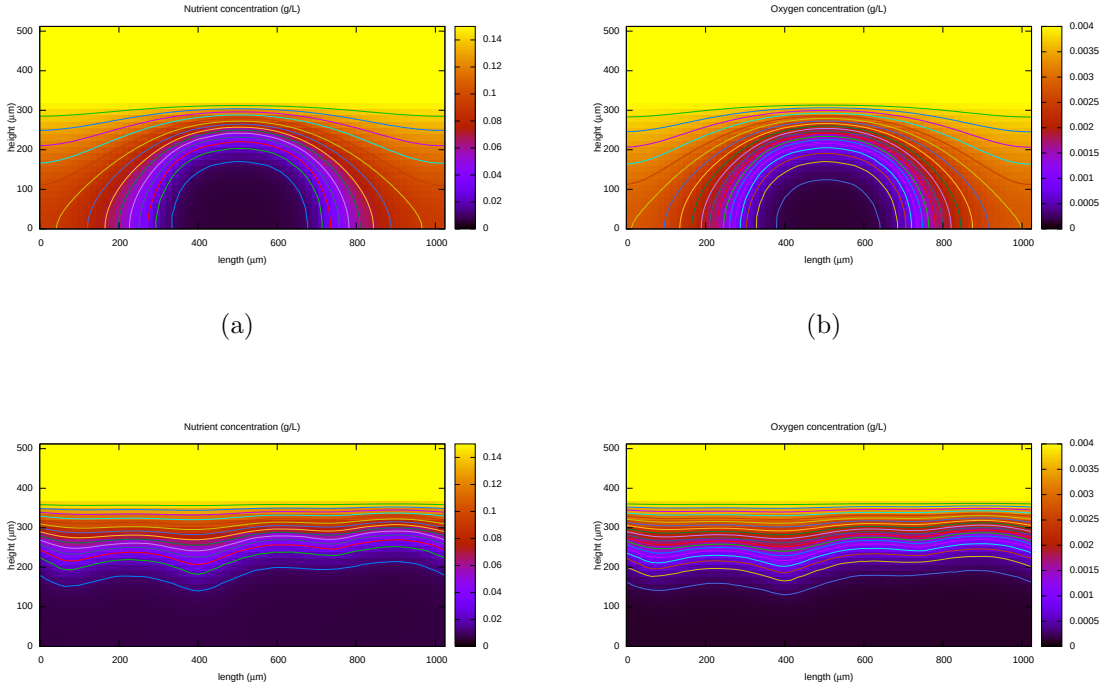

(a) (b)

(c) (d)

Figure 4.12: The nutrient and oxygen concentrations of 4-day old biofilm in Simulations 1-1 and 1-2. (a) Nutrient and (b) oxygen concentration of Simulation 1-1; (c) Nutrient and (d) oxygen concentration of Simulation 1-2.

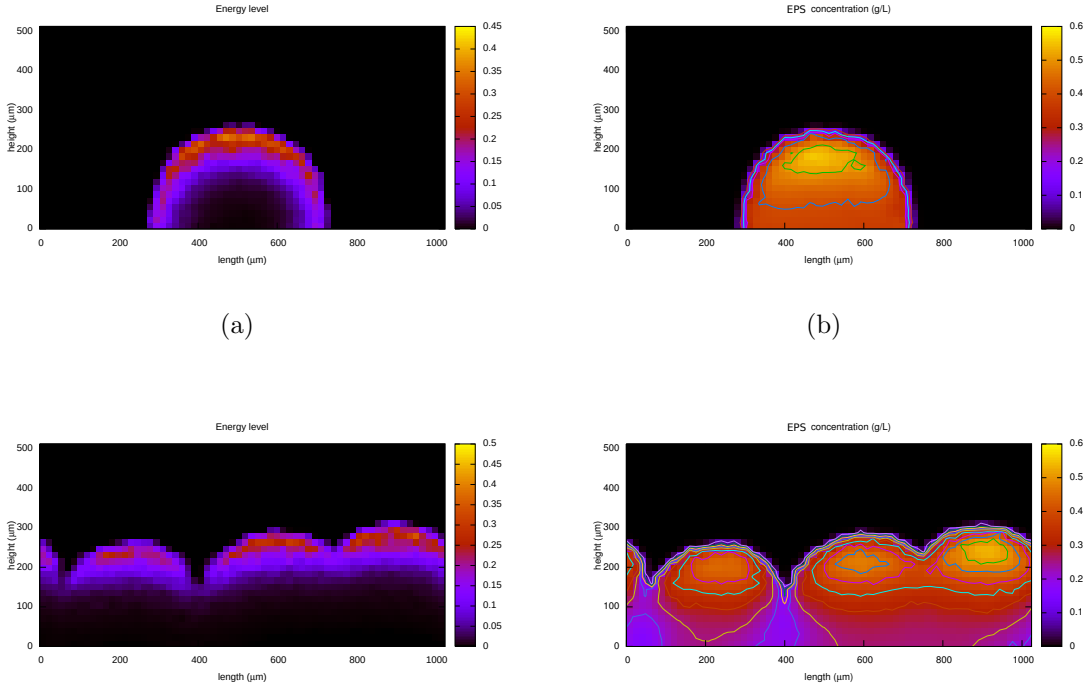

(a) (b)

(c) (d)

Figure 4.13: Plot of EPS concentration ((a) & (c)) and energy level ((b) & (d)) of 4-day old biofilm in Simulations 1-1 and 1-2. (a) and (b) are from Simulation 1-1; (c) and (d) are from Simulation 1-2.

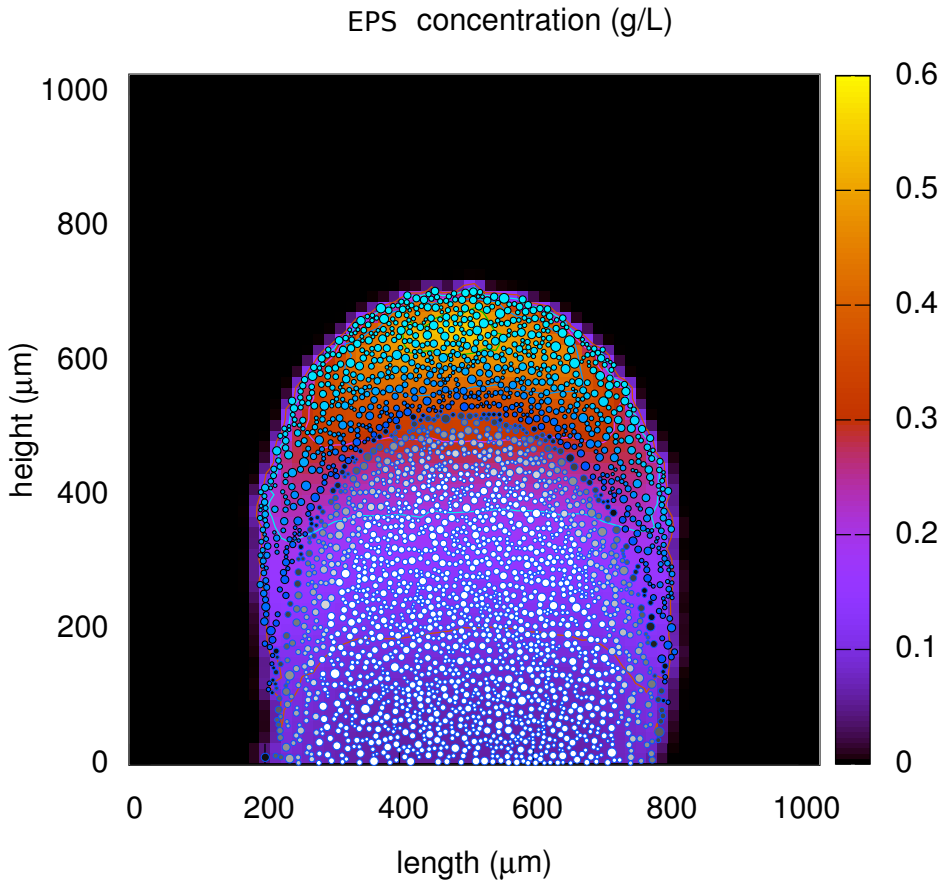

Figure 4.14: Plot of particle distribution with EPS concentration of 10-day old biofilm (Simulation 1-1).

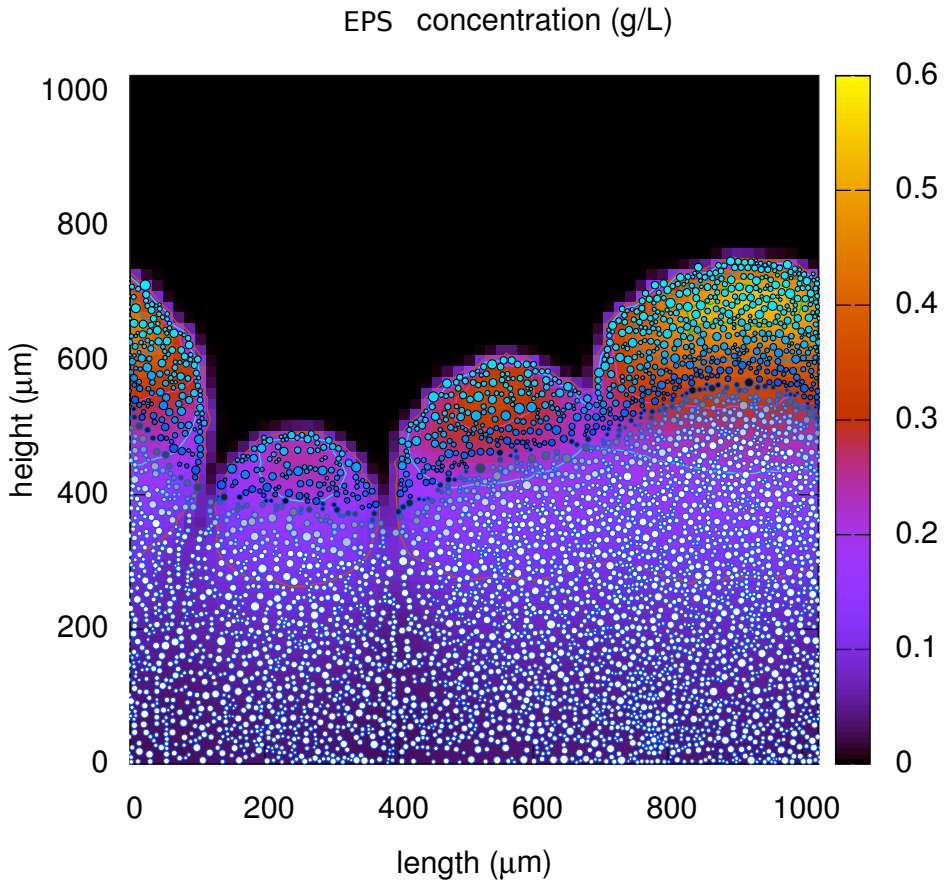

Figure 4.15: Plot of particle distribution with EPS concentration of 10-day old biofilm (Simulation 1-2).

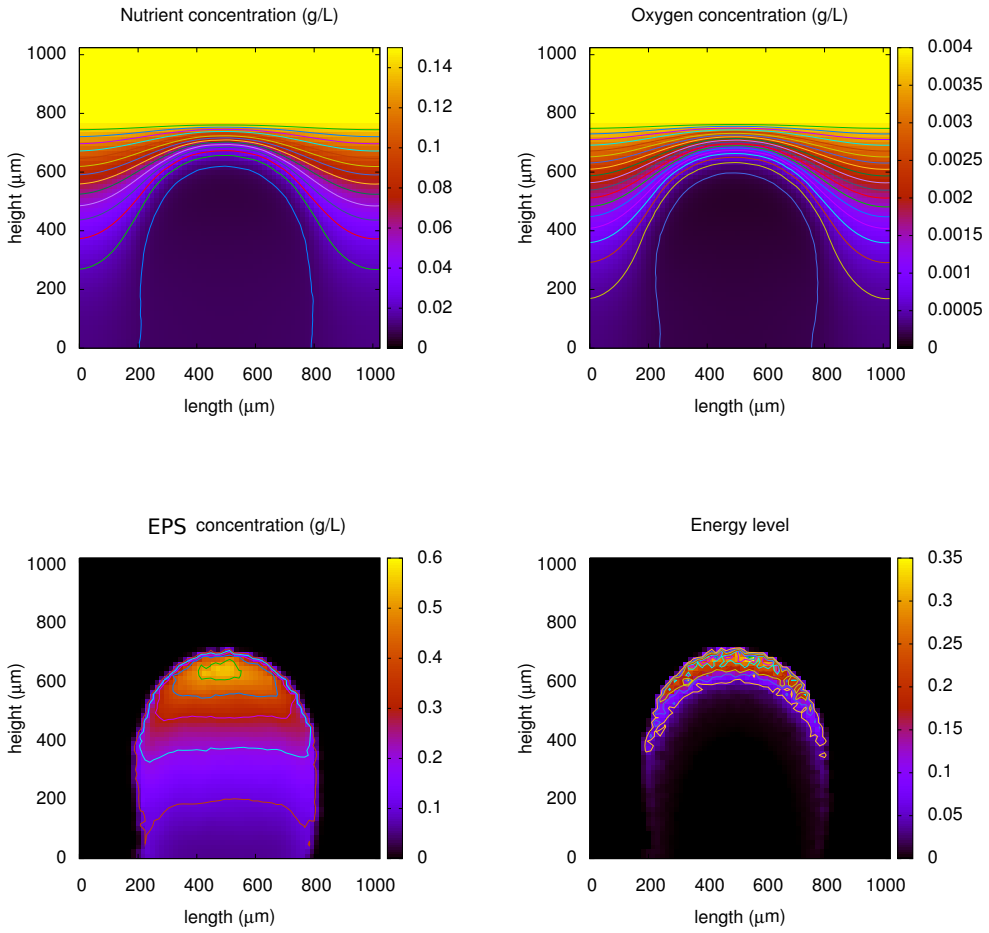

Figure 4.16: Plot of the nutrient, oxygen , EPS concentration and energy level after 10 days' growth in Simulation 1-1. Clockwise from top left: nutrient concentration, oxygen concentration, energy level and EPS concentration.

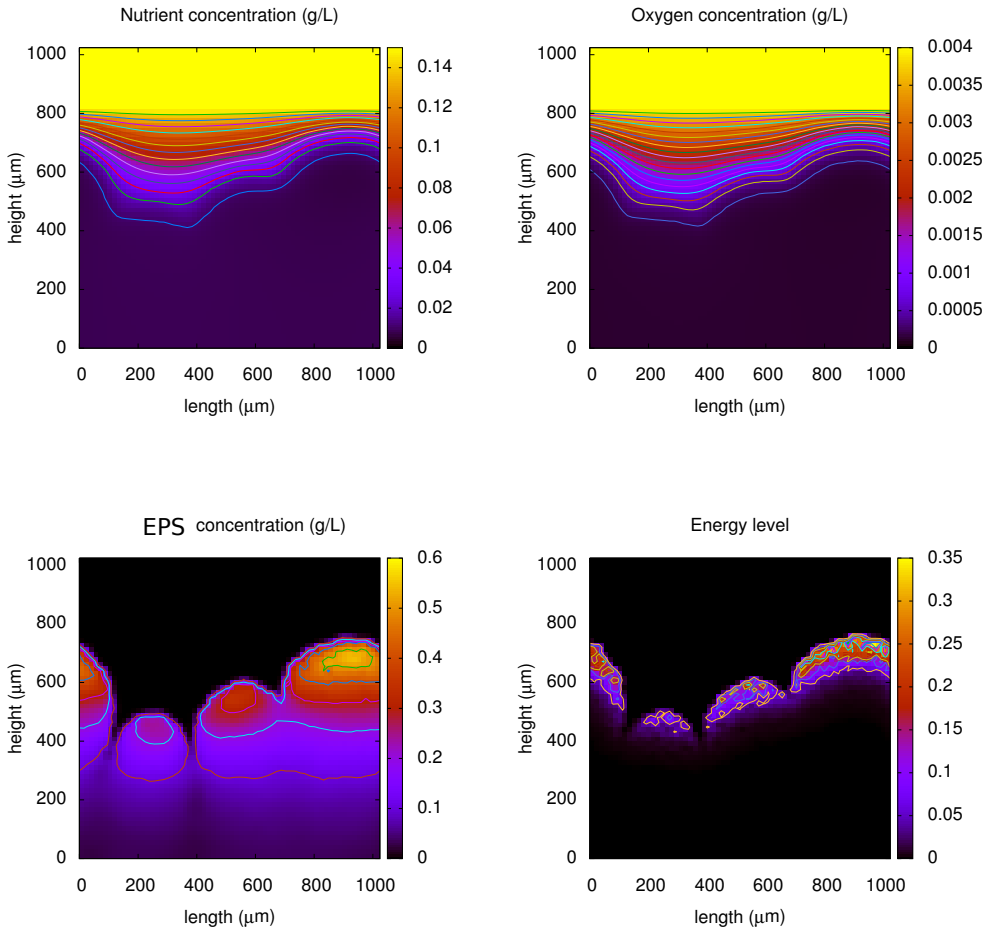

Figure 4.17: Plot of the nutrient, oxygen and EPS concentration and energy level after 10 days' growth in Simulation 1-2. Clockwise from top left: nutrient concentration, oxygen concentration, energy level and EPS concentration.

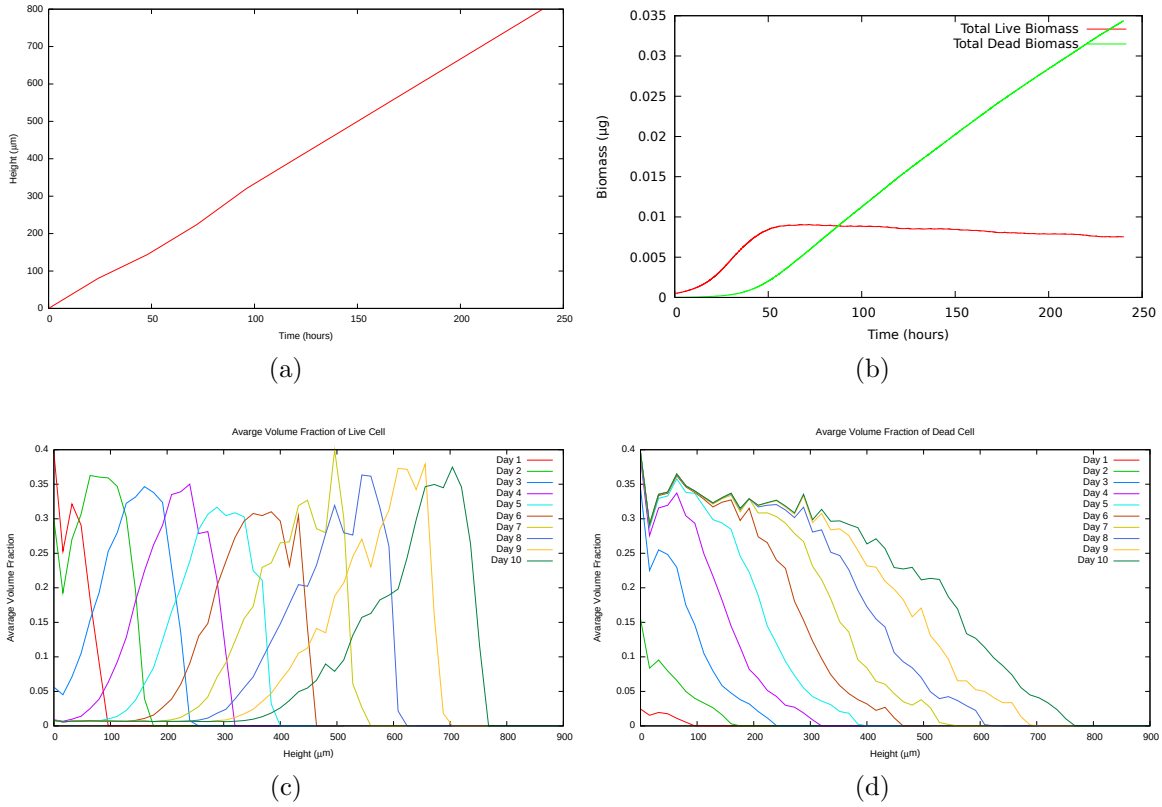

Figure 4.18: Evolution of (a) biofilm thickness, (b) live and dead biomass against time, (c) average volume fraction of live particles and (d) average volume fraction of dead particles against depth of biofilm throughout 10 days of biofilm growth in Simulation 1-2.

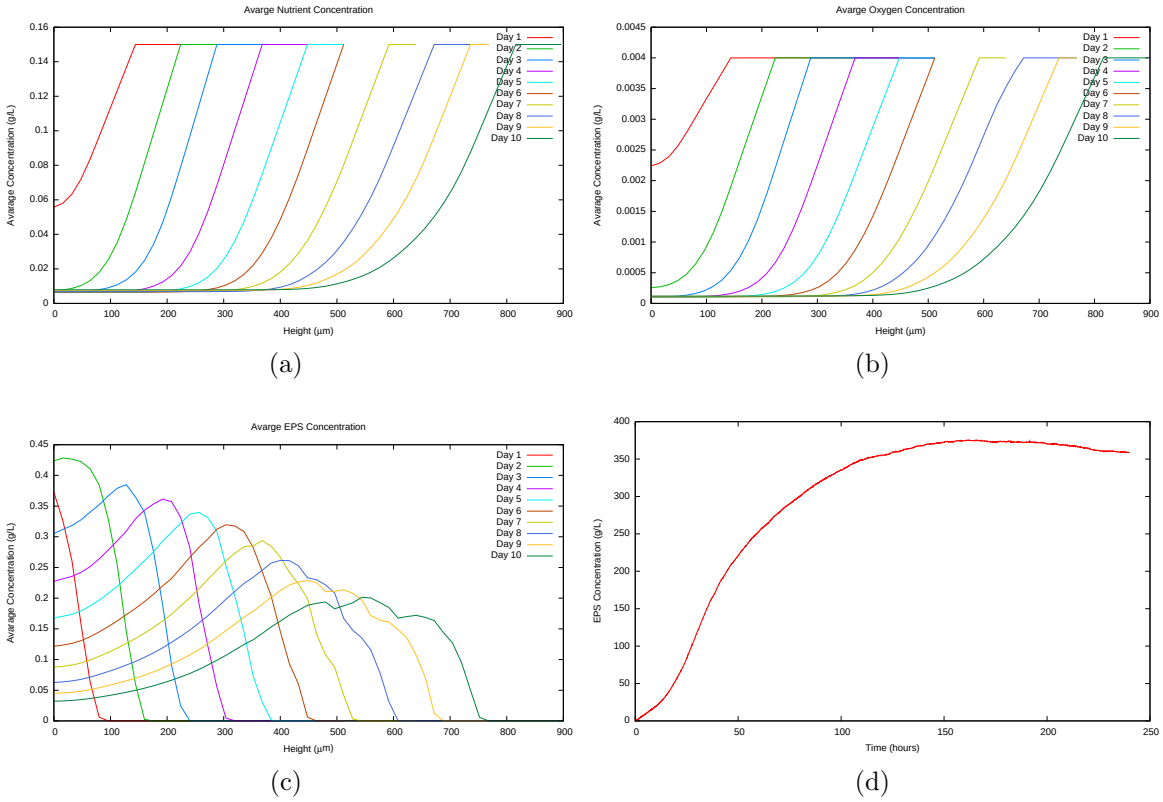

Figure 4.19: Evolution of the average concentration of (a) nutrients, (b) oxygen and (c) EPS against the biofilm thickness through 10 days of growth, and (d) the total EPS concentration in the biofilm against the time of biofilm growth in Simulation 1-2.

4.1.4.2 Simulation 2: EPS Effect on Biofilm Formation

In order to make explicit the role of EPS in biofilm formation in the previous simulation, we simulated here biofilm growth with no EPS production, i.e., an EPS production rate of $\mu_E = 0$ (Simulation 2-1), and the case in which EPS is produced but plays no part in particle movement, i.e., a drag coefficient of $\sigma = 0$ (Simulation 2-2). Furthermore, we investigated biofilm growth with a high EPS expansion rate, i.e., we increased the EPS diffusion coefficient to $500\mu m^2/h$ (Simulation 2-3). These simulations are modifications of the standard single species biofilm growth simulation Simulation 1-2 from the previous section, in which the same model and boundary conditions were applied with only a single parameter changed.

Results

Figure 4.20 shows the particle distribution after 10 days growth in Simulation 2-1 (no EPS production). In contrast with the biofilm structures in the standard case (see Figure 4.15), the biofilm in this simulation is less height (about 500 μm as opposed to 800 μm) and the particles are denser (see Figure 4.21), due to the biofilm's not having expanded its volume and having particles being forced apart by EPS. The well packed particles mean less penetration of nutrients and oxygen into the biofilm; consequently, the active particle region is thinner. However, the total cell biomass of the biofilm is slightly higher than in Simulation 1-2 (Figure 4.22): this is due to the nutrient's being preserved from EPS production and used instead to generate energy and create biomass. Like that of Simulation 1-2, towers of particles develop and the larger one having an advantage and growing more than the smaller ones. Here, the nutrients and oxygen need to travel further through the diffusion layer and to reach the lower surface towers, and the consequential reduction in the concentration of the nutrient and oxygen means the living layer is thinner than that of the larger tower.

Figure 4.23 shows the particle distribution and EPS concentration in the biofilm of Simulation 2-2 (no particle movement from EPS, i.e. $B_E = 0$) at 10 days of biofilm growth. The biofilm form is thicker than the previous case (Simulation 2-1) due to a part of the nutrient's being used to produce EPS and

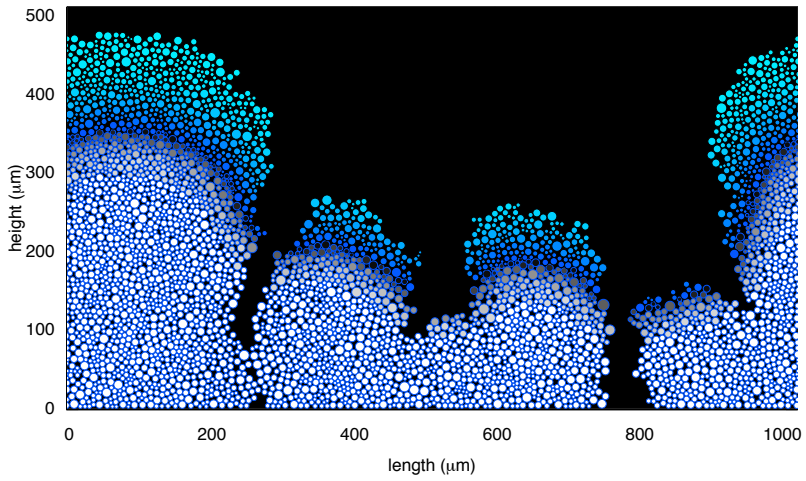

Figure 4.20: Plot of the particle distribution of Simulation 2-1 after 10 days growth.

the particles' not being expanded by an EPS flux. However, EPS still diffuses out. Hence, the particles are densely packed and embedded in a thick layer of EPS (Figure 4.23a).

Figure 4.24 shows the particle distribution and EPS concentration in Simulation 2-3 after 10 days of biofilm growth. The additional diffusivity of the EPS has a dramatic effect on growth and particle distribution. The main tower has grown to nearly 1000μm as opposed to about 700μm in Simulation 1-2 and 500μm in Simulation 2-1. Furthermore, particles are spaced much further apart due to the effective increase in drag by the faster moving EPS; we note from Equations (3.23) and (3.28) that the effective coefficient of drag is σD_E, which increases with D_E. The total live and dead biomass in these cases is similar (Figure 4.25), suggesting that EPS has little effect on bacteria growth, but is significant in how fast the biofilm grows.

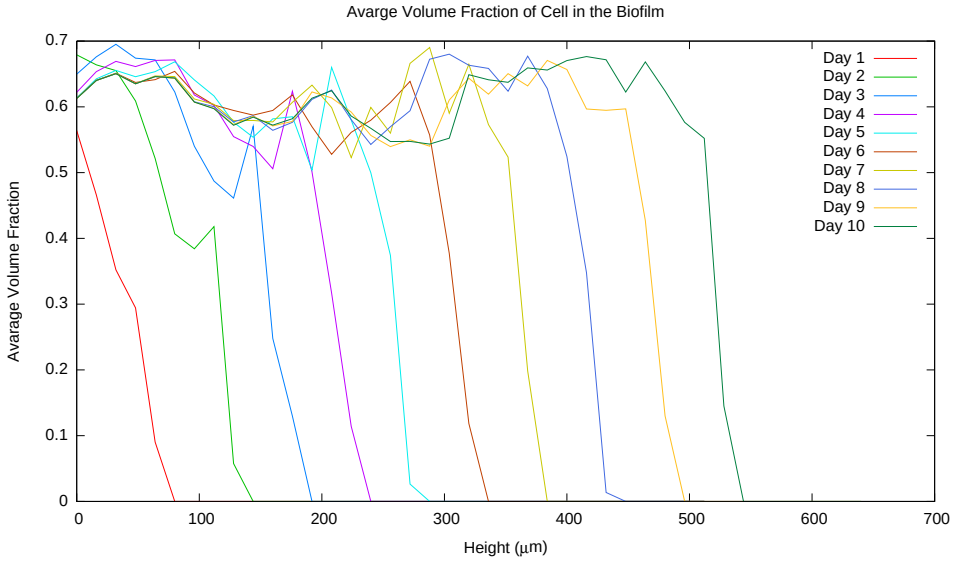

(a)

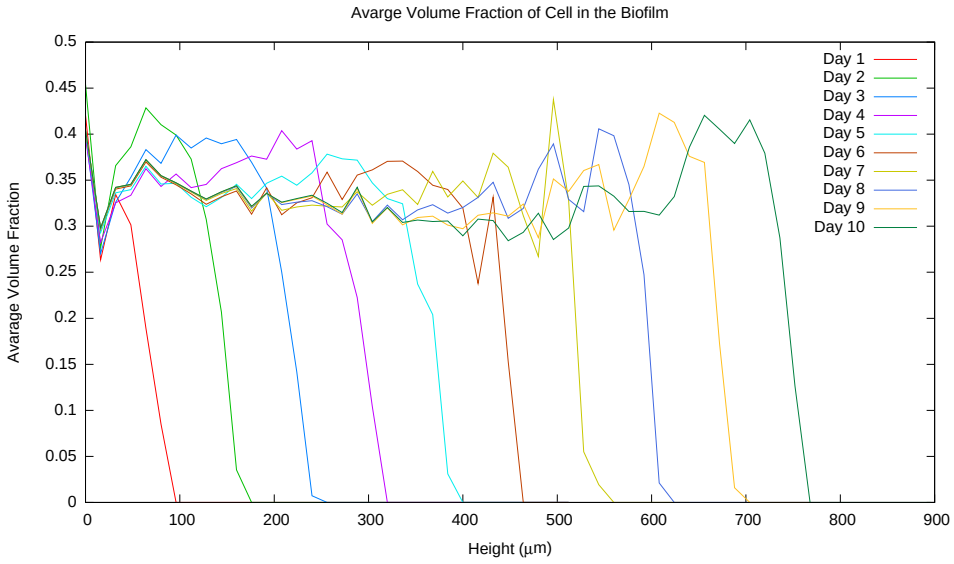

(b)

Figure 4.21: Comparison of the evolution of volume fraction of particles in (a) Simulation 2-1 and (b) 1-2.

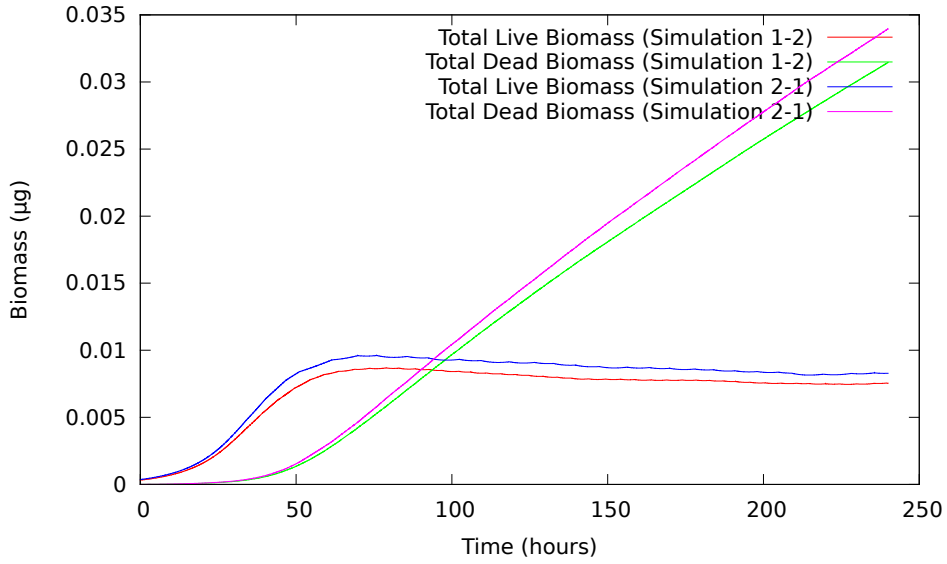

Figure 4.22: Comparison of total live and dead biomass against time between Simulations 1-2 and 2-1.

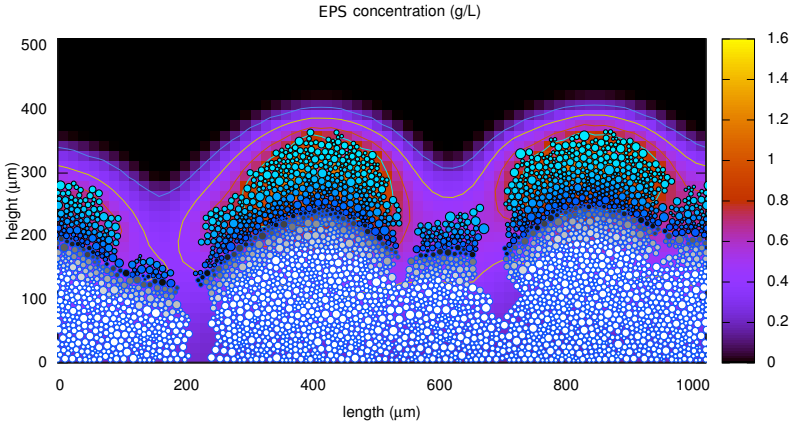

(a)

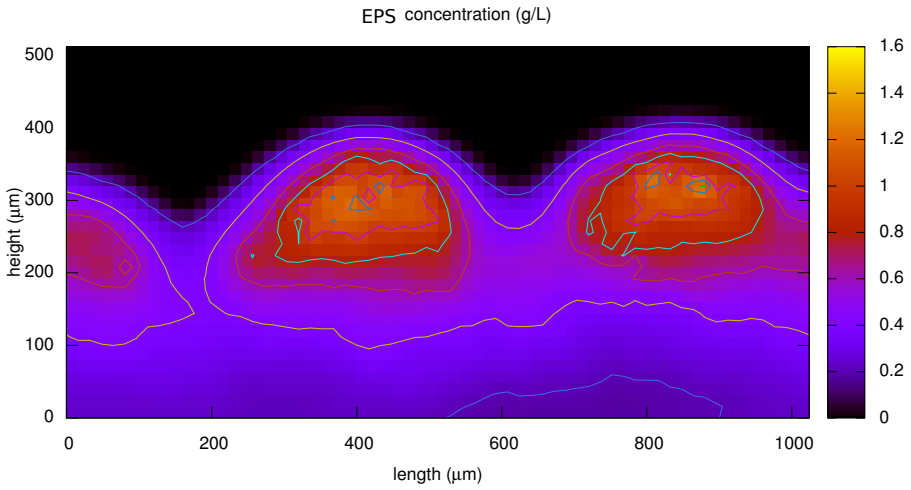

(b)

Figure 4.23: Plots of (a) the particle distribution and (b) the EPS concentration of Simulation 2-2 after 10 days.

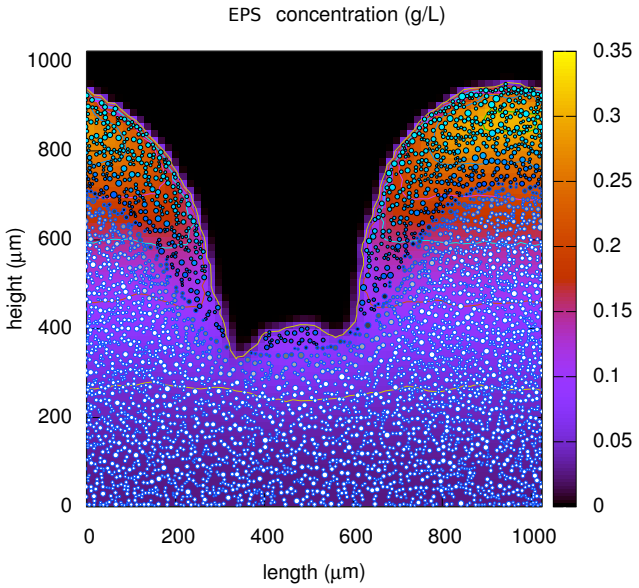

Figure 4.24: Plot of the particle and EPS distribution in the biofilm of Simulation 2-3 after 10 days.

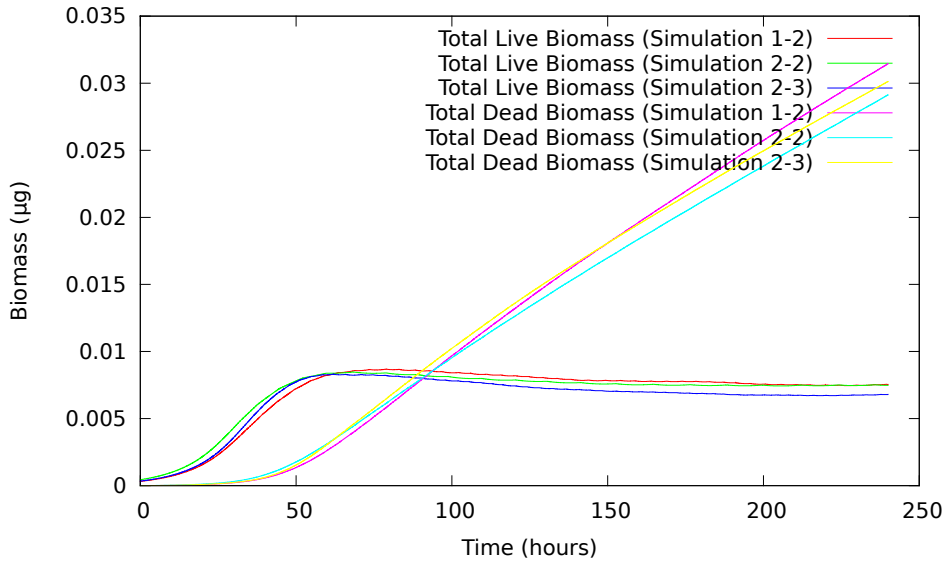

Figure 4.25: Comparison of total live and dead biomass between Simulations 1-2, 2-2 and 2-3.

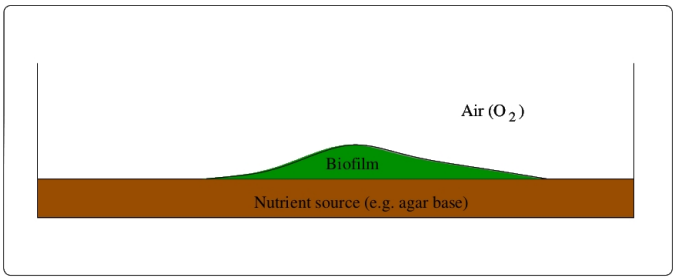

Figure 4.26: Schematic of the domains of biofilm growth on a semi-solid growth medium.

4.1.4.3 Simulation 3: Single-species of Biofilm Formation Grown on a Semi-Solid Substratum

In this section we use the model framework to simulate biofilm colonies grown on agar plates (Figure 4.26). Experiments on bacteria grown on plates are very common, including investigation of cold plasma treatment (see Chapters 5 and 6). Despite their wide spread experimental use, the mathematical modelling of biofilm in this scenario is rather minimal and limited to surface spreading bacteria an soft agar, i.e., a phenomenon known as swarming (see [179, 180, 181]).

The key difference in this scenario from that investigated in the previous sections is in the boundary conditions: here, the carbon source diffuses from the agar at the bottom, hence

$$\begin{aligned} X_s = X_{s0}, \quad \frac{\partial X_{Ox}}{\partial z} = 0, \qquad & \text{at } z = 0, \\ \nabla\Phi \cdot \nabla X_s = 0, \quad X_{Ox} = X_{Ox0}, \qquad & \text{at } \Phi(\boldsymbol{x}, t) = 0, \end{aligned} \tag{4.24}$$

i.e., the nutrient concentration is fixed at the bottom and there is zero flux of nutrient on the biofilm surface (recall that $\Phi(\boldsymbol{x}, t) = 0$ defines the biofilm edge in the domain, see Figure 3.1). The same boundary conditions in reverse are imposed for oxygen.

Results

Figure 4.27 shows the initial seeding of the particles of the simulation and the biofilm structure on day 1 of growth. By day 1, the biofilm forms several bulges and the general biofilm structure, including the particle distribution (Figure 4.27b), EPS concentration (Figure 4.27c) and energy levels (Figure 4.27d), are similar to those of Simulation 1-2 (Figure 4.8d in Figure 4.10) due to the biofilm's being similarly well nourished throughout (Figures 4.27e and 4.27f). As would be expected from this scenario, the cells near the biofilm receive the most nutrients but the least oxygen. We note that the location of the bulges correlates with the initial location of the particles.

By day 3, the bulges have merged so that the biofilm becomes relatively flat across the domain (Figure 4.28a). Because the nutrient is sourced from the bottom and the oxygen from the top, growth is more rapid along the agar surface than in the upward direction, a notable contrast to the situation in Simulation 1-2. The thinner sections of the biofilm grow faster than the thicker parts, eventually forming a structure that is fairly uniform in the x-direction, with all the substrates similarly distributed (Figures 4.28b–4.28d). We note that the oxygen only penetrates half-way through the depth of the biofilm, while a limited concentration of nutrient diffuses through to the biofilm surface. This results in most of the active particles' being present in a central band across the biofilm.

The biofilm structure after 10 days is shown in Figure 4.29. The biofilm is divided into three layers: two inert/dead particle layers, one at the surface due to a lack of nutrients and one at the bottom due to a shortage of oxygen, and an active particle layer in the middle. Since the most active particles are located in the middle of the biofilm, this is where the highest EPS production and faster particle proliferation and division occurs. This leads to the inert/dead particles to be pushed upwards or downward where they are forced to pack densely in the top and bottom region.

Figure 4.30 shows the profile of biofilm thickness and the evolution of total live and dead biomass against time, as well as the average volume fraction of live and dead particles against the height of the biofilm over 10 days of growth. Comparing this simulation to that of the standard case (Simulation 1-2), the

biofilm thickness no longer appears to be increasing linearly. Due to increasing dead particle layers at the top and bottom of the biofilm (Figure 4.30d), the active particles obtain less and less oxygen/nutrients. Consequently, the profile of total live biomass reaches a maximum at an early stage of growth and then drops slightly, and more rapidly afterwards.

The evolution of the average concentration of nutrients, oxygen, and EPS against the height of the biofilm, and the total concentration of EPS against the time of biofilm growth, are shown in Figure 4.31. It seems that oxygen is able to penetrate deeper in older biofilms as the thickening top layer consists of dead, non-oxygen consuming cells, through which oxygen can diffuse. Similarly, nutrients can penetrate a little deeper for the same reason. From Figure 4.31d, we note that the net EPS production rate is decreasing after 50 hours of growth. This is because EPS is only produced at the central band of the biofilm, and decays at the top and bottom. Therefore, the growth of the EPS concentration is slightly higher than its decomposition.

In order to confirm that the densely packed regions are caused by the particles' being pushed by the EPS, we increased the diffusion coefficient of the EPS from 100 to 200 $\mu m^2/h$ and the simulation starts with one particle placed at the middle of the basal nutrient (Simulation 3-2). Figure 4.32a shows the biofilm growth after three days. The structure of the biofilm is similar to that of the biofilm in Simulation 1-1. At this stage, the particles are adequately nourished by the nutrient and the oxygen, therefore, the biofilm's shape is semi-circular. However, after four days of growth, the bulge of the biofilm has flattened (see Figure 4.32b) due to the thick biofilm, so that less nutrient and oxygen reach the top or bottom of the biofilm than reach the side. This leads to a faster biofilm growth in the horizontal direction than vertically. By the eighth day, the structure of the biofilm (Figure 4.33a) clearly shows a spread of particles at the middle band and two denser layer with dead/inert particles above and below it. This is because the particles in the middle band are healthier than the particles in the other two regions. Hence they produce more EPS and this leads to a higher concentration of EPS in the middle layer. Consequently, EPS is forced to move in order to release the pressure and this carries the particles towards both the surface and the bottom of the biofilm. The biofilm structure after 10 days (Figure 4.33b)

shows that the biofilm become flat and smooth with clear three, dead–live–dead, layers.

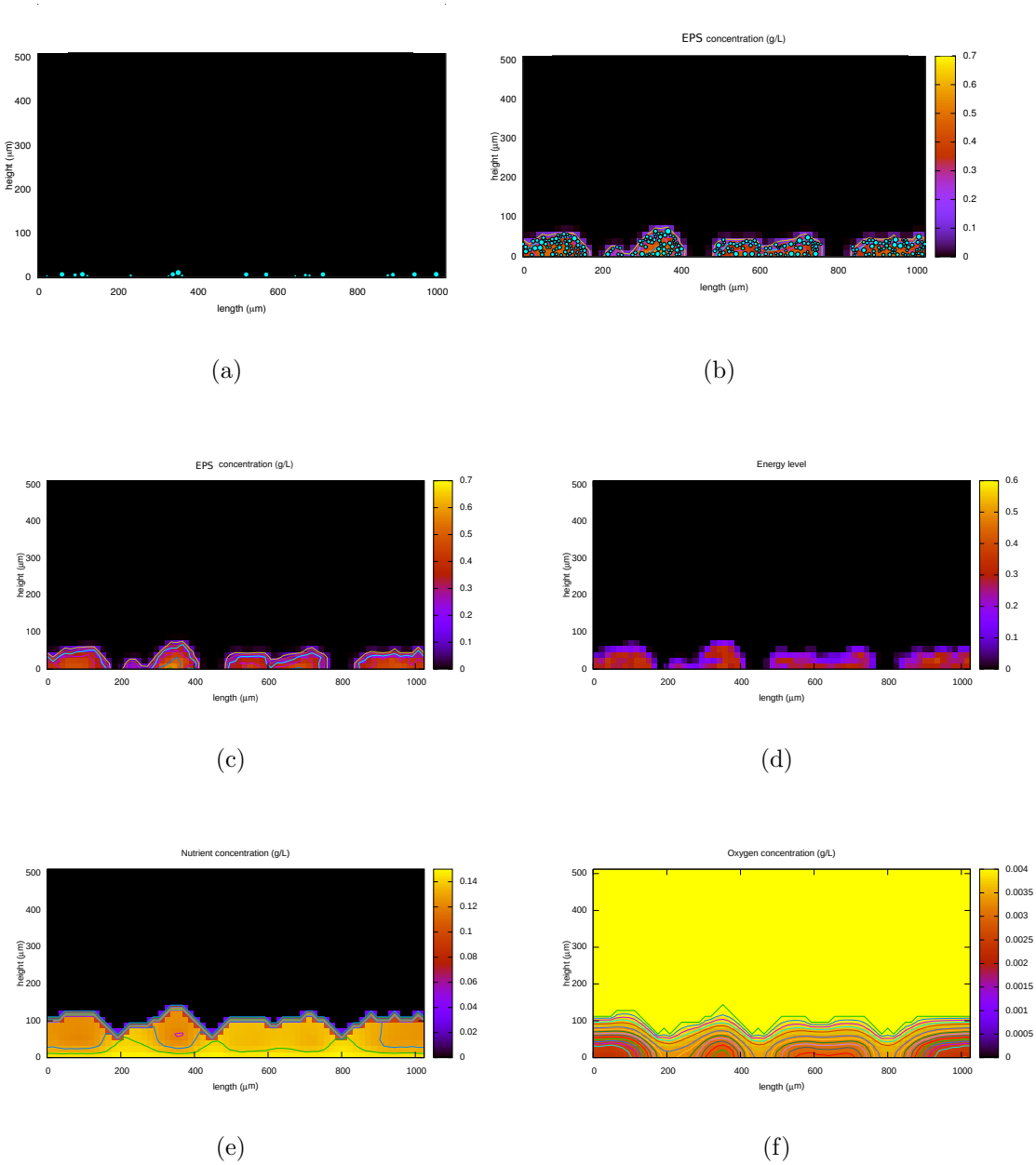

Figure 4.27: The initial seeding of the particles and the biofilm structure at day 1 of Simulation 3-1. (a) Initial particle distribution. After one day: (b) particle distribution, (c) EPS concentration, (d) energy level, (e) nutrient concentration and (f) oxygen concentration.

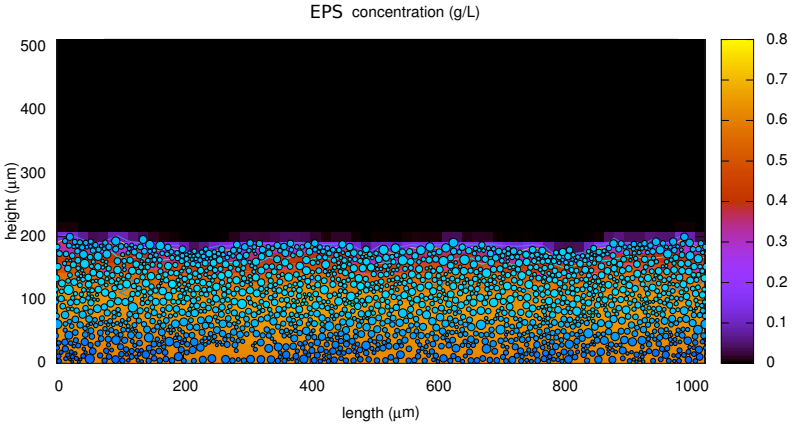

(a)

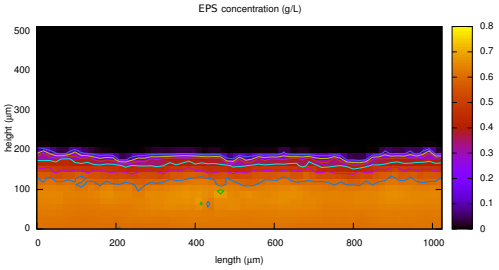

(b)

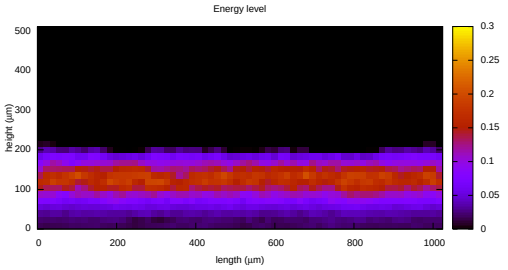

(c)

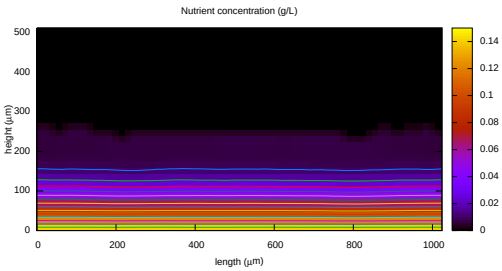

(d)

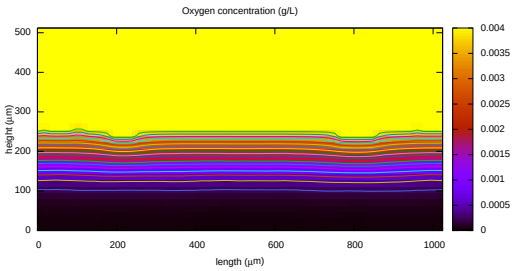

(e)

Figure 4.28: The biofilm particle distribution and the substrate concentration at day 3 in Simulation 3-1. (a) Particle distribution; (b) EPS concentration, (c) energy level, (d) nutrient concentration and (e) oxygen concentration.

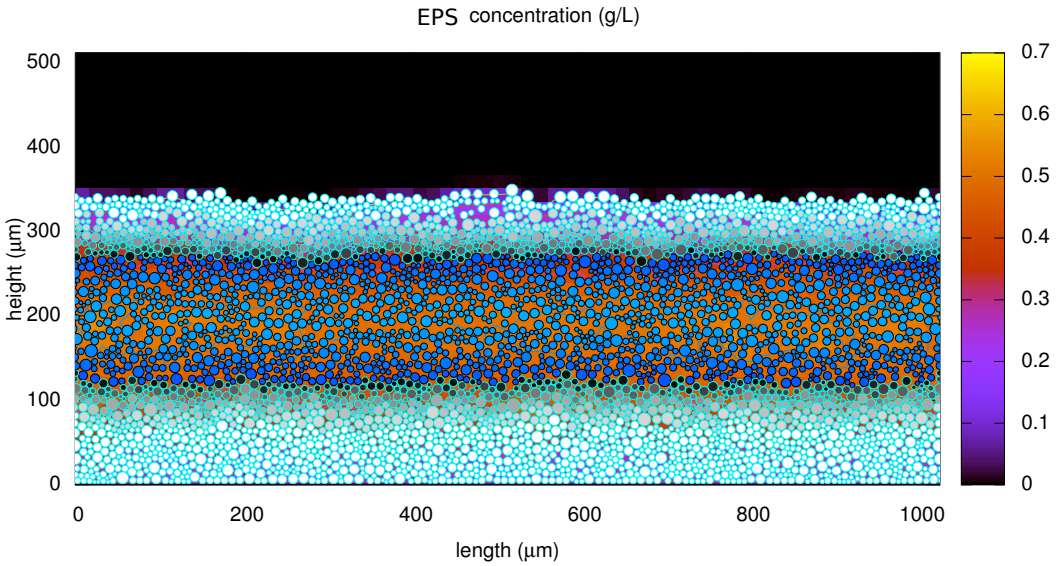

(a)

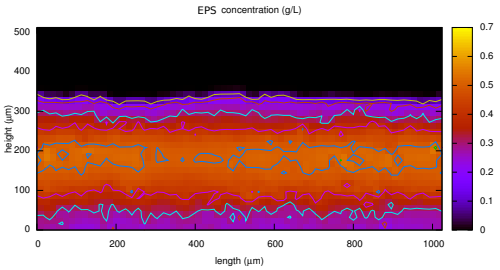

(b)

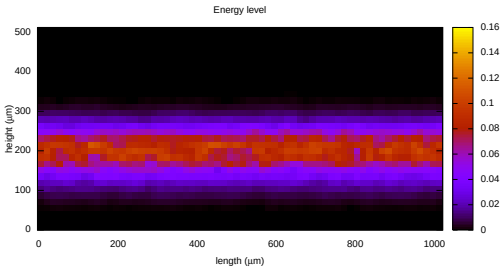

(c)

Figure 4.29: The biofilm particle distribution after 10 days in Simulation 3-1. (a) Particle distribution; (b) EPS concentration and (c) energy level.

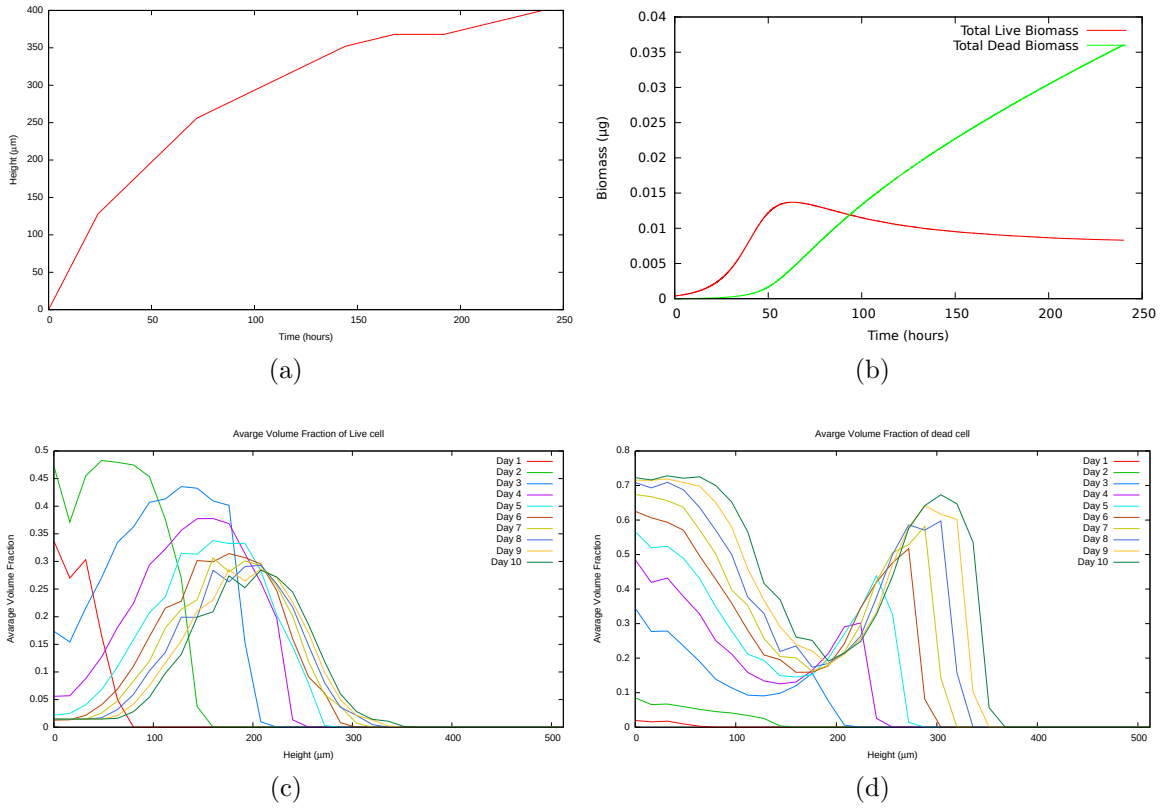

(a) (b) (c) (d)

Figure 4.30: Evaluation of (a) biofilm thickness, (b) live and dead biomass against time, (c) average volume fraction of live particles and (d) average volume fraction of dead particles against depth of biofilm over 10 days.

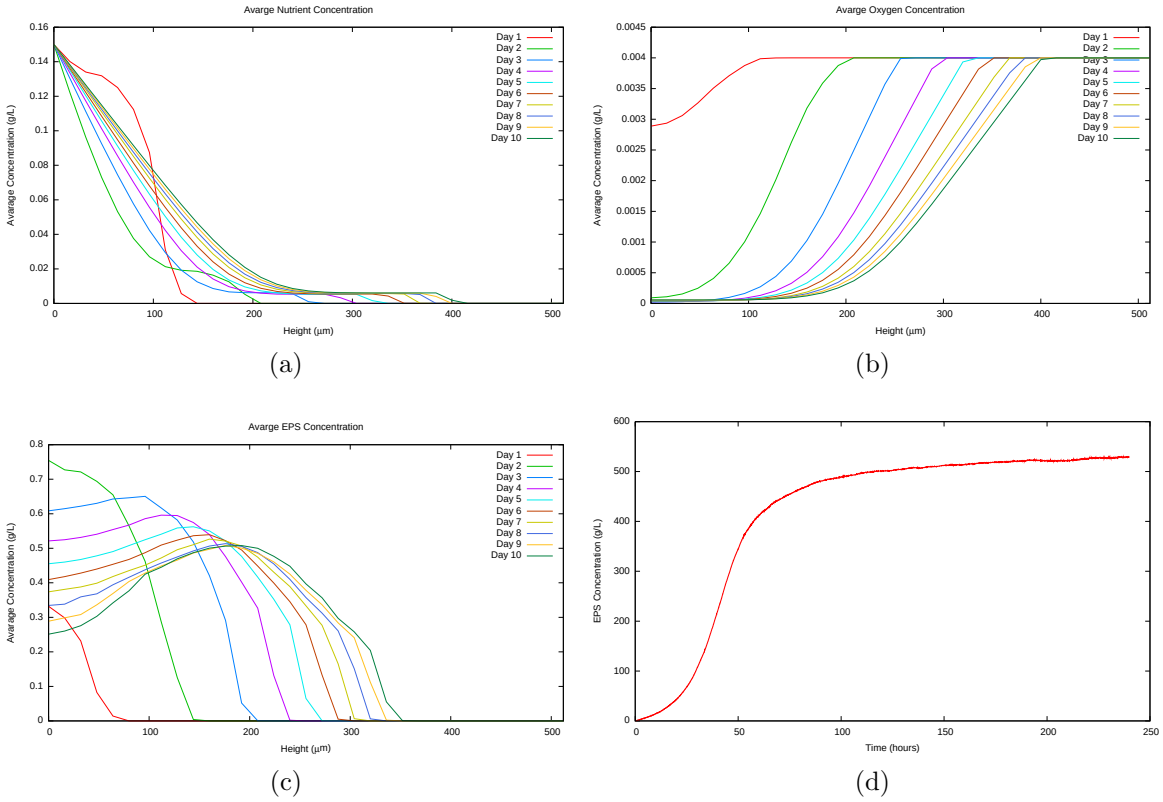

Figure 4.31: Evaluation of the average concentration of (a) nutrient concentration, (b) oxygen concentration and (c) EPS concentration against the biofilm thickness over 10 days of growth, and (d) the total EPS concentration in the biofilm against time of growth.

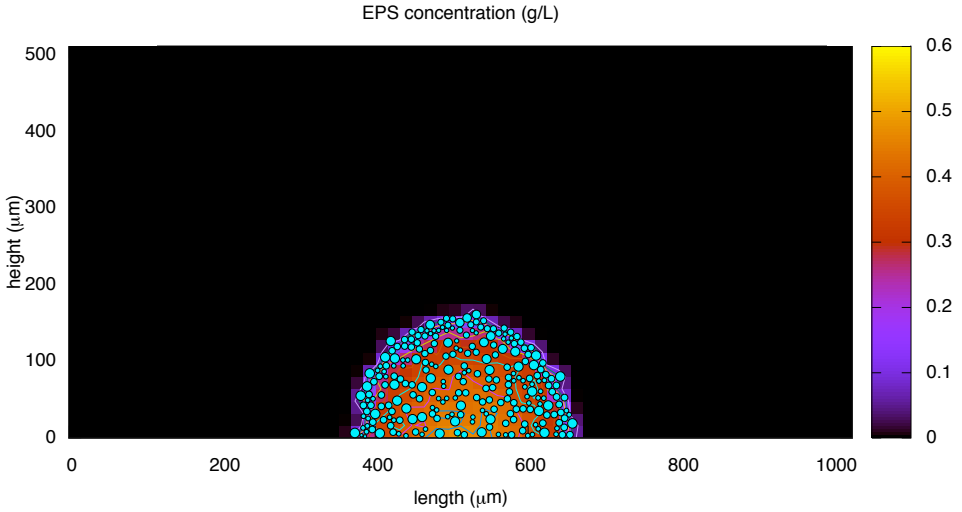

(a)

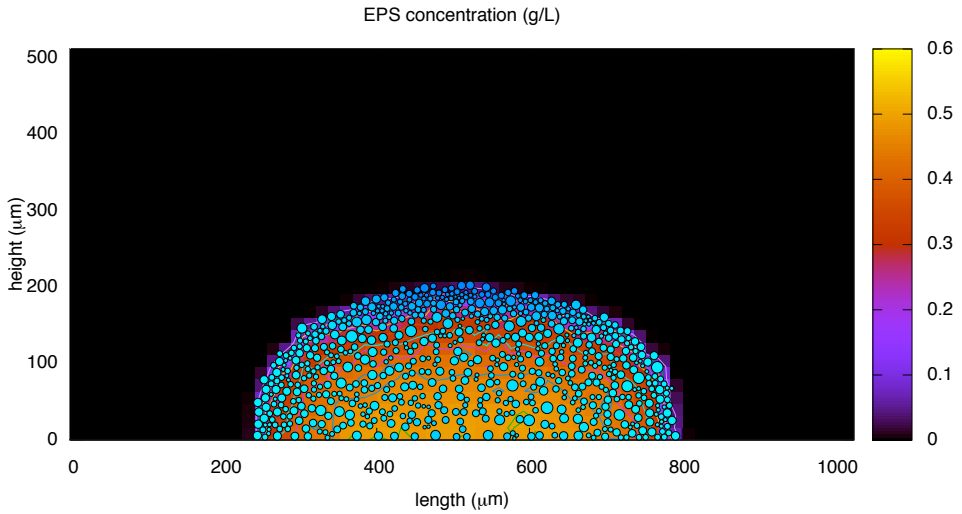

(b)

Figure 4.32: Plots of the particle distribution and EPS concentration of Simulation 3-2 after (a) 3 days' and (b) 4 days' growth.

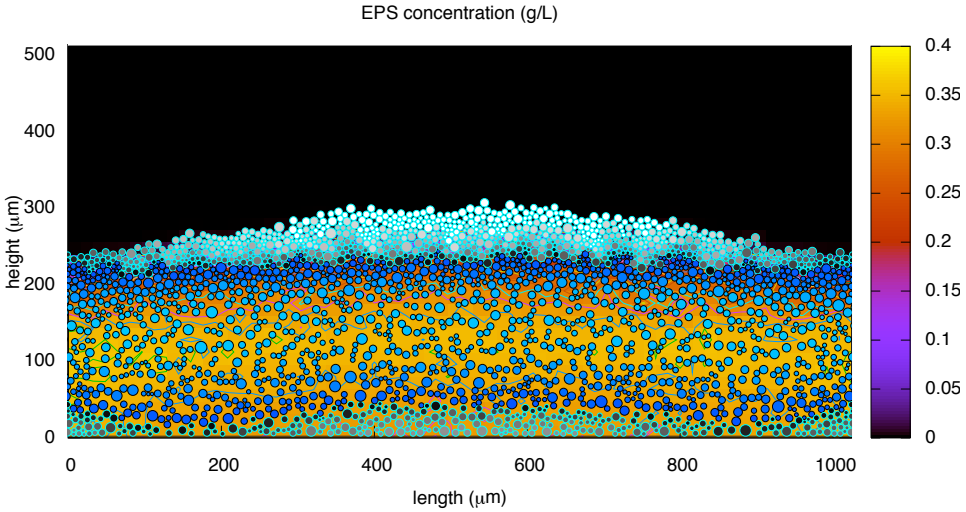

(a)

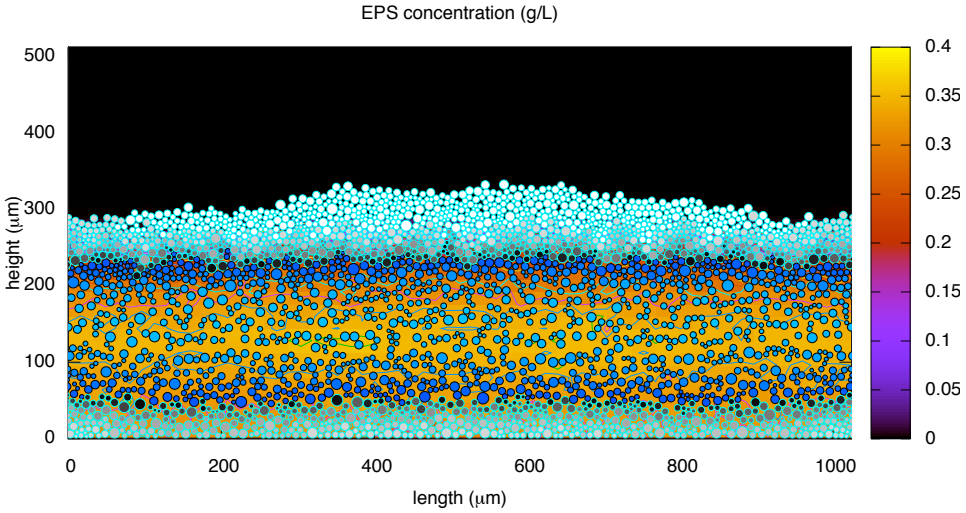

(b)

Figure 4.33: Plots of the particle distribution and EPS concentration of Simulation 3-2 after (a) 8 days' and (b) 10 days' growth.

4.1.4.4 Simulation 4: Anaerobic Growth

As mentioned in Section 4.1.1, this framework is able to simulate a biofilm which can be grown or survive in an anaerobic environment by controlling the energy "threshold" level constant k_a (see Equation (4.7)). In this section, two cases of the simulation of biofilm growth are presented: one is the standard model (Simulation 4-1) and the other is the case in which the biofilm is growing on agar with the nutrients diffusing from the bottom of the domain (Simulation 4-2). Here we set the parameter $k_a = 4.05838 \times 10^{-6}$, so that the biomass reproduction and death rates are at an equilibrium when no oxygen is present, i.e., in Equation (4.4) $\frac{dC_L^\kappa}{dt} = 0$, when $X_{Ox} = 0$. All other parameters are the same as those listed in Table 4.1.

Results

Figures 4.34–4.36 show the results of the biofilm growth over the 10 days in Simulation 4-1. Compared to the standard simulation (Simulation 1-2), the biofilm structures, including particle distribution and the concentrations of EPS, oxygen, and nutrient, are similar. The biofilm forms several tower-like bulges, with the most active particles at the top of the biofilm and the highest EPS concentration regions at the head of the bulges. The thickness of the biofilm increases approximately linearly. However, the active particle regions in Simulation 4-1 are larger compared to Simulation 1-2 due to the particles' being able to tolerate an anaerobic environment: therefore, the total live biomass in the biofilm is greater.

Figure 4.37 shows the particle distribution after 10 days and the substrate concentration in the computational domain of Simulation 4-2. Once again, the biofilm forms a flat, uniform structure with particles well packed throughout the biofilm, since the particles at the bottom are all alive and therefore proliferate to fill the space. Consequently, the EPS is compressed into the tiny spaces between the particles and, hence, the concentration of EPS is high in the biofilm. Despite the lower concentration of nutrient diffusing from the base through the biofilm to the biofilm surface, the particles at the surface are all alive at this stage due to their lesser requirements as to the nutrient concentration level needed for their

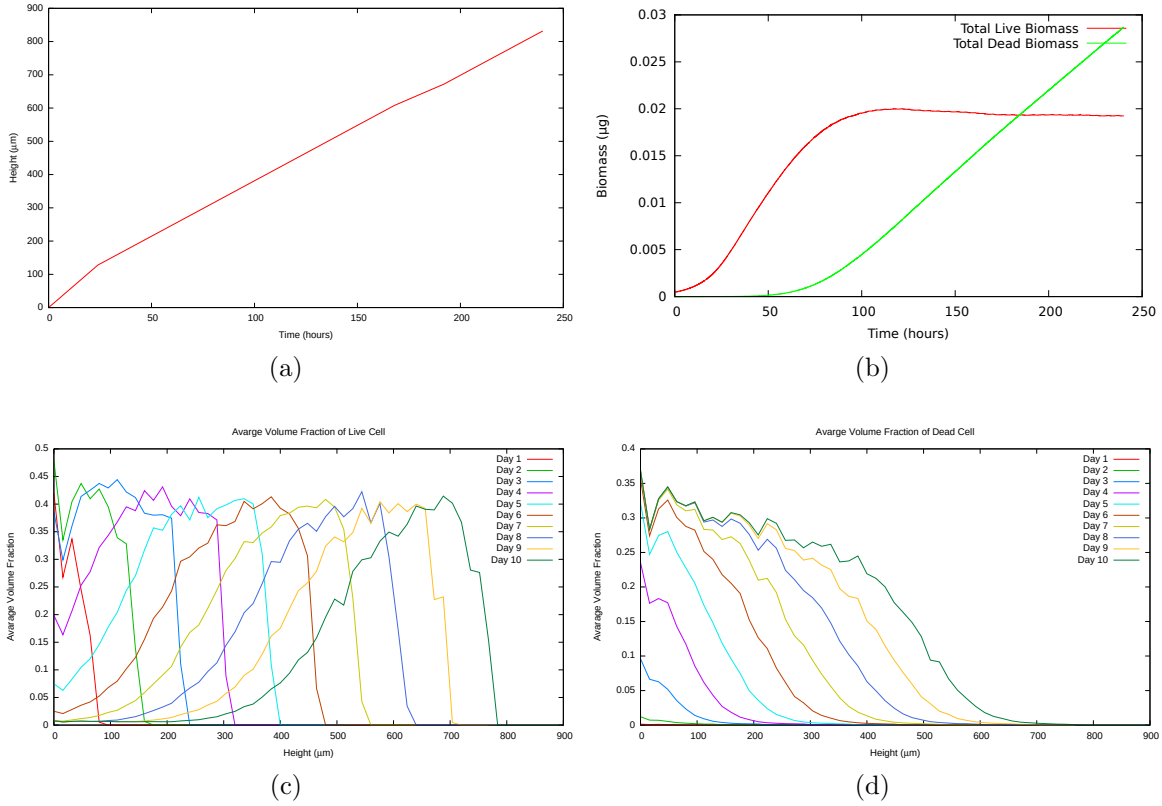

Figure 4.34: Evolution of (a) biofilm thickness, (b) live and dead biomass against time, (c) average volume fraction of live particles and (d) average volume fraction of dead particles against depth of biofilm over 10 days of biofilm growth in Simulation 4-1.

survival. However, if the biofilm growth continues after the 10-day study period, the particles at the biofilm surface will die out eventually and form a dead layer of particles.

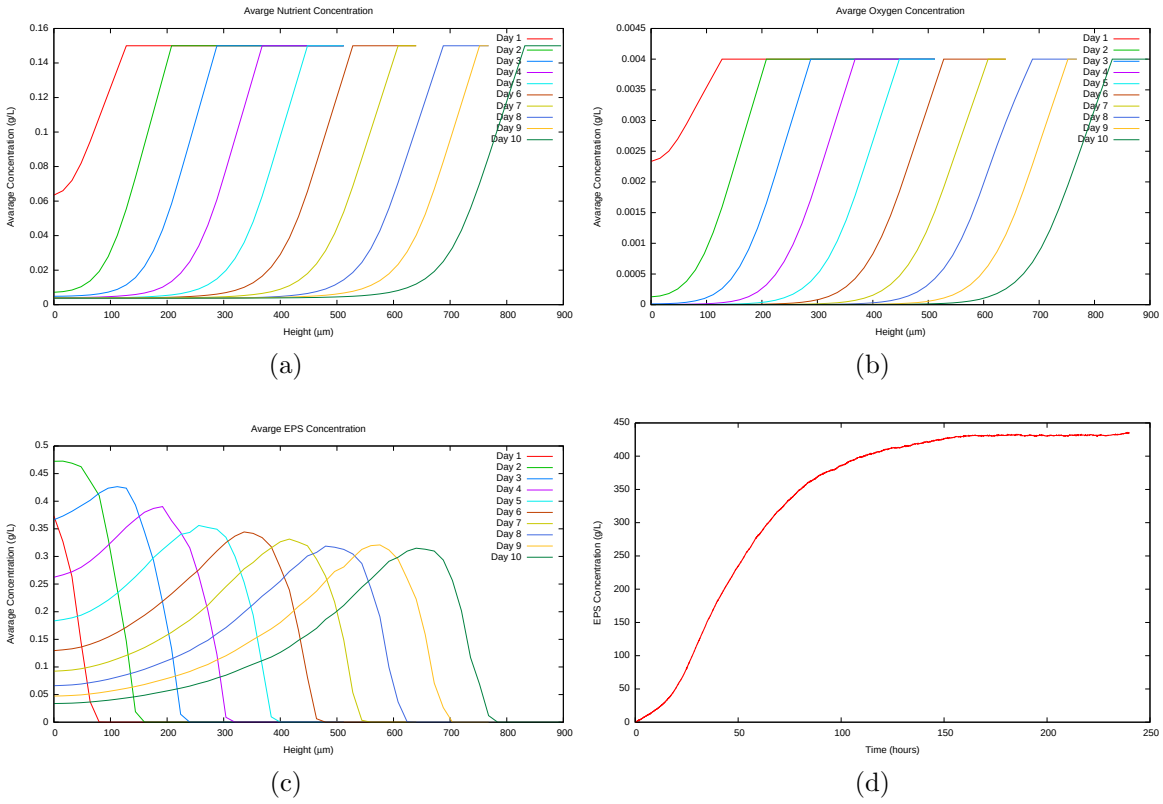

Figure 4.35: Evolution of Simulation 4-1 of the average concentration of (a) nutrients, (b) oxygen and (c) EPS against the biofilm thickness over 10 days of growth, and (d) the total EPS concentration in the biofilm against time of growth.

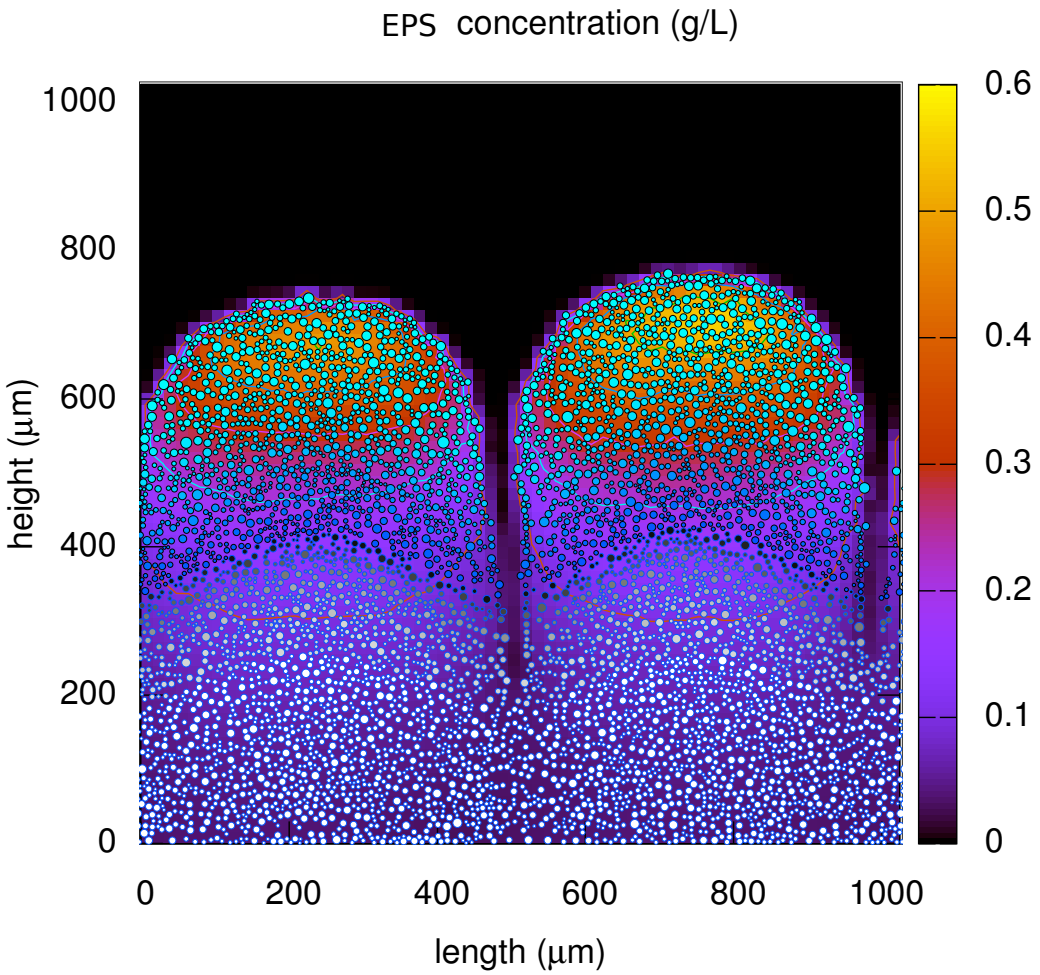

Figure 4.36: Plot of EPS concentration and particle distributions after 10 days in Simulation 4-1.

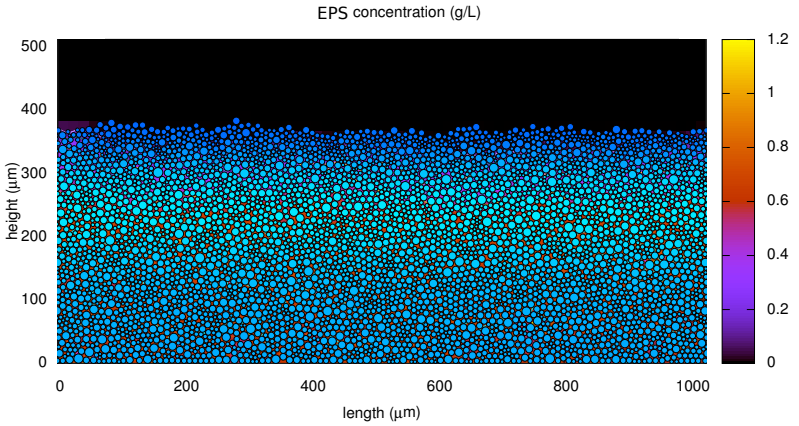

(a)

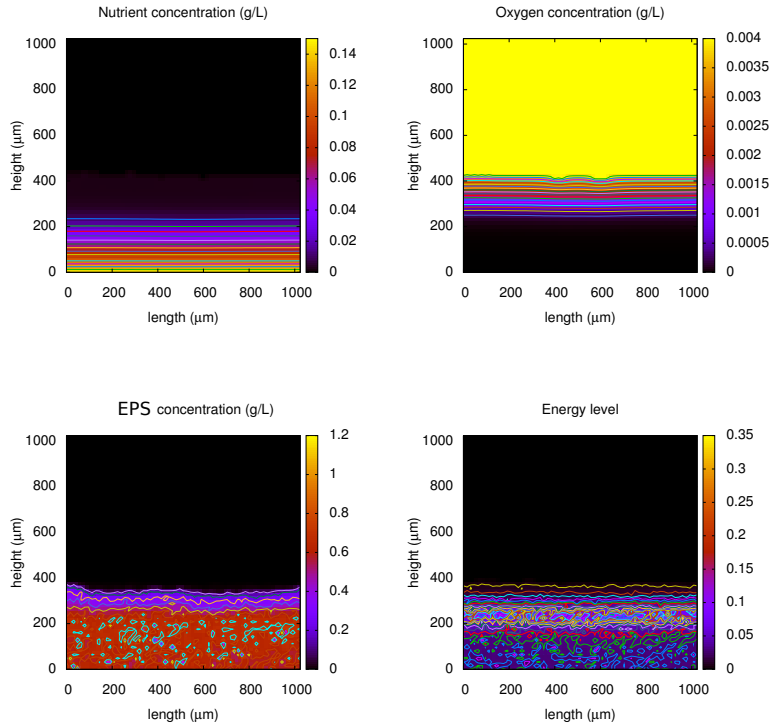

(b)

Figure 4.37: Plots of (a) the particle distribution and (b) EPS, Substance concentrations and energy level of Simulation 4-2 after 10 days' growth.

4.2 Scenario 2: A Two Species Simulation

In this section we will apply the new framework to investigate the growth of a two species biofilm, consisting of

1. An EPS-producing strain that produce EPS
2. A non EPS-producing strain (PHB-producing strain) that has the capacity to store nutrient in the form of PHB, which gives it the ability to survive for a time in low nutrient concentration.

This is a system similar to that investigated by Xavier *et al.* [166], and this investigation serves as a demonstration of the adaptability of the new framework to a multi-species system.

The cell behaviour for the EPS-producing strain is adapted from the previous simulation (see Figure 4.1), with the process of EPS production as described in Section 4.1.2. The PHB-producing strain is assumed to produce the intracellular storage energy compound PHB instead of the extracellular polymeric substances (EPS). The relevant parameter values for the standard simulation in this case are listed in Tables 2 and 3 in Appendix A.

4.2.1 Cellular Processes

The cell mechanisms of both the EPS and PHB-producing strains are assumed to be the same as presented in Figure 4.1a. The metabolisms of the EPS and energy synthesis of the EPS-producing strain are adapted from Scenario 1 (Figure 4.1). For the PHB-producing strain, the cells consume nutrients to synthesise energy, and use the energy as well as the nutrients to reproduce biomass during high levels of nutrient concentration. However, when the nutrients are absent, the PHB-producing strain converts the PHB produced and stored inside the cells to generate energy, in order to keep themselves alive. The growth and death processes are similar to the EPS-producing strain and the live and dead cell biomass evolves according to

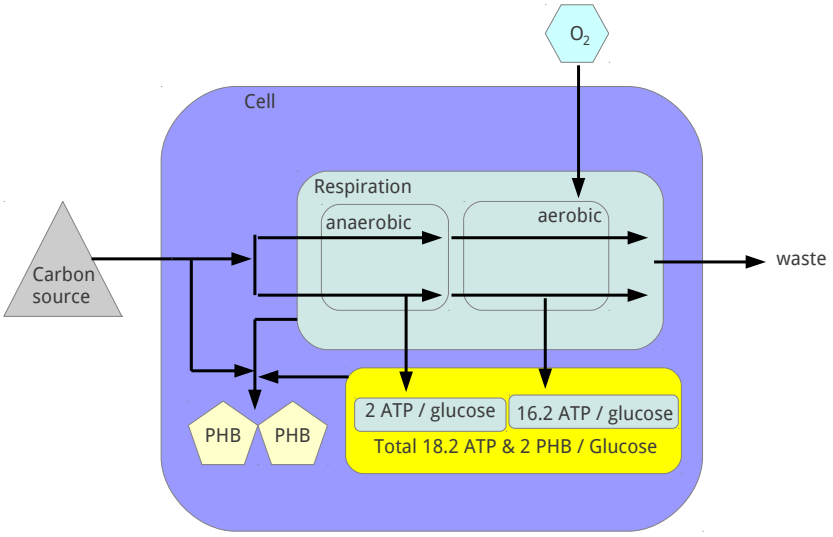

(a)

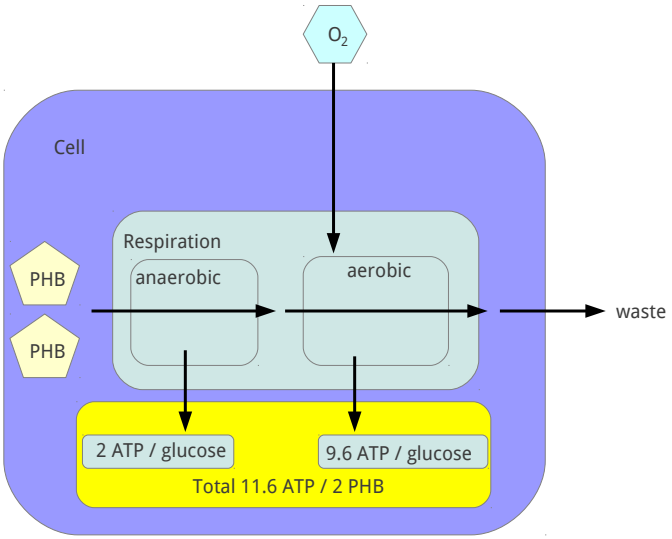

(b)

Figure 4.38: Plots of (a) PHB and ATP synthesises under well nourished condition and (b) PHB consumption and ATP synthesis under starvation.

$$\begin{aligned}
\frac{dC_L^\kappa}{dt} &= ((\mu^{\Lambda(\kappa)} + \beta^{\Lambda(\kappa)} g(1)) A_\kappa H(X_s, K_{X_s b}, m_{X_s b}) \\
&\quad -\beta^{\Lambda(\kappa)} g(A_\kappa)) C_L^\kappa, && (4.25)\\
\frac{dC_D^\kappa}{dt} &= (1-\phi)\beta^{\Lambda(\kappa)} g(A_\kappa)) C_L^\kappa, && (4.26)\\
g(A_\kappa) &= \frac{1}{1 + A_\kappa / k_a}, && (4.27)\\
H(X_s, K_{X_s b}, m_{X_s b}) &= \frac{X_s^{m_{X_s b}}}{X_s^{m_{X_s b}} + K_{X_s b}^{m_{X_s b}}}, && (4.28)
\end{aligned}$$

where the index $\Lambda(\kappa)$ indicates the strains of the particle indexed κ. Here, $\Lambda(\kappa) = 1$ refers to the EPS-producing strain and $\Lambda(\kappa) = 2$ represents the PHB-producing strain. The energy is produced by either nutrients or PHB for the PHB-producing strain particles and by nutrients only for the EPS-producing strain particles. The energy level function A_κ is given by

$$A_\kappa = (F_s^{\Lambda(\kappa)} + F_p^{\Lambda(\kappa)}), \tag{4.29}$$

where

$$\begin{aligned}
F_s^{\Lambda(\kappa)} &= H(X_s, K_{X_s A}, m_{X_s A}) \\
&\quad (\omega^{\Lambda(\kappa)} + (1-\omega^{\Lambda(\kappa)}) H(X_{Ox}, K_{X_{Ox} A}, m_{X_{Ox} A})), && (4.30)\\
F_p^{\Lambda(\kappa)} &= \psi G(X_s, P_\kappa)(\tau^{\Lambda(\kappa)} + (1-\tau^{\Lambda(\kappa)}) H(X_{Ox}, K_{X_{Ox} A}, m_{X_{Ox} A})), && (4.31)
\end{aligned}$$

where P_κ is the fraction of PHB per live biomass in particle κ ($P_\kappa = 0$ in the EPS-producing strain) and $G(X_s, P_\kappa)$ is the contribution from PHB reserves given by

$$G(X_s, P_\kappa) = \frac{P_\kappa^2}{K_p^2 + P_\kappa^2} \frac{K_{PX_s}^2}{X_s^2 + K_{PX_s}^2}. \tag{4.32}$$

The functions F_s and F_p are the energy levels generated from nutrients (equivalent to Equation 4.8) and PHB, respectively. We note that $A_\kappa = 1$ between the two species does not necessarily represent the same level of energy (i.e., ATP

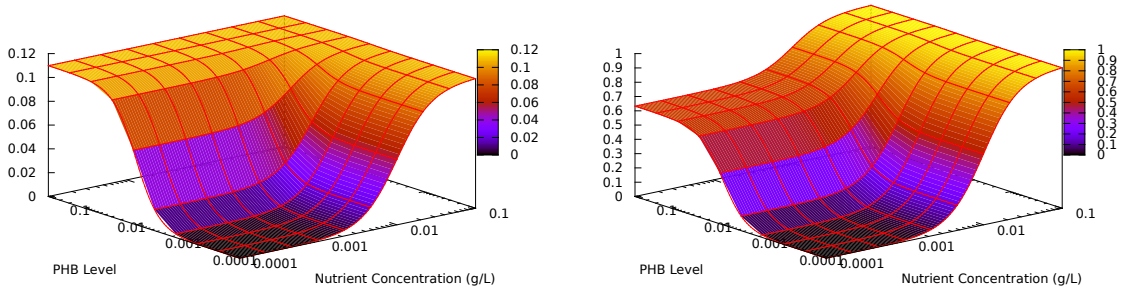

(a) (b)

Figure 4.39: Plots of energy level against nutrient concentration and PHB level (a) under anaerobic conditions and (b) in an oxygen present environment.

concentration), it is simply the upper bound of energy for the respective species. This means that $\omega^1 = 2/29.85$ (see Figure 4.1b) and $\omega^2 = 2/18.2$ (see Figure 4.38a); with ψ being the ratio of energy output between one units of PHB and one unit of nutrient, it follows from Figure 4.38b that $\tau^2 = 2/11.6$. Note that Equation 4.31 only holds if $\Lambda(\kappa) = 2$, otherwise $F_p^1 = 0$ in this case. The function $G(X_s, P_\kappa)$ governs when ATP production is dominated by nutrient or PHB, the latter only occurring when the nutrient level is low (noting $G(X_s, P_\kappa)$ will be small if $X_s \ll K_{X_s}$). The constants K_p and K_{X_s} are the threshold concentrations of PHB and nutrient, respectively, at which $G(X_s, P_\kappa)$ changes between low and high levels. Surface plots of energy levels in cell particles under different conditions are illustrated in Figure 4.39 and Figure 4.40.

4.2.2 Intra-Cellular Substance- PHB Production and Consumption

PHB is assumed to be an intracellular substrate only existing in live cells; therefore, Equations (3.7) are applicable. The mass balance of PHB production and consumption is given by

$$\frac{d(C_L^\kappa P_\kappa)}{dt} = R_P^\kappa C_L^\kappa + J_Z^\kappa - \Psi_d^\kappa P_\kappa, \tag{4.33}$$

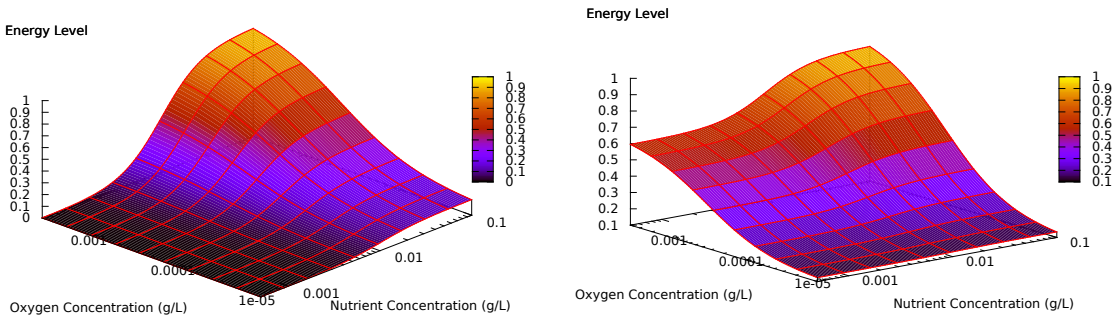

(a) (b)

Figure 4.40: Plots of energy level against oxygen and nutrient concentrations in the context of (a) no intracellular PHB and (b) a maximum level of PHB.

where P_κ is the fraction of PHB per live biomass in the particle indexed by κ, and $R_P^\kappa C_L^\kappa$ is the PHB production and consumption rate by the live biomass. The second term on the right hand side of the equation describes the PHB absorption/release rate from/to the environment. Since PHB is assumed to exist only in the live biomass, PHB is not absorbed or released by biomass, i.e., $J_Z^\kappa = 0$. The third term refers to the PHB loss when live biomass dies. Equation (4.33) can be rewritten by applying Equations (3.11):

$$\frac{dP_\kappa}{dt} = R_P^\kappa - \frac{\Psi_b^\kappa}{C_L^\kappa} P_\kappa. \tag{4.34}$$

The processes of PHB production and consumption are summarised in Figure 4.38. In order to synthesise PHB, the PHB-producing strain consumes nutrients via both aerobic and anaerobic respirations at different production rates. When nutrients are absent, the cells of the PHB-producing strain consume the PHB stored inside themselves to generate energy. We have assumed that the rate of PHB production and consumption is given by

$$\begin{aligned} R_P^\kappa &= A_\kappa Y_p^{\Lambda(\kappa)} H(X_s, K_{X_s P}, m_{X_s P})(\xi + (1-\xi) H(X_{Ox}, K_{X_{Ox} P}, m_{X_{Ox} P}))(1 - \frac{P_\kappa}{P_\kappa^*}) \\ &\quad -\delta_{PA} F_p^{\Lambda(\kappa)}, \end{aligned} \tag{4.35}$$

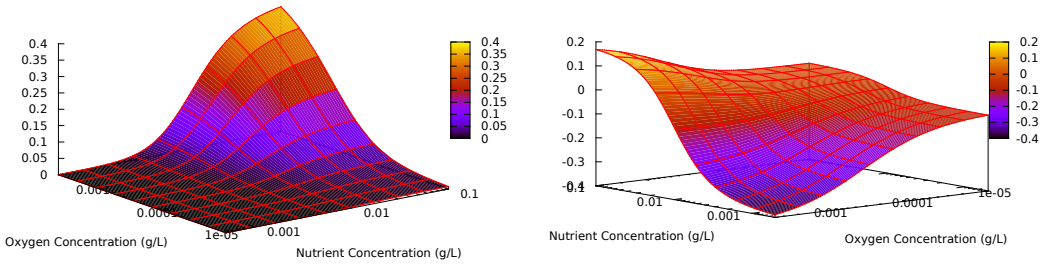

(a) (b)

Figure 4.41: Plots of net PHB production and consumption against oxygen and nutrient concentrations in (a) no intracellular PHB and (b) PHB present conditions. The negative value means consumption.

where $Y_P^{\Lambda(\kappa)}$ is the maximum production rate of PHB, ξ is the fraction of PHB production rate under anaerobic respiration, δ_{PA} is the consumption rate of PHB to produce energy when nutrients are absent, and P_κ^* is the maximum fraction of PHB contained per live biomass in a particle indexed by κ. The term $(1 - P_\kappa/P_\kappa^*)$ ensures that the total mass of PHB produced and stored in the particle indexed by κ does not exceed the maximum. The production and consumption of PHB against nutrient and oxygen concentrations is shown in Figure 4.41. The maximum PHB that may be contained in a particle being half of the live biomass in the particle [29], i.e., $P_\kappa^* = \frac{1}{2}$.

4.2.3 Freely Diffusing Substances

As presented in the first scenario, the nutrients and oxygen are considered in this scenario. Since the diffusion and reaction rates of these two solutes are assumed to be fast compared to the biofilm growth, a quasi-steady state of reaction–diffusion equation, viz., Equation (3.18), is applied. The reaction–diffusion equation for nutrient concentration is adapted from Equations (4.13) and (4.15), giving

$$0 = -\int_{\partial\Omega_c} \boldsymbol{J}_{\boldsymbol{X_s}} \cdot \boldsymbol{n} d\partial\Omega_c + \int_{\Omega_c} R_{X_s} d\Omega_c, \tag{4.36}$$

where

$$\boldsymbol{J_{X_s}} = -D_{X_s}\nabla X_s, \tag{4.37}$$

and the reaction term R_{X_s} is the same as that in Equation 4.17 but amended to account for nutrient consumption in PHB production by the PHB-producing strain. The reaction term in full is

$$\begin{aligned} R_{X_s} &= R_{X_sEX_s} \\ &+ \sum_{\kappa=1}^{N} W_\kappa(\boldsymbol{x},t)\Theta_\kappa(R^\kappa_{X_sd} - R^\kappa_{X_sA} - R^\kappa_{X_sE} - R^\kappa_{X_sb} - R^\kappa_{X_sP}), \end{aligned} \tag{4.38}$$

where

$$R_{X_sEX_s} = \mu_{X_sE}\lambda E, \tag{4.39}$$

$$R^\kappa_{X_sd} = \mu_{X_sb}\phi\beta^{\Lambda(\kappa)}g(A_\kappa), \tag{4.40}$$

$$R^\kappa_{X_sA} = \delta^{\Lambda(\kappa)}_{X_sA}H(X_s, K_{X_sA}, m_{X_sA}), \tag{4.41}$$

$$R^\kappa_{X_sE} = \mu_E\rho^{\Lambda(\kappa)}_{EX_s}A_\kappa H(X_s, K_{X_sE}, m_{X_sE}), \tag{4.42}$$

$$R^\kappa_{X_sb} = \delta_{X_sb}(\mu^{\Lambda(\kappa)} + \beta^{\Lambda(\kappa)}g(1))A_\kappa H(X_s, K_{X_sb}, m_{X_sb}), \tag{4.43}$$

$$\begin{aligned} R^\kappa_{X_sP} &= \delta^{\Lambda(\kappa)}_{X_sP}C_L^{\Lambda(\kappa)}A_\kappa Y_P^{\Lambda(\kappa)}H(X_s, K_{X_sP}, m_{X_sP}) \\ &\times (\xi + (1-\xi)H(X_{Ox}, K_{X_{Ox}P}, m_{X_{Ox}P}))(1 - \frac{P_\kappa}{P^*_\kappa}), \end{aligned} \tag{4.44}$$

where $R^\kappa_{X_sP}$ represents the nutrient consumption by PHB production and δ_{X_sP} refers to the concentration of nutrient use per concentration of PHB production. We note $\rho^2_{EX_s} = 0$ (the PHB-producing strain does not produce EPS) and $\delta^1_{X_sP} = 0$ (the EPS-producing strain does not produce PHB).

The reaction–diffusion equation for the oxygen concentration is derived from Equations (4.14) and (4.16),

$$0 = -\int_{\partial\Omega_c} \boldsymbol{J_{X_{Ox}}} \cdot \boldsymbol{n} d\partial\Omega_c + \int_{\Omega_c} R_{X_{Ox}} d\Omega_c, \tag{4.45}$$

where

$$\boldsymbol{J_{X_{Ox}}} = -D_{X_{Ox}} \nabla X_{Ox}, \tag{4.46}$$

and the reaction term, $R_{X_{Ox}}$, is the oxygen consumption rate during energy production and PHB synthesis, namely

$$R_{X_{Ox}} = \sum_{\kappa=1}^{N} W_\kappa(\boldsymbol{x}, t)\Theta_\kappa(R^\kappa_{X_{Ox}A} + R^\kappa_{X_{Ox}P}), \tag{4.47}$$

where

$$\begin{aligned} R^\kappa_{X_{Ox}A} &= (\delta_{X_{Ox}AX_s}(1-\omega^{\Lambda(\kappa)})H(X_s, K_{X_sA}, m_{X_sA}) \\ &\quad +\delta_{X_{Ox}AP}\psi(1-\tau^{\Lambda(\kappa)})G(X_s, P_\kappa))H(X_{Ox}, K_{X_{Ox}A}, m_{X_{Ox}A}), \quad (4.48) \\ R^\kappa_{X_{Ox}P} &= \delta^{\Lambda(\kappa)}_{X_{Ox}P} C_L^{\Lambda(\kappa)} Y_P^{\Lambda(\kappa)}(1-\xi)A_\kappa H(X_{Ox}, K_{X_{Ox}P}, m_{X_{Ox}P}) \\ &\quad \times H(X_s, K_{X_sP}, m_{X_sP})(1-\frac{P_\kappa}{P^*_\kappa}), \quad (4.49) \end{aligned}$$

where $R^\kappa_{X_{Ox}A}$ and $R^\kappa_{X_{Ox}P}$ are the oxygen consumption rate for energy generating and PHB production, respectively. The constant $\delta_{X_{Ox}P}$ is the oxygen concentration use per biomass of PHB yield, and $\delta_{X_{Ox}AX_s}$ and $\delta_{X_{Ox}AP}$ are the maximum oxygen consumption rates for energy and PHB production, respectively.

4.2.4 Simulation Results

In this section, two simulations of two-species biofilm growth are presented, first with the nutrients sourced at the top (Simulation 4-1), and, second, sourced from the bottom (Simulation 4-2). The activity of a particle is defined by the fraction of live biomass in the particle and is illustrated by the colour chart in Figure 4.42. The EPS-producing strain particles and the PHB-producing strain particles with fractions of live biomass from 100% to just more than 20% are coloured by light to dark blue and light yellow to red, respectively. The particles whose fraction of live biomass ranges from less than 20% down to 4% are coloured by black to light grey with dark blue or red circles depending on the particle strains. Finally, the white-coloured particles represent the inert or dead particles in which the fraction

of live biomass is less than 2%.

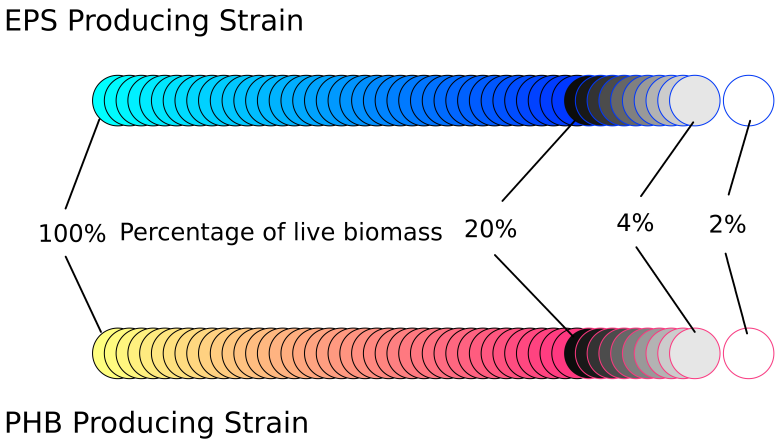

Figure 4.42: The colours of particles illustrate the percentages of live cell biomass in the two type of particles. The first line of particles represents the EPS-producing strain and the second line of particles is the PHB-producing strain. The particles with percentages of live cell biomass from less than 20% down to 4% are coloured black to light grey; the white-coloured particles represent the inert or dead particles which indicates that the percentage of live biomass in the particles is less than 2%.

In both simulations, 20 particles are initially seeded, 10 of the EPS-producing strain and 10 of the PHB-producing strain. Figure 4.43 shows the initial seeding of the particles and the particle distributions after one day of biofilm growth. After one day, the structure of both biofilms is similar. The biofilms' surfaces are rough due to the formation of several bulges. EPS is present mainly where the EPS-producing strain particles are located, though by diffusion some has infiltrated areas where the particles of the PHB-producing strain are located. We note that the particles of PHB-producing strain are highly packed, whilst the EPS-producing strain particles are slightly pushed by the EPS, resulting in more dispersion.

By day 4, the biofilms in Simulations 4-1 and 4-2 have covered the domain, where, as before, the particles are begining to form tower structures (Figure 4.44a) or becoming uniformly flat (Figure 4.45a). Due to the limited capacity for the EPS producers to resist sustained low nutrient levels, the EPS-producing strain

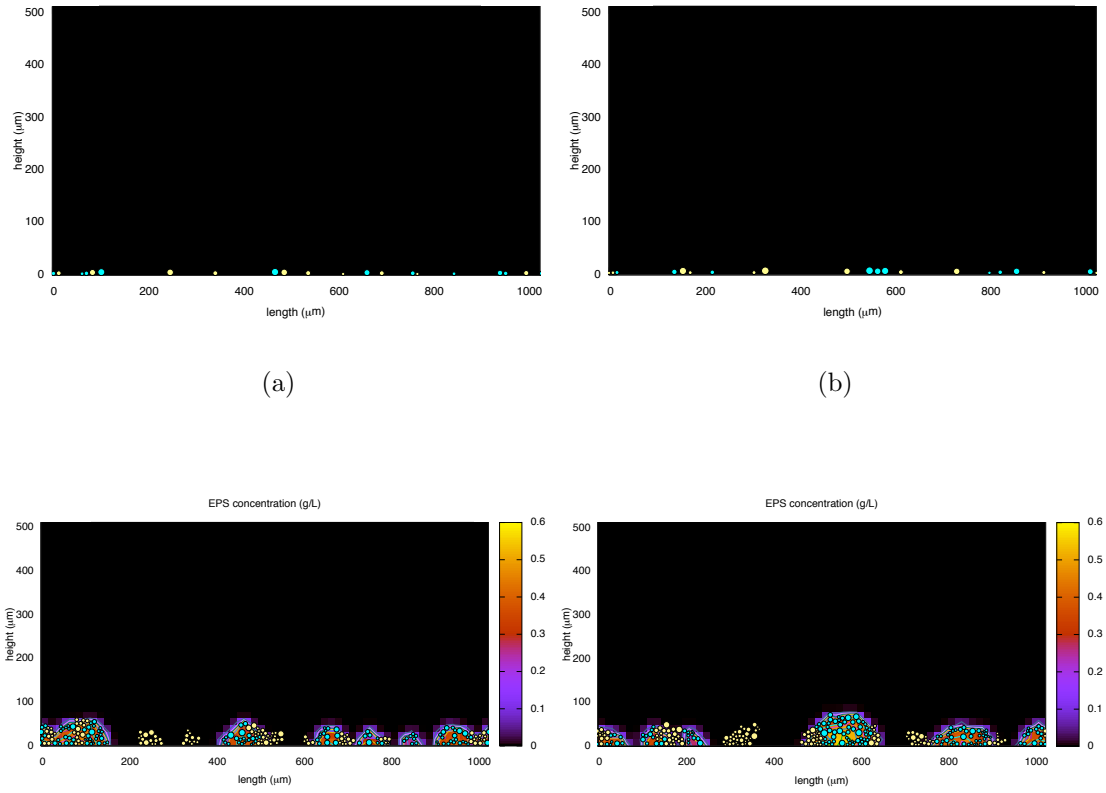

(a) (b)

(c) (d)

Figure 4.43: Particle distributions of initial seeding and after one day of biofilm growth in Simulation 4-1 (left) and Simulation 4-2 (right). (a) and (b) The initial seeding of particles, and (c) and (d) particle distribution after one day of growth.

particles located at the bottom of the biofilm are mostly inert or dead. Meanwhile, the PHB-producing strain particles at the similar locations are able to use their stored energy, PHB, to enable them to extend their lives. In Figure 4.45a, the PHB-producing strain is clearly surviving better in the lower regions near the nutrient source whilst the EPS producers are nearly dead. Despite the presence of two cell types, the resulting biofilm is relatively smooth on the surface, with the healthier particles existing in a band across the middle where non-negligible levels of nutrients and oxygen intersect. This results in the higher production of

EPS and faster proliferation of particles in the middle of the biofilm than at the surface or bottom and, consequently, the particles are pushed up- or downwards leading to the top and bottom being more packed then the middle region. Note that some EPS has diffused into regions where the PHB-producing strain particles are predominant and forces the particles to move towards each other, so that the particles are more compact at the regions of PHB-producing strain particles to which the EPS diffuses rather than in the regions of the PHB-producing strain particles with no EPS effects.

Figures 4.46 and 4.47 show the biofilm structures after 10 days of growth. Unsurprisingly, the biofilm of Simulation 4-1 develops a tower structure, mainly consisting of the EPS-producing particles with the active particles at the biofilm's surface and inert or dead particles below. The biofilm of Simulation 4-2 continues from the day 4 situation to produce, once again, a biofilm with three distinct layers: live cells sandwiched between two layers of dead cells, though the PHB particles seem to be slightly better able to survive in the dead zones. In Simulation 4-1, the EPS-producing strain particles are forced to move by the EPS, which gives them a distinct advantage as they gain the nutrients more easily from the surface than do the PHB-producing strain particles. Though it is noteworthy that a group of PHB producers have "hitched a lift" with the main tower of EPS producers (see the left side of Figure 4.46a). Figure 4.48 shows the evolution of the volume fraction of total live EPS and PHB cells in the biofilms for both simulations, i.e., the total volume of live EPS and PHB cells/volume of biofilm. In Figure 4.48a, we can clearly see the extent of the advantage the EPS producers have over the PHB producers for long term biofilm growth, as the EPS has helped move these particles to the nutrient source. For Simulation 4-2 (Figure 4.48b), the contributions of volume fractions of live EPS amd PHB-producing strain particles are shown to be similar, due to the more homogenous structure of the biofilm. Interestingly, the PHB strain has a slight adavantage due to the EPS having the adverse effect of pushing the live particles into the inert/dead layers, consequently the PHB producers seem to remain level whilst the EPS producers are continuing to decline at day 10.

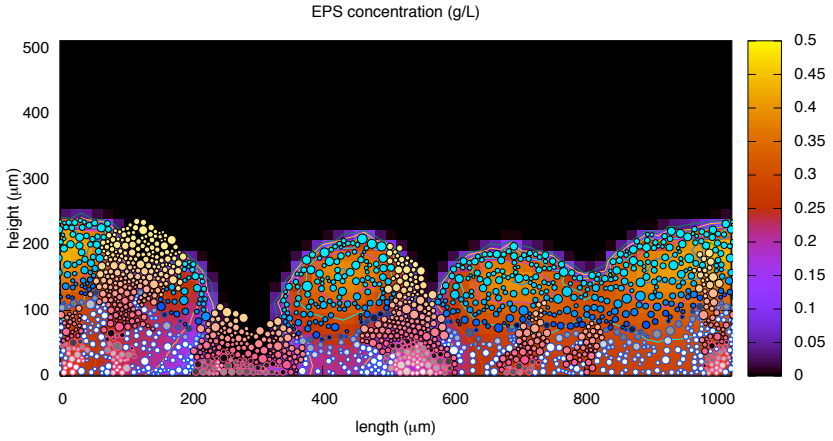

(a)

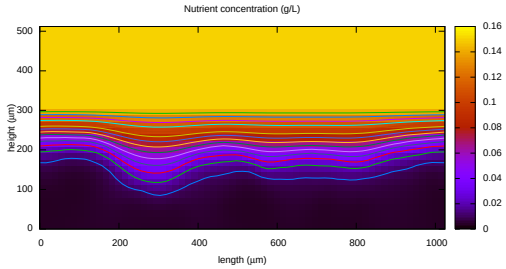

(b)

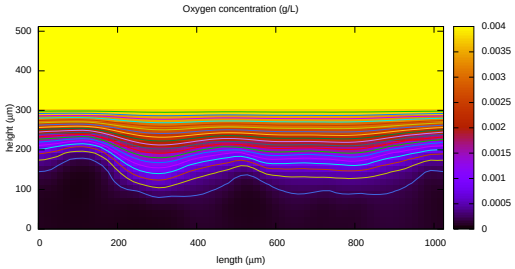

(c)

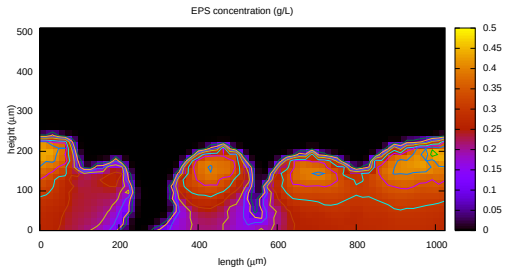

(d)

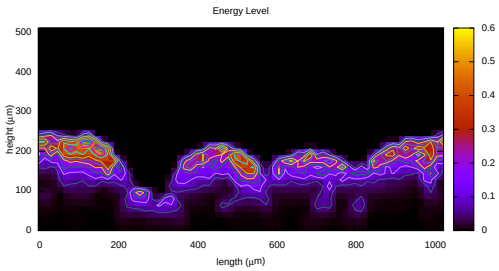

(e)

Figure 4.44: Plots of Simulation 4-1, showing (a) particle distribution, (b) nutrient, (c) oxygen, and (d) EPS concentration and (e) energy distribution of the four-day old, standard growth multi-species biofilm.

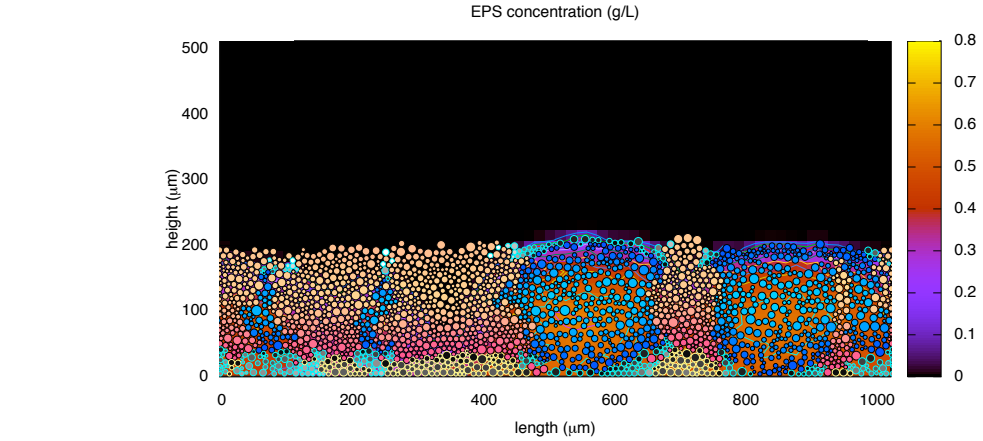

(a)

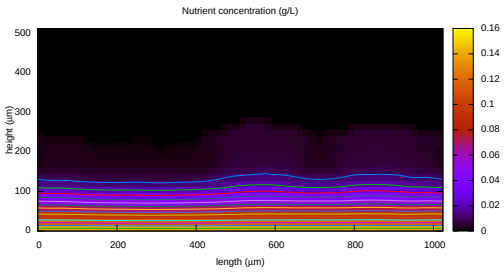

(b)

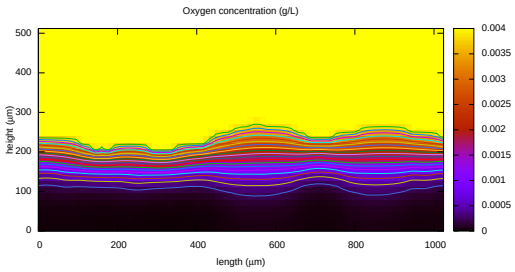

(c)

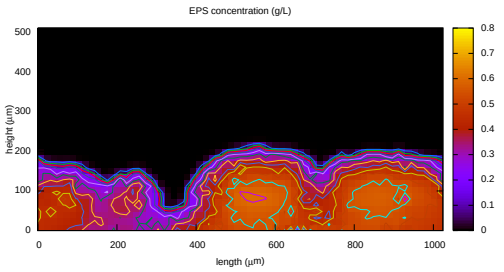

(d)

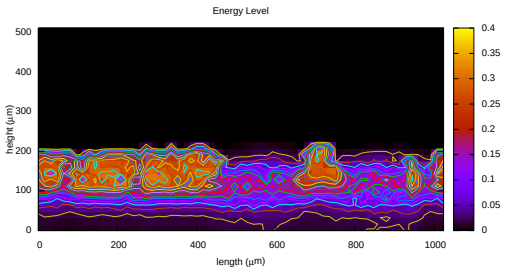

(e)

Figure 4.45: Plots of Simulation 4-2, showing (a) particles distribution, (b) nutrient, (c) oxygen, and (d) EPS concentration and (e) energy distribution of the four-days old, multi-species biofilm grown on the growth medium.

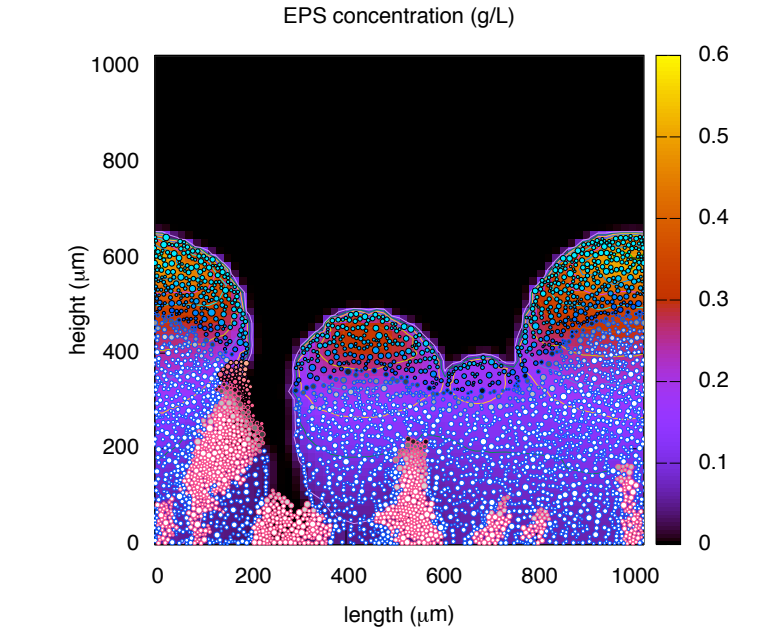

(a)

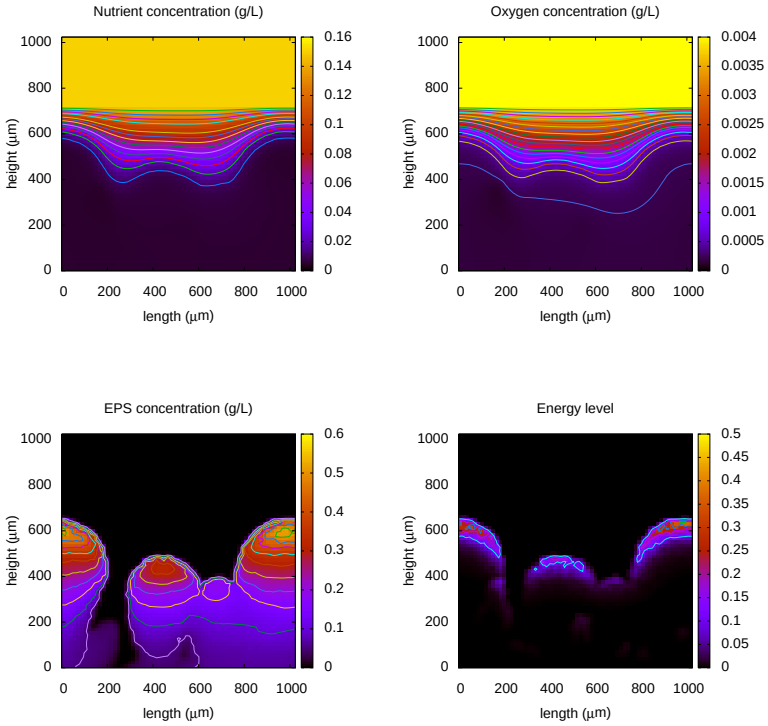

(b)

Figure 4.46: Plots of (a) particle distribution and (b) Clockwise from top left: nutrient concentration, oxygen concentration, energy level, and EPS concentration in Simulation 4-1.

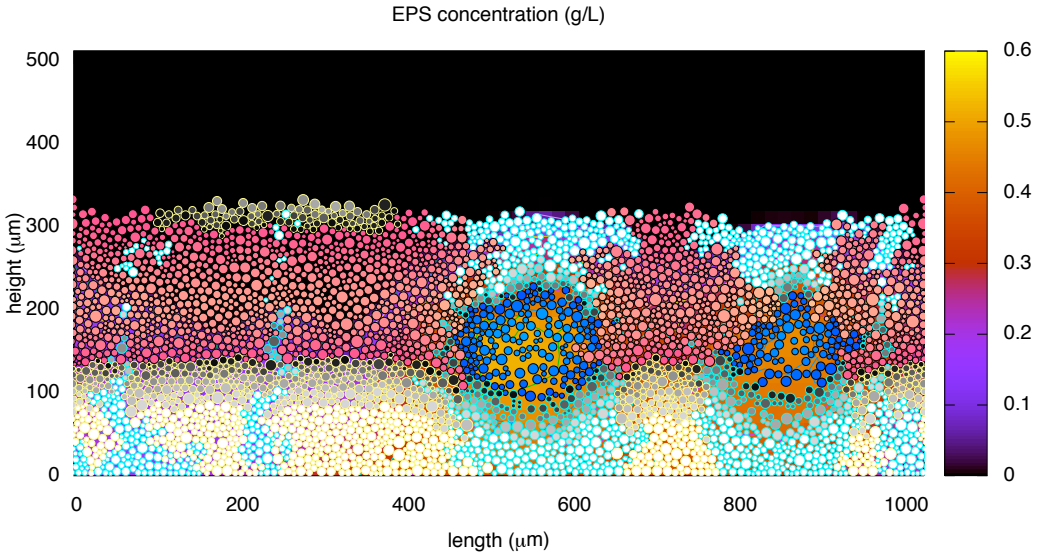

(a)

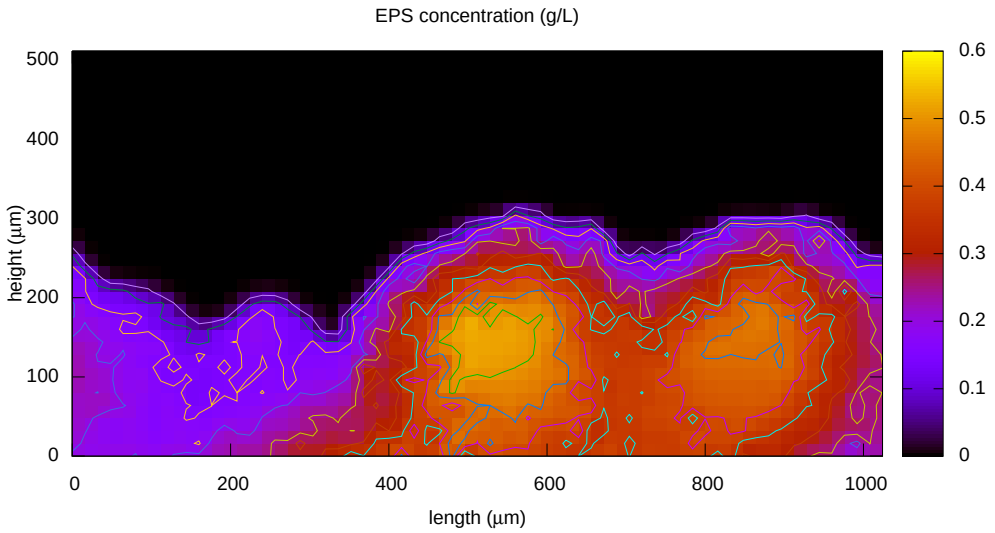

(b)

Figure 4.47: Plots of (a) particles distribution and (b) EPS concentration after 10 days of biofilm growth in Simulation 4-2.

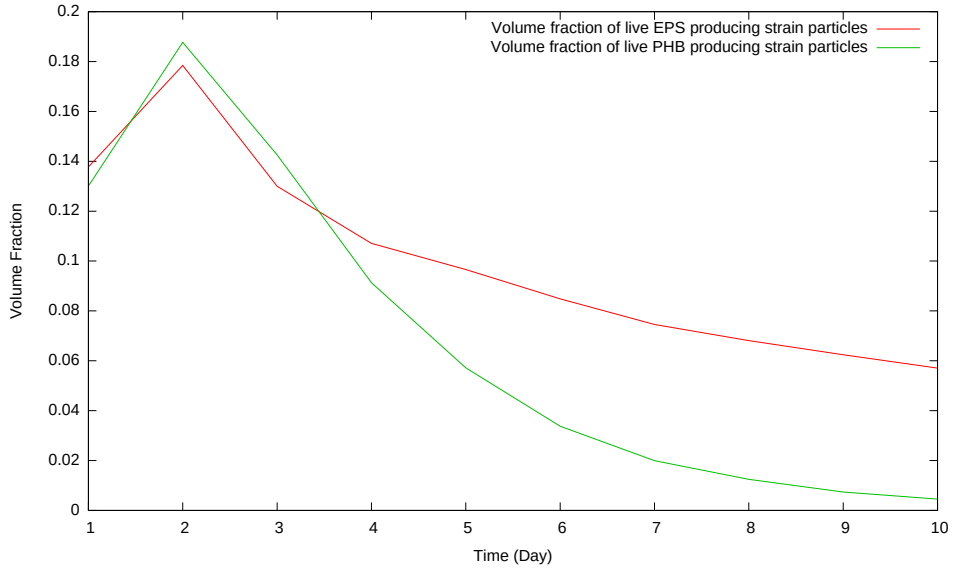

(a)

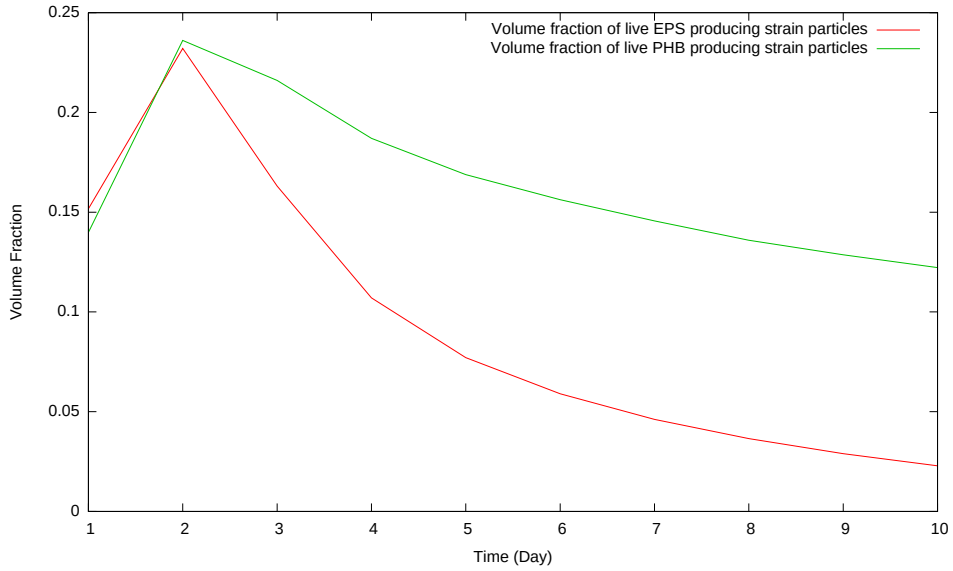

(b)

Figure 4.48: Volume fraction of live EPS and PHB-producing strain particles against time in (a) Simulation 4-1 and (b) Simulation 4-2.

To emphasise the role of PHB in cell survival, a simulation of the biofilm growth under an eight-hour feast–starvation cycle is presented (Simulation 4-3). The nutrient drops to 0.01 g/L for eight hours after every eight hours of high nutrient concentration (0.6 g/L) growth. The feast–starvation cycle is applied to the four-day old biofilm in Simulation 4-1 and continues for four days. During the starvation periods, the particles of the EPS-producing strain stop producing EPS and become inert or start dying. This leads to their stopping consuming oxygen and, as a consequence, the oxygen can pass through the region of the EPS-producing strain particles. Whilst the particles of the PHB-producing strain survive by consuming the intracellular energy source PHB and uptake oxygen. Therefore, the oxygen concentration is lower in the region occupied by the PHB-producing particles than where there are EPS-producing strain particles. The structure of the biofilm and EPS concentration after six days of growth, as well as concentrations and energy levels, are shown in Figure 4.49. The PHB-producing strain particles survive well during starvation periods and continue growing during the nutrient feast periods. Conversely, the EPS-producing strain particles die during the starvation periods and are unable to recover during the nutrient feast periods. Consequently, only small amount of the EPS-producing strain particles remain alive at the surface of the biofilm. By four days, the particles of the EPS-producing strain are nearly all dead.

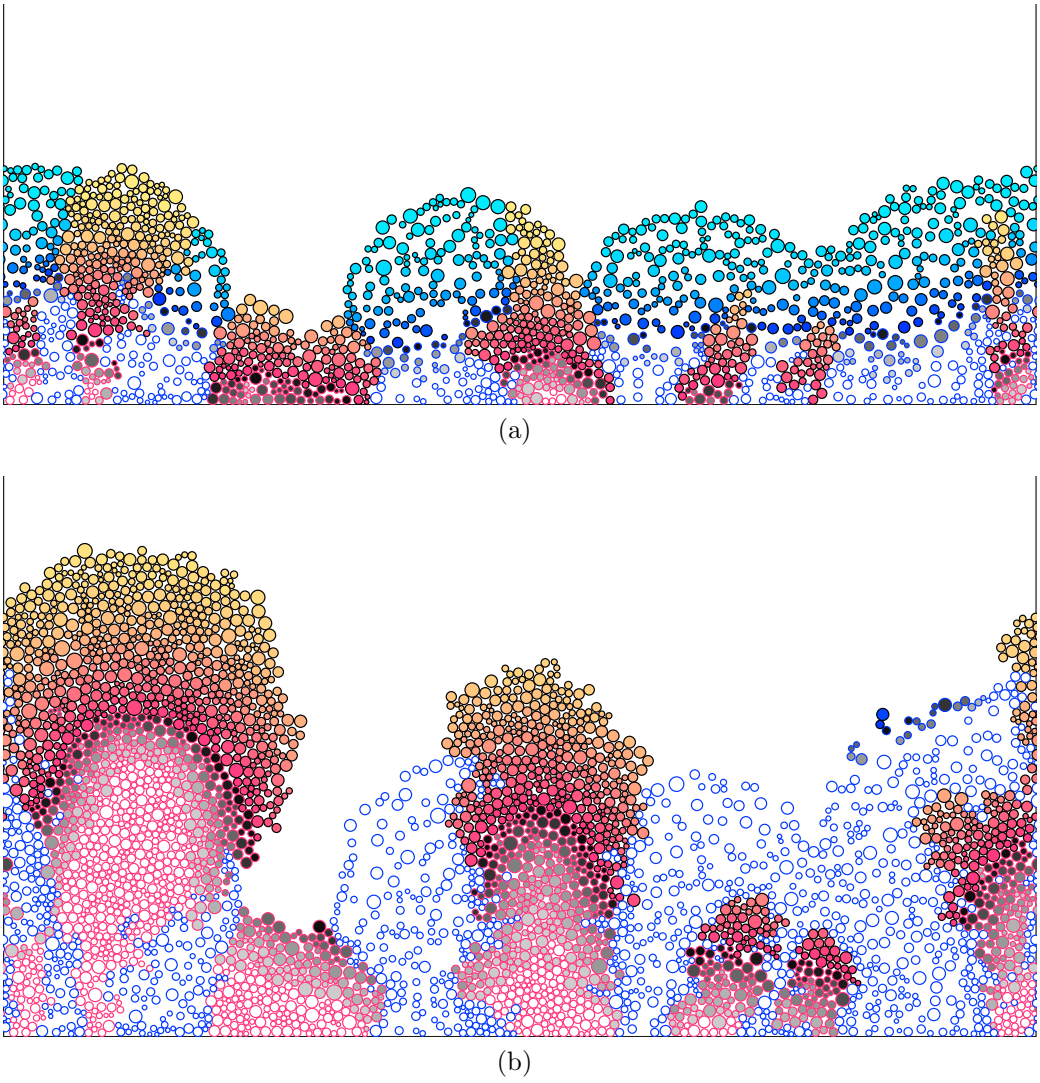

(a)

(b)

Figure 4.49: Particle distribution of the two-species biofilm (a) before the feast–starvation cycle and (b) after four days of the feast–starvation cycle.

4.3 Summary

In this chapter, the modelling framework proposed in Chapter 3 was applied to biofilms growing in various situations consisting of one or two species of bacteria. The main theme throughout was to establish the role of EPS in the various situations, to see whether or not it is always an advantage for a bacterium to produce EPS. The reaction terms used were qualitatively similar to those used

in previous studies (e.g., [166, 171]), but an explicit treatment of energy (i.e., the variable A_κ), which has been absent in previous studies, means that some adaptions were needed. The parametrisation is always a challenge in biofilm modelling and those listed in Appendix A are a combination of published values and approximations aimed at producing simulations that will provide results consistent with observation.

A recurring theme in the results of Section 4.1.4, where the nutrients were sourced from the top, is that EPS enables the biofilm to grow more rapidly and, in particular, the taller "tower" of particles out competes the particles in neighbouring towers: these EPS producers seem to be have a competitive advantage in this scenario. This is further emphasised in the two-species case, where the non-EPS producers struggle to survive, unless they get carried up a tower (Figure 4.46a).

The situation in which the nutrients are sourced at the bottom and the oxygen from the top has rarely, if ever, been modelled in a biofilm context, which is rather surprising, as this is a very common experimental assay. Though these assays are rarely grown for more than two or three days, the model predictions of how they may develop up to 10 days are interesting. For the first four to five days, the results suggest that there is relatively rapid expansion along the surface, whilst growth above the surface slows, as both the nutrient and the oxygen fail to reach all depths. Prolonged growth leads to a distinct three layer structure of dead–live–dead cells. The assumption that the particle can be dragged along with the EPS leads to a situation in which continual EPS production is a distinct disadvantage, by forcing particles into regions of low nutrients and oxygen where they perish. The PHB producers in Simulation 5-2, on the other hand, are able to persist while the EPS producers decline (Figure 4.48).

Due to the number of particles in the system, there is enormous scope for further exploration. The results in this section illustrate the compatibility with experiments as well as demonstrate the key role of EPS in biofilm development.

Chapter 5

Plasma Treatment

In the remainder of the thesis, we will focus on the use of cold plasma to treat biofilms. This will involve extending the framework to simulate cold plasma application and its subsequent effects on the biofilm. To accomplish this, we will first discuss what plasmas are and how they kill/remove biofilms. In this chapter, a general introduction to plasmas will be presented: we will then focus on one kind of plasma, called non-thermal atmospheric-pressure plasma or cold plasma. Cold plasma can be delivered in a number of ways that can trigger different effects on the biofilms. This will be discussed in detail.

5.1 Introduction to Plasma

Plasma consists of ionized gas and is considered to be the fourth state of matter, alongside the solid, liquid, and gaseous states. It consists of electrons, atoms, photons, free radicals, and negatively or positively charged ions [182], which are generated from the break up of atoms and molecules due to collisions with energetic particles. The charged ions and electrons lead to the plasma's becoming a good electrical conductor and strongly responsive to electromagnetic fields. Although plasma is an ionized gas, its total electrical status is quasi-neutral, i.e., the positively charged particles are balanced by negatively charged particles. The ionization degree of plasma is determined by the ratio of the density of the charged particles to that of the neutral gas, and in cold plasmas this ratio is usually in

High-Temperature Plasmas (Equilibrium Plasmas)	Low-Temperature Plasmas (Non-equilibrium Plasmas)	
	Thermal Plasmas	Non-thermal Plasmas
$T_i \approx T_e \geq 10^7 K$ e.g. fusion plasma	$T_e \approx T_i \approx T \leq 2 \times 10^4$K. e.g. atmosphere arc plasma.	$T_i \approx T \approx 300$K; $T_i \ll T_e \leq 10^5$K. e.g. low-pressure glow discharge

Table 5.1: The temperatures of ions and electrons in different types of plasma, where T_i is the temperature of the ions, the temperature of the electrons is represented by T_e, and T refers to the temperature of the plasma. The unit of temperature is degrees Kelvin [184].

the range of 10^{-7} to 10^{-4} [183]. For this reason, these plasmas are also called weakly ionized plasmas. On the other hand, completely ionized plasmas have an ionization degree that is close to 1. These are much hotter discharges and they are utilized in nuclear fusion systems.

Cold plasmas are non-equilibrium systems in which different species have different translational, rotational, vibrational and excitation temperatures. Due to their lighter mass, electrons are preferentially heated by the applied electric field and hence electrons have a higher temperature than the ions and the neutrals [183]. The temperature of the electrons is typically on the order of 1–10 eV (10^4–10^5K), whereas the ions and neutrals can remain close to room temperature (300K) [182].

The clinical application of plasmas will have to be highly temperature regulated for, e.g., the skin surface will be damaged if too much heat is generated. We will thus focus only on non-thermal plasmas, delivered at atmospheric pressure and room temperature (see Table 5.1).

5.1.1 Non-thermal Plasma — Gas–Liquid Electrical Discharge Plasma

Non-thermal plasmas have been applied widely in many fields, including medical treatment [6, 8, 10, 35, 185, 186] and air pollution control [187]. One type of non-thermal plasma, called the gas–liquid electrical discharge, has been investigated for water purification [10, 188, 189] and bacterial treatment (see, for

example, [2, 5, 9, 10, 190, 191, 192, 193]), including biofilm treatment [120, 194]. These gas–liquid electrical discharges use a needle as a high-voltage electrode and a liquid phase, water, as the ground electrode, with gas flowing through a tube surrounding the needle electrode (see Figure 5.1). Typical gasses include air, oxygen (O_2), nitrogen (N_2), and helium (He). When the high-voltage pin electrode is submerged in water, as in Figure 5.2, high energy and electric field (10^9 V/m) are required to produce plasma in the liquid phase [195]. On the other hand, if the pin electrode is placed just above the water–air interface, around 2–3 mm (Figure 5.1), less energy and a lower electric field (10^6 V/m) are required to generate a plasma jet that sway above the water's surface (Figure 5.3 [1]). In most applications for biofilm removal, the plasma device will be positioned with a gap of air between the pin electrode and the biofilm, and we will focus on this scenario in what follows.

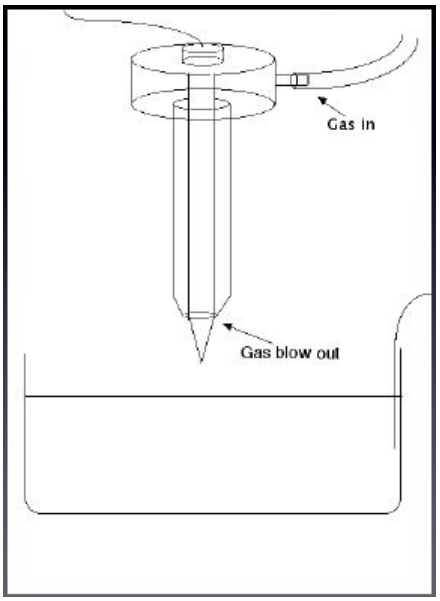

Figure 5.1: Gas–liquid electrical discharge device.

[1] These experiments were done with Jingjing Liu, School of Electronic, Electrical and Systems Engineering, Loughborough University.

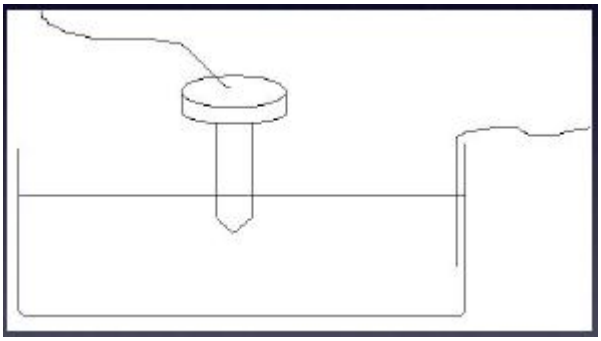

Figure 5.2: Gas–liquid electrical discharge device with needle electrode submerged in water.

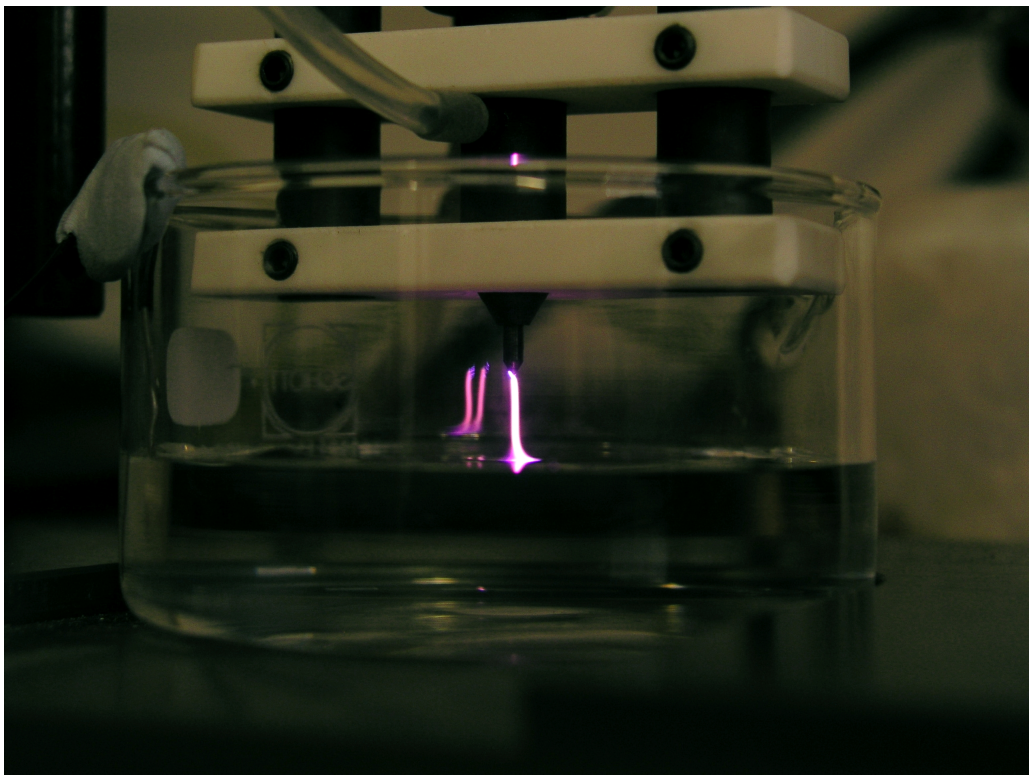

Figure 5.3: The gas–liquid electrical discharge plasma.

5.1.1.1 Plasma Geometry

The plasma jet that appears at the gap between the pin and the water can be divided into two regions: the ionization region, which is near the high-voltage

pin electrode, and the drift region (See Figure 5.4). The ionization region is a high-energy area that causes the cold gas to interact with energetic electrons, resulting in the ionization of the gas molecules in the vicinity of the needle. This area is the region of the primary production of the energetic chemical species. The drift region connects the ionization region and the ground electrode. Here charged species are forced to move by an electric field that is weaker than in the ionization region. The ions and electrons collide with the neutral species throughout the discharge, generating a rich cocktail of reactive species that reach the liquid phase.

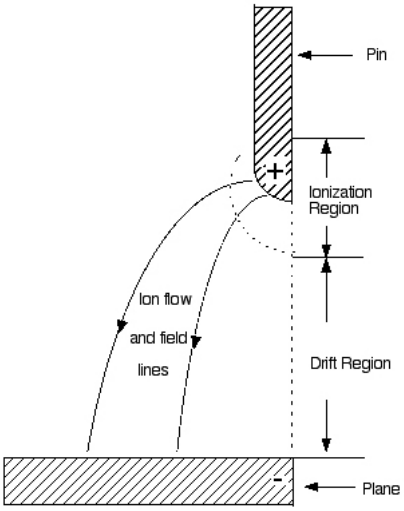

Figure 5.4: The geometry of DC plasma. Plasma flow onto a surface as a bean at the top of which ionization occurs.

5.1.1.2 Plasma Chemistry

Atmospheric pressure plasmas are highly collisional. For example, the electron-neutral collision frequency in atmospheric pressure helium plasma is on the order of THz, i.e., electrons undergo 10^{12} collisions per second. Collisions can be classified as elastic and inelastic, depending on the nature of the energy exchange between the colliding particles. If the colliding particles exchange only kinetic energy, the collision is referred to as an elastic collision. Elastic collisions lead

to momentum exchange and temperature equilibration. On the other hand, if the energy exchange involve changes in the potential energy of one or both of the colliding particles, the collision is said to be inelastic. Ionisation, excitation, and dissociation are examples of inelastic collisions. The large number of inelastic collision taking place in a plasma leads to the formation of a large number of reaction species [183]. For example, the collision of an electron with a water molecule may break one of the bonds between the hydrogen and oxygen atoms, so the water molecule is dissociated into one hydrogen atom and one hydroxyl radical:

$$e + H_2O \longrightarrow H + OH\bullet + e. \tag{5.1}$$

From a particle point of view, not only collision and reaction in the gas phase are important, but also the reaction between plasma species and the biological target.

5.2 Plasma Treatment of Biofilms

The air-liquid plasma has two effects to the biofilms, a physical effect and a chemical effect. The physical effect refers to the direct impact of the plasma jet on to the biofilms. This may result in biofilm dispersion and splash and induces the biofilm to detach. On the other hand, the chemical effect involves the chemical reaction of plasma species and the biofilms. Various agents produced by plasmas contribute to the inactivation of bacterial cells. The possible agents from cold plasma that lead to sterilization and other biological effects are listed under four categories by Laroussi and Leipold [185, 191, 192, 196]. The four categories they proposed for bacterial inactivation are

1. **Heat:** Heat generation is significant in some types of plasma: for example, in equilibrium plasmas, the temperature may be over 10^7K. For bacterial sterilisation, the temperatures do not need to be that high but should still be over 100 °C [196]. In terms of clinical application, heat is unlikely to be important in bacterial sterilisation by cold plasmas operated at room temperature.

2. **Ultraviolet radiation:** Plasmas produce radiation with wavelengths ranging from 200 nm to 1000 nm [188], which includes ultraviolet radiation, visible radiation, so-called visible light, and near-infrared radiation. The biological effects of ultraviolet (UV) light have been widely investigated [197, 198] and it has been reported that UV radiation in the range 200 nm to 400 nm induces cell mutation [199]. Furthermore, radiation in the range from 220 nm to 280 nm and doses about 0.1 1 mJ/cm^2 are able to cause cell death by damaging their DNA [200]. Laroussi and Leipold [192] measured UV radiation production in gas–liquid cold plasmas. They found that these plasmas produce UV radiation in the 200 nm to 280 nm range, but the doses were lower than 50μmJ/cm^2. Furthermore, Cvelbar *et al.* [3] reported that UV photons produced by low-temperature plasmas are restricted to about 1 μm depth in the biotic material. Therefore, they concluded that the effects of UV radiation on bacterial cell degradation are very limited in this system.

3. **Charged particles (electrons and ions):** Kelly-Wintenberg *et al.* [201] and Laroussi *et al.* [202] applied plasmas to bacterial cells and observed the disruption of the cells' membranes. Mendis *et al.* [203] proposed the hypothesis that the outer membrane of Gram-negative bacterial cells, such as *E. Coli*, is disrupted by the tension of the electrostatic force that is created by charged particles. This hypothesis was experimentally tested on Gram-positive bacterial cells, *Bacillus subtilis*, by Laroussi *et al.* [204]. They found that although Gram-positive bacterial cells lack outer membranes on their cell wall, they are able to sustain higher tensions of electrostatic force, since they have thicker cell walls.

4. **Reactive species:** Plasma chemistry is complex as it involves many reactions and species. For example, Liu *et al.* [205] identified 576 reactions and 46 chemical species in plasmas generated in $He + H_2O$ gas. These plasmas are a good source of reactive oxygen species (ROS) such as singlet oxygen ($^1O_2$), ozone (O_3), hydrogen peroxide (H_2O_2) and hydronium (H_3O^+). The reactive species formed from gas–liquid plasmas were also reported by Goree *et al.* [5], Burlica *et al.*[206], Shih and Locke [207] and

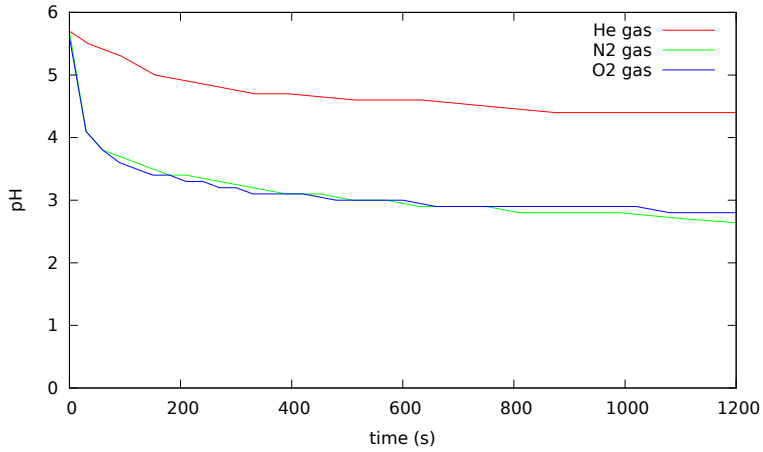

Figure 5.5: Schematic of the pH value drop in water during liquid–gas cold plasma exposure in He gas (red), N_2 gas (green) and O_2 gas (blue).

Brisset *et al.* [208]. The bactericidal properties of these reactive species have been investigated in a number of studies [114, 188, 209, 210, 211]. For example, high-oxidation-potential species, O_3 and H_2O_2, are able to oxidise cell walls and organelles to cause the cell to die. Acid species, such as nitric acid (HNO_3), lower the pH value of the environment (See Figure 5.5[1]), affecting bacteria behaviour and causing death at low pH [117].

Figure 5.6 shows the results of two cases, (1) the plasma is generated in nitrogen gas and (2) in oxygen gas, experiments shown in Figure 5.3 . In different kinds of plasma, the chemistry will be very different (see [212, 213]), but, as we see from the figure, the pH drop between these two cases are very similar in terms of evolution and asymptote (a pH $\backsimeq$ 2.8). Translated into hydrogen ion concentration, the differences are more notable with nitrogen gas, producing the slightly more acidic environment. We note that the seemingly discrete changes in concentration in Figure 5.6b are due to the rounding of the pH by the pH meter.

We simply assume an ordinary differential equation to describe the change of hydrogen ion concentration in the target water during plasma treatment. The

[1]The data is obtained from the experiment done by Jingjing Liu, School of Electronic, Electrical and Systems Engineering, Loughborough University.

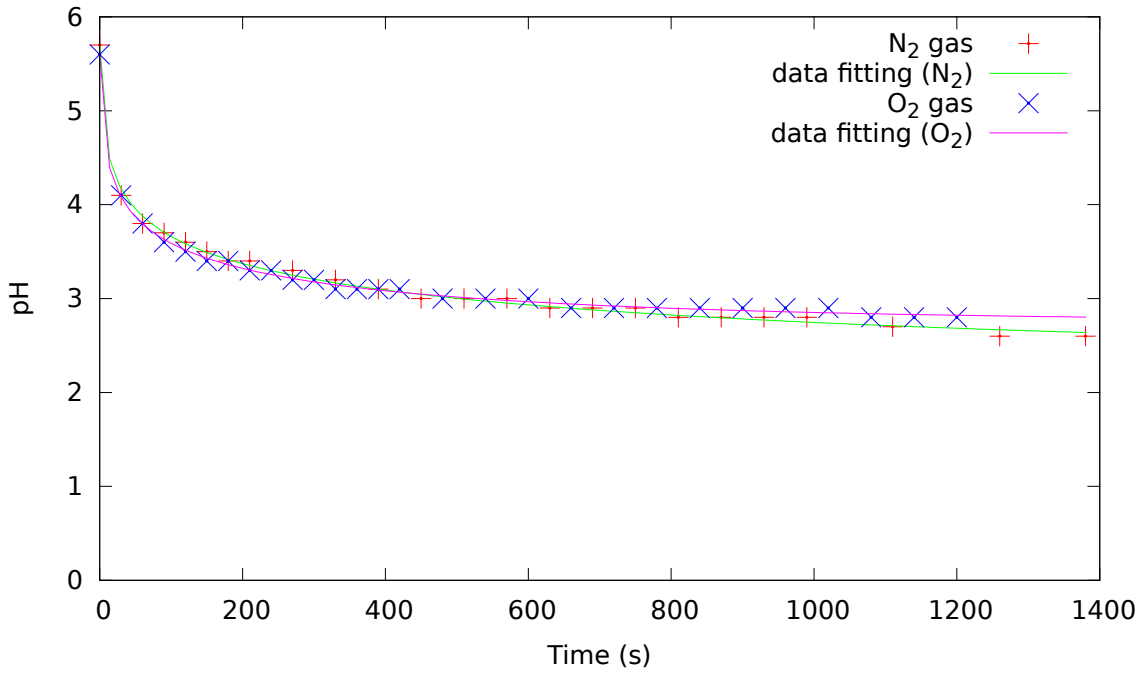

(a)

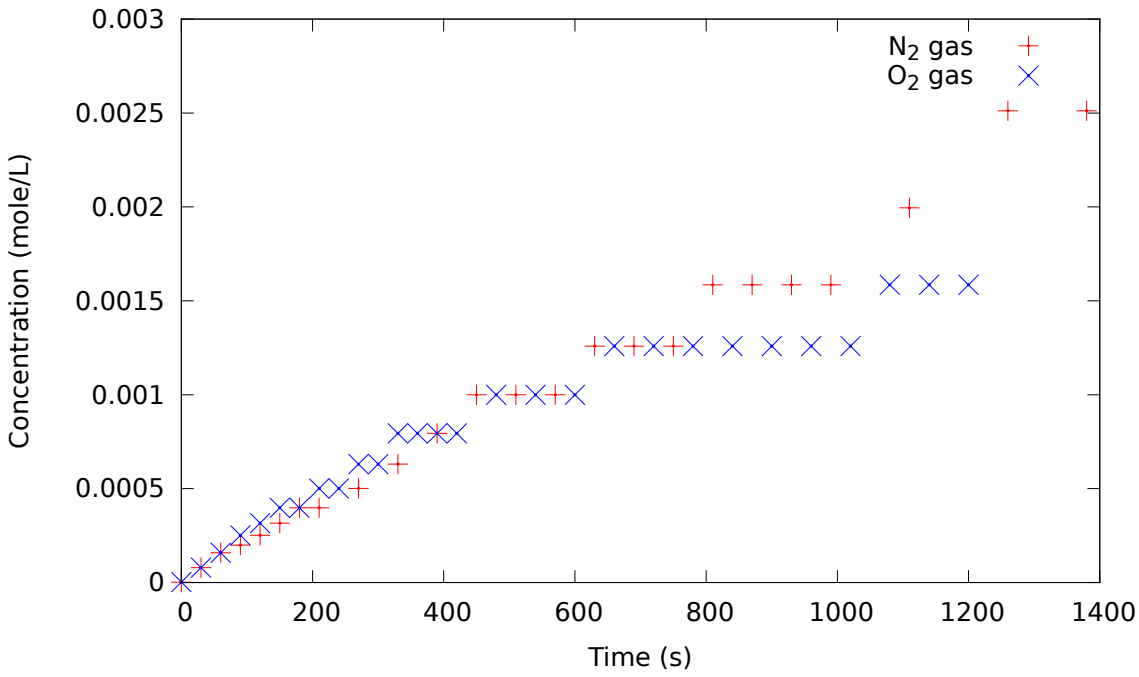

(b)

Figure 5.6: Plots of (a) pH drops and (b) hydrogen concentration produced by gas–liquid cold plasma. The plasma jets are generated in oxygen and nitrogen gas and the water capacities of the treatment target are about 300 ml.

equation is

$$\frac{dX_{H^+}}{dt} = \mu_{X_{H^+}} - \delta_{X'_{H^+}} X_{H^+}, \tag{5.2}$$

where $\mu_{X_{H^+}}$ is the rate at which hydrogen ions enter the target system and $\delta_{X'_{H^+}}$ is the hydrogen ion decay rate by acid sequester agent produced in the target system during plasma treatment. Equation (5.2) can be solved analytically and the result is

$$X_{H^+}(t) = \frac{\mu_{X_{H^+}}}{\delta_{X'_{H^+}}} + \left(X_{0H^+} - \frac{\mu_{X_{H^+}}}{\delta_{X'_{H^+}}} \right) \exp(-\delta_{X'_{H^+}} t), \tag{5.3}$$

where X_{0H^+} is the initial concentration of hydrogen ions. By fitting the experimental data to the function (5.3), we compute the rate of hydrogen ion concentration increase in the system $\mu_{X_{H^+}}$ and its decay rate $\delta_{X'_{H^+}}$ in the water. Since the total capacity of the target water in the plasma treatment experiment is 300 ml and we assume that the surface area of the plasma jet is a circle with 1 mm diameter, we obtain a constant flux of hydrogen ion through the plasma jet region into the target system.

In summary, charged particles and reactive species are the key factors that harm bacterial cells in clinically relevant cold liquid–gas plasmas. Charged particles, however, are confined by the electric field and therefore in indirect plasma treatments charged species are expected to play a negligible role. The relevant species are those that are relatively long lived and are molecularly stable enough to diffuse and penetrate deeply into the biofilms. The main agents with these properties are hydrogen peroxide (H_2O_2), ozone (O_3), and Nitric acid (HNO_3). Their action will be discussed in detail.

5.2.1 Biological Effects of Ozone on Bacterial Cells and Biofilms

The toxic effects of ozone on *E. Coli* have been reported in various studies [214, 215, 216, 217]. It has been found that cells under short-term ozone exposure are able to increase the permeability of their cell membranes [216] by oxidising the

membranes contents, such as lipids and proteins [217]. In this case, ozone has no effect on cell viability, but does damage the intracellular components of the cells, including the DNA and nucleic acid [216] and induces cell mutation [214]. As the ozone doses and contact time that are applied to the bacterial cells are increased, the membranes of the cells are destroyed [214, 215] and the DNA suffers degradation [218], resulting in cell death. The concentration of ozone that is required for *Escherichia coli* bacterial cell degradation has been studied by Finch *et al.* [219]. They found that increasing the ozone exposure time has no significant effect on further cell death. They offered the explanation that the reaction rates of the ozone and bacteria reactions are zero due to the low concentrations of either ozone or bacteria. In most of the cases they studied, it was because of the low concentration of ozone, since ozone is a highly reactive compound with a relatively short half-life, in the range from 1–1000 s. The reaction kinetics of ozone with organic compounds and inorganic compounds were also studied by Hoigne *et al.*[220, 221, 222]. Furthermore, Hunt and Marinas [223] proposed the reaction rate of ozone with *E. coli* cells.

The effects of ozone on biofilms are not completely the same as the effects of ozone on planktonic bacteria. A comparison of ozone effects on biofilms and planktonic cells was made by Viera *et al.* [224, 225], who found that the bacterial cells that live in biofilms were more resistant to ozone exposure, due to the EPS's restricting the penetration of the dissolved ozone [224]. One of their hypotheses is that ozone molecules mainly react with the EPS [211]. As stated in Section 1.2.2, EPS consists of large strands of monosaccharide units linked together by glycosidic linkages to form chains that can have a total molecular mean of over 100 KDa. Ozone reacts with the EPS at the linkage [226, 227, 228, 229] thereby breaking the chains in to smaller strands and producing O_2 as a result [230]. However, it is unlikely that the relevant levels of ozone will break up an EPS molecule completely. Wang *et al.* [228] investigated the decomposition of EPS molecules by exposing them to a constant concentration of an ozone/air mixture: the average size of the EPS molecules was found to decrease from 61 kDa to 20 kDa in an hour and to 10 kDa after 10 hours.

5.2.2 Biological Effects of Hydrogen Peroxide on Bacterial Cells and Biofilms

Hydrogen peroxide is a strong oxidiser with high-oxidation potential, which is just lower than that of ozone. These molecules diffuse freely through the cell membrane [231, 232] and cause damage to the DNA inside bacterial cells by redox reactions [231, 233]. Furthermore, hydrogen peroxide reduces ATP production by restricting electron transport from NADH to NAD^+ [234, 235] and inhibits ADP phosphorylation [236]. The magnitude of the biological effects of hydrogen peroxide depends on the cell activation. It causes larger damage to cells growing in optimal conditions than cells with an inert status [233, 234]. Although hydrogen peroxide is harmful to bacterial cells, it is one of the by-products of cells metabolic processes, such as aerobic respiration [231, 232, 237]. The production of hydrogen peroxide depends on the energy level of the cell and the respiration condition [234]. To avoid damage, bacterial cells contain an enzyme, called catalase, to decompose hydrogen peroxide and release water and oxygen as by-products [232, 238]. This enzyme has been found in almost all aerobic organisms and some anaerobic organisms intracellularly [232, 239], though there are exceptions (e.g., *Pseudomonas aeruginosa* [240]). It can be released as an extracellular enzyme. Catalase is a large-molecular-weight protein, with a molar mass of about 2.4×10^5g/mol [241], containing four heme groups [231]. During the catalase reaction, a hydrogen peroxide molecule oxidises a heme group to an oxyferryl species and releases a water molecule. The second hydrogen peroxide molecule regenerates the oxyferryl species to the resting state enzyme for the next catalase reaction and produces another water molecule and an oxygen molecule [239]. Let Enz(Por-Fe^{III}) and Cpd I($Por^+ - Fe^{IV} = O$) denote the catalase enzyme and oxyferryl species, respectively. The reaction can be summarised as follows

$$\begin{aligned} \text{Enz(Por-Fe}^{III}) + H_2O_2 &\longrightarrow \text{Cpd I(Por}^+ - \text{Fe}^{IV} = \text{O}) + H_2O, \\ \text{Cpd I(Por}^+ - \text{Fe}^{IV} = \text{O}) + H_2O_2 &\longrightarrow \text{Enz(Por-Fe}^{III}) + H_2O + O_2, \end{aligned} \tag{5.4}$$

i.e., two H_2O_2 molecules are broken down to two H_2O and one oxygen. The hydrogen peroxide decomposed by the catalase reaction has been quantified by units of catalase activity: one unit of catalase activity is defined as one μmol of hydrogen peroxide decomposed in one minute [231, 239]. The typical catalase activities are from 2.07×10^4 to 2.738×10^5 units per milligram of protein [239]. Therefore, the typical concentration of hydrogen peroxide inside a cell is about 0.1 μM [233, 234].

Although catalase activities protect bacterial cells from being oxidised by hydrogen peroxide, the capability of the activities is limited. Hydrogen peroxide may oxidise the polysaccharide cell wall before the intracellular catalase activates effectively [242], leading to the leakage of intracellular materials. The relative resistance to chemical oxidation, including the action of H_2O_2, between bacteria in biofilm and planktonic forms have been investigated by Cochran *et al.* [243] and Kiraly *et al.* [244]. It was found that bacterial cells in biofilms are more resistant and less sensitive to hydrogen peroxide than their planktonic counterparts. They concluded that the EPS matrix plays an important role in resistance to hydrogen peroxide. Hydrogen peroxide, being an active oxidant, reacts, like ozone, with polysaccharides in the EPS by oxidative depolymerization, breaking the glycosidic bonds [229, 245]. Thus this reaction with EPS limits the penetration potential of H_2O_2 in the biofilm, thereby protecting the cells from excessive exposure [246].

5.2.3 Biological Effects of an Acidic Environment on Biofilms

Bacterial species can be categorised into three groups, depending on the range of the pH value of the environment in which they can live: acidophiles (pH range 0.5–5), neutralophiles (pH range 5–9), and alkaliphiles (pH range 9–12) [16, 247]. The majority of the bacterial species are neutralophiles. Although bacterial cells live in a wide range of external pH environments, the cytoplasmic pH (i.e., the intracellular pH) of the bacterial cells is maintained in a narrow range around neutrality [247]. When bacterial cells experience an external pH shock, the cytoplasmic pH is changed. However, the cells are able to recover the intracellular pH rapidly by the application of various pH homeostasis mechanisms. The major acid-resisting mechanisms are as follows.

1. **Buffering Capacity**. The cells maintain their cytoplasmic pH by intracellular buffering molecules, including proteins, polyamines, polyphosphates and inorganic phosphates, as well as charged compounds at the cell membranes or cell walls [247].

2. **Proton Pumps**. Proton pumps refer to the F_1F_0-ATPases, also called F-ATPases, and the complex enzymes of the electric transport chain, which relate to ATP synthesis. During ATP synthesis, F_1F_0-ATPases transport the protons (hydrogen ions) into the cytoplasm: the enzymes of the electric transport chain pump the protons out of the cytoplasm through the cell membrane to maintain the proton-motive force (PMF)[1]. When cells experience an acid shock, the cytoplasmic pH drops, since a large amount of proton molecules suddenly crosses the cell membranes into the cytoplasm, leading the PMF to drop. In order to maintain the PMF, the enzymes of the electric transport chain accelerate energy consumption and the amount of protons being pumped out of the cell membrane [247, 248, 249].

3. **Production of Alkali.** Bacterial cells are able to produce alkali compounds, such as ammonia (NH_3) and arginine [247, 249, 250], which combine with protons in the cytoplam and increase the cytoplasmic pH.

4. **Inorganic Ion influxes.** Many bacteria species, including *E. Coli*, transport potassium ion (K^+) into the cytoplasm of the cells to be exchanged with the protons under low-pH environment [247, 248] leading to a rise in the intracellular pH.

5. **Regulators.** Bacterial cells are able to regulate their gene expression in response to the living environment, in order to adapt to the change in the environment [247, 249]. This induces an acid tolerance in these cells, enhancing their survival prospects in a low pH environment [251].

6. **Cell Membrane Structure Changing.** Bacterial cells also increase the acid resistance of their membrane by changing membranal composition,

[1] PMF is the chemical potential energy caused by the different proton concentrations inside and outside the cell membrane.

such as by the synthesis of cyclopropane fatty acid and tetraether lipids [247, 249].

7. **Biofilms.** It is known that biofilms are more resistant to low pH environments than are planktonic cells [252, 253, 254, 255, 256]. However, the acid resistance of the EPS matrix is limited [257, 258]. Rowbury *et al.* [259, 260] offered the explanation that when the biofilm cells experienced acid shock, this signals a warning to the other untreated cells to change their gene expression.

Although bacterial cells are protected by various mechanisms of acid tolerance, the cells are affected by pH changes. For example, acid saponifies the lipids in cell walls and leads to the cellular membrane's becoming solvable [261]; it also reduces ATP synthesis [262, 263, 264, 265]. Furthermore, in biofilm formation, acid restricts EPS production [266, 267, 268, 269] and damages the EPS structure by acid hydrolysis of the glycosidic linkages [270].

5.3 Summary

In this chapter, a brief introduction to plasma physics and chemistry was presented and how the products of cold plasma can effect biofilms. Due to the limitation of how cold plasma is to be applied in a clinical setting, features such as heat, UV, charged particles, and radical species are only likely to have a marginal effect on biofilm sterilisation, with their effects limited to a layer of about 1–2 μm at the surfaces. The main damaging effects of the treatment will be through the introduction of stable and toxic species, and chief among these are ozone, hydrogen peroxide, and acid-forming species (e.g., nitric acid).

Ozone and hydrogen peroxide are strong oxidisers and are able to diffuse freely into bacterial cells. The bacterial cell walls and the intracellular materials are oxidised when the cells are exposed to these chemical species, leading to cell death. However, in biofilms, the EPS matrix offers protection to bacterial cells. When these oxidising agents enter biofilms, they react with the EPS into oxygen and water, in which the EPS molecules are broken smaller molecules by breaking the glycosidic linkages. Due to the large size of an EPS molecule, the average

size of the EPS does not decrease significantly after a long exposure, i.e., there is a limited amount of EPS loss during the treatment. Furthermore, bacterial cells protect themselves against hydrogen peroxide by catalase activities, which are hydrogen peroxide decomposition activities caused by catalase enzymes.

The acid resistance of bacterial cells has been widely studied. Bacterial cells are able to maintain their cytoplasmic pH by various mechanisms. However, an acidic environment still affects the cells in different ways, such as decreases in the energy synthesis and in the EPS production of biofilms. The EPS matrix does not play an important role in acid resistance in biofilms. The EPS is damaged by the acidic disintegration of its glycosidic linkages when acid is added to a biofilm, but this seems to have a negligible effect on pH.

In the next chapter we will model plasma treatment as an inward flux of the main reactive species H_2O_2, O_3 and H^+, incorporating the biological activity discussed above.

Chapter 6

Mathematical Model of the Effects of Cold Plasma Species on Biofilms

In this chapter, the IbM modelling framework is applied to investigate the effects of cold plasma on biofilm removal. The simulations focus on three factors introduced by the plasma that effect biofilms, as discussed in the previous chapter, namely ozone, hydrogen peroxide, and pH changes of the environment. To describe these factors, the model described in Chapter 3 is extended. We investigate the effectiveness of cold palsma treatment on both single- and two-species biofilm growth scenarios, as well as the topical and basal nutrient sources (see Section 4).

6.1 Cold Plasma Modelling

As discussed, the physics and chemistry of cold plasma is very complicated, consisting of many usually short-lived species (lasting no more than a few nanoseconds). The more stable species, i.e., ozone, hydrogen peroxide, and acid species, are able to penetrate biofilm via diffusion and cause most of the damage. Consequently, our modelling will take a simplistic view and assume during treatment there is a localised flux of one or more of these species, which infiltrate the biofilms

variable	description	units
$X_{H_2O_2}$	hydrogen peroxide concentration	g/L
X_{O_3}	ozone concentration	g/L
X_{H^+}	hydrogen ion concentration	g/L

Table 6.1: Variables used in the plasma treatment simulations.

in a way similar to that of the nutrients. Each of these three species will affect the birth and death rates of the cells/particles and their evolution and transport will be described using reaction–diffusion equations. The three species have the following key properties.

1. **Ozone:** Ozone molecules freely infiltrate the bacterial cell wall and oxidise the organelles, leading to cell death. However, ozone molecules are decomposed into oxygen by reacting with the glycosidic linkages in the EPS molecules.

2. **Hydrogen peroxide:** The disinfection mechanisms of hydrogen peroxide are similar to those of ozone. The hydrogen peroxide molecules freely cross the bacterial cell wall and react with the wall and cell organelles. Although hydrogen peroxide is toxic to bacterial cells, it is produced during aerobic respiration processes. In order to be protected from the harmful hydrogen peroxide, bacterial cells contain catalase enzymes to decompose hydrogen peroxide molecules and stabilise its concentration inside the cell.

3. **pH:** pH effects the energy output, in which ATP production reduces in extremely high or low pH environments. The EPS can not significantly buffer the effects of the pH.

Table 6.1 shows the additional variables used in these plasma treatment simulations. The parameters are listed in Tables 5–7 in Appendix A.

6.1.1 Birth and Death Rates

According to the discussion in Section 5.2, the model assumes that antibiotic agents have no effect on cell growth, but increase the rate of cell death. The

equations of conservation of live and death mass are

$$\frac{dC_L^\kappa}{dt} = \Psi_b^\kappa - \Psi_d^\kappa, \tag{6.1}$$

$$\frac{dC_D^\kappa}{dt} = (1-\phi)\Psi_d^\kappa, \tag{6.2}$$

where Ψ_b^κ and Ψ_d^κ are modified forms of Equations (4.25) and (4.26), namely

$$\Psi_b^\kappa = ((\mu^{\Lambda(\kappa)} + \beta^{\Lambda(\kappa)} g(1)) A_\kappa H(X_s, K_{X_s b}, m_{X_{sb}}) C_L^\kappa, \tag{6.3}$$

$$\Psi_d^\kappa = \left(\beta^{\Lambda(\kappa)} g(A_\kappa) + \sum_{i=1}^{M_{[anti]}} R_{CX_i}\right) C_L^\kappa, \tag{6.4}$$

where $M_{[anti]}$ is the number of the oxidising agents and the R_{CX_i} are the biomass death rates increased by the ozone and hydrogen peroxide. We write

$$\sum_{i=1}^{M_{[anti]}} R_{CX_i} = R_{CX_{[H_2O_2]}} + R_{CX_{[O_3]}}, \tag{6.5}$$

where $R_{CX_{[H_2O_2]}}$ and $R_{CX_{[O_3]}}$ are the rates of live biomass death due to the hydrogen peroxide and ozone, respectively, defined by

$$R_{CX_{[H_2O_2]}} = \beta_{X_{H_2O_2}} H(X_{H_2O_2}, K_{X_{H_2O_2}}, m_{X_{H_2O_2}}), \tag{6.6}$$

$$R_{CX_{[O_3]}} = \beta_{X_{O_3}} H(X_{O_3}, K_{X_{O_3}}, m_{X_{O_3}}), \tag{6.7}$$

where $X_{H_2O_2}$ and X_{O_3} are the concentrations of the hydrogen peroxide and ozone, respectively, and $\beta_{X_{H_2O_2}}$ and $\beta_{X_{O_3}}$ are the maximum cell death rates due to the corresponding species. We again use a Hill function to describe the dependence of the death rate on the species concentration, where K_{X_i} and m_{X_i} are the corresponding Hill function coefficients.

6.1.2 Energy Synthesis

Energy synthesis is inhibited by the oxidative species and also influenced by the pH value of the environment. Therefore, the energy production equation (4.29)

is amended according to

$$A_\kappa = (F_s^{\Lambda(\kappa)} + F_p^{\Lambda(\kappa)})\Upsilon(X_{H^+}) \prod_{i=1}^{M_{[anti]}} \hat{H}(X_i, K_i, m_i), \tag{6.8}$$

where the functions $F_s^{\Lambda(\kappa)}$ and $F_p^{\Lambda(\kappa)}$ are given by Equations (4.30) and (4.31). The functions $\Upsilon(X_{H^+})$ and $\hat{H}(X_i, K_i, m_i)$ are the inhibition of energy production caused by the pH value of the biofilm growth environment and the oxidative species, respectively. By definition, the pH value depends on the concentration of the hydrogen ion X_{H^+}, according to $pH = -log_{10}(X_{H^+})$. In Rosso *et al.* [77] they proposed a function $\Upsilon(X_{H^+})$ to describe how bacteria are able to survive over a wide range of pH, say $[pH_{min}, pH_{max}]$, outside of which, the ATP synthesis rate is too small for the cells to survive. Figure 6.1 illustrates the function of ATP output, which is given by

$$\Upsilon(X_{H^+}) = \begin{cases} \dfrac{log_{10}\left(\frac{X_{H^+}^{min}}{X_{H^+}}\right) log_{10}\left(\frac{X_{H^+}^{max}}{X_{H^+}}\right)}{log_{10}\left(\frac{X_{H^+}^{min}}{X_{H^+}}\right) log_{10}\left(\frac{X_{H^+}^{max}}{X_{H^+}}\right) - \left(log_{10}\left(\frac{X_{H^+}^{Opt}}{X_{H^+}}\right)\right)^2} & \text{for } X_{H^+}^{min} \leq X_{H^+} \leq X_{H^+}^{max}, \\ 0 & \text{Otherwise.} \end{cases} \tag{6.9}$$

where $X_{H^+}^{Opt}$ is the value of X_{H^+} which maximises $\Upsilon(X_{H^+})$. The inhibition by oxidising species is described by

$$\prod_{i=1}^{M_{[anti]}} \hat{H}(X_i, K_i, m_i) = \hat{H}(X_{H_2O_2}, K_{X_{H_2O_2}}, m_{X_{H_2O_2}}) \hat{H}(X_{O_3}, K_{X_{O_3}}, m_{X_{O_3}}), \tag{6.10}$$

where

$$\hat{H}(X_i, K_i, m_i) = (1 - H(X_i, K_i, m_i)) = \frac{K_i^{m_i}}{X_i^{m_i} + K_i^{m_i}}, \tag{6.11}$$

is the inhibitive Hill function form. We note that as $X_i \to \infty$, $\hat{H}(x_i, K_i, m_i) \to 0$ thus inhibiting ATP production completely.

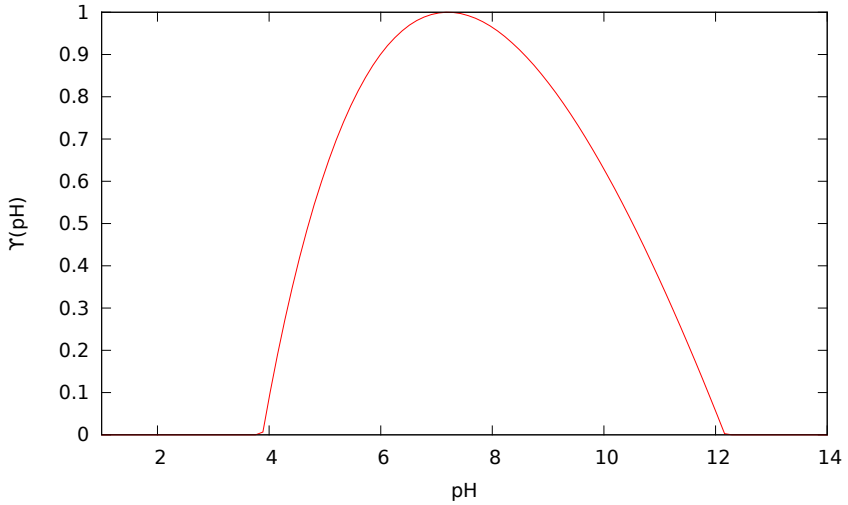

Figure 6.1: Energy production inhibition, $\Upsilon(pH)$, of *E. coli* in various pH values of the growth environment, where $pH_{max} = 12.17$, $pH_{Min} = 3.88$, and $pH_{Opt} = 7.2$ [77].

6.1.3 Cold plasma species transport

All three cold plasma species are small molecules/ions and it is assumed that they can diffuse freely across the cell membranes, in a similar manner to the oxygen and the nutrients. The finite volume form of the time-dependent reaction–diffusion equation (Equation (3.17)) for each of the species is

$$\frac{\partial}{\partial t}\int_{\Omega_c} X_i d\Omega_c = -\int_{\partial\Omega_c} \boldsymbol{J}_{\boldsymbol{X_i}} \cdot \boldsymbol{n} d\partial\Omega_c + \int_{\Omega_c} R_{X_i} d\Omega_c, \tag{6.12}$$

where X_i is the concentration of the freely diffusing species i, R_{X_i} is the turnover rate of the species, and $\boldsymbol{J}_{\boldsymbol{X_i}}$ is the flux of the diffusing species, which by applying Fick's law, is

$$\boldsymbol{J}_{\boldsymbol{X_i}} \quad = \quad -D_{X_i}\nabla X_i. \tag{6.13}$$

Here, D_{X_i} is the diffusion coefficient for species i.

The reaction rate terms of oxygen and the nutrients are affected by the cold plasma species, and we discuss separately the terms for each freely diffusible

species.

Nutrient Molecules

The killing of cells by hydrogen peroxide and ozone adds nutrients to the environment. The evolution equation for the nutrient will be presented in full, highlighting those terms that are different from the original system, i.e., Equations (4.38) to (4.44). The equation for the nutrients is

$$\frac{\partial}{\partial t}\int_{\Omega_c} X_s d\Omega_c = -\int_{\partial\Omega_c} \boldsymbol{J_{X_s}}\cdot\boldsymbol{n} d\partial\Omega_c + \int_{\Omega_c} R_{X_s} d\Omega_c, \tag{6.14}$$

where

$$\boldsymbol{J_{X_s}} = -D_{X_s}\nabla X_s, \tag{6.15}$$

$$R_{X_s} = R_{X_sEX_s} + \sum_{\kappa=1}^{N} W_\kappa(\boldsymbol{x},t)\Theta_\kappa(R^\kappa_{X_sd} - R^\kappa_{X_sA} - R^\kappa_{X_sE} - R^\kappa_{X_sb}), \tag{6.16}$$

and the reaction terms are

$$R_{X_sEX_s} = \mu_{X_sE}\lambda E, \tag{6.17}$$

$$R^\kappa_{X_sd} = \mu_{X_sb}\phi\left(\beta^{\Lambda(\kappa)}g(A_\kappa) + \sum_{i=1}^{M_{[anti]}} R_{CX_i}\right), \tag{6.18}$$

$$R^\kappa_{X_sA} = \delta^{\Lambda(\kappa)}_{X_sA} H(X_s, K_{X_sA}, m_{X_sA}), \tag{6.19}$$

$$R^\kappa_{X_sE} = \mu_E \rho^{\Lambda(\kappa)}_{EX_s} A_\kappa H(X_s, K_{X_sE}, m_{X_sE}), \tag{6.20}$$

$$R^\kappa_{X_sb} = \delta_{X_sb}(\mu^{\Lambda(\kappa)} + \beta^{\Lambda(\kappa)}g(1))A_\kappa H(X_s, K_{X_sb}, m_{X_sb}), \tag{6.21}$$

$$R^\kappa_{X_sP} = \delta^{\Lambda(\kappa)}_{X_sP} C_L^{\Lambda(\kappa)} A_\kappa Y_P^{\Lambda(\kappa)} H(X_s, K_{X_sP}, m_{X_sP}) \times (\xi + (1-\xi)H(X_{Ox}, K_{X_{Ox}P}, m_{X_{Ox}P}))(1 - \frac{P_\kappa}{P^*_\kappa}), \tag{6.22}$$

whereby the only change is in Equation 6.18, which now includes a contribution from the cells killed by the plasma species from Equation 6.14.

Oxygen Molecules

Oxygen is consumed during energy and PHB production. However, it is also obtained when oxidative species decompose. The oxygen reaction–diffusion equation is given by

$$\frac{\partial}{\partial t}\int_{\Omega_c} X_{Ox} d\Omega_c = -\int_{\partial\Omega_c} \boldsymbol{J}_{\boldsymbol{X_{Ox}}} \cdot \boldsymbol{n} d\partial\Omega_c + \int_{\Omega_c} R_{X_{Ox}} d\Omega_c, \tag{6.23}$$

where the flux $\boldsymbol{J}_{\boldsymbol{X_{Ox}}}$ and reaction term $R_{X_{Ox}}$ are given by

$$\boldsymbol{J}_{\boldsymbol{X_{Ox}}} = -D_{X_{Ox}} \nabla X_{Ox}, \tag{6.24}$$

$$R_{X_{Ox}} = \sum_{i=1}^{M_{[anti]}} R_{X_{Ox}X_i} - \sum_{\kappa=1}^{N} W_\kappa(\boldsymbol{x}, t)\Theta_\kappa(R^\kappa_{X_{Ox}A} + R^\kappa_{X_{Ox}P}) \tag{6.25}$$

where $\sum_{i=1}^{M_{[anti]}} R_{X_{Ox}X_i}$ is the increase of oxygen concentration during the decomposition of oxidative species X_i, and $R^\kappa_{X_{Ox}A}$ and $R^\kappa_{X_{Ox}P}$ are from Equation (4.48) and (4.49), which are given by

$$\begin{aligned} R^\kappa_{X_{Ox}A} &= (\delta_{X_{Ox}AX_s}(1-\omega^{\Lambda(\kappa)})H(X_s, K_{X_sA}, m_{X_sA}) \\ &\quad +\delta_{X_{Ox}AP}\psi(1-\tau^{\Lambda(\kappa)})G(X_s, P_\kappa))H(X_{Ox}, K_{X_{Ox}A}, m_{X_{Ox}A}), \end{aligned} \tag{6.26}$$

$$\begin{aligned} R^\kappa_{X_{Ox}P} &= \delta^{\Lambda(\kappa)}_{X_{Ox}P} C_L^{\Lambda(\kappa)} Y_P^{\Lambda(\kappa)}(1-\xi)A_\kappa H(X_{Ox}, K_{X_{Ox}P}, m_{X_{Ox}P}) \\ &\quad \times H(X_s, K_{X_sP}, m_{X_sP})(1-\frac{P_\kappa}{P^*_\kappa}). \end{aligned} \tag{6.27}$$

The net reaction of the decomposition of these species are summarised by the following reactions

$$H_2O_2 \rightarrow \frac{1}{2}O_2 + H_2O, \tag{6.28}$$

and

$$O_3 + X \rightarrow O_2 + OX, \tag{6.29}$$

where X is the reactant, which is oxidised by combining with an oxygen molecule

to produce the oxidised molecule OX.

The net oxygen production rate from these reactions are: one mole of hydrogen peroxide produces half a mole of oxygen and one mole of ozone releases one mole of oxygen, respectively. Hence, $\sum_{i=1}^{M_{[anti]}} R_{X_{Ox}X_i}$ is given by

$$\sum_{i=1}^{M_{[anti]}} R_{X_{Ox}X_i} = R_{X_{Ox}X_{H_2O_2}} + R_{X_{Ox}X_{O_3}} \tag{6.30}$$

$$R_{X_{Ox}X_{H_2O_2}} = \frac{1}{2}\left(R_{X_{H_2O_2}[Cat]} + R_{X_{H_2O_2}[EPS]} + R_{X_{H_2O_2}[decay]}\right), \tag{6.31}$$

$$R_{X_{Ox}X_{O_3}} = R_{X_{O_3}[bio]} + R_{X_{O_3}[EPS]} + R_{X_{O_3}[decay]}, \tag{6.32}$$

where $R_{X_{Ox}X_{H_2O_2}}$ and $R_{X_{Ox}X_{O_3}}$ are the net rates of oxygen gain during the hydrogen peroxide and ozone decompositions, respectively. Hydrogen peroxide can be broken down by inter-cellular catalase activity $R^{\kappa}_{X_{H_2O_2}[Cat]}$, reacting with EPS $R_{X_{H_2O_2}[EPS]}$ and natural decay $R_{X_{H_2O_2}[decay]}$. Similarly, ozone is broken down by oxidising cell biomass $R^{\kappa}_{X_{O_3}[bio]}$, both live and dead, and EPS $R_{X_{O_3}[EPS]}$, as well as its natural decay $R_{X_{O_3}[decay]}$. These terms will be discussed later.

Due to energy production being dependent on the pH of the environment and the concentration of the oxidative agents, the equations are modified as follows

$$\begin{aligned} R^{\kappa}_{X_{Ox}A} &= \delta_{X_{Ox}AX_s}(1-\omega^{\Lambda(\kappa)})H(X_s, K_{X_sA}, m_{X_sA}) \\ &\times H(X_{Ox}, K_{X_{Ox}A}, m_{X_{Ox}A})\Upsilon(X_{H^+})\prod_{i=1}^{M_{[anti]}}\hat{H}(X_i, K_i, m_i), \end{aligned} \tag{6.33}$$

where $\Upsilon(X_{H^+})\prod_{i=1}^{M_{[anti]}}\hat{H}(X_i, K_i, m_i)$ is the inhibition of energy production from Equation (6.8).

Hydrogen Peroxide Molecules

As discussed in Section 5.2.2, hydrogen peroxide is produced during bacterial cells' aerobic respiration, decomposed by inter-cellular catalase enzyme, and broken down during oxidising the bacterial biomass and EPS. The reaction–diffusion

equation, in finite volume form, for hydrogen peroxide is

$$\frac{\partial}{\partial t}\int_{\Omega_c} X_{H_2O_2} d\Omega_c = -\int_{\partial\Omega_c} \boldsymbol{J_{X_{H_2O_2}}} \cdot \boldsymbol{n} d\partial\Omega_c + \int_{\Omega_c} R_{X_{H_2O_2}} d\Omega_c, \tag{6.34}$$

where

$$\boldsymbol{J_{X_{H_2O_2}}} = -D_{X_{H_2O_2}} \nabla X_{H_2O_2}, \tag{6.35}$$

$$R_{X_{H_2O_2}} = R_{X_{H_2O_2}B} - R_{X_{H_2O_2}[Cat]} - R_{X_{H_2O_2}[EPS]} - R_{X_{H_2O_2}[decay]}. \tag{6.36}$$

The reaction term $R_{X_{H_2O_2}B}$ is the hydrogen peroxide production rate during aerobic respiration, $R_{X_{H_2O_2}[Cat]}$ is the decomposition rate by inter-cellular catalase activity, $R_{X_{H_2O_2}[EPS]}$ is the reaction rate of the reaction between the hydrogen peroxide and the EPS matrix, and $R_{X_{H_2O_2}[decay]}$ is the natural decay of the hydrogen peroxide. We write

$$\begin{aligned} R_{X_{H_2O_2}B} &= \sum_{\kappa=1}^{N} W_\kappa(\boldsymbol{x},t)\Theta_\kappa \hat{\mu}_{H_2O_2} \delta_{X_{O_2}AX_s}(1-\omega) H(X_s, K_{X_sA}, m_{X_sA}) \\ &\times H(X_{O_2}, K_{X_{O_2}A}, m_{X_{O_2}A}) \Upsilon(X_{H^+}) \prod_{i=1}^{M_{[anti]}} \hat{H}(X_i, K_i, m_i), \end{aligned} \tag{6.37}$$

$$R_{X_{H_2O_2}[Cat]} = \sum_{\kappa=1}^{N} W_\kappa(\boldsymbol{x},t)\delta_{Cat} H(X_{H_2O_2}, K_{MX_{H_2O_2}}, m_{X_{H_2O_2}}), \tag{6.38}$$

$$R_{X_{H_2O_2}[EPS]} = \sum_{\kappa=1}^{N} (1 - W_\kappa(\boldsymbol{x},t))\delta_{X_{H_2O_2}[EPS]} E X_{H_2O_2}, \tag{6.39}$$

$$R_{H_2O_2d} = \delta_{X_{H_2O_2}} X_{H_2O_2}, \tag{6.40}$$

where $R_{X_{H_2O_2}B}$ is modified from Equation (6.8); $\hat{\mu}_{H_2O_2}$ is the hydrogen peroxide production rate, δ_{Cat} and $\delta_{X_{H_2O_2}[EPS]}$ are the maximum catalase activity rates and the maximum reaction rate with the EPS matrix, $K_{MX_{H_2O_2}}$ is the Hill function constant for the catalase activity, and $\delta_{X_{H_2O_2}}$ is the decay rate constant. Letting $\mu_{H_2O_2} = \hat{\mu}_{H_2O_2}\delta_{X_{O_2}AX_s}(1-\omega)$ be the maximum hydrogen peroxide production

rate, we can rewrite Equation (6.37) as

$$\begin{aligned} R_{X_{H_2O_2}B} &= \sum_{\kappa=1}^{N} W_\kappa(\boldsymbol{x},t)\Theta_\kappa \mu_{H_2O_2} H(X_s, K_{X_sA}, m_{X_sA}) \\ &\times H(X_{Ox}, K_{X_{Ox}A}, m_{X_{Ox}A})\Upsilon(X_{H^+}) \prod_{i=1}^{M_{[anti]}} \hat{H}(X_i, K_i, m_i). \end{aligned} \tag{6.41}$$

Ozone Molecules

Ozone molecules break down by reacting with cells, the EPS matrix of the biofilms, and by natural decay. The finite volume form of the time dependent reaction–diffusion equation for ozone is

$$\frac{\partial}{\partial t}\int_{\Omega_c} X_{O_3} d\Omega_c = -\int_{\partial\Omega_c} \boldsymbol{J}_{\boldsymbol{X_{O_3}}} \cdot \boldsymbol{n} d\partial\Omega_c - \int_{\Omega_c} R_{X_{O_3}} d\Omega_c, \tag{6.42}$$

$$\tag{6.43}$$

where

$$\boldsymbol{J}_{\boldsymbol{X_{O_3}}} = -D_{X_{O_3}} \nabla X_{O_3}, \tag{6.44}$$

$$R_{X_{O_3}} = R_{X_{O_3}[bio]} + R_{X_{O_3}[EPS]} + R_{X_{O_3}[decay]}. \tag{6.45}$$

The reaction terms $R_{X_{O_3}[bio]}$, $R_{X_{O_3}[EPS]}$, and $R_{X_{O_3}[decay]}$ are the decomposition rates for reacting with the bacterial cells, reacting with the EPS matrix, and the natural decay, respectively. The terms for $R_{X_{O_3}[bio]}$ and $R_{X_{O_3}[decay]}$ are

$$R_{X_{O_3}[bio]} = \delta_{X_{O_3}[bio]} X_{O_3} \sum_{\kappa=1}^{N} W_\kappa(\boldsymbol{x},t), \tag{6.46}$$

$$R_{X_{O_3}[decay]} = \delta_{X_{O_3}} X_{O_3}, \tag{6.47}$$

where $\delta_{X_{O_3}[bio]}$ represents the reaction rate of ozone with biomass concentration and $\delta_{X_{O_3}}$ is the decay rate constant (half-life $\approx$ 10 minutes [210]).

Pan *et al.* [227] proposed the following reaction between ozone and glycosidic-

linkages (MβG):

$$O_3 + [M\beta G] \xrightarrow{k_1} [M\beta G - O] + O_2, \tag{6.48}$$

where k_1 is the reaction rate, $[M\beta G]$ is the linkage, and $[M\beta G - O]$ is the bond connect to an oxygen molecule. Therefore, the reaction rates of ozone and the glycosidic bonds are

$$R_{X_{O_3}[M\beta G]} = k_1 X_{O_3}[M\beta G], \tag{6.49}$$

$$R_{[M\beta G]X_{O3}} = k_1 X_{O_3}[M\beta G]. \tag{6.50}$$

One molecule of EPS consists of, on average, approximately 3000 MβG linkages [271]. Since the molar mass of EPS and MβG are 2.3×10^6 and 1.9418×10^2 g/mol, respectively, one can calculate that one g/L of EPS contains 0.25 g/L of MβG. Therefore, the ozone decomposition rate by the EPS matrix $R_{X_{O_3}[EPS]}$ is described by applying Equation (6.49), using

$$R_{X_{O_3}[EPS]} = \delta_{X_{O_3}[EPS]} X_{O_3} E, \tag{6.51}$$

where $\delta_{X_{O_3}[EPS]}$ is the reaction rate of ozone with the EPS.

Hydrogen Ion Molecules

It is well known that the diffusion of hydrogen ions is very much dependent on the sizes, and therefore the diffusion coefficients, of the negative charged ions in the solution. On macroscopic length scales, the concentrations of these ions are such that a neutral charge is maintained, and an effective transport term for hydrogen ions can be derived via the Nernst–Planck equation [272]. In order to simplify the modelling, we neglect the explicit treatment of the corresponding negative ionic species, and assume that the hydrogen ion diffusion coefficient is uniform throughout the domain, with an "effective" diffusion coefficient D_{H^+}.

The reaction–diffusion equation in finite volume form for H^+ is

$$\frac{\partial}{\partial t}\int_{\Omega_c} X_{H^+} d\Omega_c = -\int_{\partial\Omega_c} \boldsymbol{J}_{\boldsymbol{X_{H^+}}} \cdot \boldsymbol{n} d\partial\Omega_c + \int_{\Omega_c} R_{X_{H^+}} d\Omega_c, \tag{6.52}$$

where

$$\boldsymbol{J}_{\boldsymbol{X_{H^+}}} = -D_{X_{H^+}} \nabla X_{H+}, \tag{6.53}$$

The reaction term $R_{X_{H^+}}$ is the decay rate of the hydrogen ion concentration caused by the environmental acid sequester agents as mentioned in Section 5.2.3. The decay rate $R_{X_{H^+}}$ is given by

$$R_{X_{H+}} = \delta_{X_{H^+}}(X_{H_{Opt}} - X_{H^+}), \tag{6.54}$$

where $\delta_{X_{H^+}}$ is the maximum hydrogen ion decay rate by the environmental sequester agents, and $X_{H_{Opt}}$ is the natural concentration of the hydrogen ions, dependentt on the environment (e.g., the temperature).

6.1.4 Intra-cellular Production

For PHB, the equations are in the same form as 4.2.2, namely

$$\frac{dP_\kappa}{dt} = R_P^\kappa - \frac{\Psi_b^\kappa}{C_L^\kappa} P_\kappa. \tag{6.55}$$

Here, the net PHB production rate is affected by the pH value, the ozone concentraion, and the hydrogen peroxide concentration in the growth environment. The net production rate is amended to

$$\begin{aligned} R_P^\kappa = {} & A_\kappa Y_p^{\Lambda(\kappa)} H(X_s, K_{X_sP}, m_{X_sP})(\xi + (1-\xi)H(X_{Ox}, K_{X_{Ox}P}, m_{X_{Ox}P}))(1 - \frac{P_\kappa}{P_\kappa^*}) \\ & -\delta_{PA} F_p^{\Lambda(\kappa)} \Upsilon(X_{H+}) \prod_{i=1}^{M_{[anti]}} \hat{H}(X_i, K_i, m_i), \end{aligned} \tag{6.56}$$

where the last term describes the inhibitive effects of the plasma agents on cells trying to use PHB.

6.1.5 EPS Production, Reaction and Diffusion

The reaction–diffusion of EPS is described in Sections 3.6 and 4.1.2. However, long chain EPS molecules are sliced into smaller chained molecules by oxidising agents. It is assumed that the integrity of the biofilm structure will be maintained despite these oxidising processes. The EPS decay and consumption rate, R_E, in Equation (3.24) is rewritten as

$$R_E = R_{E[decay]} + \sum_{i=1}^{M[anti]} R_{E[X_i]}, \tag{6.57}$$

where $R_{E[decay]}$ is the EPS (linear) natural decay rate and $R_{E[X_i]}$ is the EPS breaking rate by oxidising agent X_i, which are given by

$$R_{E[X_{H_2O_2}]} = \delta_{E[X_{H_2O_2}]} X_{H_2O_2} E, \tag{6.58}$$

$$R_{E[X_{O_3}]} = \delta_{E[X_{O_3}]} X_{O_3} E. \tag{6.59}$$

where the constants $\delta_{E[X_{H_2O_2}]}$ and $\delta_{E[X_{O_3}]}$ are the reaction rate constants for the reactions of the hydrogen peroxide and the ozone with the EPS, respectively.

6.1.6 Boundary Conditions

As in Chapter 3, we consider the two biofilm growth scenarios depicted in Figure 3.7. We model the introduction of hydrogen peroxide, ozone, and hydrogen ions as constant input fluxes over a portion of the domain [273]. Such fluxes can be measured in gas and we assume the flux into the more fluid environment of a biofilm is some fraction of this. The two side boundaries are assumed periodic as before, and we impose impermeability conditions at the bottom boundary (see Figure 6.2). The boundary conditions of the plasma's chemical species X_i are given by

1. **Periodic Condition** at $x = 0$ and $x = L_x$

$$\begin{aligned} X_i(0, z, t) &= X_i(L_x, z, t) \quad \text{for } z \in [0, L_z] \text{ and } t \geq t_0, \\ \frac{\partial X_i(0, z, t)}{\partial x} &= \frac{\partial X_i(L_x, z, t)}{\partial x} \quad \text{for } z \in [0, L_z] \text{ and } t \geq t_0. \end{aligned} \tag{6.60}$$

2. **Impermeability Conditions** at $z = 0$ and $\Phi(\boldsymbol{x}, t) = 0$, $\boldsymbol{x} \notin \partial\Omega_P$

$$\nabla X_i \cdot \boldsymbol{n} = 0 \quad \text{at } Z = 0, \tag{6.61}$$

$$\nabla X_i \cdot \boldsymbol{n} = 0 \quad \text{at } \Phi(\boldsymbol{x}, t) = 0 \text{ for } \boldsymbol{x} \notin \partial\Omega_P, \tag{6.62}$$

where n is the inward normal vector and $\partial\Omega_P$ is the region of the boundary through which the plasma enters.

3. **Plasma input Flux Condition:**

$$-\nabla(D_{X_i} X_i) \cdot \boldsymbol{n} = \boldsymbol{J_{X_i 0}} \quad \text{at } \Phi(\boldsymbol{x}, t) = 0 \text{ for } \boldsymbol{x} \in \partial\Omega_P. \tag{6.63}$$

where $\boldsymbol{J_{X_i 0}}$ is the constant flux of the agent X_i.

In the simulation to follow, the flux conditions are applied to the topmost grid squares containing either particles or EPS.

6.2 Cold Plasma Treatment Simulations

In this section we present a number of simulations, demonstrating the predicted range of effects in a number of scenarios. In each case, the biofilm is grown untreated for a varied number of days and then we apply the treatment. As the time scale of the treatment is small (a few minutes as opposed to days for growth), the particles are fixed (i.e., no growth and movement) during the simulations, but will die due to the cold plasma species. The width of a cold plasma jet has been measured to be from 0.1 mm [274] to 0.7 cm [275], depending on the size of the needle-electrode. We thus extended the width of the domain from 1 mm to 3 mm, due to the periodic boundary conditions, this is easily achieved by fusing together three 1 mm wide biofilms exploiting the periodic side boundaries. We apply the plasma at the centre of the extended computational domain as shown in Figure 6.3. We examine the treatments by hydrogen peroxide, ozone, and acid produced by cold plasma individually to the immature and mature biofilms from both the standard and the basal nutrient source simulations. Furthermore, we simulate the effects of the combination of each of the oxidising agents and the acid

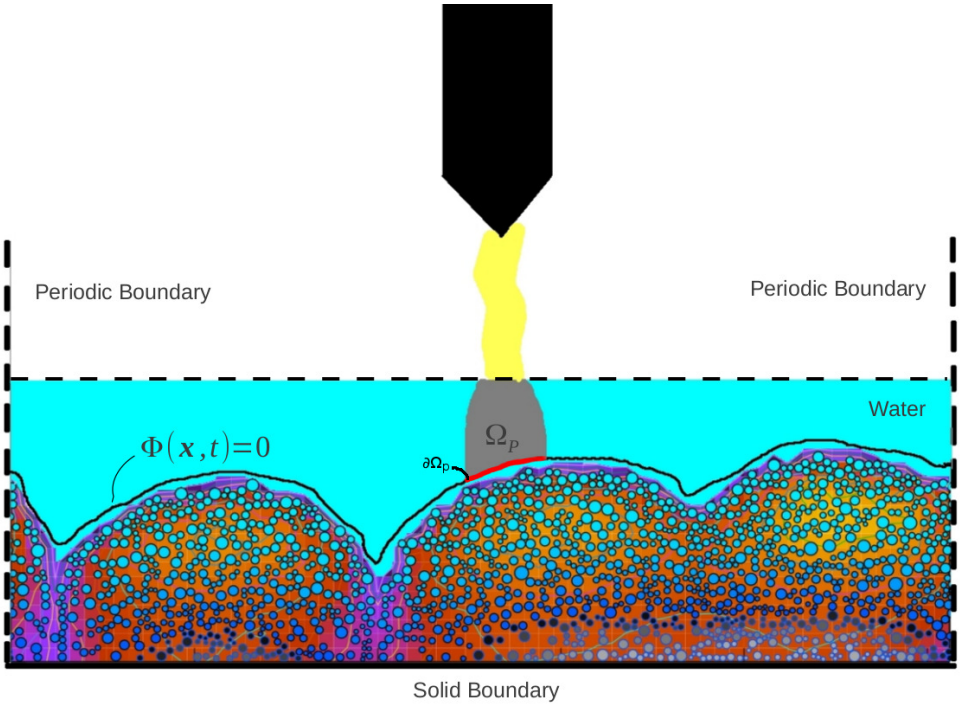

Figure 6.2: Plot of the boundaries for the plasma's chemical species. Ω_p is the drifting region of the plasma species and $\partial\Omega_p$, colour red, is the intersection of Ω_p and $\Phi(\boldsymbol{x}, t) = 0$.

as ozone and hydrogen peroxide are not typically observed in the same plasma. We also investigate the role of the EPS on cell survival and its contribution to resistance against the oxidising agents. The simulations assume that the treatment continues for up to six minutes.

6.2.1 Hydrogen Peroxide

Table 6.2 summarises the simulations presented in this section. The terms low and high flux describe 1/10 and 1/500 of the hydrogen peroxide flux produced in the air by a cold plasma jet, as given in Liu *et al.* [276], the values being 1.7475×10^{-11} and 3.495×10^{-13} mol/(μm^2·h), respectively. We firstly present the effects of hydrogen peroxide on a 3-day old biofilm (Simulation 6-1). Then in Simulation 6-2, we increase the dose of hydrogen peroxide, in this case to

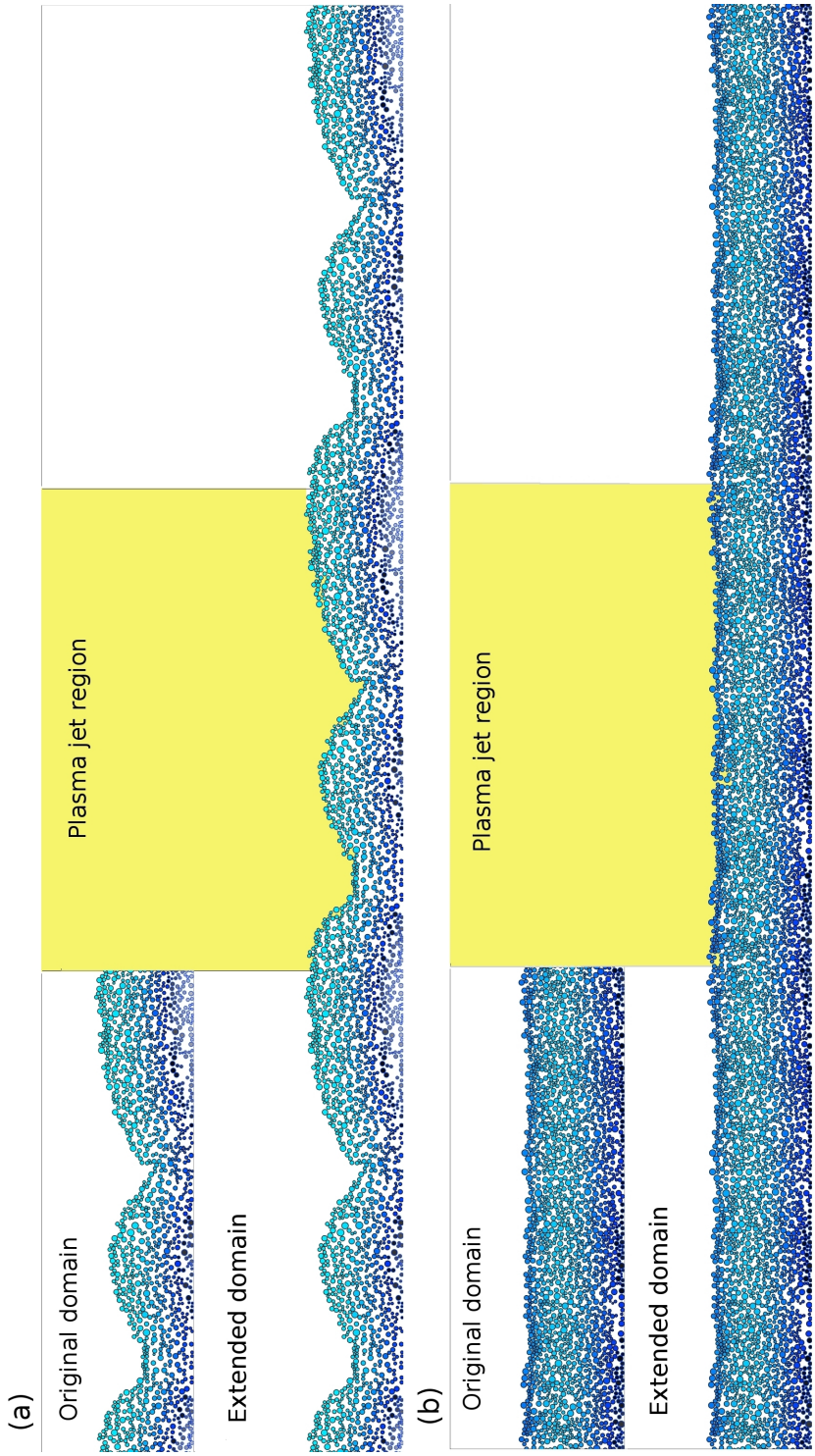

Figure 6.3: Plot of the extended computational domain and the plasma jet region in (a) standard simulation and (b) basal nutrient source.

Table 6.2: Summary of simulations of the biofilm treatment with hydrogen peroxide.

	topical nutrient growth		basal nutrient source	Two species
Low flux*	Immature [a] (Simulation 6-1)	Immature [a] no EPS effect (Simulation 6-3)	Immature [b] (Simulation 6-5)	Immature [c] (Simulation 6-8)
			Mature [e] (Simulation 6-6)	
High flux*	Immature [a] (Simulation 6-2)	Mature [d] (Simulation 6-4)	Mature [e] (Simulation 6-7)	

* 1/10 of hydrogen peroxide flux produced in air by cold plasma jet.
* 1/500 of hydrogen peroxide flux produced in air by cold plasma jet.
[a] 3-day old biofilm from Simulation 1-2.
[b] 3-day old biofilm from Simulation 3-1.
[c] 4-day old biofilm from Simulation 4-1.
[d] 10-day old biofilm from Simulation 1-2.
[e] 10-day old biofilm from Simulation 3-1.

investigate the extent of further damage. The effects of EPS on hydrogen peroxide penetration are investigated in Simulation 6-3, to establish how important is the role played by EPS in protecting a biofilm over, for example, the barrier generated by dead particles in the vicinity of the plasma jet. In order to understand the relationship between hydrogen peroxide resistance and biofilm maturity, we apply the hydrogen peroxide treatment to a mature 10-day old biofilm (Simulation 6-4). In Simulations 6-5, 6-6, and 6-7, we repeat those of Simulations 6-1 and 6-2 for the basal nutrient source case, and then compare the two scenarios.

Figure 6.4 shows the bacterial particle distribution and substrate concentration after one minute of the treatment in Simulation 6-1. At this stage, the hydrogen peroxide penetrates about 100 μm into the centre of the biofilm, causing notable particle death. Comparing the oxygen and nutrient distribution inside and outside the treated region, we observe that these substrates are able to penetrate deeper, due to the cells' at the top being dead. Furthermore, the oxygen concentration in the centre region of the biofilm has also risen by hydrogen peroxide decomposition. The live particles in this region obtain higher nutrient and

oxygen concentrations than particles in the corresponding positions outside the region. However, the energy production of these particles does not increase, due to the production's being inhibited by the hydrogen peroxide. Comparing the EPS levels between the treated and untreated regions, we observe that there has been little change, showing that any degradation of EPS by hydrogen peroxide has been relatively insignificant.

After six minutes of treatment, the hydrogen peroxide seems not to penetrate significantly further into the biofilm (see Figure 6.5). However, the dead region of the particles grows slightly thicker than after only one minute of treatment. This is a result of the fact that the particle death is not instantaneous in regions of lower hydrogen peroxide concentration. Figure 6.6 shows the survival fraction over the whole domain according to the formula

$$\text{survival rate at time t} = \frac{\text{fraction of total live biomass at time t}}{\text{fraction of total live biomass before treatment}}$$

We observe that plasma exposure has the most effect in the first minute. After this, very little further death can be seen. This figure suggests that the maximum effect can be achieved from a one minute application, and a brief application (< 10 seconds) is not likely to be significantly damaging. We note that 78% survival is due to the inclusion of the untreated cells in the calculation, the survival fraction will be much smaller in the treated area.

The hydrogen peroxide concentration and particle distribution from Simulation 6-2 are shown in Figures 6.7 and 6.8. After one minute of exposure (Figure 6.7), compared to the low hydrogen peroxide flux case (Simulation 6-1, Figure 6.4), the hydrogen peroxide diffuses wider and penetrates deeper, reaching the bottom of the biofilm, a depth of about 150 μm. This results in a thicker and wider region of dead particles than in Simulation 6-1 over the same exposure period. After six minutes of exposure (Figure 6.8), the hydrogen peroxide does not spread significantly further to the two sides. From Figure 6.6, we can see that about 10% more cells have been killed than in Simulation 6-1 after six minutes of treatment.

Figure 6.9 is a repeat of Simulation 6-2 except that the hydrogen peroxide is not reacting with the EPS (i.e., $\delta_{X_{H_2O_2}[EPS]} = 0$ and $\delta_{E\left[X_{H_2O_2}\right]} = 0$, Simulation 6-

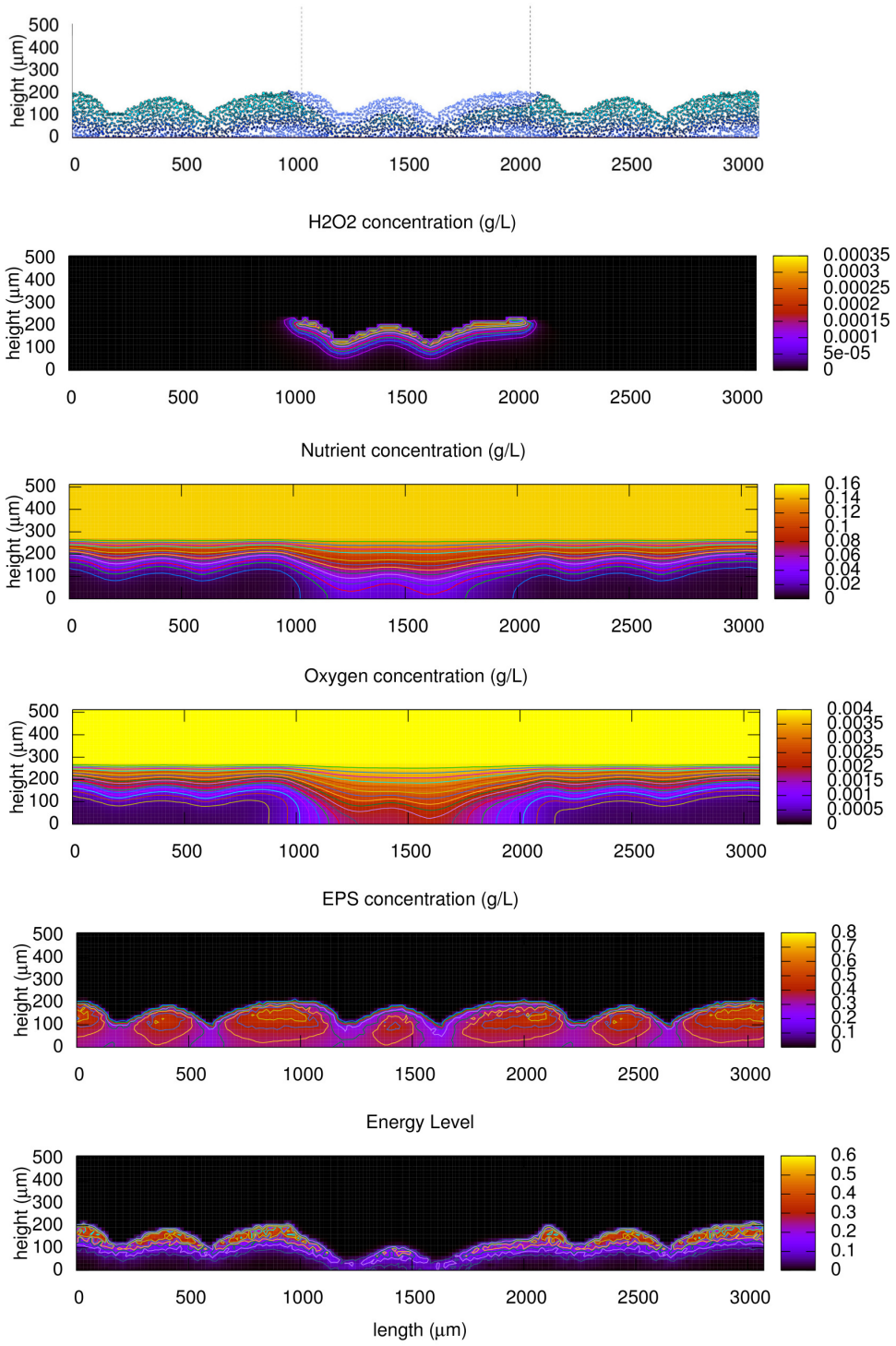

Figure 6.4: Plots of (from top to bottom) the particle distribution, hydrogen peroxide, nutrient, oxygen, and EPS concentrations, and the energy level in the biofilm of Simulation 6-1 after one minute of treatment. The plasma jet is between 1000–2000 μm in each plot. The parameters are listed in Table 5 in Appendix A.

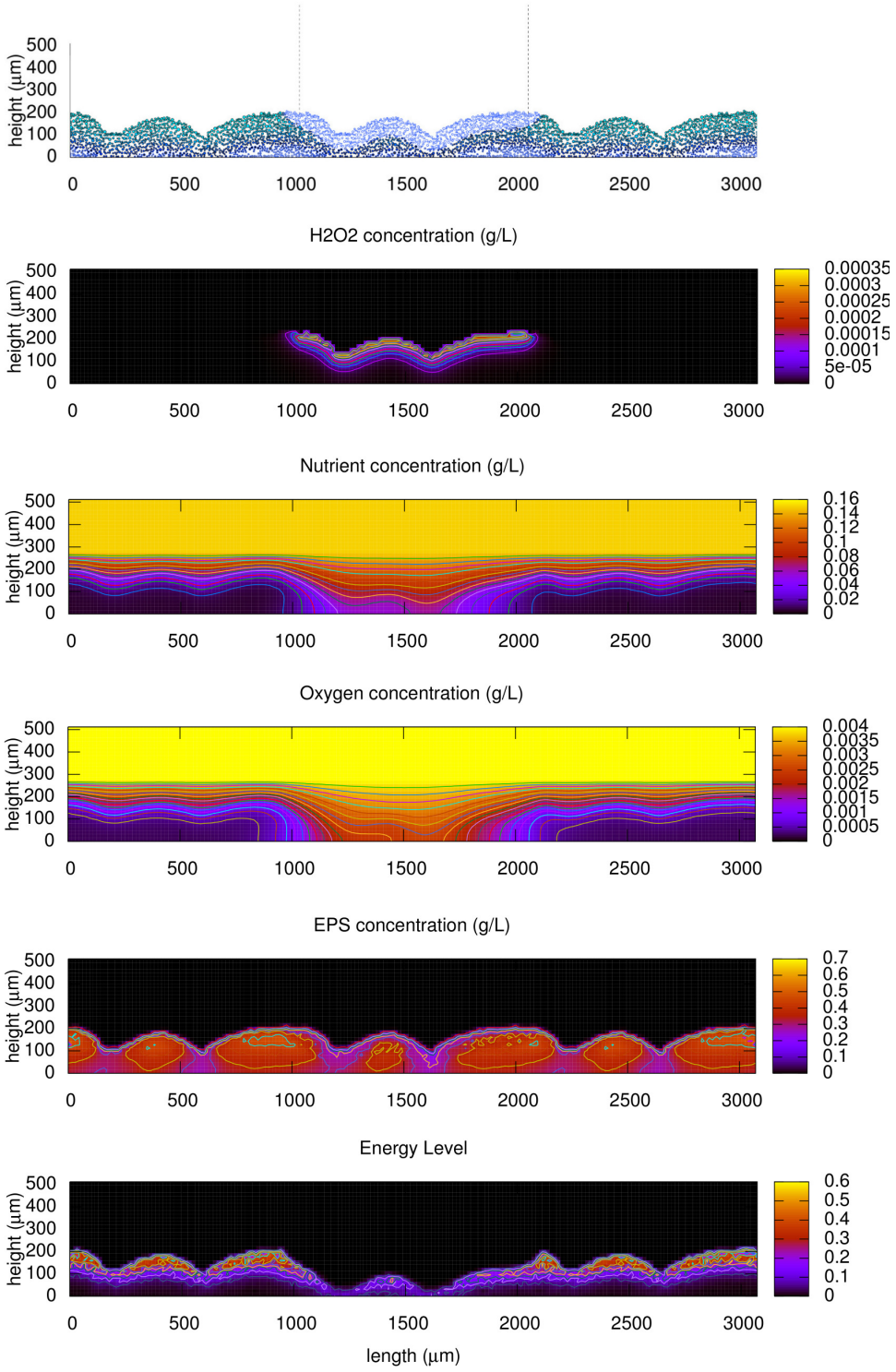

Figure 6.5: Plots of (from top to bottom) the particle distribution, hydrogen peroxide, nutrient, oxygen, and EPS concentrations, and the energy level in the biofilm of Simulation 6-1 after six minutes of treatment.

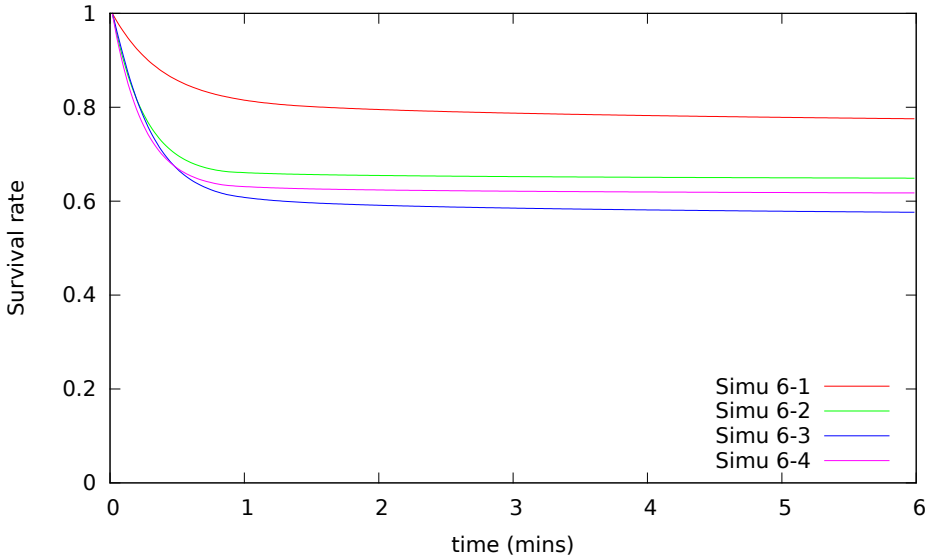

Figure 6.6: Plots of the survival rate throughout six minutes of treatment in Simulations 6-1 to 6-4.

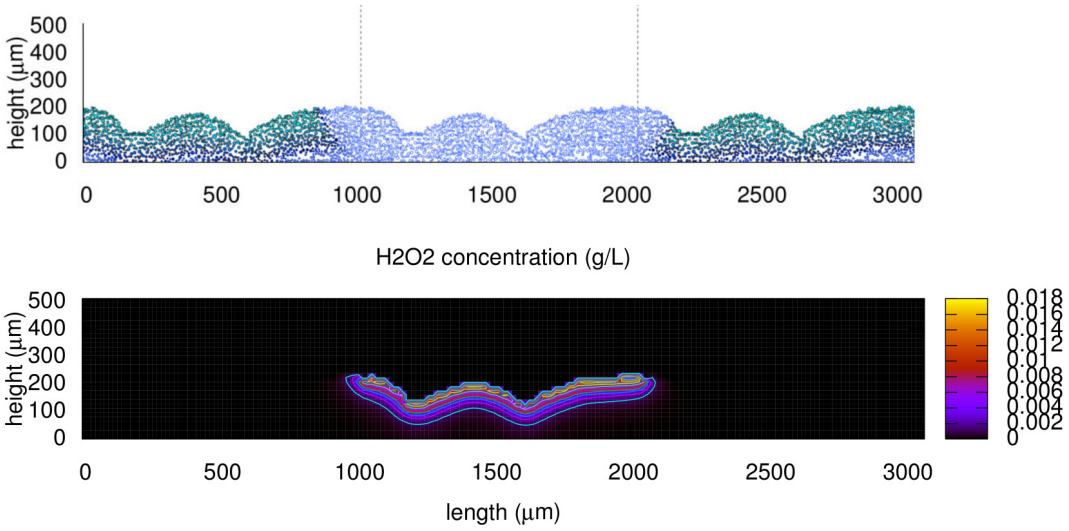

Figure 6.7: Plots of (from top to bottom) the particle distribution and hydrogen peroxide concentration in the biofilm of Simulation 6-2 after one minute of treatment.

3). The figure shows that within a minute, the hydrogen peroxide has penetrated throughout the biofilm in the treated region, killing all the cells there. We note that the hydrogen peroxide is being broken down by catalase reactions in both the live and the dead cells: this acts as a barrier for significant spread into the areas away from the plasma jet zone. Consequently, a near steady-state is reached after about a minute (Figure 6.6), without the protection of EPS, the number of cells killed has approximately doubled.

Figure 6.11 shows the particle distribution and hydrogen peroxide concentration in the mature 10-day old biofilm (Simulation 6-4) after six minutes of treatment. Because of the more uneven shape of the biofilm compared to the younger ones, the mature biofilms have a greater surface area to volume ratio, enhancing penetration of the plasma species. The number of cells killed in a mature biofilm is about 50% more than that in a younger one (Figure 6.6). The simulated biofilm strain forms a live layer near the surface and is unable to survive in the more protected region within the biofilm, consequently, the biofilm will be vulnerable to this form of treatment.

Figures 6.12–6.14 show the effect of hydrogen peroxide for Simulations 6-5, 6-6, and 6-7, respectively, in which the plasma is applied to biofilms with the nutrient source at the substratum. We observe that hydrogen peroxide penetrates deeper in a mature biofilm (Figure 6.13) than an immature one (Figure 6.12) since the EPS concentration is higher at the surface of an immature biofilm than in a mature one. However, the band of dead particles at the surface of a mature biofilm reacts and depletes most of the hydrogen peroxide before it reaches the live cell layer. Thus, a mature biofilm is more resistant than an immature one to the treatment. In the high flux case, the hydrogen peroxide penetrates further into the mature biofilm and causes further damage to the biofilm (Figure 6.14). However, most of the particles affected by the hydrogen peroxide had a low activity level or were dead. Hence, the survival rate of Simulation 6-7 after six minutes of hydrogen peroxide exposure is slightly higher than in Simulation 6-5 (Figure 6.15). We note, as expected, that the highest survival rate occurs in Simulation 6-6, which is the low flux treatment on mature biofilm.

In the simulation results shown in Figures 6.16–6.18, cold plasma treatment on a two-species biofilm is investigated. The plasma treatment is applied to the four-

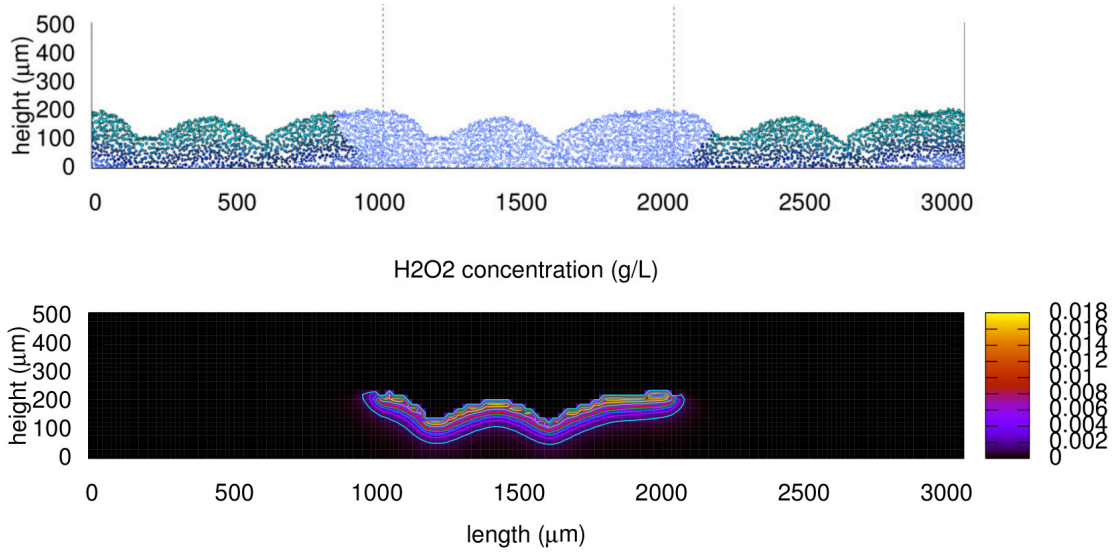

Figure 6.8: Plots of (from top to bottom) the particle distribution and hydrogen peroxide concentration in the biofilm of Simulation 6-2 after six minutes of treatment.

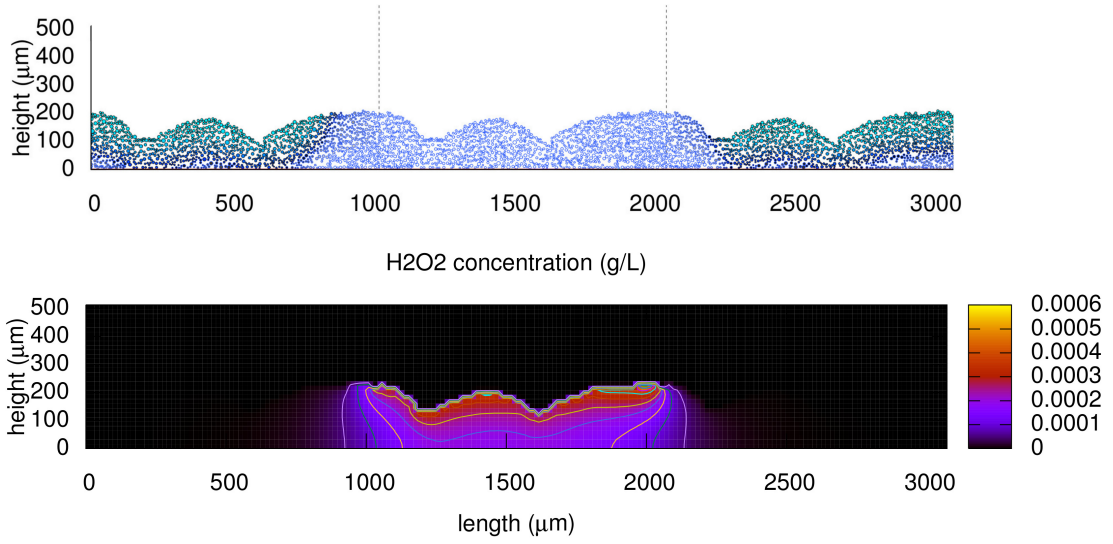

Figure 6.9: Plots of (from top to bottom) the particle distribution and hydrogen peroxide concentration in the biofilm of Simulation 6-3 after one minute of treatment.

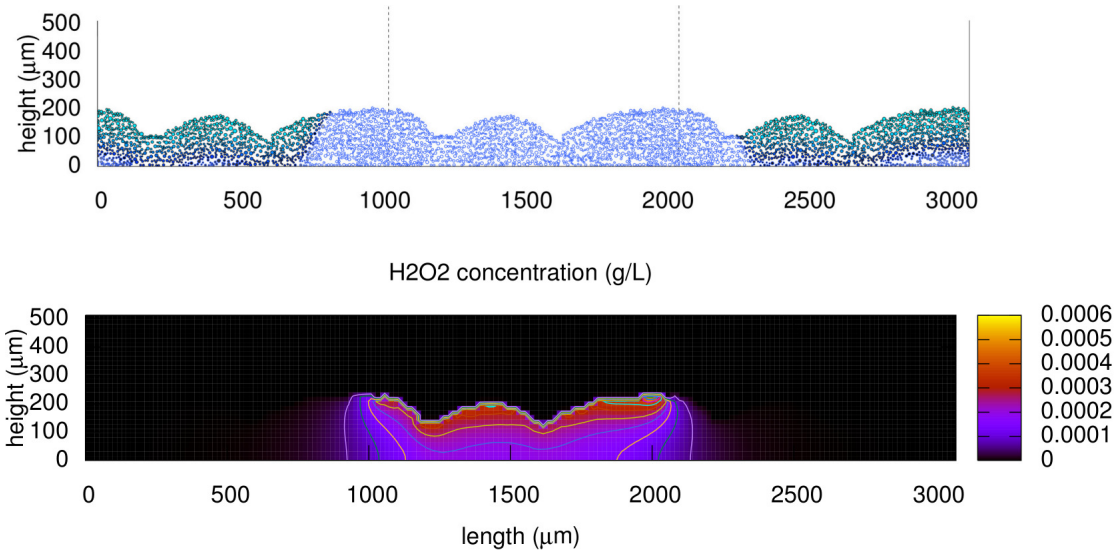

Figure 6.10: Plots of (from top to bottom) the particle distribution and hydrogen peroxide concentration in the biofilm of Simulation 6-3 after six minutes of treatment.

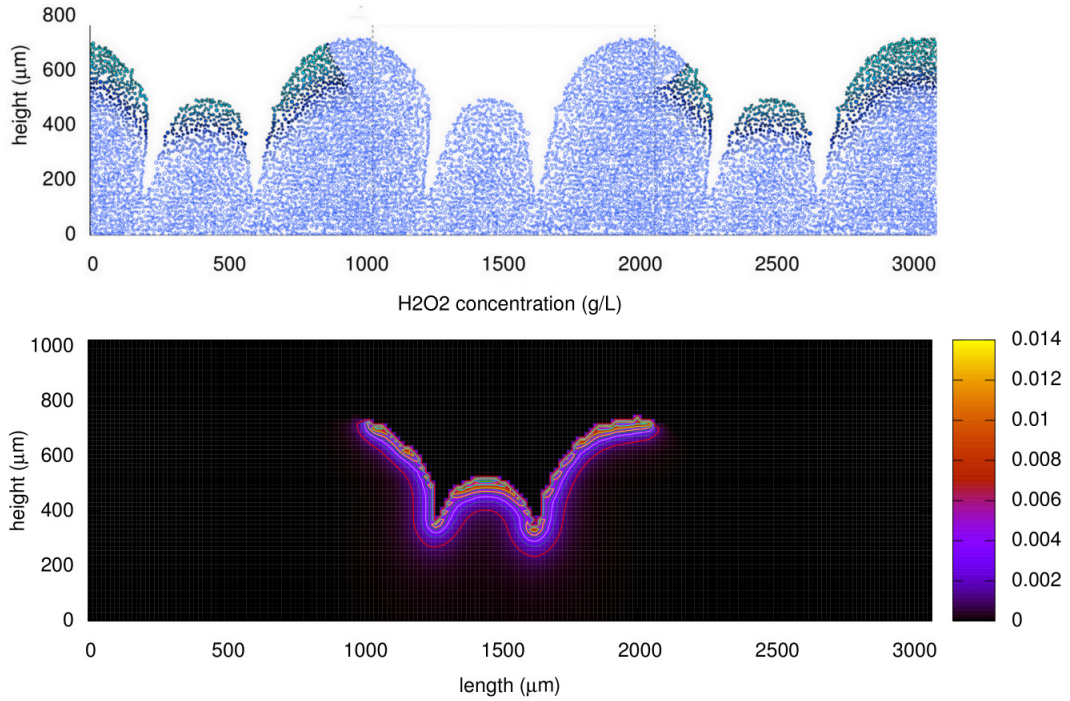

Figure 6.11: Plots of (from top to bottom) the particle distribution and hydrogen peroxide concentration in the biofilm of Simulation 6-4 after six minutes of treatment.

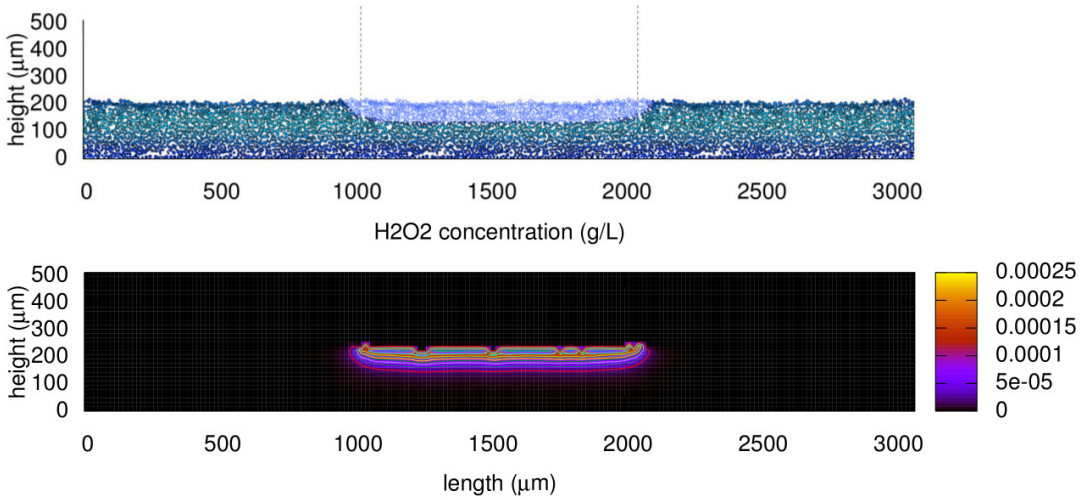

Figure 6.12: Plots of (from top to bottom) the particle distribution and hydrogen peroxide concentration in the biofilm of Simulation 6-5 after six minutes of treatment.

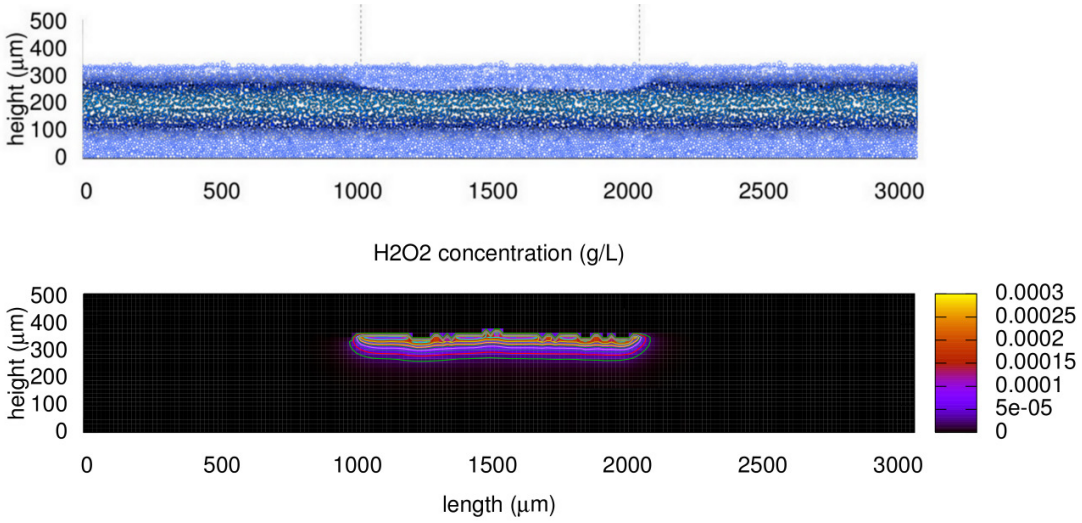

Figure 6.13: Plots of (from top to bottom) the particle distribution and hydrogen peroxide concentration in the biofilm of Simulation 6-6 after six minutes of treatment.

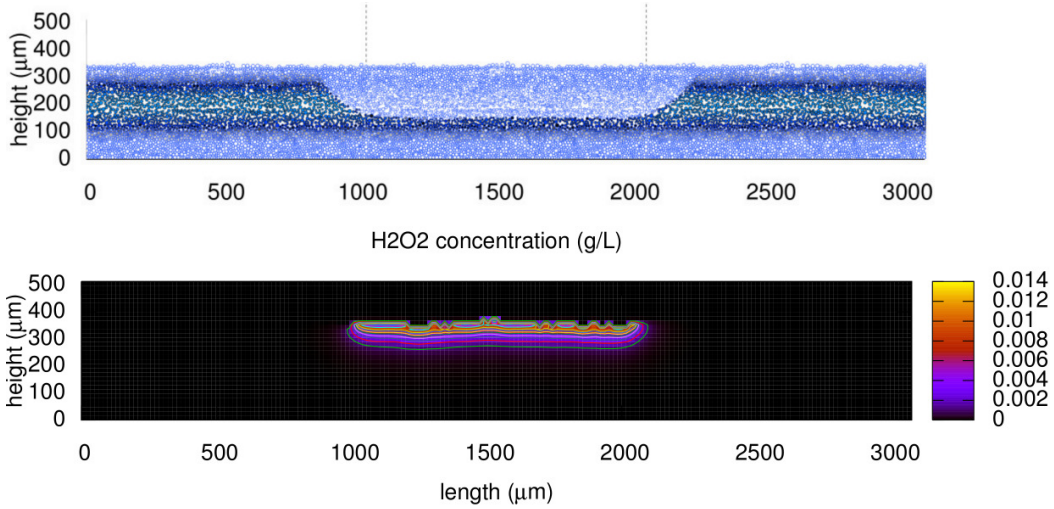

Figure 6.14: Plots of (from top to bottom) the particle distribution and hydrogen peroxide concentration in the biofilm of Simulation 6-7 after six minutes of treatment.

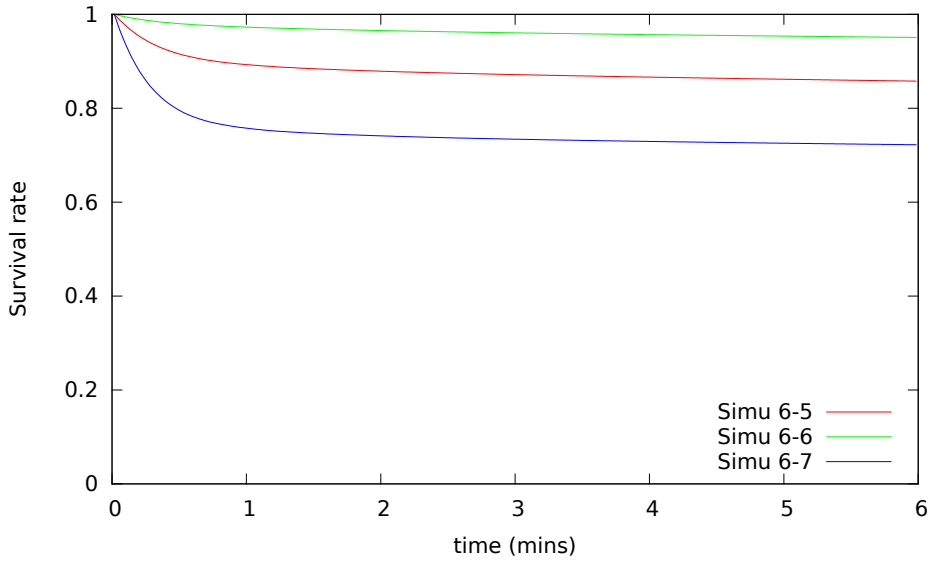

Figure 6.15: Plots of the survival rate throughout six minutes of hydrogen peroxide treatment simulations 6-5 to 6-7.

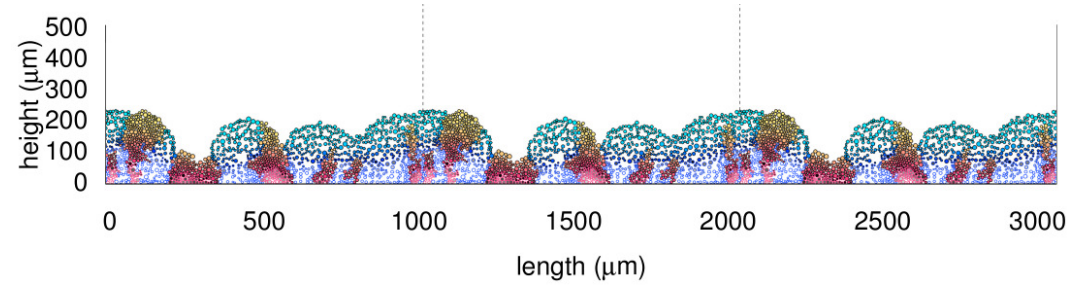

(a)

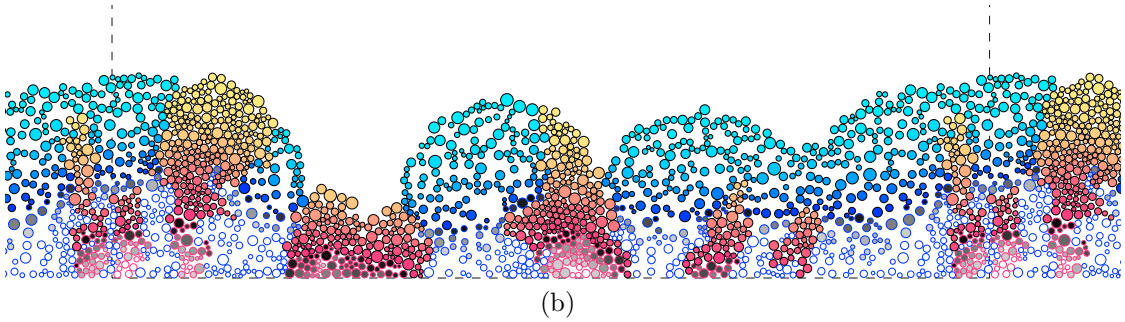

(b)

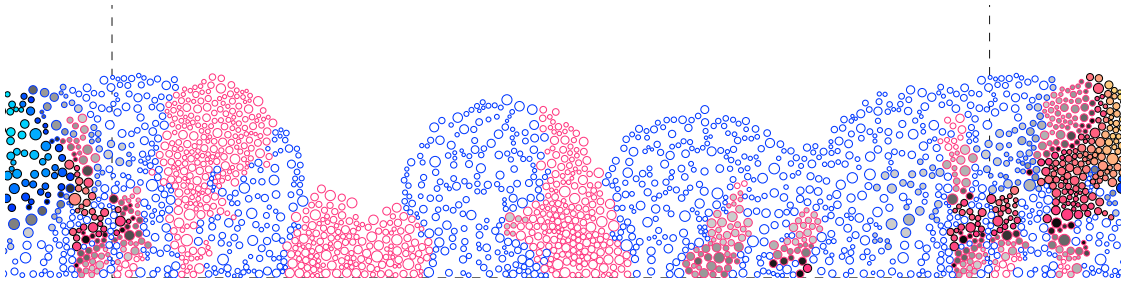

(c)

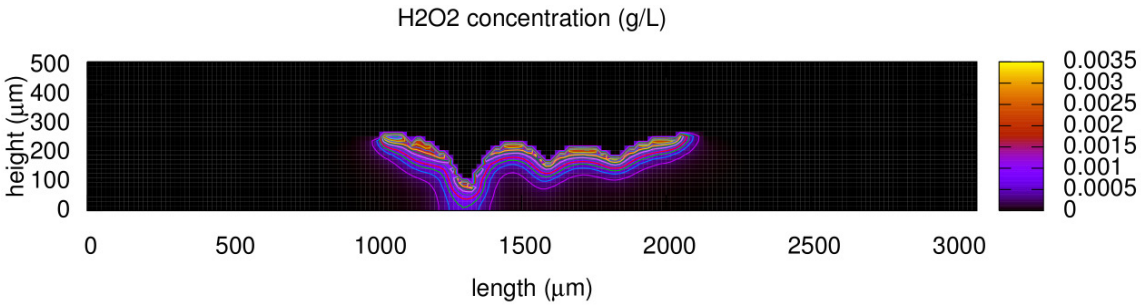

(d)

Figure 6.16: Plots of (a) the particle distributions of 4-day old two-species biofilms before plasma treatment, (b) a closer look at the biofilm before the cold plasma treatment, (c) the particle distribution and (d) the hydrogen peroxide concentration in the biofilm after one minute of treatment. The region of the plasma jet is between the two dashed lines.

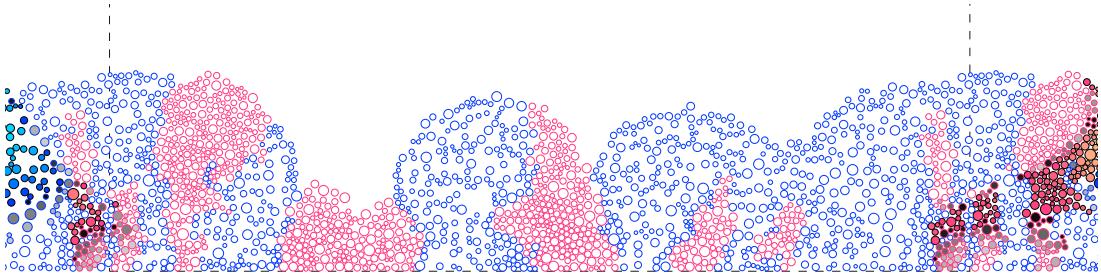

(a)

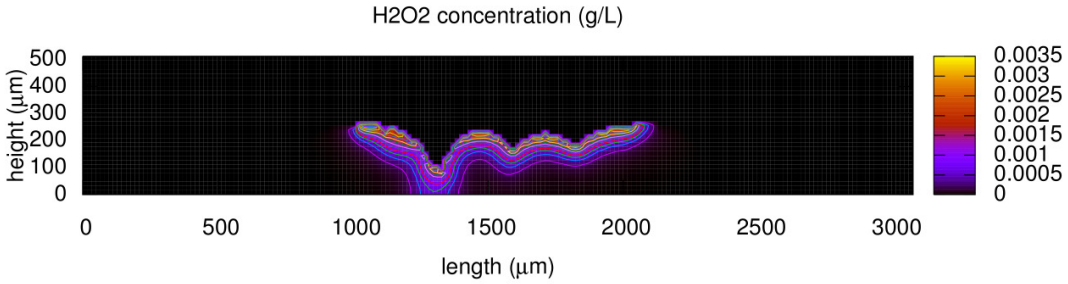

(b)

Figure 6.17: Plots of (a) a closer look at the particle distributions in the plasma treatment region, and (b) hydrogen peroxide concentration in the biofilm after six minutes of the cold plasma treatment.

day old biofilm of Simulation 4-1 (see Figures 6.16a and 6.16b) for six minutes. After one minute of treatment, we observe that hydrogen peroxide is limited in its penetration in regions predominantly occupied by EPS-producing cells, while it penetrates fully through the regions occupied by the PHB-producing strain, demonstrating the vulnerability of cells lacking an EPS barrier. Interestingly, in Figure 6.16c we observe that PHB producers that have been enveloped by EPS-producing strain (e.g., just to the right of the centre in the Figure) are relatively untouched by the treatment. These cells remain relatively unscathed after six minutes, as shown in Figure 6.17.

In Figure 6.18, we have removed the plasma jet after six minutes and allowed the biofilm to grow for a further four days. We note that the particles outside the plasma jet grow and push the dead particles killed by the plasma jet inward to the plasma jet region (see the red circle on the left in Figure 6.18b). The particles which survive the treatment and are embedded in the biofilm in the plasma jet

region recover by regaining nutrients and oxygen. The activity of these particles become even greater than before the treatment (see the red arrow on the right in Figure 6.18b). This figure illustrates the possibility that a biofilm recovering from treatment may be very different from before the treatment.

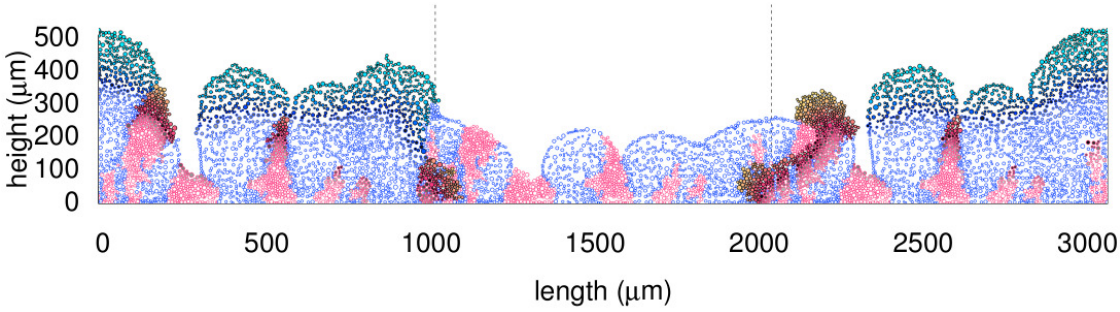

(a)

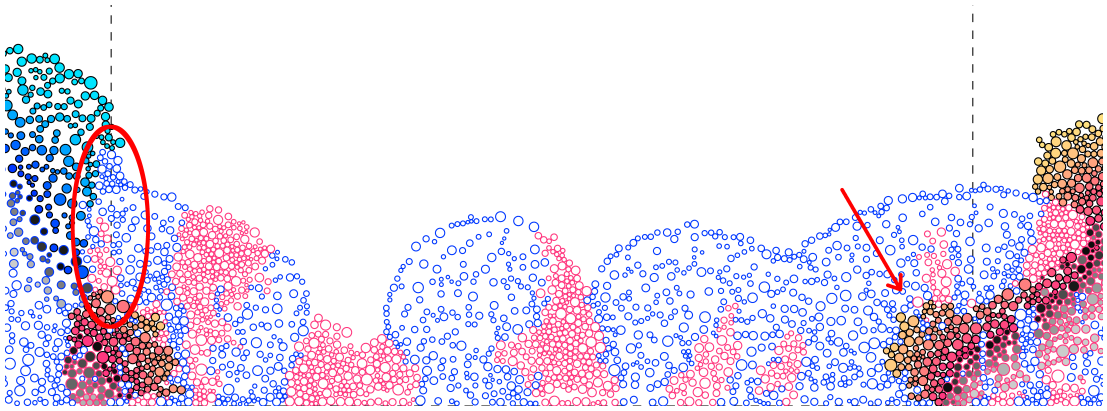

(b)

Figure 6.18: Plots of the particle distributions of (a) the four days growth biofilm and (b) the treatment region zoomed in after the plasma treatment.

6.2.2 Ozone

The effects of 1/10 and 1/500 of ozone flux produced in air by cold plasma jet (obtained from [273]) on various biofilms during six minutes of exposure are discussed and compared with the effects of those of the hydrogen peroxide treatments. The simulations are listed in Table 6.3. Simulations 7-1 – 7-7 are essentially repeats of Simulations 6-1 – 6-6, except the ozone has replaced hydrogen peroxide using the parameters listed in Table 6 in Appendix A.

Table 6.3: Simulations of the biofilm treatment by Ozone.

	topical source		basal source
Low flux*	Immature [a] (Simulation 7-1)	Immature [a] no EPS effect (Simulation 7-3)	Immature [b] (Simulation 7-5)
			Mature [d] (Simulation 7-6)
High flux*	Immature [a] (Simulation 7-2)	Mature [c] (Simulation 7-4)	Mature [d] (Simulation 7-7)

* 1/10 of ozone flux produced in air by cold plasma jet.
* 1/500 of ozone flux produced in air by cold plasma jet.
[a] 3-day old biofilm from Simulation 1-2.
[b] 3-day old biofilm from Simulation 3-1.
[c] 10-day old biofilm from Simulation 1-2.
[d] 10-day old biofilm from Simulation 3-1.

Figures 6.19 and 6.20 show the particle distributions, ozone concentrations, and the EPS, oxygen and nutrient concentrations in the three-day old biofilm after six minutes of ozone treatment from Simulation 7-1. We observe that a low flux of ozone is able to penetrate 150 μm into the biofilm, resulting in most particle death in the plasma jet zone. The treatment also has made some impact on particles outside the treated region. Similar to the hydrogen peroxide simulations, the oxygen and nutrient concentrations in the plasma jet region are notably increased over those in the regions outside the treatment zone, being able to penetrate through the dead cell regions without being consumed. Furthermore, the oxygen concentration is also increased by decomposition of the ozone. However, the ozone flux has little effect on the EPS in the biofilm.

The distribution of particles and ozone distribution after six minutes of ozone treatment for Simulation 7-2 are shown in Figure 6.21, which shows that the ozone at the high flux level can fully penetrate the biofilm and kill particles in the plasma jet region. Furthermore, toxic levels of ozone can penetrate 200 μm into the neighbouring regions away from the jet. We can see in Figure 6.22 that higher ozone flux treatment kills more particles than the lower flux treatment. These figures are very similar to those in Figures 6.19 and 6.21, but it is interesting

to note from Figure 6.22 that most cell death occurs in the first 30 seconds for ozone, as opposed to one minute for hydrogen peroxide.

The importance of an EPS's acting as a barrier to treatment is demonstrated in Figure 6.23. Here, significant quantities of ozone have penetrated to the bottom of the biofilm, as well as outside the treatment region, and killed all the bacteria there. This, again, occurring mainly in the first 30 seconds of treatment (Figure 6.22). Furthermore, without the protection of the EPS, the ozone has killed approximately twice as many cells as in Simulation 7-1.

Figures 6.11 and 6.24 show that hydrogen peroxide and ozone, given the fluxes applied, lead to similar results. As before, the particles within the larger towers are more resistant than those in the smaller ones, in which nearly all cells have been killed off after about 30 seconds (Figure 6.22).

Figures 6.25 to 6.27 show the particle distribution and ozone concentration after six minutes of plasma treatment on the basal nutrient sourced biofilm in Simulation 7-5, 7-6, and 7-7, respectively. In Simulations 7-5 and 7-6, the ozone molecules both penetrate into the biofilms about 150 μm deep, as well as diffuse out of the plasma treatment region, and cause particle death. However, the mature (10-day old) biofilm is covered by a layer of dead particles, which is about 50 μm thick, resulting in less particles' being killed by the ozone molecules in a mature biofilm than in a young biofilm (Figure 6.28). Increasing the ozone dose in the plasma treatment, we observe that, unsurprisingly, the ozone molecules penetrate further into the biofilm. However, the ozone is still unable to penetrate all the way through the biofilm and reach the bottom, yet the penetration depth is enough to pass through the layer of live particles. Consequently, the particles at the treated region are all dead (Figure 6.27).

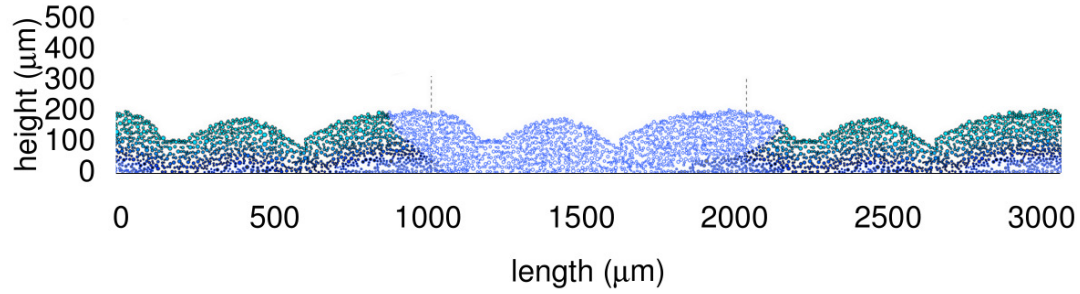

(a)

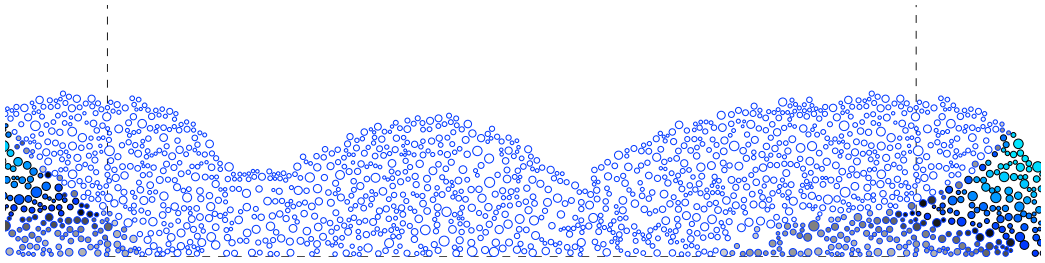

(b)

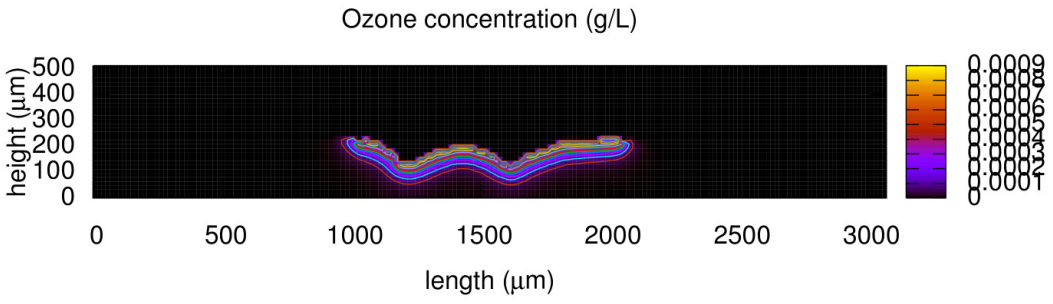

(c)

Figure 6.19: Plots of (a) the particle distribution, (b) a closer look at the plasma jet region, and (c) the ozone concentrations in the 3-day old biofilm after six minutes of treatment in Simulation 7-1. The region of plasma jet is between the two dashed lines.

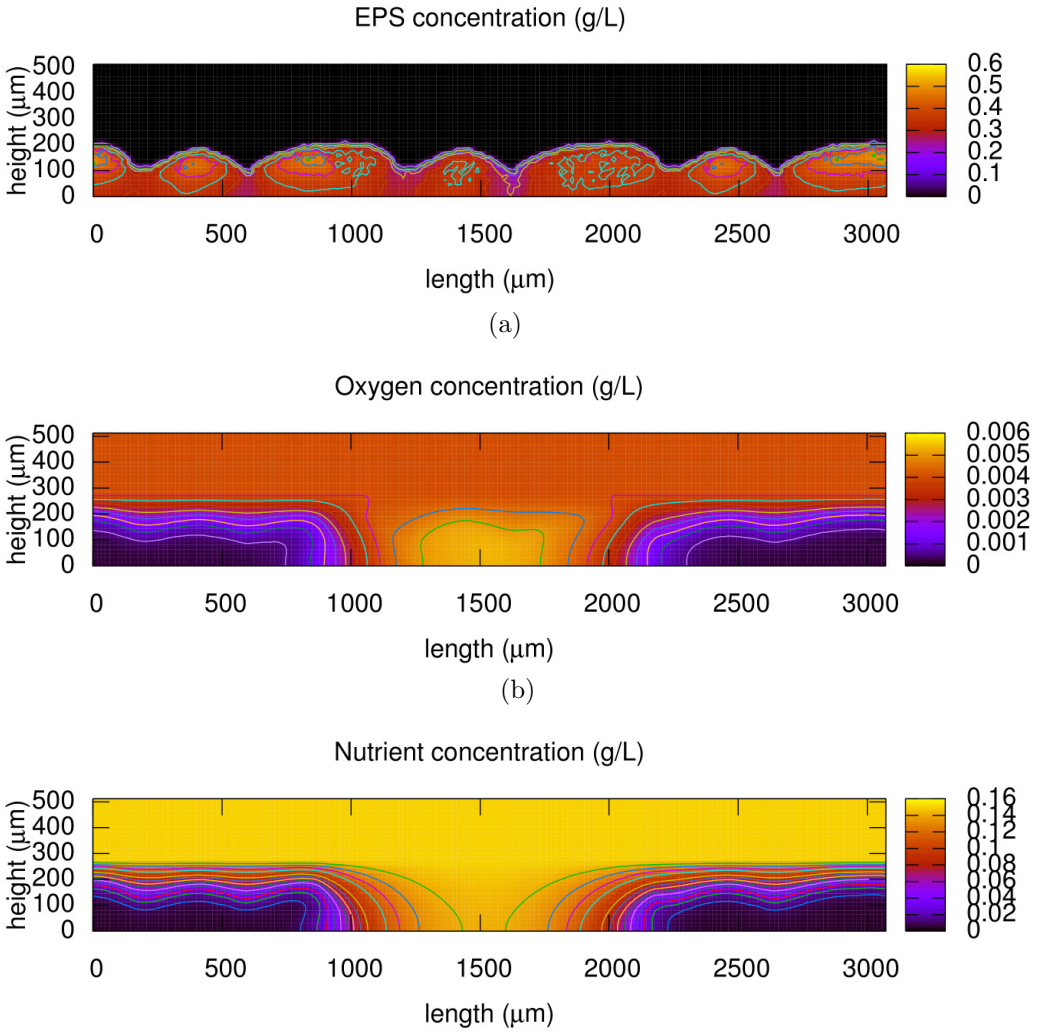

Figure 6.20: Plots of (a) EPS, (b) oxygen and (c) nutrient concentrations in the 3-day old biofilm after six minutes of treatment in Simulation 7-1.

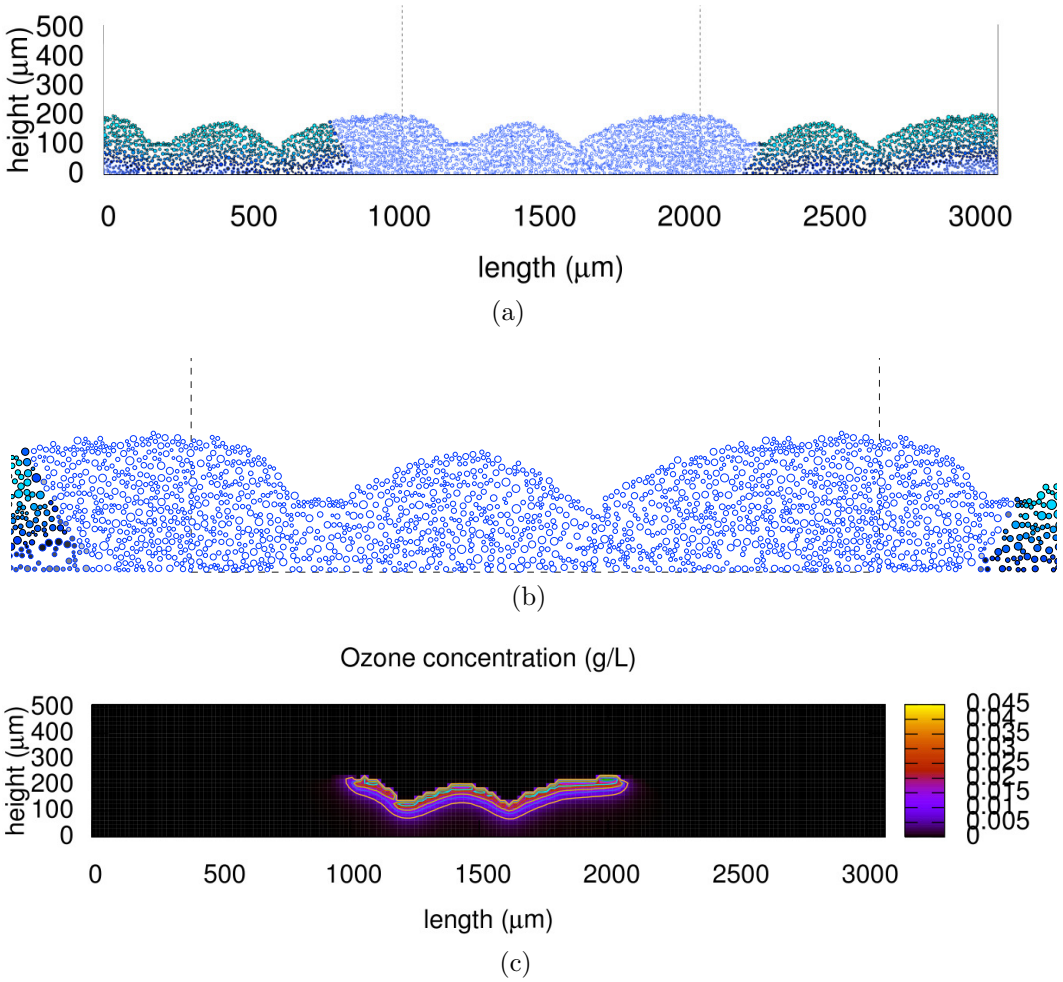

Figure 6.21: Plots of (a) the particle distribution, (b) a closer look at the plasma jet region, and (c) the ozone concentration in the biofilm after six minutes of treatment in Simulation 7-2.

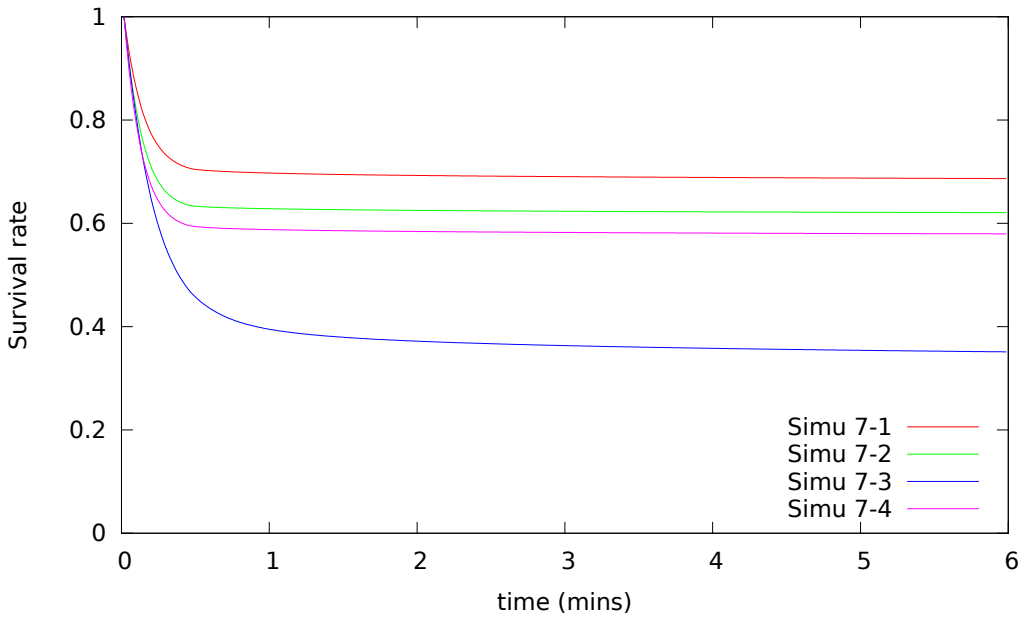

Figure 6.22: Plots of the survival rate throughout six minutes of ozone treatment in Simulations 7-1 to 7-4.

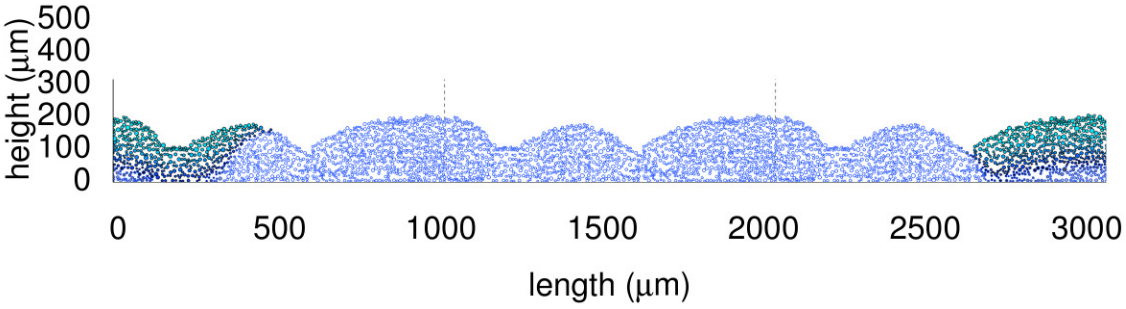

(a)

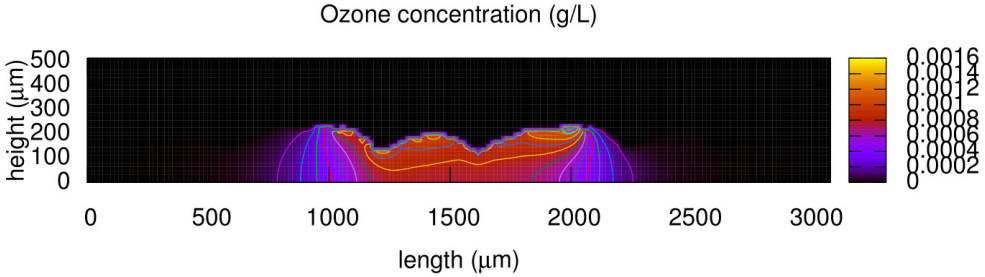

(b)

Figure 6.23: Plots of (a) the particle distribution and (b) the ozone concentration in the biofilm after six minutes of treatment in Simulation 7-3.

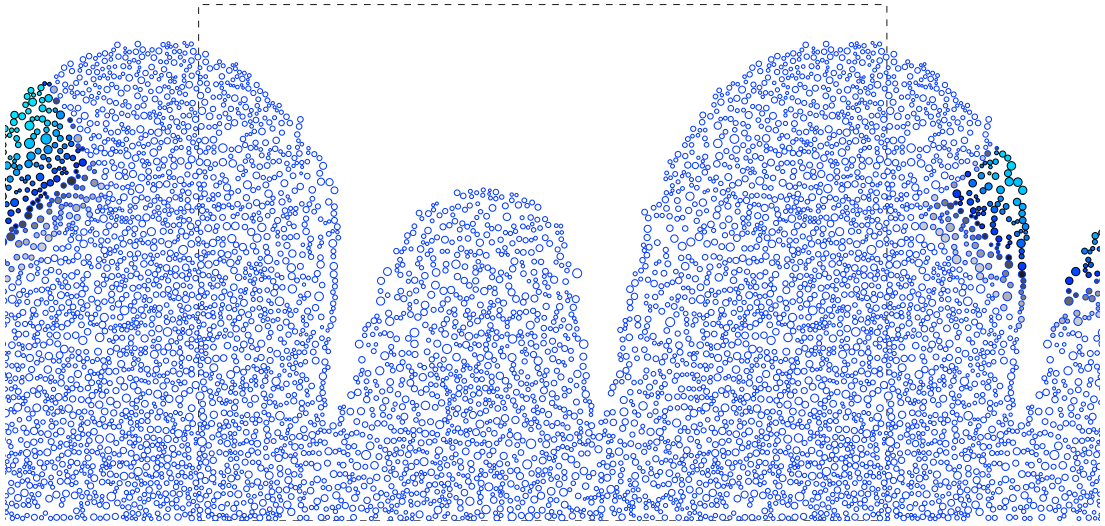

(a)

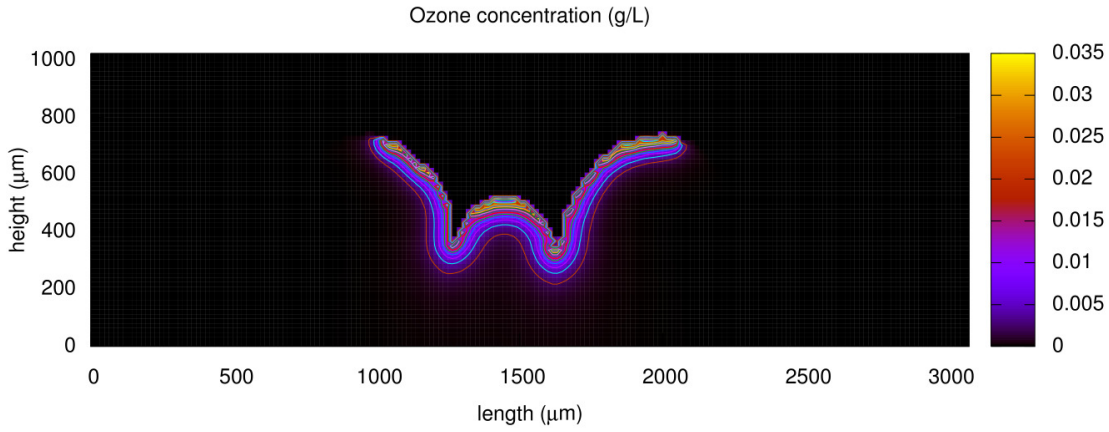

(b)

Figure 6.24: Plots of (a) particle distribution and (b) ozone concentration in the biofilm after six minutes of low flux ozone exposure in Simulation 7-4.

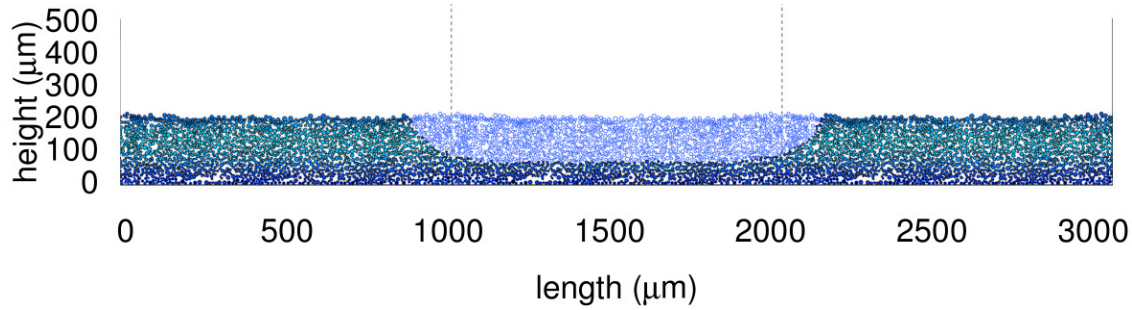

(a)

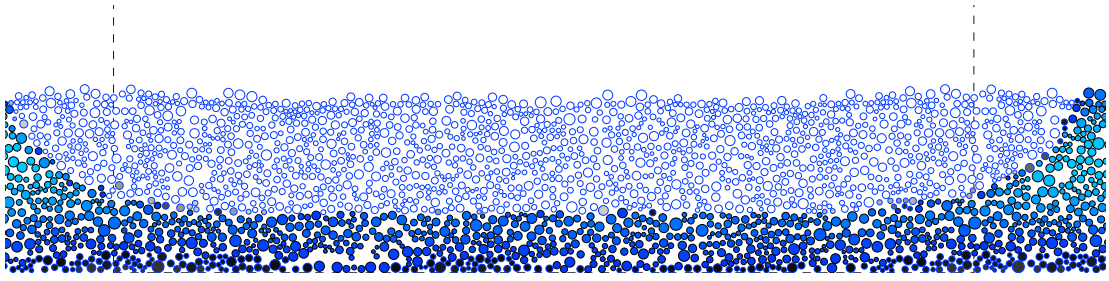

(b)

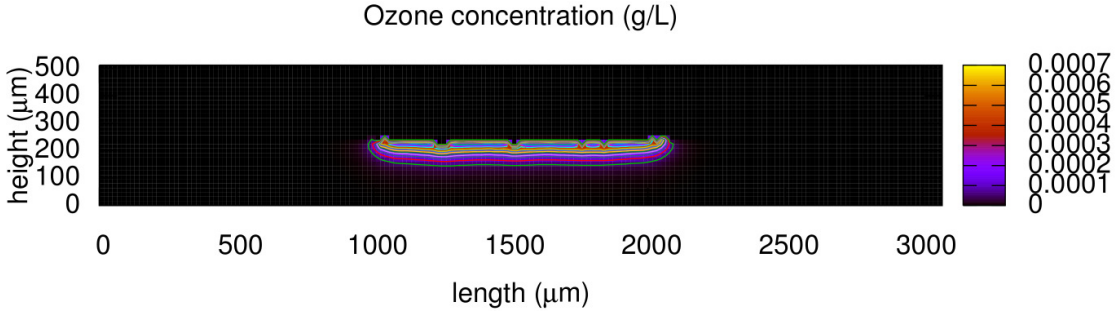

(c)

Figure 6.25: Plots of the (a) particle distributions of the biofilms after six minutes of treatment in Simulation 7-5, (b) a closer look at the plasma jet region, and (c) ozone concentration in the biofilm.

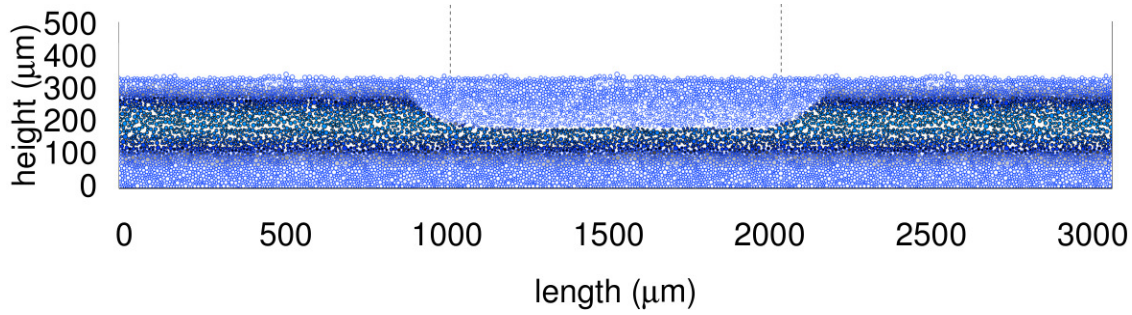

(a)

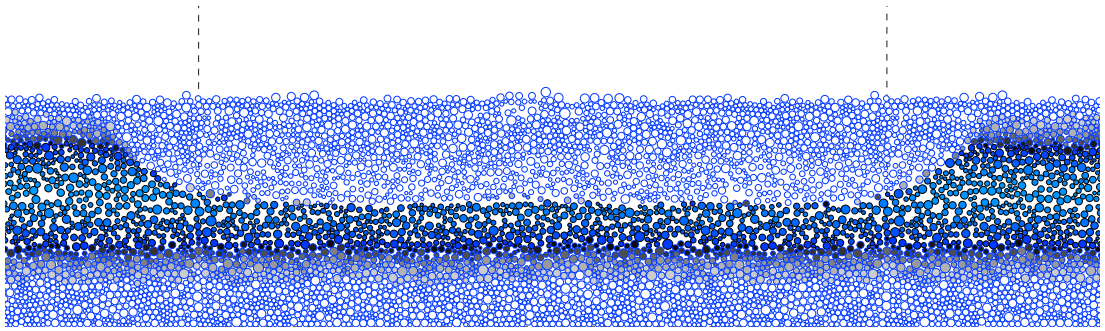

(b)

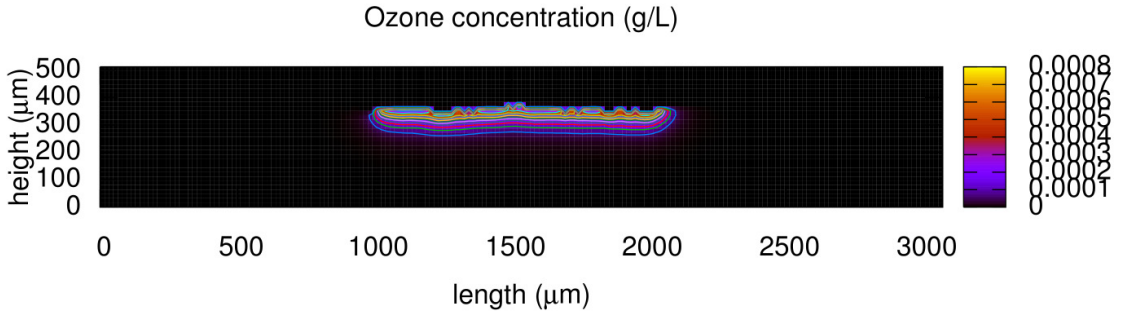

(c)

Figure 6.26: Plots of the (a) particle distributions of the biofilms after six minutes of treatment in Simulation 7-6, (b) a closer look at the plasma jet region, and (c) ozone concentration in the biofilm.

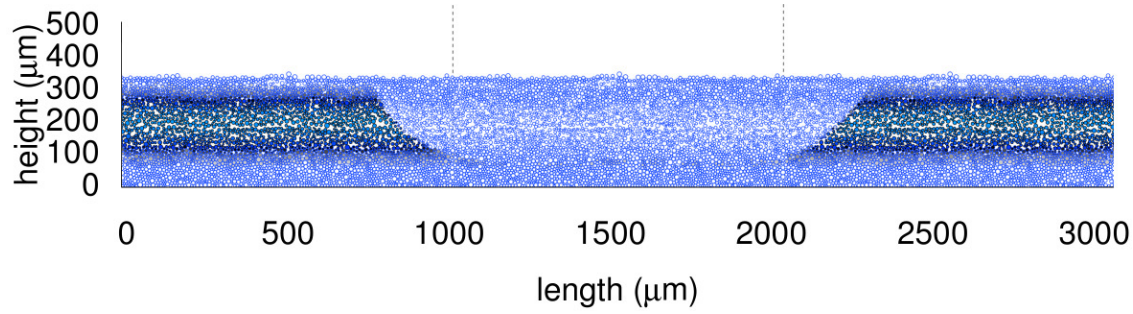

(a)

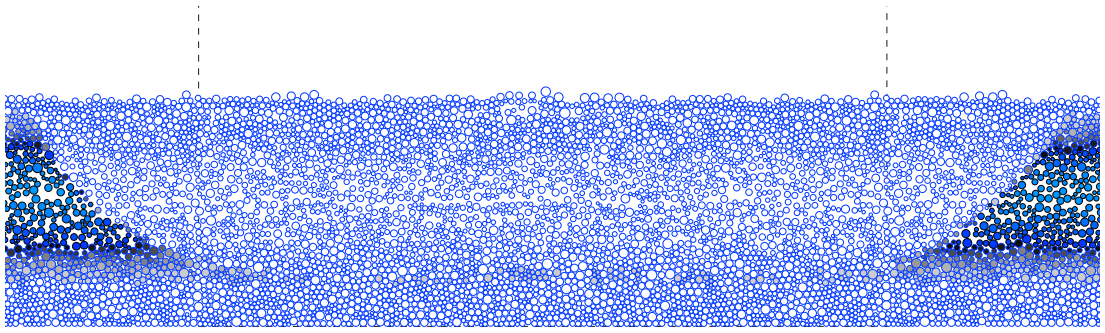

(b)

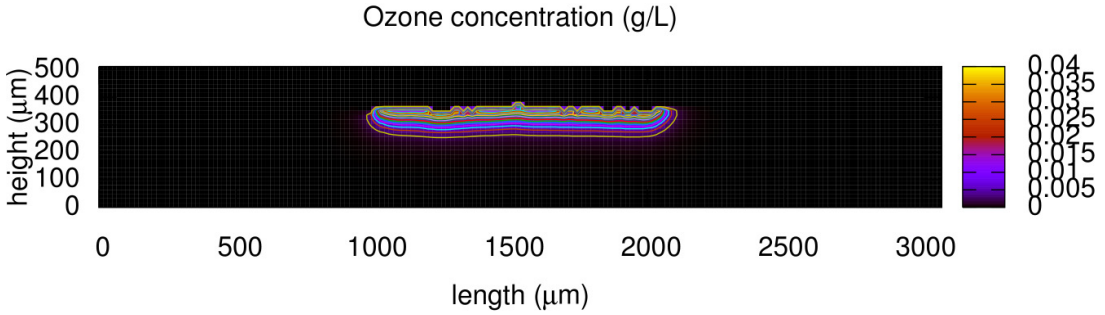

(c)

Figure 6.27: Plots of the (a) particle distributions of the biofilms after six minutes of treatment in Simulation 7-7, (b) a closer look at the plasma jet region, and (c) ozone concentration in the biofilm.

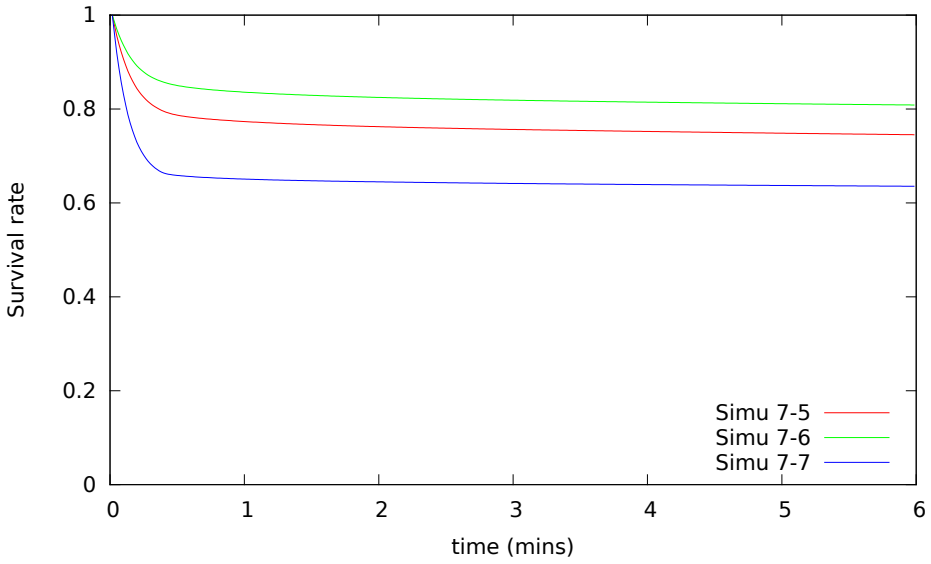

Figure 6.28: Plots of the survival rate throughout six minutes of ozone treatment in Simulations 7-5, 7-6 and 7-7.

6.2.3 pH

The hydrogen ion flux produced by gas–water cold plasma and the decay rate of hydrogen ion by sequester agents are calculated from the experimental data shown in Figure 5.6 (see Section 5.1.1.2). However, the exact hydrogen ion flux into the biofilm during cold plasma treatment and hydrogen ion sequestering capacity in the biofilm are unknown. The aim of this section is to examine the effects of different hydrogen ion fluxes on biofilms which have various acid sequestering capacities. Table 6.4 lists the simulations presented in this section. We note that the immature (3-day old) biofilms are used in Simulation 8-1 to 8-4 and 8-6 to 8-9, and the mature (10-day old) biofilms are used in Simulations 8-5 and 8-10 in order to investigate the impact of biofilm maturity on the resistance to the hydrogen ion treatment. The fluxes of the hydrogen ions are chosen to be 1/10 and 1/500 of the flux we calculated from the experimental data in Section 5.1.1.2. Low sequestering capacity refers biofilms with the same hydrogen ion "sequestering ability" as water, while high sequestering capacity refers to biofilms with 10^3 times more sequestering capacity than water. The parameters used in this section are listed in Table 7, Appendix A.

Table 6.4: Simulations of biofilm treatment by hydrogen ions.

	topical source		basal source	
Sequestering capacity	High $^{\mp}$	Low $^{\pm}$	High $^{\mp}$	Low $^{\pm}$
Low flux*	Simulation 8-1 Simulation 8-5 †	Simulation 8-2	Simulation 8-6 Simulation 8-10 ‡	Simulation 8-7
High flux*	Simulation 8-3	Simulation 8-4	Simulation 8-8	Simulation 8-9

$^{\pm}$ Low sequestering capacity refers to biofilms having a capacity no better than that of water.
$^{\mp}$ The decay rate of hydrogen ion concentration by biofilm productions is 10^3 time higher than those with low sequestering capacity.
† 10-day old biofilm from Simulation 1-2.
‡ 10-day old biofilm from Simulation 3-1.
* 1/10 of hydrogen ion flux calculated from experimental data.
* 1/500 of hydrogen ion flux calculated from experimental data.

Figure 6.29 shows the particle distribution after five seconds and six minutes of plasma treatment in Simulation 8-1 (high hydrogen ion sequestering and low input flux). In this case the hydrogen ions penetrate into the biofilm about 100 μm and bring the local environment to a lethal pH value (Figure 6.30), resulting in particle death in the treatment region (Figure 6.29c). We note that the hydrogen ion concentration in the biofilm seems to reach a steady-state after five seconds of the treatment and only has minor effects on the region outside the plasma treatment zone. The concentrations of the nutrient, oxygen, and the EPS in the biofilm after six minutes of treatment are shown in Figure 6.31. The EPS concentration is not significantly affected by the hydrogen ion treatment. However, the nutrient and oxygen concentrations rise in the plasma jet region due to their being able to diffuse through the dead particle layer. Consequently, the particles that survive in the treatment region are well nourished and increase their energy production (Figure 6.32).

Figure 6.33 shows the progress of the disinfection of biofilm particles for the case of low hydrogen ion sequestering (Simulation 8-2), so one expects greater penetration on the part of the hydrogen ions. We observe that the hydrogen ions have nearly no effect on the particles after five seconds of the treatment, although at this stage the pH value in the plasma treatment area has dropped to about

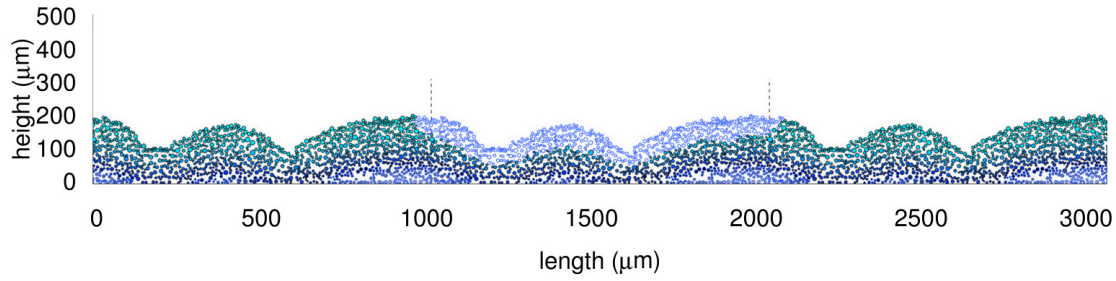

(a)

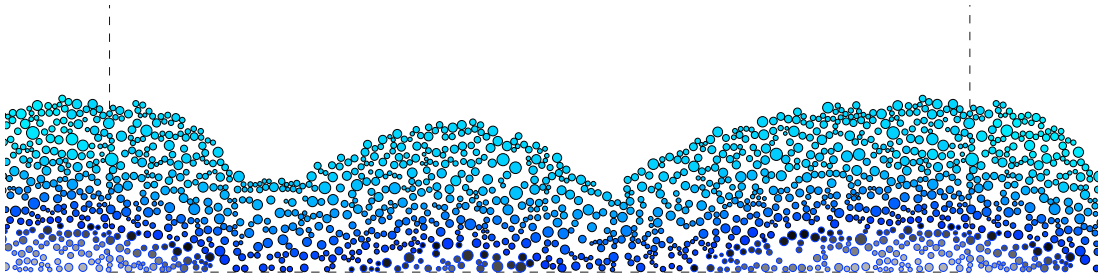

(b)

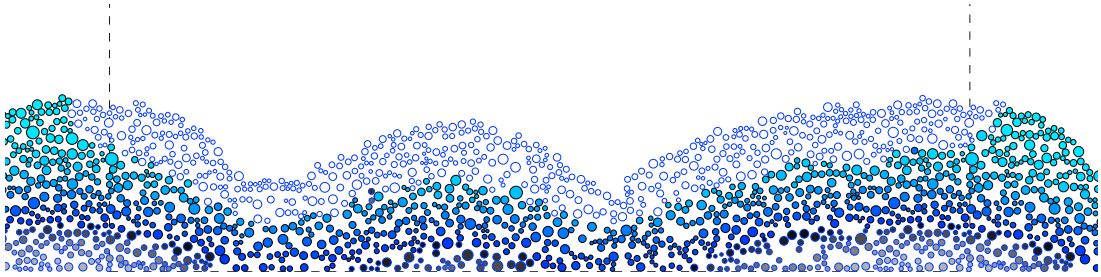

(c)

Figure 6.29: Plots of the particle distribution after (a) six minutes of treatment in Simulation 8-1. (b) and (c) give a closer look at the particle distribution after five seconds and (c) six minutes of treatment.

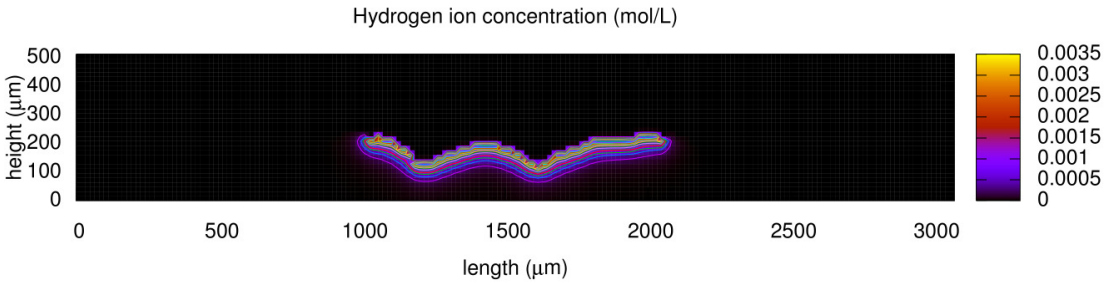

(a)

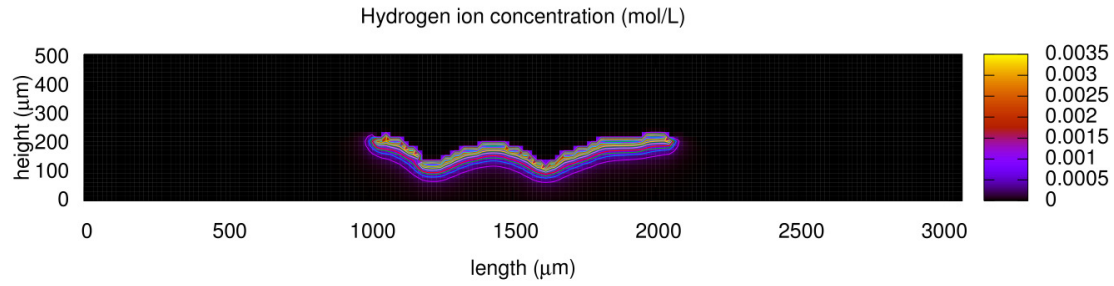

(b)

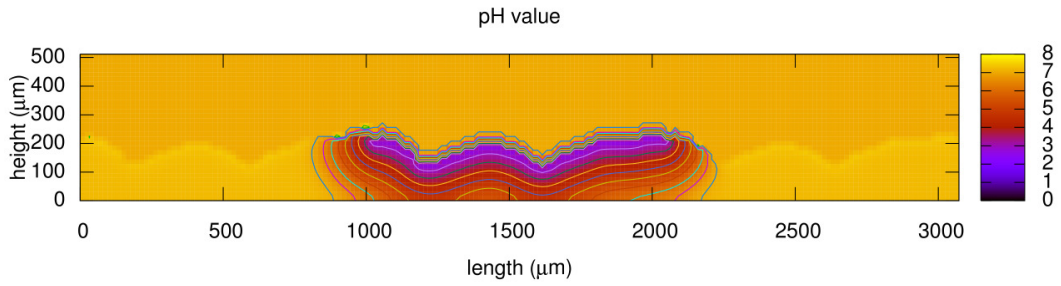

(c)

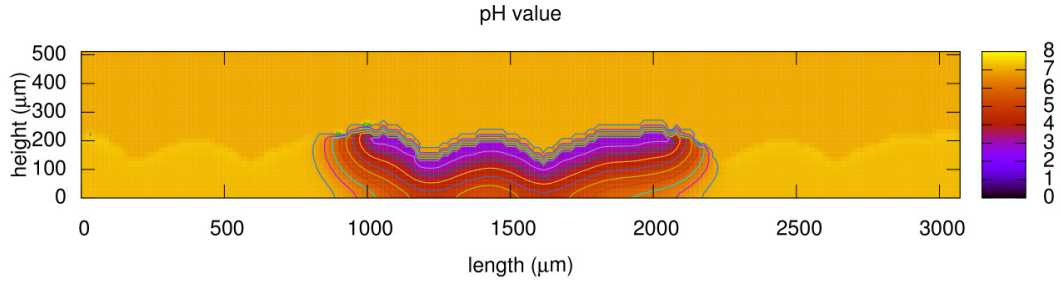

(d)

Figure 6.30: Plots of the hydrogen ion concentration and pH value in the biofilm in Simulation 8-1. (a) and (b) are the concentrations of hydrogen ions after five seconds and after six minutes of treatment, respectively. (c) and (d) are the corresponding pH values.

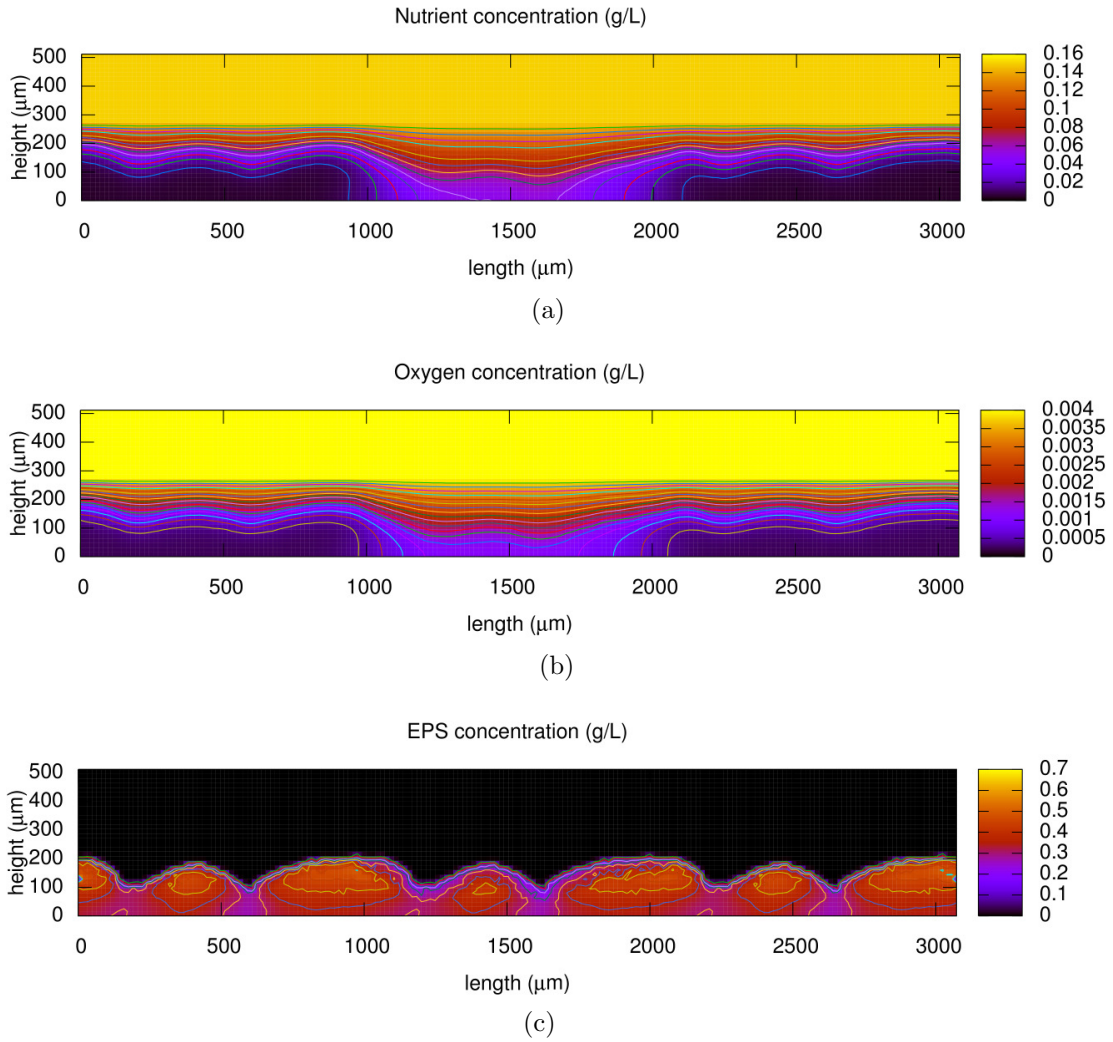

Figure 6.31: Plots of (a) nutrient, (b) oxygen, and (c) EPS concentrations after six minutes of the plasma treatment in Simulation 8-1.

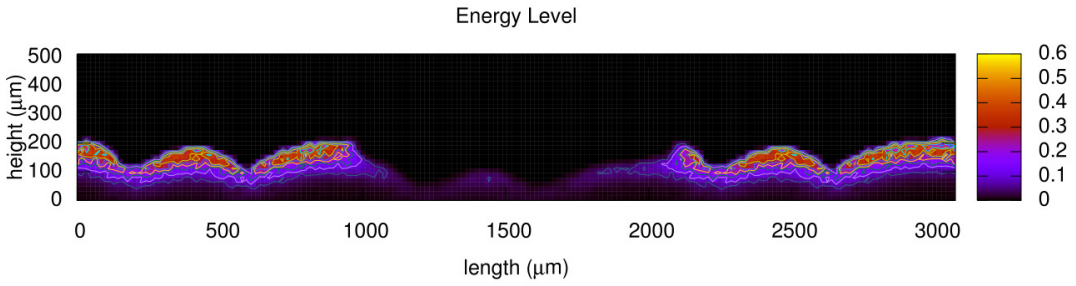

(a)

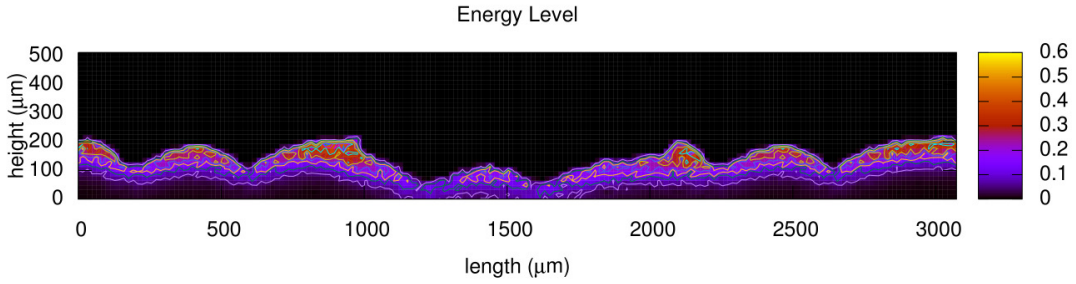

(b)

Figure 6.32: Plots of energy level after (a) five seconds and (b) six minutes of treatment in Simulation 8-1.

2–3 (Figure 6.34a). As for Simulation 8-1, the particles take a little while before dying in response to low pH. As time advances, the cells die, but interestingly, death seems to start near the base of the biofilm and rise up to the top (see Figure 6.33). This is presumably due to the cells' there having less oxygen and nutrients to produce energy, and they are the more vulnerable to the acidity. The hydrogen ions are spread out away from the plasma jet region, and damage particles up to 500 μm away (Figures 6.34c and 6.34d).

The results of Simulation 8-3, which combines high hydrogen ion flux in a biofilm with a high acid sequestering capacity, are shown in Figures 6.35 and 6.36 after six minutes of treatment. Due to the flux of hydrogen ions entering the biofilm being increased, the hydrogen ions penetrate further and cause more damage to the biofilm than in Simulation 8-1. However, due to the high acid sequestering capacity, the hydrogen ion diffusion and penetration are restricted, reaching a near steady-state after five seconds. We further note that lethal levels of acid only extend about 100 μm from the jet zone.

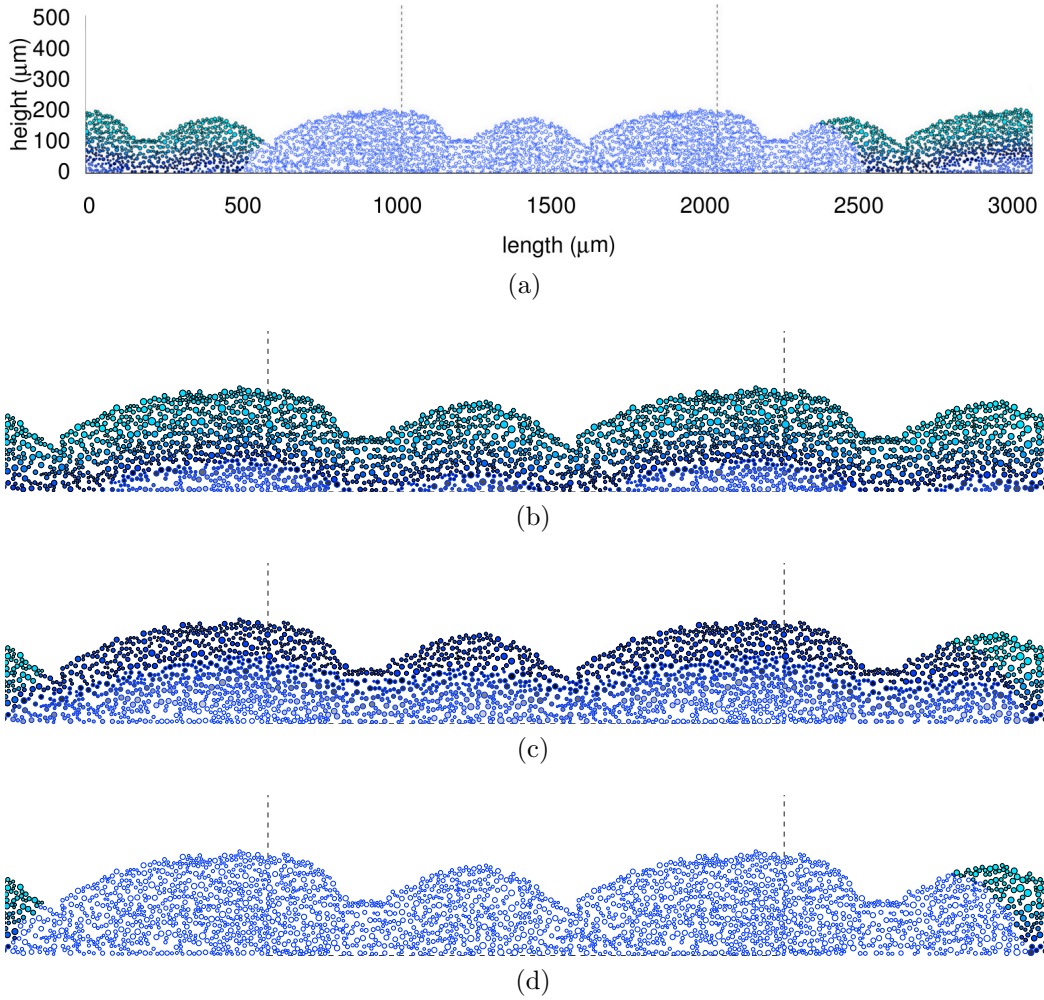

Figure 6.33: Plots of (a) particle distribution after six minutes of the treatment, closer looks at the particle distribution after (b) five seconds, (c) 60 seconds, and (d) six minutes of the treatment in Simulation 8-2.

Figure 6.37 shows the particle distribution and pH value in the biofilm after six minutes of treatment in Simulation 8-4 (high input flux, low sequestering capability). In this case, the hydrogen ions have spread all over the simulated biofilm (Figure 6.37b), killing more than 90% of the particles in three minutes (Figure 6.38). We note from Figure 6.38 that death due to acidity reaches a maximum between 90–120 seconds; this is slower than ozone and hydrogen peroxide.

We also observe from this figure how significant are the flux and acid sequestration in cell killing. In particular, how the bacteria defend themselves against

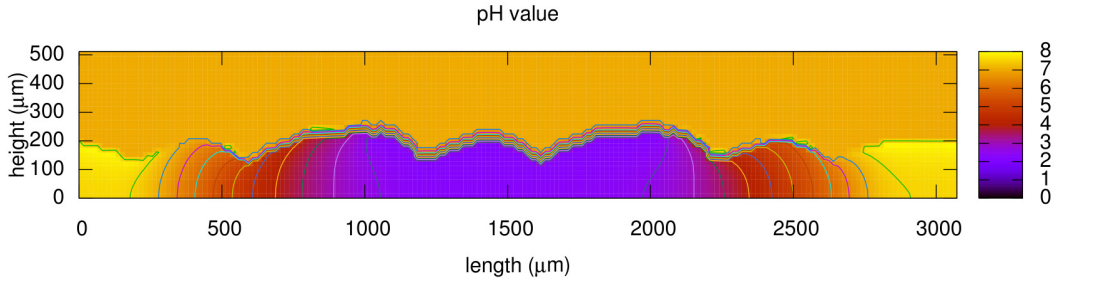

(a)

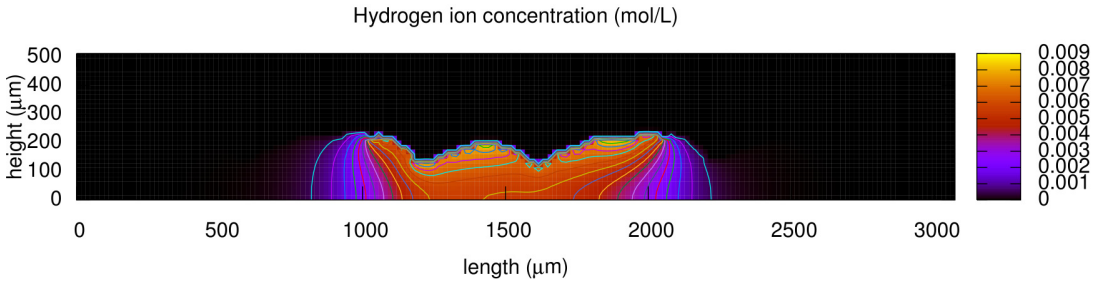

(b)

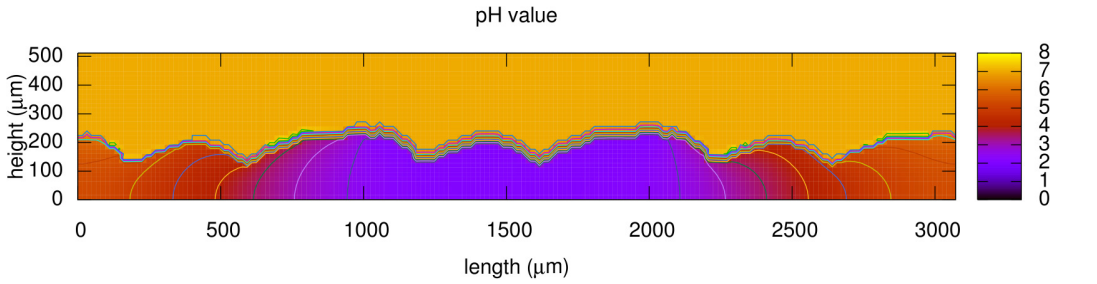

(c)

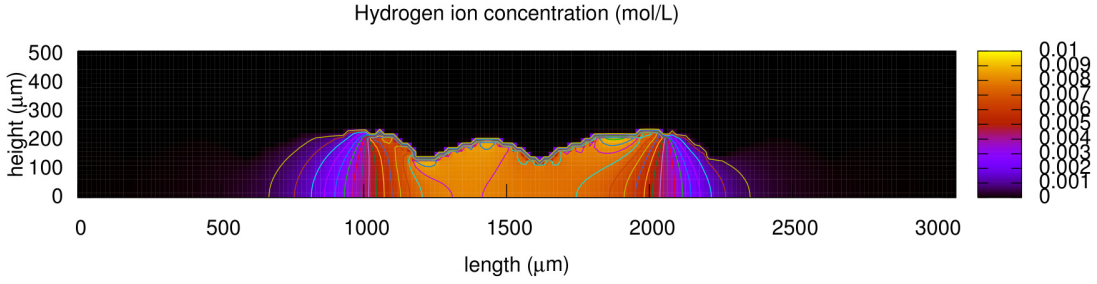

(d)

Figure 6.34: Plots of pH value and hydrogen ion concentration after five seconds and after six minutes of the treatment in Simulation 8-2. (a) pH value after five seconds of treatment. (b) hydrogen ion concentration after five seconds of treatment. (c) pH value after 60 seconds of treatment. (d) hydrogen ion concentration after 60 seconds of treatment.

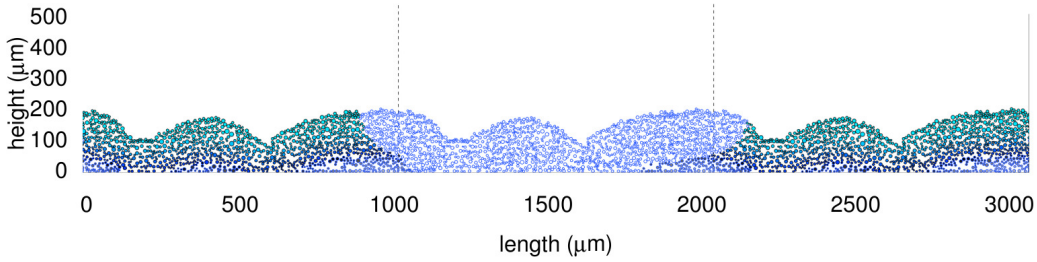

(a)

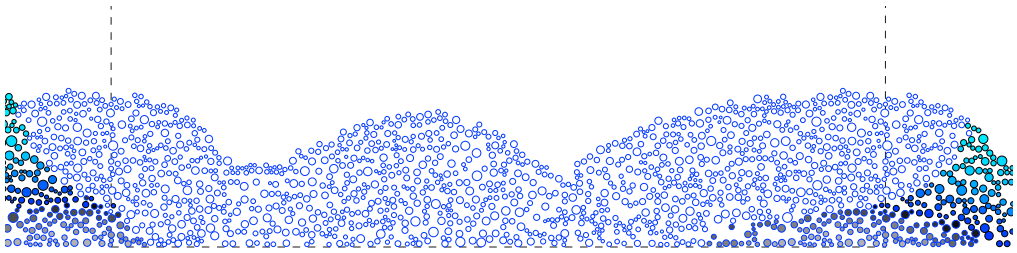

(b)

Figure 6.35: Plots of (a) particle distribution after six minutes of the treatment in Simulation 8-3 and (b) a closer look at the the treatment region.

acidic environments (e.g., using sequestors as buffers) can have a significant impact on the effectiveness of a plasma treatment.

A 10-day old biofilm is used in Simulation 8-5 and the results are compared with those of Simulation 8-1 in order to investigate the effects of the maturity of a biofilm on the effectiveness of the acid treatment. Figures 6.39 and 6.40 show the particle distribution, hydrogen ion concentration, and pH value in the biofilm after six minutes of treatment. The hydrogen ions penetrate part of the biofilm in the plasma jet region and drop the pH value to about 2 at the surface. Consequently, a thin layer of particles die. However, the hydrogen ions are not able to penetrate deeper into the biofilm or diffuse far from the plasma jet region. The killing rate in this case is higher than for the 3-day old biofilm in Simulation 8-1 (Figure 6.38), due to the impact on the surface area of the plasma jet's being slightly larger than in Simulation 8-1, but not really significantly.

Simulations 8-6 to 8-10 are repeats of Simulation 8-1 to 8-5, except the plasma treatment is on the biofilms with basal nutrient sources. Figures 6.41 and 6.42 show the particle distributions and pH value in the biofilm, respectively, in Simulations 8-6 to 8-9. The results of the particle distribution and hydrogen ion

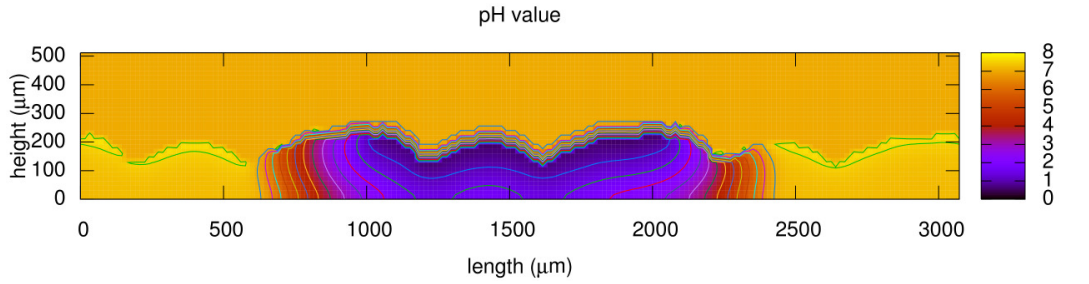

(a)

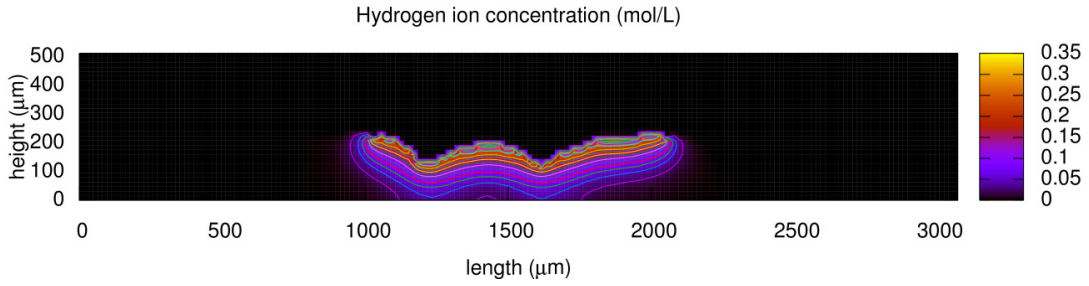

(b)

Figure 6.36: Plots of (a) pH value and (b) hydrogen ion concentration after six minutes of treatment in Simulation 8-3.

penetration caused by the treatment in the basal nutrient source biofilms are similar to the those of the corresponding simulations of the treatment on the topical nutrient source biofilms. However, we note that at the same hydrogen ion flux with the same hydrogen ion degradation conditions, the basal nutrient sourced biofilms are damaged slightly more than the topical nutrient source biofilm (Figure 6.43). This results from the hydrogen ions' being able to spread faster in the former case, since the structure of the biofilms is less rough than that of the latter case. The effects of the plasma treatment on a 10-day old basal nutrient source biofilm are shown in Figure 6.44. Although the hydrogen ions penetrate into the biofilm and decrease the pH value in the plasma jet region, they have not reached the live cell layer to a significant degree, so there is very little death.

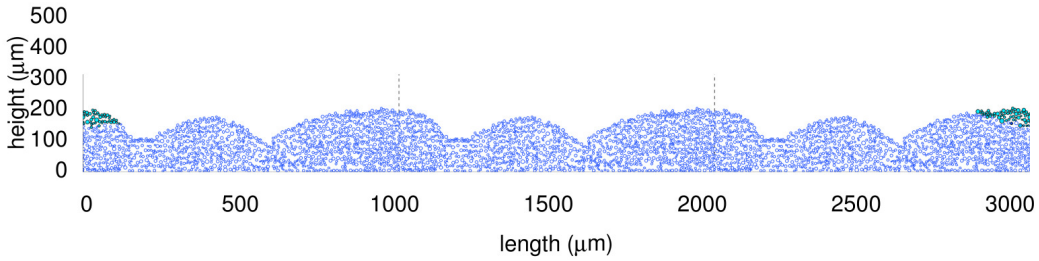

(a)

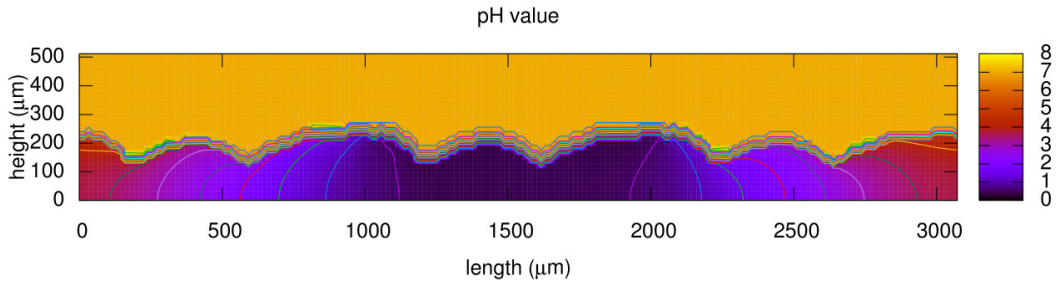

(b)

Figure 6.37: Plots of (a) particle distribution and (b) pH value after six minutes of treatment in Simulation 8-4.

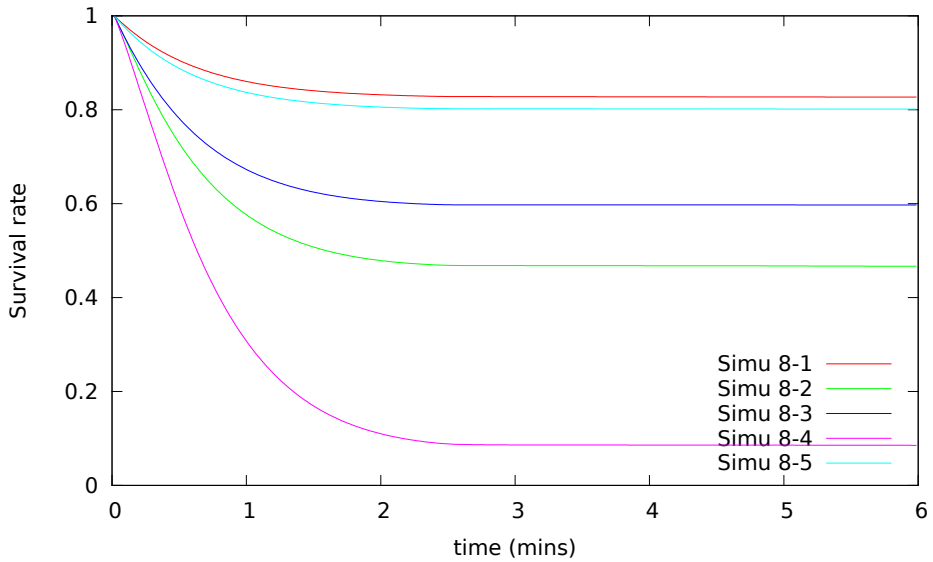

Figure 6.38: Plots of survival rates in Simulation 8-1 to 8-5 throughout six minutes.

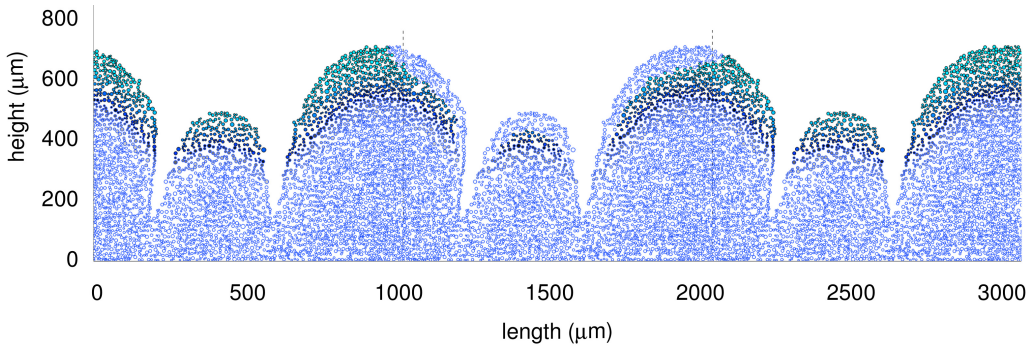

(a)

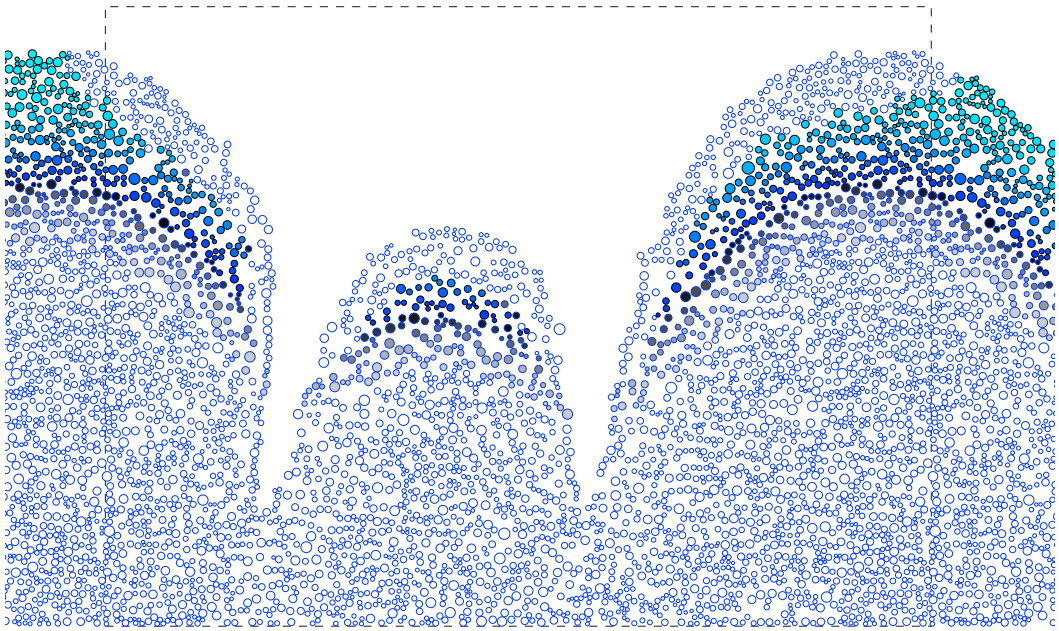

(b)

Figure 6.39: Plots of (a) particle distribution after six minutes of treatment and (b) a closer look at the plasma jet region in Simulation 8-5.

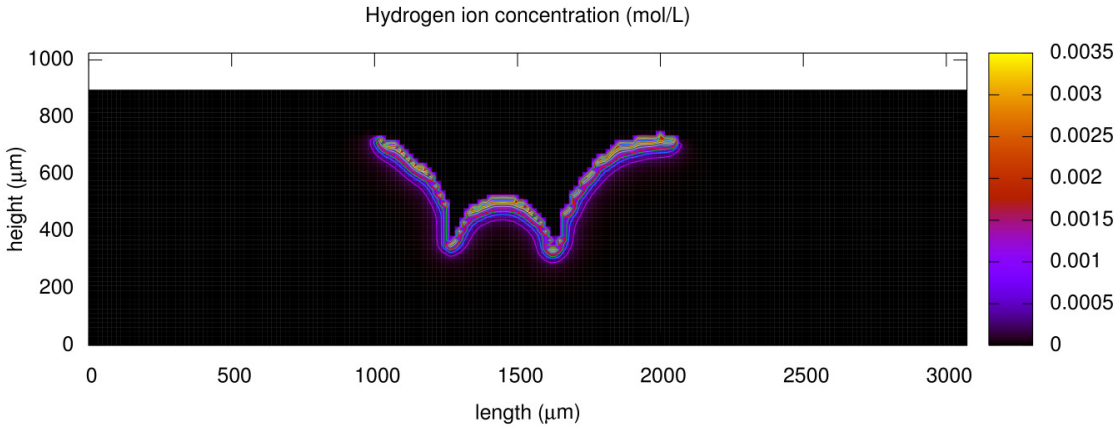

(a)

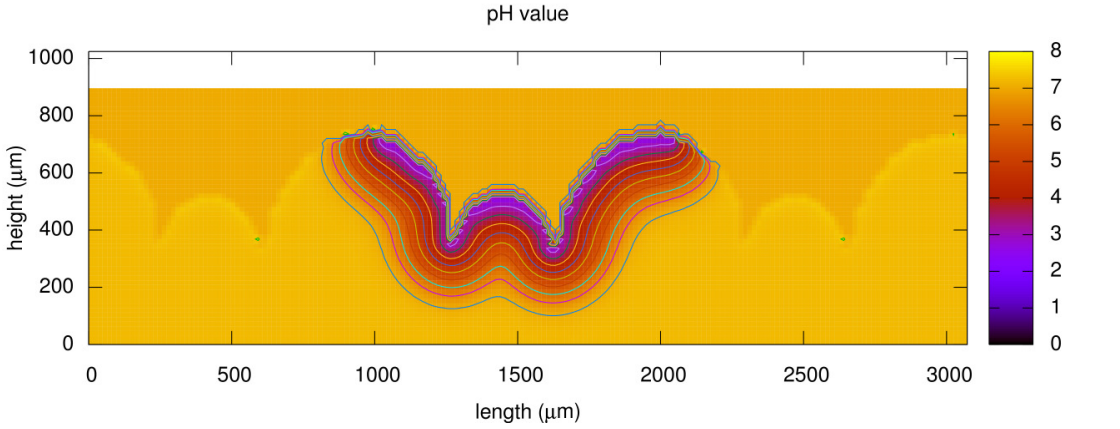

(b)

Figure 6.40: Plots of (a) hydrogen ion concentration and (b) pH value after six minutes of the treatment in Simulation 8-5.

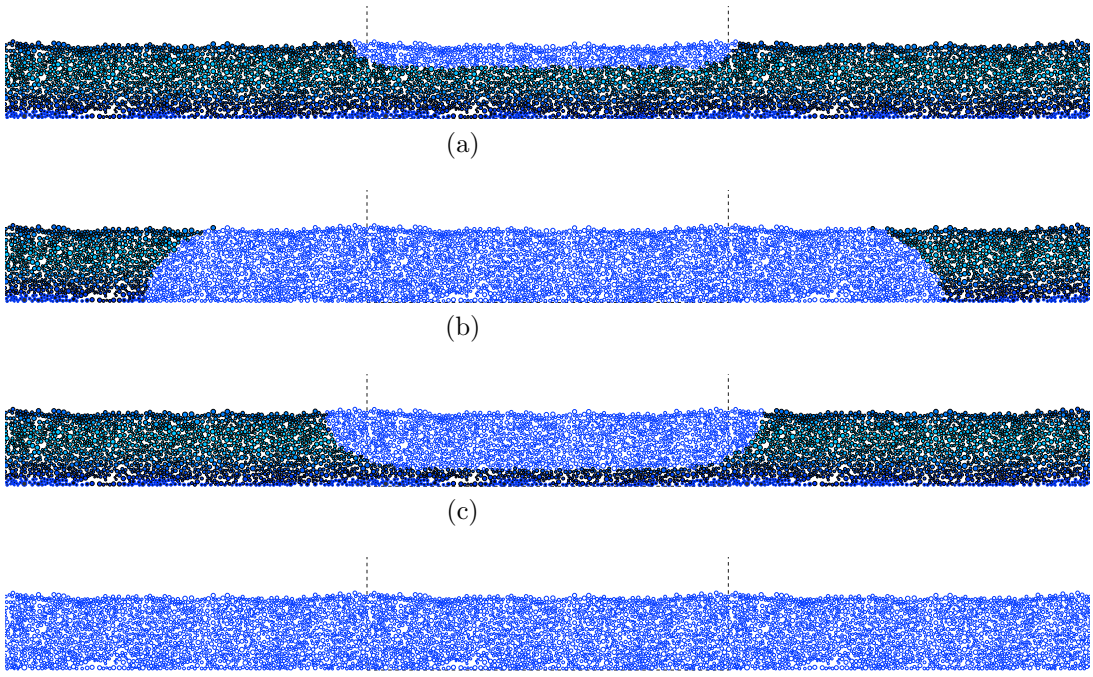

(a)

(b)

(c)

(d)

Figure 6.41: Plots of particle distribution after six minutes of the treatment in Simulations (a) 8-6, (b) 8-7, (c) 8-8 and (d) 8-9.

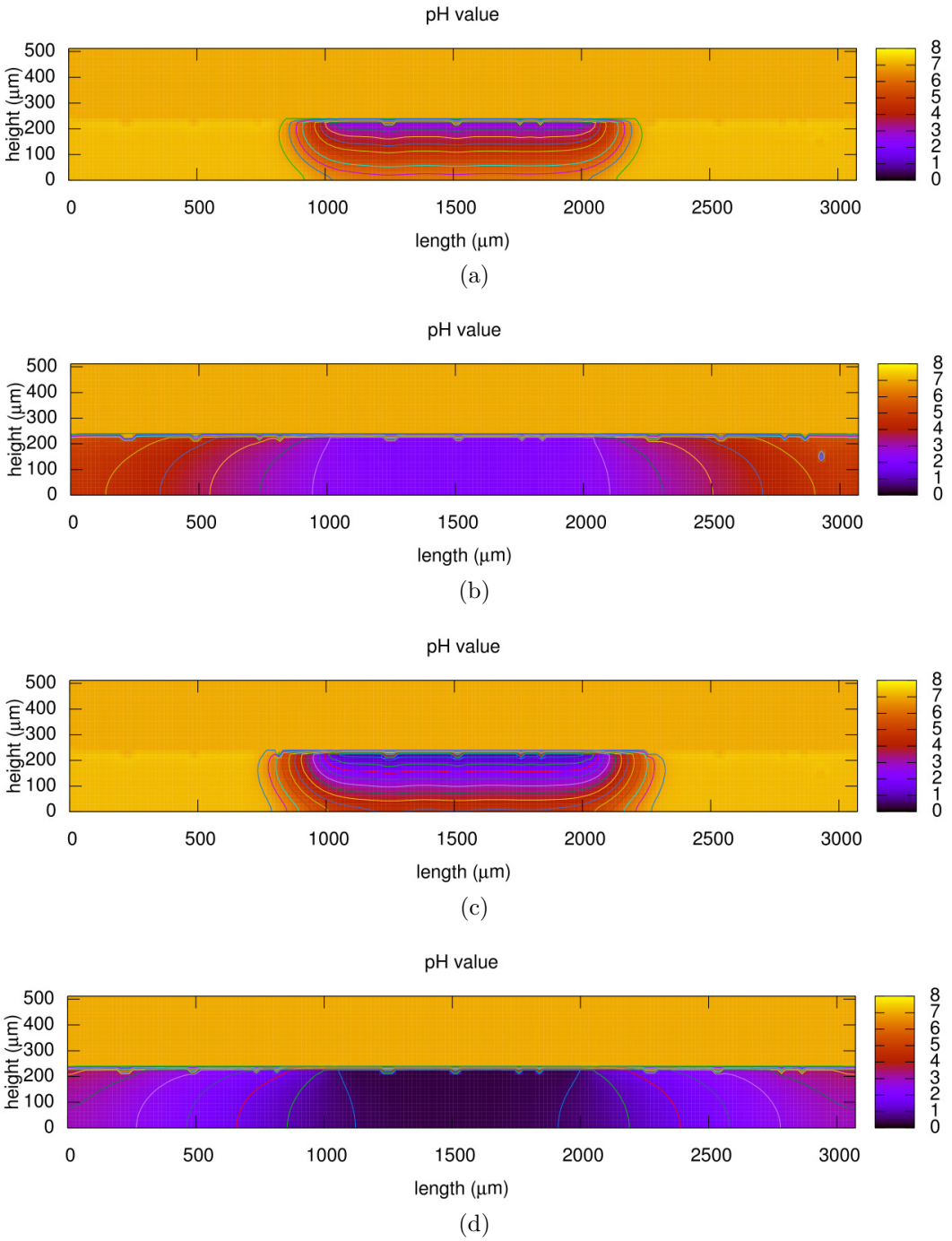

Figure 6.42: Plots of pH values after six minutes of the treatments in Simulations (a) 8-6, (b) 8-7, (c) 8-8 and (d) 8-9.

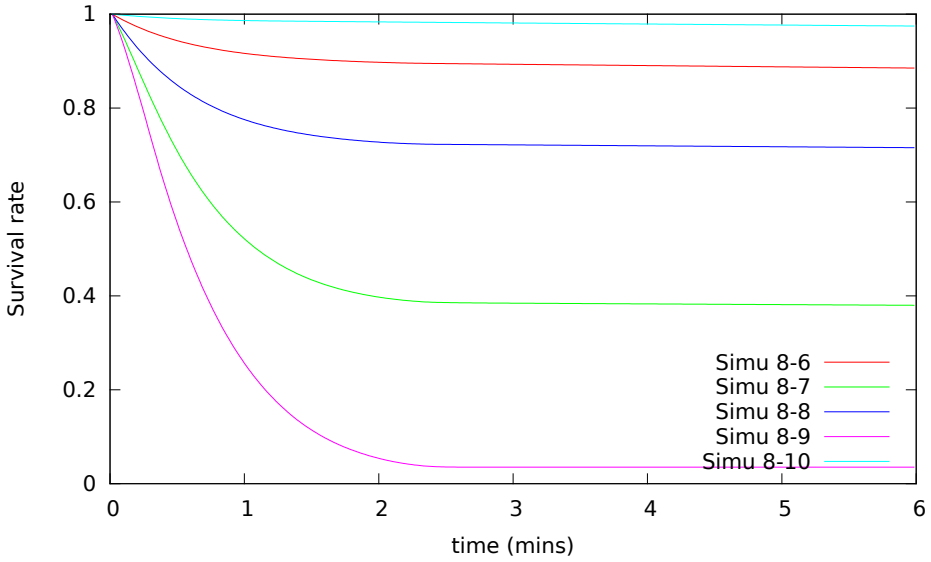

Figure 6.43: Plots of the survival rates throughout six minutes of the treatments in Simulations 8-6 to 8-10.

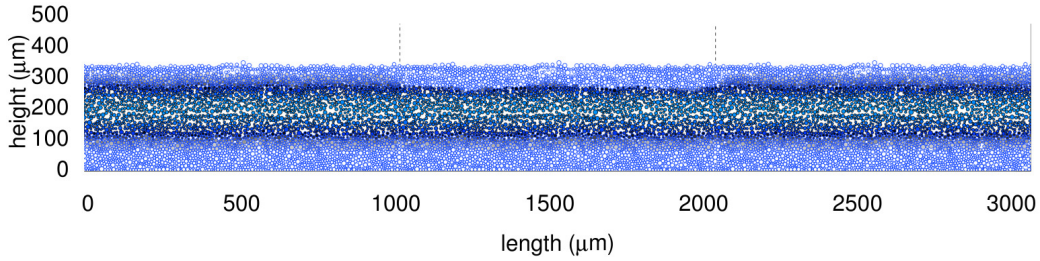

(a)

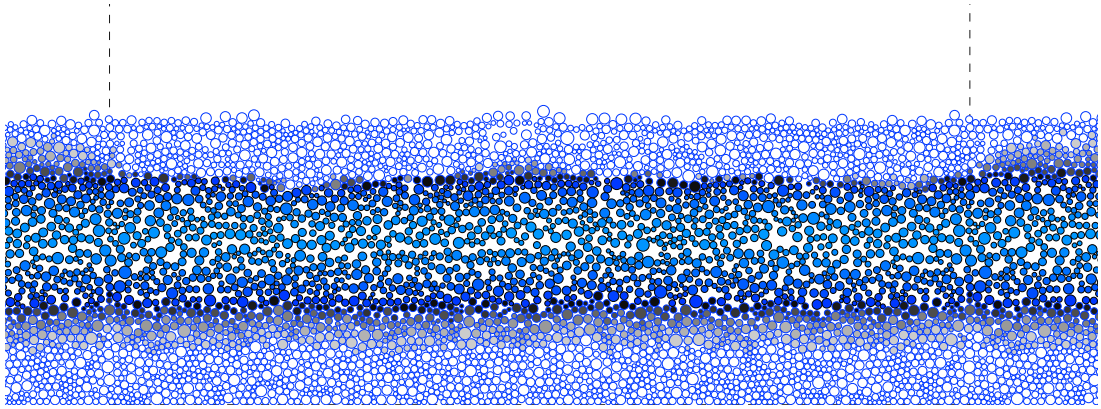

(b)

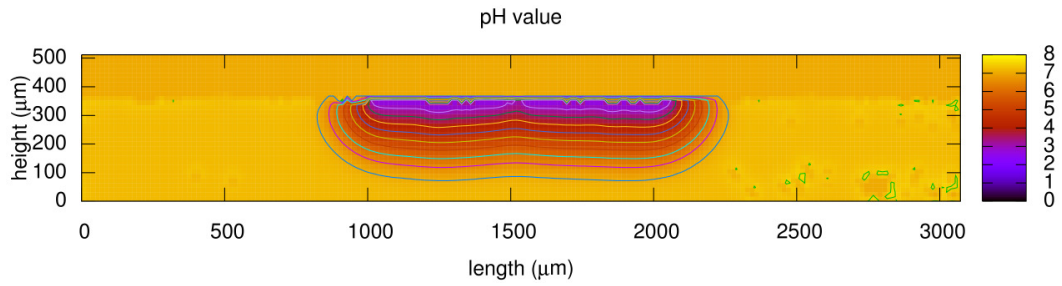

(c)

Figure 6.44: Plots of (a) particle distribution, (b) a closer look at the treatment area, and (c) pH value after six minutes of treatment in Simulation 8-10.

Table 6.5: Simulations of biofilm treatments by combination of Hydrogen Peroxide/Ozone and pH.

Oxidising agent	H_2O_2		O_3	
Sequestering capacity$^{\pm}$ / Fluxes $^{\mp}$	High	Low	High	Low
High fluxes	Simu 9-1	Simu 9-2	Simu 10-1	Simu 10-2
Low fluxes	Simu 9-3	Simu 9-4	Simu 10-3	Simu 10-4

$^{\mp}$ Fluxes of hydrogen peroxide/ozone and hydrogen ions are both high or both low. The fluxes are adopted from the corresponding simulations in the previous sections.

$^{\pm}$ The sequestering capacities are adopted from the previous section.

6.2.4 Combination of Hydrogen Peroxide/Ozone with pH

In this section we combine each of the oxidising agents with hydrogen ions to investigate how this affects biofilm disinfection. Table 6.5 lists the simulations of plasma treatment on 3-day old topical nutrient sourced biofilms. We assume that the fluxes of the oxidising agent and the hydrogen ions are both high or low in each simulation. In order to analyse which compound dominates the degradation of biofilms, the results are compared to the simulations in the previous sections.

Figure 6.45 compares the survival rates in Simulations 9-1 to 9-4 with those of the corresponding simulations from the previous sections. We observe that the effects of combining hydrogen peroxide and hydrogen ions on biofilms are not additive. In the case of biofilms with a low hydrogen ion sequestering capacity, the hydrogen ions dominate the killing rates. Hydrogen peroxide dominates the degradation of the biofilms which have a high hydrogen ion sequestering capacity.

Figure 6.46 compares the survival rates in Simulations 10-1 to 10-4 with those of corresponding simulations from the previous sections. The results are similar to the previous comparison: hydrogen ions dominate the killing of biofilms with a low acid sequestering capacity, and ozone dominates for the high acid sequestering capacity biofilms. However, in Simulations 10-2 and 10-4, the killing rates are affected by the ozone in the first 30 seconds, since the hydrogen ions have not yet

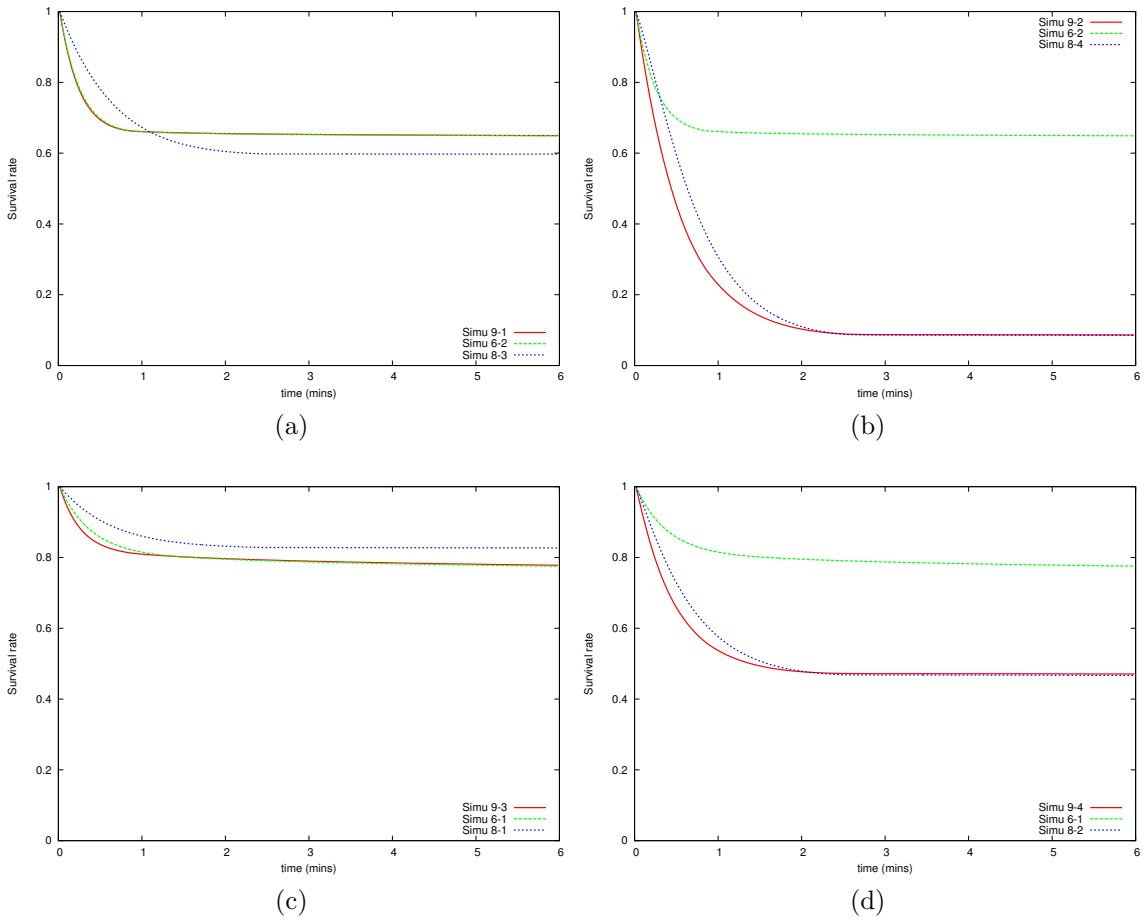

Figure 6.45: Comparison of the effects on 3-day old topical sourced biofilms of treatments which combine hydrogen peroxide and hydrogen ions. See Tables 6.2, 6.4 and 6.5 for simulation details. Note that in (a) the results for Simulation 9-1 and 6-2 are almost identical.

spread sufficiently widely in the biofilm.

6.3 Summary

In this chapter, the IbM modelling framework was applied to simulate the effects of plasma treatment on biofilms. Three plasma species were considered: ozone, hydrogen peroxide, and hydrogen ion. The results show that higher doses of ozone and hydrogen peroxide cause greater damage to the biofilms. However,

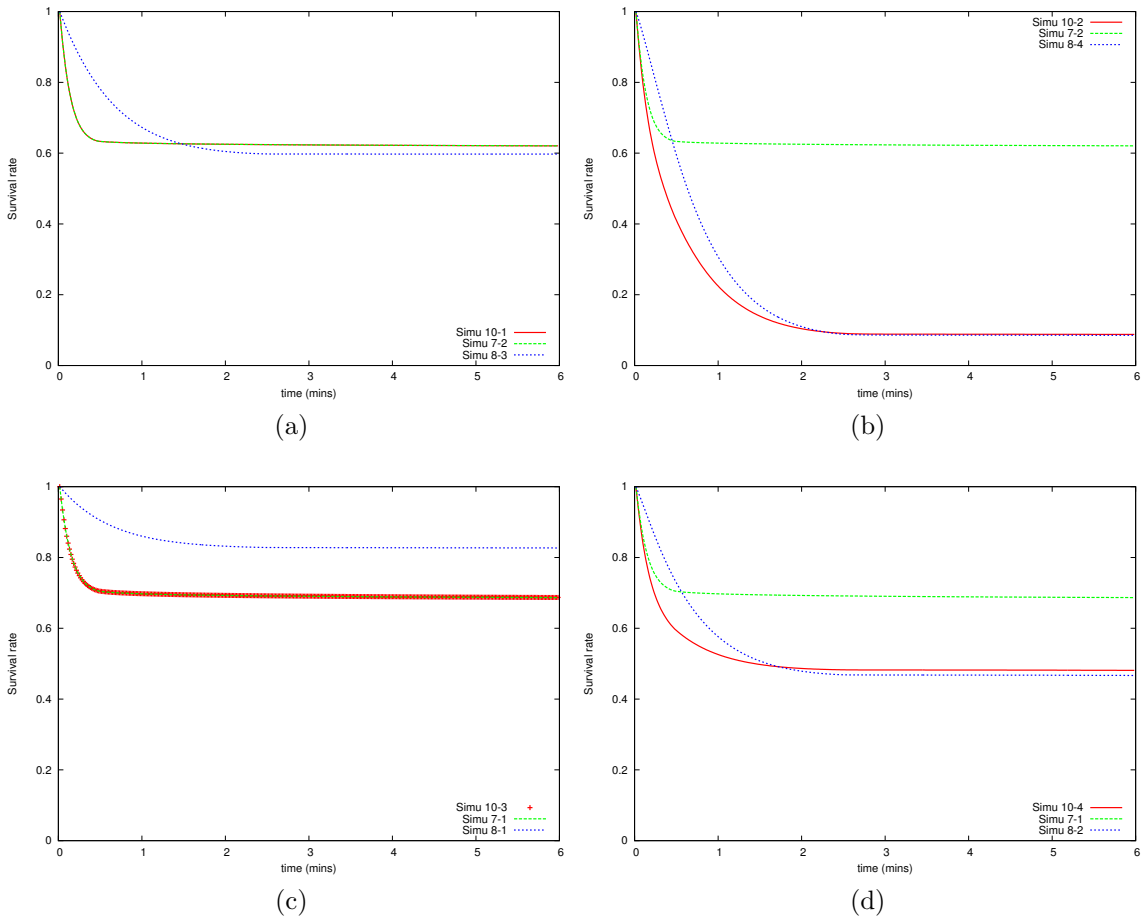

Figure 6.46: Comparison of the effects on 3-day old topical sourced biofilms of treatments which combine ozone and hydrogen ions. See Tables 6.3, 6.4 and 6.5 for simulation details.

the duration of the exposure does not cause significant further damage after about 30 seconds of ozone treatments, and one minute for the hydrogen peroxide treatments.

In the disinfection of biofilms, the dose of ozone required to kill the bacteria is less than that required by hydrogen peroxide. The simulations show that the diffusion of these oxidising agents is blocked by EPS, and diffusion into the regions away from the plasma treatment zone is very limited because of this. Comparing the simulations in which the EPS reacts or does not react with the agent shows significant differences in cell killing (in the simulations, cell death is doubled in

the non-reacting case).

In the two-species simulations, the non EPS-producing PHB strain was vulnerable to direct exposure, but those PHB-particles that were located deep within the biofilm were protected by the EPS produced by the other species. While the EPS strain and surface PHB producers were all destroyed by the treatment, the remaining PHB cells survived and will recolonise the region. Consequently, the composition of the recovering biofilm may be very different from its starting composition, which may have important consequences depending on the bacteria and the scenario.

The maturity of a biofilm also affects the efficiency of its disinfection by plasma treatment. Mature biofilms grown in the topical nutrient source condition have a better ability to decompose these oxidising agents than have the immature ones. However, the biofilm surface area in contact with the jet plays an important role in the treatment. Due to the heterogeneous surface of the mature biofilms in our simulations, the surface area exposed to the cold plasma species is larger than that of the immature ones. Thus more oxidising agent per unit volume is delivered into the mature biofilm than to the younger ones. Consequently, more particles are killed in the former case. On the other hand, the biofilms grown under basal nutrient source conditions show that the oxidising agents are able to penetrate more deeply into a mature biofilm than into an immature one, due to the fact that the concentration of EPS for the immature biofilm is higher. However, mature biofilms are covered by a layer of dead particles, which act as a barrier against the oxidising species by being consumed by the dead biomass before reaching the live particles. Thus, oxidising agents appear inefficient at disinfecting mature biofilms. The dead particle surface layers formed in the basal nutrient source biofilm also help protect the "medium-aged" three-day old biofilm, as they are more resistant to treatment than the topical nutrient sourced biofilms at this stage. Nevertheless, plasma treatment has been shown to clear biofilms from agar surfaces [5, 277, 278, 279, 280], which suggests that simulations with the jets possessing stronger effects (e.g. high input flux, low hydrogen ion sequestering, etc.) are more likely to represent the biologically relevant situation.

For the acid effects case, hydrogen ion molecules are not blocked and consumed by EPS. However, they can be neutralised by the sequestering agents in

the biofilms and their growth environments. Therefore, biofilms with a higher acid sequestering capacity have a better survival rate than biofilms with a low acid sequestering capacity. The maturity of the biofilm does not decrease the concentration of hydrogen ions entering the biofilms, nor reduce the penetration depth. However, the layer of dead particles in the basal nutrient growth biofilm protects it and reduces the damage caused by the hydrogen ions.

The combined treatment simulations suggest, on the whole, that the agents have independent effects and do not combine to produce more damage. The dropping of the pH value of the environment to a lethal pH level can be a key factor in biofilm degradation in the case of biofilms with a low acid sequestering capacity. However, for biofilms with a high acid sequestering capacity, the oxidising species dominate the killing of the biofilms.

Chapter 7

Overall Conclusions

In this thesis, we investigated the growth of bacterial biofilms and the impact on them of cold plasma treatments of various types, using a new individual-based modelling (IbM) framework. The framework treats bacteria as discrete particles whilst all the other factors are treated as a continuum, defined over the whole computational domain (e.g., the nutrients, oxygen), within the particle (e.g., ATP), and outside the particles (e.g., the exopolysacchurades (EPS) matrix). There are a number of novel aspects of this modelling approach, including the explicit treatment of energy (as ATP), its preserving the centre of mass in particle movement, and, in particular, the treatment of the EPS as a continuum. In the few IbM models that do consider the EPS explicitly, it is either treated as discrete [124, 166] or as an incompressible substance of fixed concentration [171]. EPS makes up only a few percentage points of the total biofilm mass, yet it plays a vital role in biofilm growth as well as protecting the bacteria within (e.g., against the oxidising agents of cold plasma as demonstrated in Chapter 6).

In our investigation of cold plasma treatment, the model was required to have the following properties.

- multi-dimensional: to investigate how far beyond the plasma jet region the treatment will be effective.
- A realistic treatment of EPS, allowing for variation in its concentration, which will affect the ability of an oxidising agent to penetrate the matrix.
- Energy levels, so that factors such as hydrogen ions ability to affect the

production of ATP can be explicitly modelled.

- Easily extendable to include additional factors (e.g., multi-species biofilms, PHB, etc., and arrangements (e.g., arrangements of the sourcing of the nutrients).

The prior literature has not included a model satisfying all these requirements, so the new model framework presented in this was developed in Chapter 3 to take into account all these factors as well as the other factors usually included in IbMs of biofilms.

In Chapter 4, the basic framework was demonstrated using simulations describing biofilm growth in various scenarios. The simulations with the topical sourced nutrients are consistent with much that is reported in the experimental literature, for example, the structural heterogeneity of live and dead cells due to nutrient/oxygen limitation. Despite the fact that it is very common to grow biofilms in agar plates in the laboratory (including in cold plasma studies), they have been the subject of very little mathematical modelling and, as far as I know, the simulation of bottom nutrient sourced biofilms has not been undertaken before. Unlike the top nutrient source case, the bottom fed biofilms grow very uniformly across the surface with a live layer of cells being sandwiched between two layers of dead cells that are starved of either oxygen or of nutrients. This is a very interesting result which, as far as I know, has not been described experimentally. Nevertheless, the simulations suggest that the qualitative structure of colonies grown on agar are very uniform and probably robust to perturbations (an interesting scenario that warrants further mathematical investigation).

The chemistry of cold plasma is very complicated, involving many chemical species, most of which are highly reactive and very short lived. For simplicity, we focussed on the more stable products resulting from plasma jets. Hydrogen peroxide and ozone are two well known products that are relatively stable and potentially damaging to biofilms. From the simple experiment described in Chapter 5, acid species will also be significant.

The modelling framework was extended to include these plasma species, together with simulations, and was described in Chapter 6. With the absence of direct experimental results for comparison, the simulations do offer some new

insights and predictions that warrant validation or experimental investigation. Firstly, the EPS provides a significant barrier against the oxidative species in their reaction with the oxygen links in the polysaccharide chain; however, with so much EPS present, EPS decay seems insignificant over the course of a six minute treatment. The timescale for equilibration varies between species, about 30 seconds for ozone, 60 seconds for hydrogen peroxide, and 90 seconds for the acid species. This suggests that a rapid exposure to a jet is not likely to be effective, and each locality must be treated for about a minute to get the full effect. In practice, the main products of a plasma will be acid and hydrogen peroxide or acid and ozone: these simulations suggest that the combined treatment is no more effective than the best one of the individual treatments. Finally, the simulations of the treatment of the two-species biofilm could mean that the recovering biofilm may be very different from the pretreated one. With biofilms grown on agar being very straightforward to grow and treat, there are many investigations that would be of interest to help validate the model. These include the effects of plasma exposure (to test the $\mathcal{O}$ (one minute) timescale of effectiveness), comparing resistances between species with different EPS producing properties and acid-handling properties. The study in this thesis represents a first step into a theoretical investigation of plasma treatment and new and more detailed experiments will help to drive this work forward.

7.1 Future Work

Though the modelling framework considers a number of factors important to biofilm growth, it is very much a simplification of reality. The model can produce results consistent with observations and should be applicable to modelling many biofilm varieties in different settings. However, there is a wide scope for validating and improving model, as outlined below.

- **EPS dynamics.** In this modelling framework, the diffusion and expansion of the EPS are described by the flux which depends on the pressure generated by the local EPS concentration. However, how the pressure drives the EPS to move and the rate of movement are unknown. Furthermore, how

the EPS movement interacts with the bacterial cells in the biofilm is also unclear. There is no, or at least very little, information in the experimental literature on the mechanics of EPS in biofilms. The proposed model is very simple and is likely to be reasonable, at least qualitatively, but any experiments that measure EPS diffusion or movement in biofilms will help validate the existing assumptions or indicate the need for modifications of the model.

- **Biofilm detachment.** Biofilm detachment is an important, and poorly understood, process in biofilm development. Such processes could have a significant effect on biofilm structure, and consequently how they respond to treatment. For example, if the dead cells on the surface of colonies growing on agar can be removed (or sloughed off) then the cells in the living layer will be exposed to more oxygen and thus will grow more. However, they will be more vulnerable to plasma treatment.

- **Fluid media.** In the laboratory, biofilms are often grown in flow chambers in which the fluid media surrounding a biofilm is allowed to flow, thereby imposing shear forces on the biofilm. Numerous experiments have shown that shear can have a considerable effect on the biofilm structure and the transport of oxygen and nutrients. The effects of such flow have been investigated using IbM approaches (e.g., [142, 281]), and would require a major extension of the current model.

For the second part of the thesis, the modelling framework was amended and applied to the research of plasma treatment on biofilms. However, some of the issues listed below would be interesting to investigate further.

- **Plasma species.** The chemical species produced in a plasma jet depend on the gas used to generate it. So, the chemical species can vary considerably. Thus, the damage to the biofilms by different plasmas can be completely different. An analysis of which chemical species can penetrate biofilms (or in water) and in what quantity from a particular cold plasma arrangement would be very useful in formulating an appropriate model.

- **Acid resistance.** The simulation results suggest that the acid created by a plasma jet can be a key factor in biofilm disinfection. However, we assumed in our simulations a very simple mechanism protecting against significant pH change in the biofilm growth environment. Yet, there are several such mechanisms of acid resistance possessed by bacterial cells, such as cytoplasmic pH maintenance, ion transport, and alkali production. These mechanisms may change the hydrogen ion concentration locally and possibly lead to a different response on the part of a biofilm.

Some of the suggested investigations only require small extensions or modifications to the current modelling framework. However, others require greater experimental support. It is hoped that the work described in this thesis offers a deeper understanding of biofilm growth and response to cold plasma treatments, which will hopefully motivate and oriente future research in this area.

Appendix A: Parameters and Variables

The parameters used in the simulations are listed in the following tables. Due to lack of experimental data, some of the parameters are assumed or verified by simulation results. There are 4 crucial parameters which are assumed or verified are marked by red star, *. Changing the values of these parameters may not changes general shape of biofilms, however, they may change the structure of the biofilms and the distribution of live/dead particles and EPS (See Section 4.1.4.2 and Section 4.1.4.4). Here, we discuses these parameters in detail below.

- D_E is the EPS diffusion coefficient. It controls the movement of the EPS. Increasing the value of D_E increases the spreading of EPS. Therefore, the biofilms grow higher and wider than with small value of D_E. Conversely, Reducing the value of D_E results the compact EPS and small biofilms.

- σ is the coefficient of particle movement push by EPS. If the value is chosen too large, the particles may move a long distance in a small push by EPS, i.e. too sensitive to EPS movement. However, if the value is chosen too small, e.g. $\sigma = 0$, the particles remain stationary.

- β is the maximum biomass death rate. It relates to how fast the particles die out. When the value of β is small, the particles may delay to die out for several days, even when there is no nutrient and oxygen present. However, When the value is large, the particles die rapidly, even when the environment is full of nutrient and oxygen.

- k_a is the energy threshold. It relates to the biofilms survival ability under anaerobic condition. According to the calculation, when $k_a \leq 4.058 \times 10^{-6}$ and in high nutrient concentration environment, $\frac{dC_L}{dt} \geq 0$. This means that the particles are able to survive, even reproducing, under anaerobic condition. On the other hand, when k_a greater than that value, the biofilms die in anaerobic conditions. Changing the value of k_a affects the thickness of live particle layer in the biofilms.

Table 1: The global parameters including size of computational domain and time and space steps. These constants are used in all simulations unless otherwise stated.

parameter	description	value	unit
R_{min}	minimum radius for which particle division occurs	3	μm
R_{max}	maximum radius of particles can grow	8	μm
L_x	width of the computational domain	1024	μ
L_z	height of the computational domain	1024	μ
L_y	the height of cylindrical particles	1	μm
d_x	step size of the computational grids in horizontal direction	16	μ
d_y	step size of the computational grids in vertical direction	16	μ
h_z	the distance of upper boundary of diffusion layer from the highest point of the biofilm	48	μm

Table 2: The parameters of EPS-producing strain (Section 4.1).

parameter	description	value	unit	reference
$D_{X_{Ox}}$	oxygen diffusion coefficient	8.33×10^6	$\mu m^2/h$	[282]
D_{X_s}	nutrient diffusion coefficient	4.1667×10^6	$\mu m^2/h$	[282]
D_E	EPS diffusion coefficient	100	$\mu m^2/h$	Varied*
K_E	EPS concentration at which the EPS flux is half its maximum	0.3	g/L	Assumed
η	slope constant of Hill function of EPS flux	3	dimensionless	Assumed
k	the constant which adjusts average minimum distance between particles	1.3	dimensionless	[169]
σ	drag coefficient of particle movement pushed by EPS	2	dimensionless	Varied *
ϕ	ratio of dead biomass decomposed and converted to nutrient when live biomass dies	0.4	dimensionless	[166]
q_w	the fraction of biomass loss to become water when live cells die	0	dimensionless	Assumed
ρ_c	density of the biomass	200	g/L	[171]
μ	maximum biomass production rate	0.09	1/h	[283]
μ_E	maximum EPS production rate	5.44×10^{-2}	g/(Lh)	[178]

μ_{X_sb}	amount of nutrient produced per fraction of biomass lost per volume	10^{-4}	dimensionless	Assumed
β	maximum biomass death rate	10^2	1/h	Estimated*
β_E	EPS decay constant	1.4×10^{-2}	1/h	[171]
K_{X_sb}	nutrient concentration at which biomass production is half its maximum	4×10^{-3}	g/L	[282]
m_{X_sb}	slope constant of Hill function of biomass production using nutrient source	2	dimensionless	Assumed
K_{X_sA}	nutrient concentration at which energy production is half of its maximum	10^{-2}	g/L	Assumed
m_{X_sA}	slope constant of Hill function of energy production using nutrient source	2	dimensionless	Assumed
$K_{X_{Ox}A}$	oxygen concentration at which energy production is half its maximum	3.5×10^{-4}	g/L	[282]
$m_{X_{Ox}A}$	slope constant of Hill function of energy production using oxygen source	1	dimensionless	Assumed
K_{X_sE}	nutrient concentration at which EPS production of half its maximum	4×10^{-3}	g/L	same as K_{X_sb}

m_{X_sE}	slope constant of Hill function of EPS production using nutrient source	3	dimensionless	Assumed
ω	weight constant for energy production via aerobic respiration	2/29.85	dimensionless	See Figure 1.6 [27]
δ_{X_sA}	maximum nutrient consumption rate during energy synthesis	1.086×10^2	g/(Lh)	[284]
ρ_{EX_s}	the amount of nutrient consumed per EPS production	$1/2 \times 10^{-3}$	dimensionless	[93]
k_a	energy threshold	4.058×10^{-6} (bacteria survive in anaerobic environment) 8.126×10^{-5}	dimensionless (for standard simulations)	calculation$^{\pm *}$
δ_{X_sb}	nutrient consumption for biomass reproduction	1.504×10^3 (bacteria survive in anaerobic environment) 1.38598×10^3	g/L (for standard simulations)	calculation$^{\mp}$
$\delta_{X_{Ox}AX_s}$	the maximum oxygen consumption rate for energy production using nutrient source	12	g/(Lh)	Assumed

$\pm$ It is calculated from $\frac{dC_L^{\kappa}}{dt} = 0$.

$\mp$ It is assumed that the ratio of nutrient consumption of EPS production and biomass formation is 0.2, i.e., $\frac{\mu_E \rho_{EX_s}}{\delta_{X_sb}(\mu+\beta g(1))} = 0.2$, and then δ_{X_sb} is solved for.

Table 3: Parameters for PHB-producing strain, i.e., the species index $\Lambda(\kappa) = 2$ in scenario 2 (Section 4.2).

parameter	description	value	unit	reference
$\mu^{\Lambda(\kappa)}$	maximum biomass production rate for bacterial strain $\Lambda(\kappa)$	0.09	1/h	[283]
$\beta^{\Lambda(\kappa)}$	maximum death rate for bacterial strain $\Lambda(\kappa)$	10^2	1/h	Assumed
$\omega^{\Lambda(\kappa)}$	weight constant for energy production via anaerobic respiration using nutrient source for bacterial strain $\Lambda(\kappa)$	2/18.2	dimensionless	$\Lambda(\kappa) = 2$ PHB-producing strain (see Figure 1.7a[31])
ψ	the ratio of energy produced from nutrient and PHB	11.6/18.2 ($\omega^{\Lambda(\kappa)}/\tau^{\Lambda(\kappa)}$ for $\Lambda(\kappa) = 2$)	dimensionless	
$\tau^{\Lambda(\kappa)}$	weight constant for energy production via anaerobic respiration using PHB source for bacterial strain $\Lambda(\kappa)$	2/11.6	dimensionless	See Figure 1.7b[29]
K_p	PHB level at which energy production is half of its maximum	10^{-2}	g/L	Assumed
K_{PX_s}	critical X_s concentration for PHB usage, $G(X_s, P_\kappa) \approx 0$ if X_s is large	10^{-4}	g/L	Assumed
K_{X_sP}	nutrient concentration at which PHB production is half its maximum	4×10^{-3}	g/L	same as K_{X_sb}

m_{X_sP}	slope constant of Hill function of PHB production using nutrient source	1	dimensionless	Assumed
$Y_{P_{ana}}^{\Lambda(\kappa)}$	maximum PHB production rate via anaerobic respiration for bacterial strain $\Lambda(\kappa)$	0.0514	1/h	[30]*
$Y_{P_{aer}}^{\Lambda(\kappa)}$	maximum PHB production rate via aerobic respiration for bacterial strain $\Lambda(\kappa)$	0.46255	1/h	[30]*
$K_{X_{Ox}P}$	oxygen concentration at which PHB production via aerobic respiration is half its maximum	3.5×10^{-4}	g/L	same as $K_{X_{Ox}A}$
$m_{X_{Ox}P}$	slope constant of Hill function of PHB production via aerobic respiration using oxygen source	1	dimensionless	Assumed
δ_{PA}	maximum PHB consumption rate	0.65956	1/h	[30]*
δ_{X_sP}	nurient concentration consumption per PHB production	0.1167	g/(L fg)	[30]
$\delta_{X_{Ox}P}$	the maximum oxygen consumption rate in PHB production via aerobic respiration	0.021	g/(L fg)	Assumed (five times less than δ_{X_sP})

$\delta_{X_{Ox}AP}$	the maximum oxygen consumption rate in energy production via aerobic respiration using PHB source	12	g/(Lh)	Assumed

⁎ The units of $Y_{P_{ana}}^{\Lambda(\kappa)}$, $Y_{P_{aer}}^{\Lambda(\kappa)}$, and δ_{PA} are $\text{Cmole}_{[PHB]}/(\text{Cmole}_{[biomass]}\text{h})$, which are converted to $\text{g}_{[PHB]}/(\text{g}_{[biomass]}\text{h})$, i.e., 1/h, by applying molecular weight of biomass, 25.1 g/Cmole, and molecular weight of PHB, 21.5 g/Cmole [30].

Table 4: Variables used in the simulations.

variable	description	units
C_L^κ	live biomass in particle κ	fg
C_D^κ	inert/death biomass in particle κ	fg
A_κ	energy level in particle κ	dimensionless
X_s	nutrient concentration	g/L
X_{Xo}	oxygen concentration	g/L
E	EPS concentration	g/L
P_κ	mass of PHB per live biomass in particle κ	dimensionless
r_κ	radius of particle κ	μm
t	time	h

Table 5: A list of parameters for the hydrogen peroxide simulations in plasma treatment (Section 6.2.1).

parameter	description	value	unit	reference
$\beta_{X_{H_2O_2}}$	maximum death rate caused by H_2O_2	1.8×10^2	1/h	Assumed
$K_{X_{H_2O_2}}$	H_2O_2 concentration at which energy production is half its maximum	1.7×10^{-5}	g/L	[285]
$m_{X_{H_2O_2}}$	slope constant of Hill function of energy production effected by H_2O_2	5	dimensionless	Assumed
$D_{X_{H_2O_2}}$	H_2O_2 diffusion coefficient	7.8×10^6	$\mu m^2/h$	[286]
$\mu_{H_2O_2}$	the H_2O_2 production rate	3.4×10^{-13}	g/(Lh)	[285]
δ_{Cat}	the maximum catalase activity rate	2.792×10^3	g/(Lh)	[239]
$\delta_{X_{H_2O_2}[EPS]}$	the maximum reaction rate of H_2O_2 with EPS	2.691×10^4	g/L	[227]
$\delta_{X_{H_2O_2}}$	the decay rate constant of H_2O_2	$\ln(2)/8$	1/h	
$\delta_{E[X_{H_2O_2}]}$	the reaction rate constants for H_2O_2 with EPS	51.23	g/L	[227]
$K_{MX_{H_2O_2}}$	H_2O_2 concentration at which half maximum catalase activity	2.176	g/L	[239]
$\boldsymbol{J_{X_{H_2O_2}0}}$	the constant flux of H_2O_2 entering the target biofilms	5.9415×10^4	$fg/(\mu m^2 h)$	[276]

Table 6: A list of parameters for the ozone simulations in plasma treatment (Section 6.2.2).

parameter	description	value	unit	reference
$\beta_{X_{O_3}}$	maximum death rate caused by O_3	3.994×10^2	1/h	[223]
$K_{X_{O_3}}$	Hill function coefficient for O_3	3.4×10^{-6}	g/L	Assumed
$m_{X_{O_3}}$	Hill function constant	5	dimensionless	Assumed
$D_{X_{O_3}}$	diffusion coefficient of O_3	6.84×10^6	$\mu m^2/h$	[286]
$\delta_{X_{O_3}[bio]}$	the reaction rate of O_3 with biomass	3.994×10^2	1/h	[223]
$\delta_{X_{O_3}}$	the decay rate constant of O_3	6ln(2)	1/h	[210]
$\delta_{X_{O_3}[EPS]}$	the reaction rate of O_3 with EPS	2.691×10^4	g/L	[227]
$\delta_{E[X_{O_3}]}$	the reaction rate constants for O_3 reaction with EPS	36.29	g/L	[227]
$\boldsymbol{J_{X_{O_3}0}}$	the constant flux of O_3 entering the target biofilms	1.435×10^5	$fg/(\mu m^2 h)$	[273]

Table 7: A list of parameters for the hydrogen peroxide simulations in plasma treatment.

parameter	description	value	unit	reference
$X_{H^+}^{min}$	the minimum H^+ concentration at which cells survive	$10^{-3.88}$	g/L	[77]
$X_{H^+}^{max}$	the maximum H^+ concentration at which cells survive	$10^{-12.17}$	g/L	[77]
$X_{H^+}^{Opt}$	the optimum H^+ concentration at which cells live	$10^{-7.2}$	g/L	[77]
$D_{X_{H^+}}$	diffusion coefficient of H^+	1.53×10^7	$\mu m^2/h$	[287]
$\delta_{X_{H^+}}$	the maximum H^+ decay rate	5.56	g/L	From data fitting (Section 5.2)
$\boldsymbol{J_{X_{H^+}0}}$	the constant flux of H^+ entering the target biofilms	2.526×10^6	$fg/(\mu m^2 h)$	From data fitting

References

[1] M. Vleugels, G. Shama, X. Deng, E. Greenacre, T. Brocklehurst, and M. Kong, "Atmospheric plasma inactivation of biofilm-forming bacteria for food safety control," *IEEE Transactions on Plasma Science*, vol. 33, pp. 824–828, Apr. 2005. 1

[2] R. E. J. Sladek, S. K. Filoche, C. H. Sissons, and E. Stoffels, "Treatment of Streptococcus mutans biofilms with a nonthermal atmospheric plasma," *Letters in applied microbiology*, vol. 45, pp. 318–23, Sept. 2007. 1, 17, 113

[3] U. Cvelbar, D. Vujošević, Z. Vratnica, and M. Mozetič, "The influence of substrate material on bacteria sterilization in an oxygen plasma glow discharge," *Journal of Physics D: Applied Physics*, vol. 39, pp. 3487–3493, Aug. 2006. 1, 117

[4] A. Asadinezhad, I. Novák, M. Lehocký, V. Sedlaík, A. Vesel, I. Junkar, P. Sáha, and I. Chodák, "A Physicochemical Approach to Render Antibacterial Surfaces on Plasma-Treated Medical-Grade PVC: Irgasan Coating," *Plasma Processes and Polymers*, vol. 7, pp. 504–514, Feb. 2010. 1

[5] J. Goree, B. Liu, D. Drake, and E. Stoffels, "Killing of S. mutans Bacteria Using a Plasma Needle at Atmospheric Pressure," *IEEE Transactions on Plasma Science*, vol. 34, pp. 1317–1324, Aug. 2006. 1, 17, 113, 117, 186

[6] G. Fridman, G. Friedman, A. Gutsol, A. B. Shekhter, V. N. Vasilets, and A. Fridman, "Applied Plasma Medicine," *Plasma Processes and Polymers*, vol. 5, pp. 503–533, Aug. 2008. 1, 112

[7] F. Iza, G. J. Kim, S. M. Lee, J. K. Lee, J. L. Walsh, Y. T. Zhang, and M. G. Kong, "Microplasmas: Sources, Particle Kinetics, and Biomedical Applications," *Plasma Processes and Polymers*, vol. 5, pp. 322–344, June 2008. 1

[8] G. E. Morfill, M. G. Kong, and J. L. Zimmermann, "Focus on Plasma Medicine," *New Journal of Physics*, vol. 11, p. 115011, Nov. 2009. 1, 112

[9] A. C. Schuerger, S. Trigwell, and C. I. Calle, "Use of non-thermal atmospheric plasmas to reduce the viability of Bacillus subtilis on spacecraft surfaces," *International Journal of Astrobiology*, vol. 7, pp. 47–57, Jan. 2008. 1, 113

[10] M. G. Kong, G. Kroesen, G. Morfill, T. Nosenko, T. Shimizu, J. van Dijk, and J. L. Zimmermann, "Plasma medicine: an introductory review," *New Journal of Physics*, vol. 11, p. 115012, Nov. 2009. 1, 112, 113

[11] D. Kaiser, C. Manoil, and M. Dworkin, "Myxobacteria: cell interactions, genetics, and development," *Annual Reviews in Microbiology*, vol. 33, no. 1, pp. 595–639, 1979. 2

[12] M. Dworkin, "Myxobacteria," in *Encyclopedia of Life Sciences*, no. c, pp. 1–5, John Wiley & Sons, Ltd., 2007. 2

[13] W. Whitman, D. Coleman, and W. Wiebe, "Prokaryotes: the unseen majority," *Proceedings of the National Academy of Sciences*, vol. 95, no. 12, p. 6578, 1998. 2

[14] C. R. Woese, O. Kandler, and M. L. Wheelis, "Towards a natural system of organisms: proposal for the domains Archaea, Bacteria, and Eucarya," *Proceedings of the National Academy of Sciences of the United States of America*, vol. 87, pp. 4576–9, June 1990. 2

[15] R. B. Weart, A. H. Lee, A.-C. Chien, D. P. Haeusser, N. S. Hill, and P. A. Levin, "A metabolic sensor governing cell size in bacteria," *Cell*, vol. 130, pp. 335–47, July 2007. 2

[16] S. Hogg, *Essential Microbiology*. Chichester, England: John Wiley & Sons Ltd, 2005. 2, 4, 6, 8, 13, 123

[17] G. Lipps, *Plasmids: Current Research and Future Trends*. Caister Academic Press, 2008. 3

[18] P. S. Meadows, "The attachment of bacteria to solid surfaces," *Archiv für Mikrobiologie*, vol. 75, pp. 374–81, Jan. 1971. 4

[19] S. Köhler, "The Bacterial flagella," tech. rep., Laboratory of Computational Engineering, Helsinki University of Technology, Helsinki, 2004. 4

[20] E. F. Elstner, "Oxygen activation and oxygen toxicity," *Reactions*, vol. 33, pp. 73–96, 1982. 6

[21] N. A. Campbell, B. Williamson, and R. Heyden, *Biology: Exploring Life*. Boston, Massachusetts: Pearson Prentice Hall, 2006. 6

[22] B. Chance, H. Lees, and J. R. Postgate, "The Meaning of "Reversed Electron Flow" and "High Energy Electron" in Biochemistry," *Nature*, vol. 238, no. 5363, pp. 330–331, 1972. 6

[23] J. Koolam and K. Roehm, *Color Atlas of Biochenistry*. New York: Georg Thieme Verlag, 2 ed., 2005. 6

[24] J. M. Berg, J. L. Tymoczko, and L. Stryer, *Biochemistry*. New York: W.H. Freeman, 5 ed., 2002. 6

[25] I. Beis and E. a. Newsholme, "The contents of adenine nucleotides, phosphagens and some glycolytic intermediates in resting muscles from vertebrates and invertebrates," *The Biochemical journal*, vol. 152, pp. 23–32, Oct. 1975. 6

[26] D. G. Nicholls and S. J. Ferguson, *Bioenergetics 3*. London: Academic Press, 3 ed., 2002. 7

[27] P. Rich, "The molecular machinery of Keilins respiratory chain," *Biochem. Soc. T.*, vol. 31, pp. 1095–1105, 2003. 7, 8, 197

[28] J. Wilkinson, "The Extracellular Polysaccharides of Bacteria," *Microbiology and Molecular Biology Reviews*, vol. 22, no. 1, p. 46, 1958. 8

[29] E. Dawes and D. Ribbons, "Some Aapects of the Endogenous Metabolism of Bacteria," *Microbiol. Mol. Biol. R.*, vol. 28, no. 2, p. 126, 1964. 9, 10, 14, 97, 198

[30] J. J. Beun, K. Dircks, M. C. M. Van Loosdrecht, and J. J. Heijnen, "Poly-beta-hydroxybutyrate metabolism in dynamically fed mixed microbial cultures," *Water Res.*, vol. 36, pp. 1167–80, Mar. 2002. 9, 199, 200

[31] R. Carlson, A. Wlaschin, and F. Srienc, "Kinetic studies and biochemical pathway analysis of anaerobic poly-(R)-3-hydroxybutyric acid synthesis in Escherichia coli," *Applied and environmental microbiology*, vol. 71, no. 2, p. 713, 2005. 9, 10, 198

[32] M. A. van Aalst-van Leeuwen, M. A. Pot, M. C. M. van Loosdrecht, and J. J. Heijnen, "Kinetic Modeling of Poly (Beta-hydroxybutyrate) Production and Consumption by Paracoccus pantotrophus under Dynamic Substrate Supply," *Biotechnology and bioengineering*, vol. 55, pp. 773–82, Sept. 1997. 10

[33] P. H. Janssen and B. Schink, "Pathway of anaerobic poly-beta-hydroxybutyrate degradation by Ilyobacter delafieldii," *Biodegradation*, vol. 4, no. 3, pp. 179–185, 1993. 10

[34] J. W. Costerton, "Direct Observation," in *The Biofilm Primer*, ch. 1, p. 199, Springer, 1 ed., 2007. 11

[35] D. Dobrynin, G. Fridman, Y. V. Mukhin, M. A. Wynosky-dolfi, J. Rieger, R. F. Rest, A. F. Gutsol, and A. Fridman, "Cold Plasma Inactivation of Bacillus cereus and Bacillus anthracis (Anthrax) Spores," *IEEE Transactions on Plasma Science*, vol. 38, no. 8, pp. 1878–1884, 2010. 11, 112

[36] F. Torrella and R. Y. Morita, "Microcultural study of bacterial size changes and microcolony and ultramicrocolony formation by heterotrophic bacteria

in seawater," *Applied and Environmental Microbiology*, vol. 41, no. 2, p. 518, 1981. 11

[37] J. W. Costerton, Z. Lewandowski, D. E. Caldwell, D. R. Korber, and H. M. Lappin-Scott, "Microbial biofilms," *Annual review of microbiology*, vol. 49, pp. 711–45, Jan. 1995. 11

[38] R. Donlan and J. W. Consterton, "Biofilms: survival mechanisms of clinically relevant microorganisms," *Clin. Microbiol. Rev.*, vol. 15, no. 2, pp. 167–193, 2002. 11, 12, 13, 14

[39] R. M. Donlan, "Biofilms: microbial life on surfaces," *Emerg. Infect. Dis.*, vol. 8, pp. 881–90, Sept. 2002. 12, 15, 16

[40] K. Kierek-Pearson and E. Karatan, "Biofilm Development in Bacteria," *Adv. Appl. Microbiol.*, vol. 57, pp. 97–111, 2005. 12, 13, 14, 15, 16

[41] G. H. Bowden and Y. H. Li, "Nutritional influences on biofilm development," *Adv. Dent. Res.*, vol. 11, pp. 81–99, Apr. 1997. 12

[42] K. Okuda, T. Kato, and K. Ishihara, "Involvement of periodontopathic biofilm in vascular diseases," *Oral Dis.*, vol. 10, pp. 5–12, 2004. 12, 17

[43] J. Wimpenny, "Structural Determinants in Biofilm Formation," in *Biofilms: Recent Advences in Their Study and Control* (L. Evans, ed.), ch. 3, pp. 35–49, Amsterdam: harwood academic publishers, 2000. 12

[44] P. Nielsen, A. Jahn, and R. Palmgren, "Conceptual model for production and composition of exopolymers in biofilms," *Wat. Sci. Tech.*, vol. 36, no. 1, pp. 11–19, 1997. 12

[45] B. Christensen and W. Characklis, "Physical and chemical properties of biofilms," in *Biofilms* (W. Characklis and K. Marshall, eds.), pp. 93–130, New York: John Wiley & Sons, 1990. 12

[46] H. C. Flemming and J. Wingender, "Relevance of microbial extracellular polymeric substances (EPSs)–Part I: Structural and ecological aspects," Jan. 2001. 12, 15, 17

[47] H.-C. Flemming, J. Wingender, T. Griebe, and C. Mayer, "Physico-chemical Properties of Biofilms," in *Biofilms: Recent Advences in Their Study and Control* (L. Evans, ed.), ch. 2, pp. 19–34, Amsterdam: harwood academic publishers, 2000. 12, 15

[48] Z. Lewandowski, "Structure and Function of Biofilms," in *Biofilms: Recent Advences in Their Study and Control* (L. Evans, ed.), ch. 1, pp. 1–17, Amsterdam: harwood academic publishers, 2000. 12

[49] P. Stoodley, J. Boyle, D. DeBeer, and H. Lappin-Scott, "Evolving perspectives of biofilm structure," *Biofouling*, vol. 14, pp. 75–90, June 1999. 12

[50] S. Karthikeyan and T. J. Beveridge, "Pseudomonas aeruginosa biofilms react with and precipitate toxic soluble gold," *Environ. Microbiol.*, vol. 4, pp. 667–75, Nov. 2002. 12, 15

[51] K. Garny, H. Horn, and T. R. Neu, "Interaction between biofilm development, structure and detachment in rotating annular reactors," *Bioproc. Biosyst. Eng.*, vol. 31, pp. 619–29, Oct. 2008. 12, 13

[52] N. Cogan and J. Keener, "The Role of the Biofilm Matrix in Structural," *Mathematical Medicine and Biology*, vol. 21, no. 2, p. 147, 2004. 13, 20

[53] M. Y. Chen, D. J. Lee, and J. H. Tay, "Distribution of extracellular polymeric substances in aerobic granules," *Appl. Microbiol. Biot.*, vol. 73, pp. 1463–9, Jan. 2007. 13

[54] S. S. Adav and D.-J. Lee, "Extraction of extracellular polymeric substances from aerobic granule with compact interior structure," *J. Hazard. Mater.*, vol. 154, pp. 1120–6, June 2008. 13

[55] M. Wagner, N. P. Ivleva, C. Haisch, R. Niessner, and H. Horn, "Combined use of confocal laser scanning microscopy (CLSM) and Raman microscopy (RM): investigations on EPS-Matrix," *Water Res.*, vol. 43, pp. 63–76, Jan. 2009. 13

[56] S. Matsumoto, A. Terada, Y. Aoi, S. Tsuneda, E. Alpkvist, C. Picioreanu, and M. van Loosdrecht, "Experimental and simulation analysis of community structure of nitrifying bacteria in a membrane-aerated biofilm," *Water Sci. Technol.*, vol. 55, p. 283, May 2007. 13

[57] J. R. Lawrence, D. R. Korber, B. D. Hoyle, J. W. Costerton, and D. E. Caldwell, "Optical sectioning of microbial biofilms," *J. Bacteriol.*, vol. 173, pp. 6558–67, Oct. 1991. 13

[58] R. Möhle, T. Langemann, M. Haesner, W. Augustin, S. Scholl, T. Neu, D. Hempel, and H. Horn, "Structure and shear strength of microbial biofilms as determined with confocal laser scanning microscopy and fluid dynamic gauging using a novel rotating disc biofilm reactor," *Biotechnol. Bioeng.*, vol. 98, no. 4, pp. 747–755, 2007. 13

[59] C. Staudt, H. Horn, D. C. Hempel, and T. R. Neu, "Volumetric measurements of bacterial cells and extracellular polymeric substance glycoconjugates in biofilms," *Biotechnol. Bioeng.*, vol. 88, pp. 585–92, Dec. 2004. 13, 15

[60] M.-Y. Chen, D.-J. Lee, J.-H. Tay, and K.-Y. Show, "Staining of extracellular polymeric substances and cells in bioaggregates," *Appl. Microbiol. Biot.*, vol. 75, pp. 467–74, May 2007. 13

[61] K. L. Swope and M. C. Flickingerjt, "The Use of Confocal Scanning Laser Microscopy and Other Tools to Characterize Escherichia coli in a High-Cell-Density Synthetic Biofilm," *Biotechnology*, vol. 52, pp. 340–356, 1996. 13

[62] P. Lejeune, "Contamination of abiotic surfaces: what a colonizing bacterium sees and how to blur it," *Trends in Microbiology*, vol. 11, pp. 179–184, Apr. 2003. 13

[63] L. a. Pratt and R. Kolter, "Genetic analysis of Escherichia coli biofilm formation: roles of flagella, motility, chemotaxis and type I pili," *Molecular microbiology*, vol. 30, pp. 285–93, Oct. 1998. 13

[64] P.-C. Shih and C.-T. Huang, "Effects of quorum-sensing deficiency on Pseudomonas aeruginosa biofilm formation and antibiotic resistance," *Journal of Antimicrobial Chemotherapy*, vol. 49, pp. 309–314, 2002. 13

[65] T. R. De Kievit, R. Gillis, S. Marx, C. Brown, and B. H. Iglewski, "Quorum-sensing genes in Pseudomonas aeruginosa biofilms: their role and expression patterns," *Applied and environmental microbiology*, vol. 67, no. 4, pp. 1865–1873, 2001. 13

[66] J. D. Shrout, D. L. Chopp, C. L. Just, M. Hentzer, M. Givskov, and M. R. Parsek, "The impact of quorum sensing and swarming motility on Pseudomonas aeruginosa biofilm formation is nutritionally conditional," *Molecular microbiology*, vol. 62, pp. 1264–77, Dec. 2006. 13

[67] V. E. Wagner, D. Bushnell, L. Passador, A. I. Brooks, and B. H. Iglewski, "Microarray analysis of Pseudomonas aeruginosa quorum-sensing regulons: effects of growth phase and environment," *Journal of Bacteriology*, vol. 185, no. 7, pp. 2080–2095, 2003. 13

[68] R. E. McKinney, "Bacteria Growth," in *Environmental Pollution Control Microbiology*, ch. 3, pp. 43–71, New York: Marcel Dekker, Inc., 2004. 13

[69] M. C. van Loosdrecht, D. Eikelboom, A. Gjaltema, A. Mulder, L. Tijhuis, and J. J. Heijnen, "Biofilm Structures," *Water science and technology*, vol. 32, no. 8, pp. 35–43, 1995. 13

[70] S. N. Medírcio, V. a. Leão, and M. C. Teixeira, "Specific growth rate of sulfate reducing bacteria in the presence of manganese and cadmium," *Journal of hazardous materials*, vol. 143, pp. 593–6, May 2007. 13

[71] J. Russell, W. Sharp, and R. Baldwin, "The effect of pH on maximum bacterial growth rate and its possible role as a determinant of bacterial competition in the rumen," *Journal of Animal Science*, vol. 48, no. 2, p. 251, 1979. 13

[72] J. Therion, A. Kistner, and J. Kornelius, "Effect of pH on Growth Rates of Rumen Amylolytic and Lactilytic Bacteria," *Applied and environmental microbiology*, vol. 44, no. 2, p. 428, 1982. 13

[73] J.-M. Membré, M. Kubaczka, and C. Chéné, "Combined effects of pH and sugar on growth rate of Zygosaccharomyces rouxii, a bakery product spoilage yeast," *Applied and environmental microbiology*, vol. 65, pp. 4921–5, Nov. 1999. 13

[74] V. Allan, L. Macaskie, and M. Callow, "Development of a pH gradient within a biofilm is dependent upon the limiting nutrient," *Biotechnology Letters*, vol. 21, no. 5, pp. 407–413, 1999. 13

[75] K. a. Presser, D. a. Ratkowsky, and T. Ross, "Modelling the growth rate of Escherichia coli as a function of pH and lactic acid concentration," *Applied and environmental microbiology*, vol. 63, pp. 2355–60, June 1997. 13

[76] P. Stoodley, D. DeBeer, and H. M. Lappin-Scott, "Influence of electric fields and pH on biofilm structure as related to the bioelectric effect," *Antimicrobial agents and chemotherapy*, vol. 41, pp. 1876–9, Sept. 1997. 13

[77] L. Rosso, J. R. Lobry, S. Bajard, and J. P. Flandrois, "Convenient Model To Describe the Combined Effects of Temperature and pH on Microbial Growth," *Applied and environmental microbiology*, vol. 61, pp. 610–6, Feb. 1995. 13, 130, 131, 203

[78] H.-C. Flemming and J. Wingender, "The biofilm matrix," *Nat. Rev. Microbiol.*, vol. 8, no. 9, pp. 623–633, 2010. 15, 16

[79] I. Sutherland, "Biofilm exopolysaccharides: a strong and sticky framework," *Microbiology*, vol. 147, p. 3, Jan. 2001. 15

[80] J. Wingender, T. R. Neu, and H.-C. Flemming, *Microbial Extracellular Polymeric Substances: characterization, Structure, and Function*. Berlin: Springer, 1999. 15

[81] A. Decho, "Exopolymer microdomains as a structuring agent for heterogeneity within microbial biofilms," in *Microbial sediments* (R. E. Riding and S. M. Awramik, eds.), pp. 1–9, Springer Verlag, 2000. 15

[82] M. Marvasi, P. T. Visscher, and L. Casillas Martinez, "Exopolymeric substances (EPS) from Bacillus subtilis: polymers and genes encoding their synthesis," *FEMS microbiology letters*, vol. 313, pp. 1–9, Dec. 2010. 15, 16

[83] H.-C. Flemming, T. R. Neu, and D. J. Wozniak, "The EPS matrix: the "house of biofilm cells"," *Journal of bacteriology*, vol. 189, pp. 7945–7, Nov. 2007. 15, 16

[84] M. Kuehn, M. Mehl, M. Hausner, H. J. Bungartz, and S. Wuertz, "Time-resolved study of biofilm architecture and transport processes using experimental and simulation techniques: the role of EPS," *Water Sci. Technol.*, vol. 43, pp. 143–50, Jan. 2001. 15

[85] D. de Beer, P. Stoodley, F. Roe, and Z. Lewandowski, "Effects of biofilm structures on oxygen distribution and mass transport," *Biotechnology and bioengineering*, vol. 43, pp. 1131–8, May 1994. 15, 59

[86] H. C. Flemming and J. Wingender, "Relevance of microbial extracellular polymeric substances (EPSs)–Part II: Technical aspects," *Water science and technology : a journal of the International Association on Water Pollution Research*, vol. 43, pp. 9–16, Jan. 2001. 16, 17

[87] S. D. Weber, W. Ludwig, K.-H. Schleifer, and J. Fried, "Microbial composition and structure of aerobic granular sewage biofilms," *Applied and environmental microbiology*, vol. 73, pp. 6233–40, Oct. 2007. 16, 17

[88] H. Ivnitsky, I. Katz, D. Minz, G. Volvovic, E. Shimoni, E. Kesselman, R. Semiat, and C. G. Dosoretz, "Bacterial community composition and structure of biofilms developing on nanofiltration membranes applied to wastewater treatment," *Water research*, vol. 41, pp. 3924–35, Sept. 2007. 16, 17

[89] H. J. Eberl and R. Sudarsan, "Exposure of biofilms to slow flow fields: the convective contribution to growth and disinfection," *Journal of theoretical biology*, vol. 253, pp. 788–807, Aug. 2008. 16, 17

[90] B. E. Rittmann, D. Stilwell, J. C. Garside, G. L. Amy, C. Spangenberg, A. Kalinsky, and E. Akiyoshi, "Treatment of a colored groundwater by ozone-biofiltration: pilot studies and modeling interpretation," *Water research*, vol. 36, pp. 3387–97, July 2002. 16, 17

[91] W. Fang, J. Y. Hu, and S. L. Ong, "Influence of phosphorus on biofilm formation in model drinking water distribution systems," *Journal of applied microbiology*, vol. 106, pp. 1328–35, Apr. 2009. 16, 17

[92] C. S. Laspidou and B. E. Rittmann, "Modeling the development of biofilm density including active bacteria, inert biomass, and extracellular polymeric substances," *Water research*, vol. 38, no. 14-15, pp. 3349–61, 2004. 16, 17, 21

[93] a. P. Miqueleto, C. C. Dolosic, E. Pozzi, E. Foresti, and M. Zaiat, "Influence of carbon sources and C/N ratio on EPS production in anaerobic sequencing batch biofilm reactors for wastewater treatment," *Bioresource technology*, vol. 101, pp. 1324–30, Feb. 2010. 16, 17, 197

[94] J. Wingender, M. Strathmann, A. Rode, A. Leis, and H. C. Flemming, "Isolation and biochemical characterization of extracellular polymeric substances from Pseudomonas aeruginosa," *Methods Enzymol.*, vol. 336, pp. 302–314, 2001. 16

[95] Y. Zhang, "An analysis tool to quantify the efficiency of cell tethering and firm-adhesion in the parallel-plate flow chamber," *Journal of Immunological Methods*, vol. 278, pp. 305–317, July 2003. 16

[96] S. Ude, D. L. Arnold, C. D. Moon, T. Timms-Wilson, and A. J. Spiers, "Biofilm formation and cellulose expression among diverse environmental Pseudomonas isolates," *Environmental microbiology*, vol. 8, pp. 1997–2011, Nov. 2006. 16

[97] H. Laue, A. Schenk, H. Li, L. Lambertsen, T. R. Neu, S. r. Molin, and M. S. Ullrich, "Contribution of alginate and levan production to biofilm formation by Pseudomonas syringae," *Microbiology (Reading, England)*, vol. 152, pp. 2909–18, Oct. 2006. 16

[98] P. Hoa, *Effect of Nutrients on Extracellular Polymeric Substance Production and Sludge Characteristics*. PhD thesis, Asian Institute of Technology, 2002. 16

[99] A. Varki and N. Sharon, "Historical Background and Overview," in *Essentials of Glycobiology* (A. Varki, R. D. Cummings, J. D. Esko, H. H. Freeze, P. Stanley, C. R. Bertozzi, G. W. Hart, and M. E. Etzler, eds.), ch. 1, Cold Spring Harbor Laboratory Press, 2 ed., 2009. 16

[100] K. Kajiwara and T. Miyamoto, "Progress in Structural Characterization of Functional Polysaccharides," in *Polysaccharides: Structural Diversity And Functional Versatility* (S. Dumitriu, ed.), ch. 1, pp. 1–40, CRC Press, 2 ed., 2005. 16

[101] L. J. Stal, "Microphytobenthos, their extracellular polymeric substances, and the morphogenesis of intertidal sediments," *Geomicrobiology Journal*, vol. 20, pp. 463–478, 2003. 16

[102] N. Vazquez-Laslop, H. Lee, R. Hu, and A. A. Neyfakh, "Molecular sieve mechanism of selective release of cytoplasmic proteins by osmotically shocked Escherichia coli," *Journal of Bacteriology*, vol. 183, no. 8, pp. 2399–2404, 2001. 16

[103] S. Geresh, I. Adin, E. Yarmolinsky, and M. Karpasas, "Characterization of the extracellular polysaccharide of Porphyridium sp.: molecular weight determination and rheological properties," *Carbohydrate polymers*, vol. 50, pp. 183–189, 2002. 16

[104] C. Picioreanu, I. M. Head, K. P. Katuri, M. C. M. van Loosdrecht, and K. Scott, "A computational model for biofilm-based microbial fuel cells," *Water Res.*, vol. 41, pp. 2921–40, July 2007. 17

[105] C. S. Huey, *Polyhydroxybutyrate (PHB) Production from Cafeteria Wastes under Anoxic and Aerobic Conditions in Sequencing Batch Reactor*. PhD thesis, Universiti Teknologi Malaysia, 2006. 17

[106] J. Zhu and J. J. Mekalanos, "Quorum sensing-dependent biofilms enhance colonization in Vibrio cholerae," *Developmental cell*, vol. 5, pp. 647–56, Oct. 2003. 17

[107] S. M. Faruque, K. Biswas, S. M. N. Udden, Q. S. Ahmad, D. A. Sack, G. B. Nair, and J. J. Mekalanos, "Transmissibility of cholera: in vivo-formed biofilms and their relationship to infectivity and persistence in the environment," *Proceedings of the National Academy of Sciences of the United States of America*, vol. 103, pp. 6350–6355, Apr. 2006. 17

[108] J. W. Costerton, "Bacterial Biofilms: A Common Cause of Persistent Infections," *Science*, vol. 284, pp. 1318–1322, May 1999. 17

[109] R. Donlan, "Biofilms: survival mechanisms of clinically relevant microorganisms," *Clin. Microbiol. Rev.*, vol. 15, no. 2, pp. 167–193, 2002. 17

[110] M. E. Davey and G. A. O'toole, "Microbial biofilms: from ecology to molecular genetics," *Microbiology and molecular biology reviews : MMBR*, vol. 64, pp. 847–67, Dec. 2000. 17

[111] M. R. Parsek and P. K. Singh, "Bacterial biofilms: an emerging link to disease pathogenesis," *Annual review of microbiology*, vol. 57, pp. 677–701, Jan. 2003. 17

[112] G. A. James, E. Swogger, R. Wolcott, E. deLancey Pulcini, P. Secor, J. Sestrich, J. W. Costerton, and P. S. Stewart, "Biofilms in chronic wounds," *Wound Repair and Regeneration*, vol. 16, no. 1, pp. 37–44, 2008. 17

[113] I. B. Beech and J. Sunner, "Biocorrosion: towards understanding interactions between biofilms and metals," *Curr. Opin. Biotech.*, vol. 15, pp. 181–6, June 2004. 17

[114] E. Alt, F. Leipold, D. Milatovic, G. Lehmann, S. Heinz, and A. Schömig, "Hydrogen peroxide for prevention of bacterial growth on polymer biomaterials," *The Annals of thoracic surgery*, vol. 68, pp. 2123–8, Dec. 1999. 17, 118

[115] E. Presterl, M. Suchomel, M. Eder, S. Reichmann, A. Lassnigg, W. Graninger, and M. Rotter, "Effects of alcohols, povidone-iodine and hydrogen peroxide on biofilms of Staphylococcus epidermidis," *The Journal of antimicrobial chemotherapy*, vol. 60, pp. 417–20, Aug. 2007. 17

[116] P. S. Stewart, F. Roe, J. Rayner, J. G. Elkins, Z. Lewandowski, U. a. Ochsner, and D. J. Hassett, "Effect of catalase on hydrogen peroxide penetration into Pseudomonas aeruginosa biofilms," *Applied and environmental microbiology*, vol. 66, pp. 836–8, Feb. 2000. 17

[117] T. Zmantar, B. Kouidhi, H. Miladi, K. Mahdouani, and A. Bakhrouf, "A microtiter plate assay for Staphylococcus aureus biofilm quantification at various pH levels and hydrogen peroxide supplementation," *The new microbiologica : official journal of the Italian Society for Medical, Odontoiatric, and Clinical Microbiology (SIMMOC)*, vol. 33, pp. 137–45, Apr. 2010. 17, 118

[118] H. Goossens, M. Ferech, R. Vander Stichele, and M. Elseviers, "Outpatient antibiotic use in Europe and association with resistance: a cross-national database study," *Lancet*, vol. 365, no. 9459, pp. 579–87, 2005. 17

[119] R. Pompl, F. Jamitzky, T. Shimizu, B. Steffes, W. Bunk, H.-U. Schmidt, M. Georgi, K. Ramrath, W. Stolz, R. W. Stark, T. Urayama, S. Fujii, and G. E. Morfill, "The effect of low-temperature plasma on bacteria as observed by repeated AFM imaging," *New Journal of Physics*, vol. 11, p. 115023, Nov. 2009. 17

[120] A. Poiata, I. Motrescu, A. Nastuta, D. Creanga, and G. Popa, "Microorganism response to atmospheric pressure helium plasma DBD treatment," *Journal of Electrostatics*, vol. 68, pp. 128–131, Apr. 2010. 17, 113

[121] L.-n. Li, "Targeted Antimicrobial Therapy Against Streptococcus mutans Establishes Protective Non-cariogenic Oral Biofilms and Reduces Subsequent Infection," *International Journal of Oral Science*, vol. 2, pp. 66–73, Apr. 2010. 17

[122] J. Ward, "Mathematical modelling of quorum sensing control in biofilms," in *Control of biofilm infections by signal manipulation* (N. Balaban, ed.), ch. 5, pp. 79–108, Springer Berlin Heidelberg, 2008. 19, 20

[123] M. A. S. Chaudhry and S. a. Beg, "A Review on the Mathematical Modeling of Biofilm Processes: Advances in Fundamentals of Biofilm Modeling," *Chem. Eng. Technol.*, vol. 21, pp. 701–710, Sept. 1998. 19

[124] C. Picioreanu, J.-U. Kreft, M. Klausen, J. Haagensen, T. Tolker-Nielsen, and S. Molin, "Microbial motility involvement in biofilm structure formation a 3D modelling study," *Water Science & Technology*, vol. 55, p. 337, May 2007. 19, 188

[125] J. B. Xavier, C. Picioreanu, and M. C. M. van Loosdrecht, "Assessment of three-dimensional biofilm models through direct comparison with confocal microscopy imaging," *Water Sci. Technol.*, vol. 49, pp. 177–85, Jan. 2004. 19, 23

[126] A. Stevens and F. Schweitzer, "Aggregation Induced by Diffusing and Nondiffusing Media," in *Dynamics of Cell and Tissue Motion* (W. Alt, A. Deutsch, and G. Dunn, eds.), pp. 183–192, Birkhäuser, 1997. 19

[127] J. W. Choi, J. Min, W. H. Lee, and S. B. Lee, "Mathematical model for a three-phase fluidized bed biofilm reactor in wastewater treatment," *Biotechnol. Bioproc. E.*, vol. 4, pp. 58–58, Apr. 1999. 19

[128] K. Anguige, J. R. King, and J. P. Ward, "A multi-phase mathematical model of quorum sensing in a maturing Pseudomonas aeruginosa biofilm," *Math. Biosci.*, vol. 203, pp. 240–76, Oct. 2006. 19, 20

[129] B. P. Ayati and I. Klapper, "A Multiscale Model of Biofilm as a Senescence-Structured Fluid," *Multiscale Modeling & Simulation*, vol. 6, no. 2, pp. 347–365, 2007. 19

[130] B. G. Smith, B. L. Vanughan Jr., and D. L. Chopp, "The Extended Finite Element Method For Boundary Layer Problems in Biofilm Growth," *Communications in Applied Mathematics and Computational Science*, vol. 2, no. 1, pp. 35–56, 2007. 19

[131] E. Casey, B. Glennon, and G. Hamer, "Biofilm development in a membrane-aerated biofilm reactor: effect of flow velocity on performance," *Biotechnology and bioengineering*, vol. 67, pp. 476–86, Feb. 2000. 19

[132] H. T. Chang and B. E. Rittmann, "Mathematical modeling of biofilm on activated carbon," *Environmental Science & Technology*, vol. 21, pp. 273–280, Mar. 1987. 19

[133] N. Cogan, "Two-fluid model of biofilm disinfection," *Bulletin of mathematical biology*, vol. 70, pp. 800–19, Apr. 2008. 19, 20

[134] R. Duddu, D. L. Chopp, and B. Moran, "A two-dimensional continuum model of biofilm growth incorporating fluid flow and shear stress based detachment," *Biotechnol. Bioeng.*, vol. 103, pp. 92–104, May 2009. 20

[135] J. Dockery and I. Klapper, "Finger Formation in Biofilm Layers," *SIAM J. Appl. Math.*, vol. 62, no. 3, pp. 853–869, 2001. 20

[136] M. Gardner, "Mathematical Games: The fantastic combinations of John Conway's new solitaire game "life"," *Scientific American*, vol. 223, no. 4, pp. 120–123, 1970. 20

[137] E. Ben-Jacob, O. Schochet, A. Tenenbaum, I. Cohen, A. Czirok, and T. Vicsek, "Generic modelling of cooperative growth patterns in bacterial colonies," *Nature*, vol. 368, pp. 46–49, 1994. 20

[138] J. W. Wimpenny and R. Colasanti, "A Uniifying Hypothesis for the Structure of Microbial Biofilms Based on Cellular Automaton Models," *FEMS Microbiology Ecology*, vol. 22, pp. 1–16, 1997. 20

[139] C. Picioreanu, M. C. van Loosdrecht, and J. J. Heijnen, "A new combined differential-discrete cellular automaton approach for biofilm modeling: application for growth in gel beads," *Biotechnol. Bioeng.*, vol. 57, pp. 718–31, Mar. 1998. 21

[140] G. Pizarro, D. Griffeath, and D. R. Noguera, "Quantitative cellular automaton model for biofilms," *Journal of Environmental Engineering*, vol. 127, p. 782, 2001. 21

[141] G. E. Pizarro, C. García, R. Moreno, and M. E. Sepúlveda, "Two-dimensional cellular automaton model for mixed-culture biofilm," *Water science and technology : a journal of the International Association on Water Pollution Research*, vol. 49, pp. 193–8, Jan. 2004. 21

[142] C. Picioreanu, M. C. van Loosdrecht, and J. J. Heijnen, "Two-dimensional model of biofilm detachment caused by internal stress from liquid flow," *Biotechnol. Bioeng.*, vol. 72, pp. 205–18, Jan. 2001. 21, 191

[143] S. M. Hunt, M. A. Hamilton, J. T. Sears, G. Harkin, and J. Reno, "A computer investigation of chemically mediated detachment in bacterial biofilms," *Microbiology*, vol. 149, pp. 1155–1163, May 2003. 21

[144] H. Eberl, C. Picioreanu, J. J. Heijnen, and M. C. M. van Loosdrecht, "A three-dimensional numerical study on the correlation of spatial structure, hydrodynamic conditions, and mass transfer and conversion in biofilms," *Chem. Eng. Sci.*, vol. 55, pp. 6209–6222, Dec. 2000. 21

[145] M. C. M. van Loosdrecht, J. J. Heijnen, H. Eberl, J. Kreft, and C. Picioreanu, "Mathematical modelling of biofilm structures," *Antonie van Leeuwenhoek*, vol. 81, pp. 245–56, Aug. 2002. 21

[146] I. Chang, "A three-dimensional, stochastic simulation of biofilm growth and transport-related factors that affect structure," *Microbiology*, vol. 149, pp. 2859–2871, Oct. 2003. 21

[147] S. Lee, J. Park, and H. Pak, "Stochastic Cellular Automata Modeling on Biofilm Growth in Allelopathy," *Journal-Korean*, vol. 48, no. February, pp. 231–235, 2006. 21

[148] C. S. Laspidou and B. E. Rittmann, "A unified theory for extracellular polymeric substances, soluble microbial products, and active and inert biomass," *Water research*, vol. 36, pp. 2711–20, June 2002. 21

[149] C. S. Laspidou and B. E. Rittmann, "Non-steady state modeling of extracellular polymeric substances, soluble microbial products, and active and inert biomass," *Water research*, vol. 36, pp. 1983–92, Apr. 2002. 21

[150] C. S. Laspidou and B. E. Rittmann, "Evaluating trends in biofilm density using the UMCCA model," *Water research*, vol. 38, no. 14-15, pp. 3362–3372, 2004. 21

[151] F. Graner and J. Glazier, "Simulation of biological cell sorting using a two-dimensional extended Potts model," *Phys. Rev. Lett.*, vol. 69, pp. 2013–2016, Sept. 1992. 19, 21

[152] E. L. Stott, N. F. Britton, J. A. Glazier, and M. Zajac, "Stochastic Simulation of Benign Avascular Tumour growth using the Potts Model," *the Potts model, Mathematical and Computer Modelling*, vol. 30, pp. 183–198, 1999. 22

[153] N. J. Poplawski, A. Shirinifard, M. Swat, and J. a. Glazier, "Simulation of single-species bacterial-biofilm growth using the Glazier-Graner-Hogeweg model and the CompuCell3D modeling environment," *Math. Biosci. Eng.*, vol. 5, pp. 355–88, Apr. 2008. 22

[154] A. Balter, M. H. Merks, N. J. Poplawski, M. Swat, and J. A. Glazier, "II. 4 The GlazierGranerHogeweg Model: Extensions, Future Directions, and Opportunities for Further Study," in *Single-Cell-Based Models in Biology and Medicine* (A. A. R. A., M. A. J. Chaplain, and K. A. Rejniak, eds.), ch. II.4, pp. 151–167, Birkhäuser, 2007. 22

[155] J. J. Tapia and R. M. D'Souza, "Parallelizing the Cellular Potts Model on graphics processing units," *Computer Physics Communications*, vol. 182, pp. 857–865, Apr. 2011. 22

[156] D. Drasdo and S. Hohme, "Individual-based approaches to birth and death in avascular tumors," *Math. Comput. Model.*, vol. 37, pp. 1163–1175, June 2003. 22, 24

[157] D. Drasdo and S. Höhme, "A single-cell-based model of tumor growth in vitro: monolayers and spheroids," *Phys. biol.*, vol. 2, pp. 133–47, Sept. 2005. 22

[158] J. Galle, G. Aust, G. Schaller, T. Beyer, and D. Drasdo, "Individual cell-based models of the spatialtemporal organization of multicellular systemsAchievements and limitations," *Cytom. Part A*, vol. 710, no. June, pp. 704–710, 2006. 22

[159] D. Drasdo and M. Loeffler, "Individual-based models to growth and folding in one-layered tissues: intestinal crypts and early development," *Prog. Nonlin.*, vol. 47, pp. 245–256, Aug. 2001. 22

[160] A. M. Martins, C. Picioreanu, J. J. Heijnen, and M. C. van Loosdrecht, "Three-dimensional dual-morphotype species modeling of activated sludge flocs," *Environ. Sci. Technol*, vol. 38, no. 21, pp. 5632–5641, 2004. 22, 24

[161] A. Janulevicius, M. C. M. van Loosdrecht, A. Simone, and C. Picioreanu, "Cell flexibility affects the alignment of model myxobacteria," *Biophysical journal*, vol. 99, pp. 3129–38, Nov. 2010. 22, 23

[162] J. U. Kreft and J. W. Wimpenny, "Effect of EPS on biofilm structure and function as revealed by an individual-based model of biofilm growth," *Water Sci. Technol.*, vol. 43, pp. 135–41, Jan. 2001. 22, 23, 39

[163] J. U. Kreft, "Biofilms promote altruism," *Microbiology (Reading, England)*, vol. 150, pp. 2751–60, Aug. 2004. 22

[164] C. Picioreanu, J. Kreft, and M. van Loosdrecht, "Particle-based multidimensional multispecies biofilm model," *Appl. Environ. Microb.*, vol. 70, no. 5, p. 3024, 2004. 22, 23, 24, 31, 39

[165] J. B. Xavier, C. Picioreanu, and M. C. M. van Loosdrecht, "A modelling study of the activity and structure of biofilms in biological reactors," *Biofilms*, vol. 1, pp. 377–391, Oct. 2004. 22, 39

[166] J. B. Xavier, C. Picioreanu, and M. C. M. van Loosdrecht, "A framework for multidimensional modelling of activity and structure of multispecies biofilms," *Environ. Microbiol.*, vol. 7, pp. 1085–103, Aug. 2005. 22, 23, 24, 30, 31, 39, 92, 110, 188, 195

[167] J. B. Xavier, C. Picioreanu, S. A. Rani, M. C. M. van Loosdrecht, and P. S. Stewart, "Biofilm-control strategies based on enzymic disruption of the extracellular polymeric substance matrix–a modelling study," *Microbiology (Reading, England)*, vol. 151, pp. 3817–32, Dec. 2005. 22

[168] J. U. Kreft, G. Booth, and J. W. Wimpenny, "BacSim, a simulator for individual-based modelling of bacterial colony growth," *Microbiology (Reading, England)*, vol. 144 Pt 1, pp. 3275–87, Dec. 1998. 22, 39

[169] J. U. Kreft, C. Picioreanu, J. W. Wimpenny, and M. C. van Loosdrecht, "Individual-based modelling of biofilms," *Microbiology (Reading, England)*, vol. 147, pp. 2897–912, Nov. 2001. 23, 24, 26, 31, 39, 195

[170] L. Lardon, J.-P. Steyer, N. Bernet, and C. Le Page, "Modeling and Analysis of Biofilms Formation and Evolution in Wastewater Treatment Processes using Multi-Agent Systems," in *Integrated assessment and decision support. iEMSs. 1st biennial meeting of the International Environmental Modelling and Software Society* (A. Rizzoli and A. Jakeman, eds.), (Lugano, Swizerland), pp. 226–231, 2002. 23

[171] E. Alpkvist, C. Picioreanu, M. C. M. van Loosdrecht, and A. Heyden, "Three-dimensional biofilm model with individual cells and continuum EPS matrix," *Biotechnol. Bioeng.*, vol. 94, no. 5, pp. 961–979, 2006. 23, 24, 26, 110, 188, 195, 196

[172] N. Mabrouk, J.-D. Mathias, and G. Deffuant, "Viability and Resilience of a Bacterial Biofilm Individual-Based Model," in *Viability and Resilience of Complex Systems* (G. Deffuant and N. Gilbert, eds.), ch. 6, pp. 131–157, Springer, 2011. 23

[173] M. A. Newstead, *Modelling the Development and Growth of Bacterial Biofilm*. PhD thesis, Loughborough University, 2010. 24

[174] H. M. Byrne, J. R. King, D. L. S. McElwain, and L. Preziosi, "A two-phase model of solid tumour growth," *Applied Mathematics*, vol. 16, pp. 567–573, 2003. 24

[175] R. Chandler and P. Northrop, "Random number generation," 2003. 31

[176] D. Drasdo, R. Kree, and J. McCaskill, "Monte Carlo approach to tissue-cell populations," *Physical review E*, vol. 52, no. 6, pp. 6635–6657, 1995. 39

[177] Y. Chen and D. Cai, "Inexact overlapped block Broyden methods for solving nonlinear equations," *Applied Mathematics and Computation*, vol. 136, pp. 215–228, Mar. 2003. 43

[178] S. Kimmel, R. Roberts, and G. Ziegler, "Optimization of exopolysaccharide production by Lactobacillus delbrueckii subsp. bulgaricus RR grown in a semidefined medium," *Applied and environmental microbiology*, vol. 64, p. 659, Feb. 1998. 56, 195

[179] C. J. Ingham and E. Ben Jacob, "Swarming and complex pattern formation in Paenibacillus vortex studied by imaging and tracking cells," *BMC microbiology*, vol. 8, p. 36, Jan. 2008. 76

[180] M. a. Bees, P. Andresén, E. Mosekilde, and M. Givskov, "The interaction of thin-film flow, bacterial swarming and cell differentiation in colonies of Serratia liquefaciens," *Journal of mathematical biology*, vol. 40, pp. 27–63, Jan. 2000. 76

[181] E. Ben-Jacob, "Learning from bacteria about natural information processing," *Annals of the New York Academy of Sciences*, vol. 1178, pp. 78–90, Oct. 2009. 76

[182] V. Nehra, A. Kumar, and H. Dwivedi, "Atmospheric Non-Thermal Plasma Sources," *International Journal of Engineering*, vol. 2, no. 1, pp. 53–68, 2008. 111, 112

[183] A. Fridman, *Plasma Chemistry*. Cambridge: Cambridge Univ Pr, 1st ed., 2008. 112, 116

[184] R. Hippler, *Low temperature plasma physics: fundamental aspects and applications*. Wiley-VCH, 1st ed., 2001. 112

[185] M. Laroussi, "Low-Temperature Plasmas for Medicine?," *IEEE Transactions on Plasma Science*, vol. 37, pp. 714–725, June 2009. 112, 116

[186] M. Kuzuya, S.-i. Kondo, and Y. Sasai, "Addendum - Recent advances in plasma techniques for biomedical and drug engineering," *Pure and Applied Chemistry*, vol. 77, no. 4, pp. 667–682, 2005. 112

[187] U.S. Environmental Protection Agency (E143-03), "Using Non-Thermal Plasma to Control Air Pollutants Using Non-Thermal Plasma to Control Air Pollutants (Report No. EPA-456/R-05-001)," tech. rep., 2005. 112

[188] B. R. Locke, M. Sato, P. Sunka, M. R. Hoffmann, and J.-S. Chang, "Electrohydraulic Discharge and Nonthermal Plasma for Water Treatment," *Industrial & Engineering Chemistry Research*, vol. 45, pp. 882–905, Feb. 2006. 112, 117, 118

[189] C. M. Du, J. Wang, L. Zhang, H. X. Li, H. Liu, and Y. Xiong, "The application of a non-thermal plasma generated by gasliquid gliding arc discharge in sterilization," *New Journal of Physics*, vol. 14, p. 013010, Jan. 2012. 112

[190] E. Sosnin, E. Stoffels, M. Erofeev, I. Kieft, and S. Kunts, "The Effects of UV Irradiation and Gas Plasma Treatment on Living Mammalian Cells and Bacteria: A Comparative Approach," *IEEE Transactions on Plasma Science*, vol. 32, pp. 1544–1550, Aug. 2004. 113

[191] M. Laroussi, "Nonthermal decontamination of biological media by atmospheric-pressure plasmas: review, analysis, and prospects," *IEEE*

Transactions on Plasma Science, vol. 30, pp. 1409–1415, Aug. 2002. 113, 116

[192] M. Laroussi and F. Leipold, "Evaluation of the roles of reactive species, heat, and UV radiation in the inactivation of bacterial cells by air plasmas at atmospheric pressure," *International Journal of Mass Spectrometry*, vol. 233, pp. 81–86, Apr. 2004. 113, 116, 117

[193] J. Goree, B. Liu, and D. Drake, "Gas flow dependence for plasma-needle disinfection of S. mutans bacteria," *Journal of Physics D: Applied Physics*, vol. 39, pp. 3479–3486, Aug. 2006. 113

[194] E. Stoffels, I. E. Kieft, and R. E. J. Sladek, "Superficial treatment of mammalian cells using plasma needle," *Journal of Physics D: Applied Physics*, vol. 36, pp. 2908–2913, Dec. 2003. 113

[195] P. Sunka, M. Babicky, M. Clupek, M. Fuciman, P. Lukes, M. Simek, J. Benes, B. Locke, and Z. Majcherova, "Potential Applications of Pulse Electrical Discharges in Water," *acta physica slovaca*, vol. 54, no. 2, pp. 135–145, 2004. 113

[196] M. Laroussi, "Low Temperature Plasma-Based Sterilization: Overview and State-of-the-Art," *Plasma Processes and Polymers*, vol. 2, pp. 391–400, June 2005. 116

[197] B. L. Diffey, "A mathematical model of the biologically effective dose of solar UVA received by patients undergoing oral psoralen photochemotherapy for psoriasis," *Physics in medicine and biology*, vol. 26, pp. 1129–35, Nov. 1981. 117

[198] E. Witkin, "Ultraviolet mutagenesis and inducible DNA repair in Escherichia coli," *Bacteriological reviews*, vol. 40, no. 4, p. 869, 1976. 117

[199] T. Matsunaga, K. Hieda, and O. Nikaido, "Wavelength Dependent Formation of Thymine Dimers and (6-4) Photoproducts in DNA by Monochromatic Ultraviolet light Rangeing From 150 to 365 nm," *Photochemistry and photobiology*, vol. 54, no. 3, pp. 403–410, 1991. 117

[200] J. Cadet, E. Sage, and T. Douki, "Ultraviolet radiation-mediated damage to cellular DNA," *Mutation research*, vol. 571, pp. 3–17, Apr. 2005. 117

[201] K. Kelly-Wintenberg, T. C. Montie, C. Brickman, J. R. Roth, A. K. Carr, K. Sorge, L. C. Wadsworth, and P. P. Y. Tsai, "Room temperature sterilization of surfaces and fabrics with a One Atmosphere Uniform Glow Discharge Plasma," *Journal of Industrial Microbiology and Biotechnology*, vol. 20, pp. 69–74, Jan. 1998. 117

[202] M. Laroussi, G. S. Sayler, B. B. Glascock, B. McCurdy, M. E. Pearce, N. G. Bright, and C. M. Malott, "Images of Biological Samples Undergoing Sterilization by a Glow Discharge at Atmospheric Pressure," *IEEE Transactions on Plasma Science*, vol. 27, no. 1, pp. 34–35, 1999. 117

[203] D. A. Mendis, M. Rosenberg, and F. Azam, "A note on the possible electrostatic disruption of bacteria," *IEEE Transactions on Plasma Science*, vol. 28, no. 4, pp. 1304–1306, 2000. 117

[204] M. Laroussi, D. A. Mendis, and M. Rosenberg, "Plasma interaction with microbes," *New Journal of Physics*, vol. 41, no. 5, pp. 41.1–41.10, 2003. 117

[205] D. X. Liu, P. Bruggeman, F. Iza, M. Z. Rong, and M. G. Kong, "Global model of low-temperature atmospheric-pressure He + H 2 O plasmas," *Plasma Sources Science and Technology*, vol. 19, p. 025018, Apr. 2010. 117

[206] R. Burlica, M. Kirkpatrick, and B. Locke, "Formation of reactive species in gliding arc discharges with liquid water," *Journal of Electrostatics*, vol. 64, pp. 35–43, Jan. 2006. 117

[207] K.-Y. Shih and B. R. Locke, "Chemical and Physical Characteristics of Pulsed Electrical Discharge Within Gas Bubbles in Aqueous Solutions," *Plasma Chemistry and Plasma Processing*, vol. 30, pp. 1–20, Dec. 2009. 117

[208] J.-L. Brisset, B. Benstaali, D. Moussa, J. Fanmoe, and E. Njoyim-Tamungang, "Acidity control of plasma-chemical oxidation: applications to

dye removal, urban waste abatement and microbial inactivation," *Plasma Sources Science and Technology*, vol. 20, p. 034021, June 2011. 118

[209] R. Burlica, R. Grim, K.-Y. Shih, D. Balkwill, and B. R. Locke, "Bacteria Inactivation Using Low Power Pulsed Gliding Arc Discharges with Water Spray," *Plasma Processes and Polymers*, vol. 7, pp. 640–649, Aug. 2010. 118

[210] M. Tachikawa, K. Yamanaka, and K. Nakamuro, "Studies on the Disinfection and Removal of Biofilms by Ozone Water Using an Artificial Microbial Biofilm System," *Ozone: Science & Engineering*, vol. 31, pp. 3–9, Jan. 2009. 118, 136, 202

[211] R. Barnes and D. Caskey, "Using Ozone in the Prevention of Bacterial Biofilm Formation and Scaling," *Water Conditioning and Purification International*, pp. 70–77, 2002. 118, 121

[212] B. Eliasson and U. Kogelschatz, "Nonequilibrium volume plasma chemical processing," *IEEE Transactions on Plasma Science*, vol. 19, no. 6, pp. 1063–1077, 1991. 118

[213] I. Tanarro, V. J. Herrero, E. Carrasco, and M. Jiménez-Redondo, "Cold plasma chemistry and diagnostics," *Vacuum*, vol. 85, pp. 1120–1124, June 2011. 118

[214] C. Hamelin and Y. S. Chung, "Optimalconditions for mutagenesis by ozone in Escherichia coli K-12," *Mutation Research*, vol. 24, pp. 271–279, 1974. 120, 121

[215] C. Hamelin and Y. Chung, "Rapid test for assay of ozone sensitivity in Escherichia coli," *Molecular & general genetics : MGG*, vol. 145, pp. 191–4, May 1976. 120, 121

[216] I. R. Komanapalli and B. H. Lau, "Ozone-induced damage of Escherichia coli K-12," *Applied microbiology and biotechnology*, vol. 46, pp. 610–4, Dec. 1996. 120, 121

[217] W. a. Pryor, G. L. Squadrito, and M. Friedman, "A new mechanism for the toxicity of ozone," *Toxicology letters*, vol. 82-83, pp. 287–93, Dec. 1995. 120, 121

[218] C. Hamelin, F. Sarhan, and Y. S. Chung, "Induction of deoxyribonucleic acid degradation inEscherichia coli by ozone," *Cellular and Molecular Life Sciences*, vol. 1, pp. 1578–1579, 1978. 121

[219] G. R. Finch, D. W. Smith, and M. E. Stiles, "Doseresponse of Escherichia coli in ozone demand-free phosphate buffer," *Water research*, vol. 22, no. 12, pp. 1563–1570, 1988. 121

[220] J. Hoigné and H. Bader, "Rate Constants of Reactions of Ozone with Organic and Inorganic Compounds in Water - I Non-Dissociation Organic Compounds," *Water Research*, vol. 17, pp. 173–183, 1983. 121

[221] J. Hoigné and H. Bader, "Rate constants of reactions of ozone with organic and inorganic compounds in waterII:: Dissociating organic compounds," *Water Research*, vol. 17, no. 2, pp. 185–194, 1983. 121

[222] J. Hoigné, H. Bader, W. Haag, and J. Staehelin, "Rate constants of reactions of ozone with organic and inorganic compounds in waterIII. Inorganic compounds and radicals," *Water Research*, vol. 19, no. 8, pp. 993–1004, 1985. 121

[223] N. Hunt, "Inactivation of Escherichia coli with ozone: chemical and inactivation kinetics," *Water Research*, vol. 33, pp. 2633–2641, Aug. 1999. 121, 202

[224] M. Viera, P. Guiamet, M. de Mele, and H. Videla, "Use of dissolved ozone for controlling planktonic and sessile bacteria in industrial cooling systems," *International Biodeterioration & Biodegradation*, vol. 44, pp. 201–207, Dec. 1999. 121

[225] M. Viera, P. Guiamet, M. De Mele, and H. Videla, "Biocidal action of ozone against planktonic and sessile Pseudomonas fluorescens," *Biofouling*, vol. 14, no. 2, pp. 131–141, 1999. 121

[226] V. Puri, "Ozone pretreatment to increase digestibility of lignocellulose," *Biotechnology letters*, vol. 5, no. 11, pp. 773–776, 1983. 121

[227] G. Y. Pan, C.-L. Chen, J. S. Gratzl, and H.-m. Chang, "Model compound studies on the cleavage of glycosidic bonds by ozone in aqueous solution," *Research on chemical*, vol. 21, no. 3-5, p. 205, 1995. 121, 136, 201, 202

[228] Y. Wang, R. I. Hollingsworth, and D. L. Kasper, "Ozonolysis for selectively depolymerizing polysaccharides containing beta-D-aldosidic linkages," *Proceedings of the National Academy of Sciences of the United States of America*, vol. 95, pp. 6584–9, June 1998. 121

[229] J. Duan and D. L. Kasper, "Oxidative depolymerization of polysaccharides by reactive oxygen/nitrogen species," *Glycobiology*, vol. 21, pp. 401–9, Apr. 2011. 121, 123

[230] M. Dytczak, K. Londry, H. Siegrist, and J. Oleszkiewicz, "Extracellular polymers in partly ozonated return activated sludge: impact on flocculation and dewaterability," *Water Science & Technology*, vol. 54, p. 155, Aug. 2006. 121

[231] S. M. Brown, M. L. Howell, M. L. Vasil, a. J. Anderson, and D. J. Hassett, "Cloning and characterization of the katB gene of Pseudomonas aeruginosa encoding a hydrogen peroxide-inducible catalase: purification of KatB, cellular localization, and demonstration that it is essential for optimal resistance to hydrogen peroxide," *Journal of bacteriology*, vol. 177, pp. 6536–44, Nov. 1995. 122, 123

[232] B. Chance, H. Sies, and A. Boveris, "Hydroperoxide metabolism in mammalian organs," *Physiological reviews*, vol. 59, pp. 527–605, July 1979. 122

[233] G. K. Nyberg and J. Carlsson, "Metabolic inhibition of Peptostreptococcus anaerobius decreases the bactericidal effect of hydrogen peroxide," *Antimicrobial agents and chemotherapy*, vol. 20, pp. 726–30, Dec. 1981. 122, 123

[234] B. González-Flecha and B. Demple, "Metabolic sources of hydrogen peroxide in aerobically growing Escherichia coli," *Journal of Biological Chemistry*, vol. 270, no. 23, pp. 13681–13687, 1995. 122, 123

[235] J. DiGuiseppi, "Oxygen toxicity in Streptococcus sanguis. The relative importance of superoxide and hydroxyl radicals," *Journal of Biological Chemistry*, vol. 257, no. 8, pp. 4046–4051, 1982. 122

[236] P. A. Hyslop, D. B. Hinshaw, W. A. Halsey, I. U. Schraufstatter, Jr., R. D. Sauerheber, R. G. Spragg, J. H. Jackson, and C. G. Cochrane, "Mechanisms of oxidant-mediated cell injury. The glycolytic and mitochondrial pathways of ADP phosphorylation are major intracellular targets inactivated by hydrogen," *Journal of Biological*, vol. 263, no. 4, pp. 1665–1675, 1988. 122

[237] C. Bonnineau, B. Bonet, N. Corcoll, and H. Guasch, "Catalase in fluvial biofilms: a comparison between different extraction methods and example of application in a metal-polluted river," *Ecotoxicology (London, England)*, vol. 20, pp. 293–303, Jan. 2011. 122

[238] X. Liu, F. Roe, A. Jesaitis, and Z. Lewandowski, "Resistance of biofilms to the catalase inhibitor 3-amino-1,2, 4-triazole," *Biotechnology and bioengineering*, vol. 59, p. 156, Oct. 1998. 122

[239] J. Switala and P. C. Loewen, "Diversity of properties among catalases," *Archives of biochemistry and biophysics*, vol. 401, pp. 145–54, May 2002. 122, 123, 201

[240] D.-H. Shin, Y.-S. Choi, and Y.-H. Cho, "Unusual properties of catalase A (KatA) of Pseudomonas aeruginosa PA14 are associated with its biofilm peroxide resistance," *Journal of bacteriology*, vol. 190, pp. 2663–70, Apr. 2008. 122

[241] T. Samejima and J. T. Yang, "Reconstitution of Acid-Denatured Catalase," *The Journal of biological chemistry*, vol. 730, no. 14, pp. 3256–3261, 1963. 122

[242] S. C. Fry, "Oxidative scission of plant cell wall polysaccharides by ascorbate-induced hydroxyl radicals," *Biochemical Journal*, vol. 332, no. Pt 2, p. 507, 1998. 123

[243] W. L. Cochran, G. a. McFeters, and P. S. Stewart, "Reduced susceptibility of thin Pseudomonas aeruginosa biofilms to hydrogen peroxide and monochloramine," *Journal of applied microbiology*, vol. 88, pp. 22–30, Jan. 2000. 123

[244] Z. Kiraly, H. M. El-Zahaby, and Z. Klement, "Role of extracellular polysaccharide (EPS) slime of plant pathogenic bacteria in protecting cells to reactive oxygen species," *Journal of Phytopathology*, vol. 145, no. 2-3, pp. 59–68, 1997. 123

[245] J. S. Park, H. Choi, and K. H. Ahn, "The reaction mechanism of catalytic oxidation with hydrogen peroxide and ozone in aqueous solution," *Water science and technology : a journal of the International Association on Water Pollution Research*, vol. 47, pp. 179–84, Jan. 2002. 123

[246] B. r. E. Christensen, H. N. Trø nnes, K. Vollan, O. Smidsrø d, and R. Bakke, "Biofilm removal by low concentrations of hydrogen peroxide," *Biofouling: The Journal of Bioadhesion and Biofilm Research*, vol. 2, no. 2, pp. 165–175, 1990. 123

[247] J. L. Slonczewski, M. Fujisawa, M. Dopson, and T. A. Krulwich, "Cytoplasmic pH measurement and homeostasis in bacteria and archaea," *Advances in microbial physiology*, vol. 55, pp. 1–79, Jan. 2009. 123, 124, 125

[248] R. D. Kitko, J. C. Wilks, G. M. Garduque, and J. L. Slonczewski, "Osmolytes contribute to pH homeostasis of Escherichia coli," *PloS one*, vol. 5, p. e10078, Jan. 2010. 124

[249] P. D. Cotter and C. Hill, "Surviving the acid test: responses of gram-positive bacteria to low pH," *Microbiology and Molecular Biology Reviews*, vol. 67, no. 3, 2003. 124, 125

[250] R. E. Marquis, "Oxygen metabolism, oxidative stress and acid-base physiology of dental plaque biofilms," *Journal of industrial microbiology*, vol. 15, pp. 198–207, Sept. 1995. 124

[251] G. Svensäter, U. B. Larsson, E. C. Greif, D. G. Cvitkovitch, and I. R. Hamilton, "Acid tolerance response and survival by oral bacteria," *Oral microbiology and immunology*, vol. 12, pp. 266–73, Oct. 1997. 124

[252] H. Boke, B. Aslim, and G. Alp, "The role of resistance to bile salts and acid tolerance of exopolysaccharides (EPSS) produced by yogurt starter bacteria," *Archives of Biological Sciences*, vol. 62, no. 2, pp. 323–328, 2010. 125

[253] J. Welin-Neilands and G. Svensäter, "Acid tolerance of biofilm cells of Streptococcus mutans," *Applied and environmental microbiology*, vol. 73, pp. 5633–8, Sept. 2007. 125

[254] J. Welin, J. Wilkins, D. Beighton, K. Wrzesinski, S. Fey, P. Mose-Larsen, I. Hamilton, and G. Svensäter, "Effect of acid shock on protein expression by biofilm cells of Streptococcus mutans," *FEMS Microbiology Letters*, vol. 227, pp. 287–293, Oct. 2003. 125

[255] K. McNeill and I. Hamilton, "Acid tolerance response of biofilm cells of Streptococcus mutans," *FEMS Microbiology Letters*, vol. 221, pp. 25–30, Apr. 2003. 125

[256] K. Scher, U. Romling, and S. Yaron, "Effect of heat, acidification, and chlorination on Salmonella enterica serovar Typhimurium cells in a biofilm formed at the air-liquid interface," *Applied and environmental*, vol. 71, no. 3, pp. 1163–1168, 2005. 125

[257] Y.-H. Li, M. N. Hanna, G. Svensäter, R. P. Ellen, and D. G. Cvitkovitch, "Cell density modulates acid adaptation in Streptococcus mutans: implications for survival in biofilms," *Journal of*, vol. 183, no. 23, pp. 6875–6884, 2001. 125

[258] R. A. Burne, R. G. Quivey, and R. E. Marquis, "Physiologic homeostasis and stress responses in oral biofilms," in *Biofilms, Volume 310 of Methods in enzymology* (J. N. Abelson, M. I. Simon, and R. J. Doyle, eds.), vol. 310, ch. 33, pp. 441–460, Academic Press, 1999. 125

[259] R. J. Rowbury, N. H. Hussain, and M. Goodson, "Extracellular proteins and other components as obligate intermediates in the induction of a range of acid tolerance and sensitisation responses in Escherichia coli," *FEMS microbiology letters*, vol. 166, pp. 283–8, Sept. 1998. 125

[260] R. J. Rowbury and M. Goodson, "An extracellular acid stress-sensing protein needed for acid tolerance induction in Escherichia coli," *FEMS microbiology letters*, vol. 174, pp. 49–55, May 1999. 125

[261] A. Erdincler and P. Vesilind, "Effect of sludge cell disruption on compactibility of biological sludges," *Water science and technology*, vol. 42, no. 9, pp. 119–126, 2000. 125

[262] D. a. Cherepanov, a. Y. Mulkidjanian, and W. Junge, "Transient accumulation of elastic energy in proton translocating ATP synthase," *FEBS letters*, vol. 449, pp. 1–6, Apr. 1999. 125

[263] K. Förster, P. Turina, F. Drepper, W. Haehnel, S. Fischer, P. Gräber, and J. Petersen, "Proton transport coupled ATP synthesis by the purified yeast H+ -ATP synthase in proteoliposomes," *Biochimica et biophysica acta*, vol. 1797, pp. 1828–37, Nov. 2010. 125

[264] P. Kaczmarek, W. Szczepanik, and M. Jezowska-Bojczuk, "Acidbase, coordination and oxidative properties of systems containing ATP, L-histidine and Ni(II) ions," *Dalton Trans.*, pp. 3653–3657, 2005. 125

[265] S. Jain and S. Nath, "Kinetic model of ATP synthase: pH dependence of the rate of ATP synthesis," *FEBS letters*, vol. 476, pp. 113–7, July 2000. 125

[266] D. Banerjee, M. Jana, and S. Mahapatra, "Production of Exopolysaccharide by Endophytic Stemphylium SP," *Micología Aplicada International*, vol. 21, no. 2, pp. 57–62, 2009. 125

[267] B. Zisu and N. P. Shah, "Effects of pH, temperature, supplementation with whey protein concentrate, and adjunct cultures on the production of exopolysaccharides by Streptococcus thermophilus 1275," *Journal of dairy science*, vol. 86, pp. 3405–15, Nov. 2003. 125

[268] A. Kuntiya, P. Hanmoungjai, C. Techapun, K. Sasaki, and P. Seesuriyachan, "Influence of pH , sucrose concentration and agitation speed on exopolysaccharide production by Lactobacillus confusus TISTR 1498 using coconut water as a raw material substitute," *Journal of Science and Technology*, vol. 4, no. 02, pp. 318–330, 2010. 125

[269] A. El-Shamy and E. Nehad, "Optimization of polysaccharide production by Alternaria alternata," *www.Gate2Biotech.com*, vol. 1, no. 9, pp. 1–6, 2010. 125

[270] J. Wingender, K.-E. Jäger, and H.-C. Flemming, "Interaction between extracellular polysaccharides and enzymes," in *Microbial Extracellular Polymeric Substances: Characterization, Structure, and Function* (J. Wingender, T. R. Neu, and H.-C. Flemming, eds.), ch. 13, p. 231, Springer, 1999. 125

[271] J. Sherma, *High Performance Liquid Chromatography in Phytochemical Analysis: Volume 102 of Chromatographic Science Series*. CRC Press, 2010. 137

[272] B. Kirby, "Species and charge transport," in *Micro- and Nanoscale Fluid Mechanics: Transport in Microfluidic Devices* (B. Kirby, ed.), ch. 11, Cambridge University Press, 2010. 137

[273] D. X. Liu, a. J. Yang, X. H. Wang, M. Z. Rong, F. Iza, and M. G. Kong, "Wall fluxes of reactive oxygen species of an rf atmospheric-pressure plasma and their dependence on sheath dynamics," *Journal of Physics D: Applied Physics*, vol. 45, p. 305205, Aug. 2012. 139, 155, 202

[274] E. Stoffels, a. J. Flikweert, W. W. Stoffels, and G. M. W. Kroesen, "Plasma needle: a non-destructive atmospheric plasma source for fine surface treatment of (bio)materials," *Plasma Sources Science and Technology*, vol. 11, pp. 383–388, Nov. 2002. 140

[275] C.-C. Hsu and Y.-J. Yang, "The Increase of the Jet Size of an Atmospheric-Pressure Plasma Jet by Ambient Air Control," *IEEE Transactions on Plasma Science*, vol. 38, pp. 496–499, Mar. 2010. 140

[276] J. Liu, *Generation and characterisation of cold atmospheric liquid-containing plasmas*. PhD thesis, Loughborough University, 2011. 141, 201

[277] C. Jiang, M.-T. Chen, C. Schaudinn, A. Gorur, P. T. Vernier, J. W. Costerton, D. E. Jaramillo, P. P. Sedghizadeh, and M. A. Gundersen, "Pulsed Atmospheric-Pressure Cold Plasma for Endodontic Disinfection," *IEEE Transactions on Plasma Science*, vol. 37, no. 7, pp. 1190–1195, 2009. 186

[278] M. Laroussi, C. Tendero, X. Lu, S. Alla, and W. L. Hynes, "Inactivation of Bacteria by the Plasma Pencil," *Plasma Processes and Polymers*, vol. 3, pp. 470–473, Aug. 2006. 186

[279] F. Marchal, H. Robert, N. Merbahi, C. Fontagné-Faucher, M. Yousfi, C. E. Romain, O. Eichwald, C. Rondel, and B. Gabriel, "Inactivation of Gram-positive biofilms by low-temperature plasma jet at atmospheric pressure," *Journal of Physics D: Applied Physics*, vol. 45, p. 345202, Aug. 2012. 186

[280] G. Fridman, A. D. Brooks, M. Balasubramanian, A. Fridman, A. Gutsol, V. N. Vasilets, H. Ayan, and G. Friedman, "Comparison of Direct and Indirect Effects of Non-Thermal Atmospheric-Pressure Plasma on Bacteria," *Plasma Processes and Polymers*, vol. 4, pp. 370–375, May 2007. 186

[281] C. Picioreanu, M. Van Loosdrecht, and J. Heijnen, "Discrete-Differential Modelling of Biofilm Structure," *Water Sci. Technol.*, vol. 39, no. 7, pp. 115–122, 1999. 191

[282] B. E. Rittmann, a. O. Schwarz, H. J. Eberl, E. Morgenroth, J. Perez, M. van Loosdrecht, and O. Wanner, "Results from the multi-species bench-

mark problem (BM3) using one-dimensional models," *Water Sci. Technol.*, vol. 49, pp. 163–8, Jan. 2004. 195, 196

[283] C. Picioreanu, M. C. Van Loosdrecht, and J. J. Heijnen, "Effect of diffusive and convective substrate transport on biofilm structure formation: a two-dimensional modeling study," *Biotechnol. Bioeng.*, vol. 69, pp. 504–15, Sept. 2000. 195, 198

[284] J. Rychlik and T. May, "The effect of a methanogen, Methanobrevibacter smithii, on the growth rate, organic acid production, and specific ATP activity of three predominant ruminal cellulolytic bacteria," *Current microbiology*, vol. 40, no. 3, pp. 176–180, 2000. 197

[285] M. Twiner and C. Trick, "Possible physiological mechanisms for production of hydrogen peroxide by the ichthyotoxic flagellate Heterosigma akashiwo," *Journal of Plankton Research*, vol. 22, no. 10, pp. 1961–1975, 2000. 201

[286] P. S. Stewart, G. A. McFeters, and C.-T. Huang, "biofilm Control by Antimicrobial Agents," in *Biofilms II: Process Analysis and Appications* (J. D. Bryers, ed.), ch. 11, p. 373, Wily-Liss, 2000. 201, 202

[287] N. Al-Baldawi and R. Abercrombie, "Cytoplasmic hydrogen ion diffusion coefficient," *Biophysical journal*, vol. 61, no. 6, pp. 1470–1479, 1992. 203